

DEFORMATION ASSOCIATED WITH DISCONTINUITIES
ALONG STRIKE-SLIP FAULTS

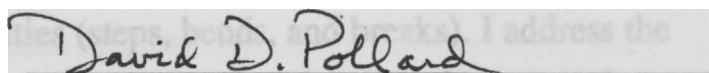
A DISSERTATION
SUBMITTED TO THE DEPARTMENT OF GEOLOGY
AND THE COMMITTEE ON GRADUATE STUDIES
OF STANFORD UNIVERSITY
IN PARTIAL FULFILLMENT OF THE REQUIREMENTS
FOR THE DEGREE OF
DOCTOR OF PHILOSOPHY

Roland Bürgmann

August 1993

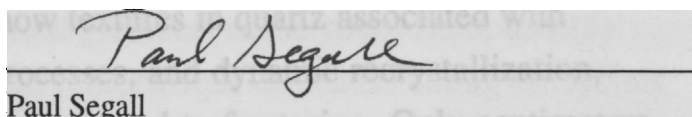
© Copyright by Roland Bürgmann 1993
All Rights Reserved

I certify that I have read this dissertation and that in my opinion it is fully adequate, in scope and quality, as a dissertation for the degree of Doctor of Philosophy.

A rectangular box containing a handwritten signature in cursive script that reads "David D. Pollard".

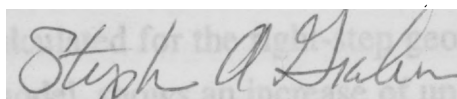
David D. Pollard (Principal Adviser)

I certify that I have read this dissertation and that in my opinion it is fully adequate, in scope and quality, as a dissertation for the degree of Doctor of Philosophy.

A rectangular box containing a handwritten signature in cursive script that reads "Paul Segall".

Paul Segall

I certify that I have read this dissertation and that in my opinion it is fully adequate, in scope and quality, as a dissertation for the degree of Doctor of Philosophy.

A rectangular box containing a handwritten signature in cursive script that reads "Stephen A. Graham".

Stephen A. Graham

Approved for the University Committee on Graduate Studies:

A rectangular box containing a handwritten signature in cursive script that reads "Judith J. Maloster".

ABSTRACT

Deformation associated with faults is concentrated near fault terminations and discontinuities (steps, bends, and breaks). I address the character of this deformation at a variety of scales, both in time and space.

Left-lateral strike-slip faults in the Lake Edison Granodiorite (central Sierra Nevada, California) are composed of echelon segments. Relative displacements across the faults apparently are transferred between segments by ductile shearing at right steps, and by extensional fracturing at left steps. The granodiorite within right steps displays mylonitic foliation, and thin sections show textures in quartz associated with dislocation glide, recovery processes, and dynamic recrystallization, whereas textures in feldspar are related to fracturing. Only centimeters outside the right steps, the rock fabric is approximately isotropic and deformation is accommodated by mineralized, opening-mode fractures. To accommodate slip transfer across right steps, rock apparently was squeezed vertically out of the step by ductile flow. Concentrations of mobile and immobile elements indicate that mass solution transfer was not significant. The stress field calculated for the right-step geometry, using an elastic boundary element model, shows an increase of up to 25 MPa in the mean compressive stress within the step relative to that outside. This difference in stress may have produced the contrasting behaviors of the granitic rock.

The structures associated with fault terminations in the Lake Edison Granodiorite change from dilatant splay fractures only, to splay fractures and ductile fabrics on opposing sides of the fault, to ductile fabrics ahead of the fault, with decreasing distance from a younger neighboring pluton and, presumably, with increased temperatures. The local magnitudes and spatial distributions of the maximum tensile stress, the mean stress, and the maximum shear stress correlate, respectively, with the distributions of different deformation mechanisms. Most experimentally derived power-

law flow laws do not predict these behaviors. A constitutive flow law that includes a pressure effect through correlation with pressure-dependent solidus temperatures appears to be more successful in predicting the observed distribution of ductile fabrics.

Fault slip distributions are commonly assumed to be symmetrical about a central slip maximum. However, slip distributions in nature are often asymmetric. While slip along a blade- or penny-shaped fault is expected to follow an elliptical distribution after a single slip event in an elastic material, the slip distribution may be modified if the fault propagates or if additional slip events occur. Analytically and numerically computed fault-slip distributions indicate that: (1) changes in the (frictional) strength along a fault; (2) spatial gradients in the stress field; and (3) inelastic deformation near fault terminations can cause strong deviations from idealized symmetrical distributions. In particular, the interaction of faults that are located within about one fault radius of one another, strongly influences slip gradients. Inelastic processes, caused by stress perturbations in the stepover region of echelon faults, may link individual segments along a fault zone whose slip distribution resembles that of a single fault of the combined segment lengths.

The southern Santa Cruz Mountains are closely associated with a left bend along the right-lateral San Andreas fault (SAF). The Loma Prieta area on the northeast side of the SAF consists of fault-bounded blocks that rise along active, deeply rooted, reverse and oblique-slip faults. Six samples from a transect across this area yield concordant apatite fission track ages averaging 4.6 ± 0.5 Ma. These ages date the time of cooling below ≈ 110 °C and suggest that about 3 km of unroofing has occurred over the last 4.6 m.y. To further define the extent and distribution of this young uplift, we used morphometric analyses of the youthful topography of the area. Steep drainage slopes and high local relief indicate that the area northeast of the SAF forms a well-defined zone of high uplift bounded on the northeast by the southwest-dipping Foothills thrust system. In contrast, the region on the southwest side of the SAF is

characterized by a broad upwarping and folding, more subdued topography, old fission track ages, and mean Quaternary uplift rates of $\approx 0.1-0.4$ mm/yr. Geodetic data suggest that the southern Santa Cruz Mountains repeatedly rise and subside due to strain accumulation and earthquakes on several active faults. An additional deformation element that involves reverse slip, averaging 2-3 mm/yr on the Foothills thrust system, must occur to explain the longer-term uplift pattern in the Loma Prieta area. The asymmetry in deformation on opposite sides of the SAF reflects the contrasting rock types on opposite sides of the fault, the influence of preexisting structures, and the interaction with neighboring faults of the SAF system.

Transient increases in strain rate following large earthquakes may be responsible for clustering of seismic events in space and time. The post-seismic velocity field in the epicentral region of the Loma Prieta earthquake differs significantly from displacement rates measured in the two decades preceding the event. The post-earthquake displacement rates along the Black Mountain profile, crossing the San Andreas fault 40 km northwest of the Loma Prieta epicenter, do not differ significantly from those determined from 20 years of trilateration measurements and more recent GPS and VLBI measurements. However, station velocities along the Loma Prieta profile, through the epicentral region, significantly exceed pre-earthquake rates and changed orientation within 20 km of the Loma Prieta rupture. Aseismic oblique reverse slip at a rate of 8 cm/yr on a sub-vertical fault and reverse slip at a rate of 6 cm/yr on a thrust fault of the Sargent-Berrocal fault zone can explain the observed motions. Rapid post-earthquake fault slip may be a precursory phenomenon to impending rupture, and could influence the timing of future earthquakes on nearby faults affected by the associated stress field.

ACKNOWLEDGMENTS

Thanks are due to a great number of people for their help with my research efforts and for their general support. Special thanks go to my advisers Dave Pollard and Paul Segall. They are great role models as scientists and teachers and have been extremely supportive throughout the last four years. I would like to thank them and the members of my research committee for guiding and supporting my research of such a diverse number of exciting problems that resulted in this dissertation. It has been a privilege to be a member of the Geomechanics and Crustal Deformation research groups and I thank all my fellow students and postdocs for their help, moral support, fun conversations, and friendship. Especially, I would like to thank Ramón Arrowsmith for being a great friend and collaborator and for sharing his excitement about our work and life beyond geology. Thora Arnadottir, Yijun Du, Jeff Freymuller, and Andy Thomas wrote helpful programs and gave advice on various aspects of this dissertation. I was also fortunate to have been able to collaborate and interact with several researchers at Stanford and at the U.S.G.S. in Menlo Park. In particular, I would like to thank Trevor Dumitru, Mike Lisowski, Grant Marshall, Bob McLaughlin, Mark Murray, and Jerry Svarc for their advice and help. Steve Martel helped introduce me to the geologic and natural wonders of the Lake Edison area, and I thank him for many fun discussions and his cooperation in several of the projects. Financial support in the form of a Stanford - U.S.G.S. Graduate Fellowship, a Donath Honors Fellowship in Earth Sciences, several Geological Society of America Grants and Mc Gee Awards, and support provided by the Stanford Rock Fracture Project allowed me to carry out my thesis work.

Foremost of all, I would like to thank my parents for always supporting my plans, even when it meant being separated by such a great distance (Danke für alles Mum und Paps!). And finally, my thanks go to Betty for being my best buddy for life.

TABLE OF CONTENTS

ABSTRACT.....	iv
ACKNOWLEDGMENTS.....	vii
TABLE OF CONTENTS.....	viii
LIST OF TABLES.....	xii
LIST OF ILLUSTRATIONS.....	xiii
INTRODUCTION.....	1
1. INFLUENCE OF THE STATE OF STRESS ON THE BRITTLE- DUCTILE TRANSITION IN GRANITIC ROCK: EVIDENCE FROM FAULT STEPS IN THE SIERRA NEVADA, CALIFORNIA.....	4
Abstract.....	4
Introduction.....	5
Fault zones in the Mt. Abbott Quadrangle: Previous work.....	6
Deformation associated with fault steps.....	8
Stress field associated with fault steps.....	11
Discussion.....	14
Conclusions.....	18
Acknowledgments.....	18
References.....	19
2. STRAIN ACCOMMODATION ABOUT STRIKE-SLIP FAULT DISCONTINUITIES IN GRANITIC ROCK UNDER BRITTLE- TO-DUCTILE CONDITIONS.....	22
Abstract.....	22
Introduction.....	23
Deformation along discontinuous faults.....	25
Brittle-to-ductile deformation.....	27
Structural Development of fault zones in the Lake Edison Granodiorite.....	28
Left-lateral strike-slip faults.....	28
Timing.....	31

Fluid flow.....	31
Brittle fracture and ductile flow.....	32
Fault terminations.....	33
Left stepovers.....	34
Right stepovers.....	37
Macroscale structure.....	37
Microscale structure	47
Mass solution transfer: mineralogic and geochemical analyses	52
Temperature dependent deformation style at fault terminations	56
Stress-dependent deformation about echelon faults	60
Left steps.....	62
Right steps	64
Conclusions.....	69
Acknowledgments.....	70
References	70

3. SLIP DISTRIBUTIONS ON FAULTS: EFFECTS OF STRESS

GRADIENTS, INELASTIC DEFORMATION AND FAULT

INTERACTION.....	78
Abstract.....	78
Introduction	79
Measured slip distributions and elementary models.....	84
Single-slip-event fault displacements.....	84
Cumulative fault displacements	90
Slip distributions on single faults with non-uniform stress drops.....	93
Linear stress distributions along single faults.....	93
Non-linear stress distributions: An end zone model....	96
A symmetric linear stress distribution.....	100
Effects of inelastic strain at fault ends and fault interaction on slip distributions.....	103

Effects of inelastic deformation at fault ends	103
Fault interaction across echelon steps.....	106
Discussion and conclusions.....	113
References	117
4. RISE AND FALL OF THE SOUTHERN SANTA CRUZ MOUNTAINS, CALIFORNIA, FROM FISSION TRACKS, GEOMORPHOLOGY, AND GEODESY	124
Abstract.....	124
Introduction	125
Methods.....	128
Apatite fission-track dating.....	128
Geomorphic analysis.....	132
Geodetic analysis	134
Tectonics of the Santa Cruz Mountains.....	135
Results.....	143
Fission track dating.....	143
Geomorphic analysis.....	146
Recent crustal deformation	153
Interpretation and conclusions.....	167
Acknowledgments.....	170
Appendix: Fission track laboratory methods.....	171
References	172
5. POST-SEISMIC STRAIN FOLLOWING THE 1989 LOMA PRIETA EARTHQUAKE FROM REPEATED GPS MEASUREMENTS AND LEVELING	183
Abstract.....	183
Introduction and motivation.....	184
Methods: GPS data collection, processing, and error analysis ...	189
Data collection	189
Data analysis	190
Data precision and accuracy.....	193
Methods: Leveling data and analysis.....	198

Corrections and error analysis	203
Post-Loma Prieta earthquake displacement field.....	210
Horizontal displacement field from GPS	210
Vertical displacements from leveling	216
Pre-Loma Prieta earthquake displacement field.....	218
Data interpretation and model	223
Post-seismic strain anomaly	223
Alternative models.....	224
Mechanical models from nonlinear inversions	226
Discussion of model results.....	230
Discussion.....	232
Thrusting northeast of the San Andreas fault	232
Post-seismic rate changes.....	236
Implications for seismic hazard in the San Francisco Bay region.....	237
References	241

LIST OF TABLES

Table 2.1	Major and trace element concentrations of undeformed and deformed granite samples from XRF analyses.....	54
Table 4.1	Fission track counting, age, and track length data.	145
Table 5.1	Post-seismic elevation changes along leveling Line 4.....	201
Table 5.2	Well water changes between surveys of Line 1	207
Table 5.3	Fault parameters for geodetically determined models from non-linear inversion of GPS and leveling data.	229

LIST OF ILLUSTRATIONS

Figure 1.1	Map showing Bear Creek region of Mt. Abbot quadrangle, outcrop map of faults, fractures and right steps, and detailed map of step analyzed here.	7
Figure 1.2	Microscopic images of thin sections under crossed Nichols from ductilely deformed step and from outside of step.	10
Figure 1.3	Mean stress and maximum shear-stress distribution and principal-stress trajectories near right step.	13
Figure 1.4	Deformation-mechanism map in principal-stress space based on brittle and ductile deformation laws in strike-slip environment.	16
Figure 2.1	Map showing Bear Creek region of Mt. Abbot quadrangle and the location of the outcrops.	24
Figure 2.2	Map views of Late Cretaceous development of joints and faults in the Mt. Abbot quadrangle.	30
Figure 2.3	Outcrop map of two left-stepping echelon fault segments at site HE90.	36
Figure 2.4	Outcrop map of faults, fractures and right steps at location BA90.	38
Figure 2.5	Outcrop map of faults, fractures and right steps at location HB90.	40
Figure 2.6	Fault-termination structures in the Lake Edison Granodiorite observed at various distances from the neighboring Mono Creek Granite.	41
Figure 2.7	Close-up photograph of fabric contrast across the step-bounding fault at BA80 and HB90.	43
Figure 2.8	Photo micrographs of thin sections from cores 6 and 8 under crossed nichols.	45
Figure 2.9	Thin section maps of quartz, feldspars, and opaques in cores 1 & 9.	49

Figure 2.10	Three mutually perpendicular thin section maps of quartz domains for core 8 from within the stepover at outcrop HB90.....	51
Figure 2.11	Concentration ratios of SiO ₂ , TiO ₂ and Zr between undeformed and deformed samples.....	55
Figure 2.12	Boundary conditions and model geometry of a fault in an elastic, isotropic, and homogeneous material.	58
Figure 2.13	Schematic illustrations of fault-termination structures and components of the stress field that appear to control the deformation processes.....	61
Figure 2.14	Components of the stress field about two faults in left and right-stepping geometry.	63
Figure 2.15	Experimentally determined solidus for Mt. Givens Granodiorite with excess water from 100 - 1000 MPa. ...	67
Figure 2.16	Contour plot of deformation rates at 350 °C as a function of pressure and differential stress.	68
Figure 3.1	Schematic illustration of a structural discontinuity.....	80
Figure 3.2	Schematic illustration of a three-dimensional fault with irregular periphery.....	82
Figure 3.3	Slip distribution measured along the 1987 Superstition Hills earthquake rupture at the earth's surface and contoured slip distribution determined from seismologic strong motion data.....	86
Figure 3.4	The analytically and numerically computed displacement discontinuity D along an isolated fault in an infinite body after a unit shear-stress drop.	88
Figure 3.5	Cumulative slip distributions measured along faults exhumed in mines or along outcrops that provide abundant offset markers.	92
Figure 3.6	Effects of a linear stress distribution along a model fault.	95

Figure 3.7	Effects of non-linear stress distributions along a model fault with a weak center portion and stronger end zones.	98
Figure 3.8	Effects of linear symmetric stress distributions along a model fault.....	102
Figure 3.9	Influence of inelastic deformation (opening splay fractures) at fault terminations on slip.....	105
Figure 3.10	Slip distribution along the left most echelon segment of a pair of faults with zero overlap and various amounts of separation.	108
Figure 3.11	Slip distribution along frictional right-lateral echelon fault segments with 0.1a overlap and 0.1a separation.	110
Figure 3.12	Influence of opening fractures in a right step on fault slip distributions.	112
Figure 3.13	Measured slip distribution in comparison with model of increased frictional resistance of the fault segment in the sandstone bed.	114
Figure 3.14	Measured slip distribution along echelon fault segments in comparison with model of mechanical interaction and inelastic deformation near fault discontinuities.....	116
Figure 4.1	Geologic and fault map of the San Francisco Bay area with existing and new fission track ages.	126
Figure 4.2	Schematic illustration of fission track data patterns expected from latest Cenozoic uplift along the San Andreas.	130
Figure 4.3	Apatite fission track ages shown on geologic map and cross-section of the Loma Prieta area	138
Figure 4.4	Drainage network map of the San Francisco Peninsula digitized from 1:125,000 scale topographic map.	148
Figure 4.5	Subenvelope and envelope contour maps of the San Francisco Peninsula determined from elevations of streams and ridge crests.....	150

Figure 4.6	Residual map (envelope elevations minus subenvelope elevations) showing the distribution of local relief.....	152
Figure 4.7	Modeled uplift magnitudes in the San Francisco Bay area associated with slip on the San Andreas fault at the time of the M 8.3 1906 San Francisco earthquake.....	155
Figure 4.8	Modeled uplift magnitudes (in mm) in the San Francisco Bay area associated with post-seismic relaxation following the 1906 earthquake.....	158
Figure 4.9	Horizontal displacement rates based on 20 years of trilateration measurements and more recent GPS and VLBI results.	159
Figure 4.10	Horizontal displacements derived from GPS, VLBI, and trilateration measurements and modeled uplift magnitudes (in mm) in the Bay Area associated with the M 7.1 1989 Loma Prieta earthquake.....	162
Figure 4.11	Vertical displacement rates in mm/yr computed from a model of the known components of the Bay Area displacement cycle.	164
Figure 4.12	Horizontal displacement rates based on 2 years of post-Loma Prieta-earthquake GPS measurements.....	166
Figure 5.1	Trilateration network, GPS and VLBI station locations in the south San Francisco Bay-Monterey Bay area.....	188
Figure 5.2	Occupation schedule of the Black Mountain profile following the Loma Prieta earthquake.....	191
Figure 5.3	Relative changes in the N, E, and vertical baseline components and line length changes along the Black Mountain profile.....	195
Figure 5.4	Time-displacement plots of pre- and post-Loma Prieta earthquake VLBI measurements in the San Francisco Bay area (Presidio, Fort Ord, and Fort Ord S), relative to a North American reference frame.	197

Figure 5.5	Schematic geologic map of southern San Francisco Bay area showing the location of benchmarks of the leveling line.	199
Figure 5.6	Fault parallel and perpendicular site velocities and uplift rates along the Loma Prieta profile determined from repeated GPS measurements between January 1990 and December 1992	200
Figure 5.7	Topographic profile and elevation changes following the Loma Prieta earthquake determined by leveling.....	202
Figure 5.8	Comparison of uncorrected relative height measurements and the relative heights after corrections and plot of tilt against topographic slope.	205
Figure 5.9	Close-up of NE section of leveling line showing the location of leveling benchmarks and water wells used to test for effects of water-withdrawal.	206
Figure 5.10	Height changes relative to a bedrock site 24 km along leveling Line 1.	208
Figure 5.11	Changes in the N, E, and fault-normal and parallel station positions along the Loma Prieta profile as a function of time.....	211
Figure 5.12	Post-seismic velocity field from GPS and VLBI measurements.....	215
Figure 5.13	SW-to-NE cross-section of the geology (modified from McLaughlin, 1990) and Loma Prieta aftershocks across the San Andreas fault system with post-seismic elevation changes from leveling.....	217
Figure 5.14	Comparison of pre-Loma Prieta earthquake site velocities in the southern San Francisco Bay region with displacements computed from an elastic model. Slip rates on segments of the Bay area fault system used to model the pre-seismic displacement field.	219

Figure 5.15	Post-seismic station velocities with pre-seismic displacement rates subtracted from measured rates together with the model displacements. Cross-section showing the two model faults and aftershocks.	225
Figure 5.16	Measured elevation changes and vertical displacements predicted from the two-fault model.	231
Figure 5.17	Map view of Loma Prieta aftershocks and focal plane solutions of earthquakes > M 2 near the Berrocal fault zone.	233
Figure 5.18	Contoured stress changes induced by the Loma Prieta earthquake on 45° SW dipping fault planes.	235
Figure 5.19	Horizontal stress changes at 10 km depth on N45°W striking strike-slip faults caused by the Loma Prieta earthquake and induced by post-seismic fault slip.	238

INTRODUCTION

The five chapters of this dissertation address the character of deformation associated with faults at a variety of scales, both in time and space. Each chapter forms an independent study and has been prepared for publication in a scientific journal. The common approach to each project is the combination of detailed observations (e.g., microstructural rock fabric analyses, geochemical analyses, field mapping, fission track dating, and geodetic measurements using the Global Positioning System) with mathematical models of deformation to develop a better understanding of the underlying mechanics of deformation near faults. To adequately address these problems, I employed a large number of research tools. Therefore, some of the research work was carried out as collaborative efforts and resulted in multiple authorships of research papers.

Chapter 1, *Influence of the state of stress on the brittle-ductile transition in granitic rock: Evidence from fault steps in the Sierra Nevada, California*, and Chapter 2, *Strain accommodation about strike-slip fault discontinuities in granitic rock under brittle-to-ductile conditions*, are coauthored with David Pollard. He helped initiate the research, joined in the field work, and the papers benefited from our discussions and his careful editing. Chapter 1 is published in *Geology* (1992, v. 20, p. 645-648), and Chapter 2 has been submitted to the *Journal of Structural Geology*. We studied m-scale fault zones in granitic rock in the central Sierra Nevada. Field mapping and microstructural analyses of brittle and ductile deformation near fault terminations and discontinuities allowed us to determine the effects of the faulting-induced stress perturbations on deformation mechanisms. The results have implications for deformation laws of granitic rocks at conditions near the brittle-to-ductile transition.

Chapter 3, *Slip distributions on faults: Effects of stress gradients, inelastic deformation and fault interaction*, will be submitted to the

Journal of Structural Geology. David Pollard contributed to the analytical solutions of slip distributions and patiently reviewed and improved the manuscript. We analytically and numerically determined first-order factors that influence slip distributions along faults in elastic materials. Our results suggest that significant deviations from idealized symmetric slip distributions occur along most faults due to these first-order effects. The submitted paper will benefit from a section on the effects of changes in elastic properties surrounding a fault by Steve Martel. This section is not included in Chapter 3.

Chapter 4, *Rise and fall of the southern Santa Cruz Mountains, California, from fission tracks, geomorphology, and geodesy*, coauthored by myself, Ramón Arrowsmith, Trevor Dumitru, and Bob McLaughlin, has been submitted to the *Journal of Geophysical Research* to be included in a Special Volume on "Tectonics and Topography". Sample preparation and the initial apatite fission track dating was carried out with Ramón Arrowsmith. Trevor Dumitru redated all the samples and contributed sections on fission track analysis and statistics. The discussion of the local geology benefited greatly from recent work by Bob McLaughlin who also helped with the sample collection. We addressed the uplift history along the Santa Cruz Mountains bend of the San Andreas fault since the Pliocene. Geologic information, apatite fission track dates, geomorphic analyses, and geodetic measurements allow us to compare the longer-term uplift with the historic uplift patterns. Our results indicate that faults of the Foothills thrust system northeast of the San Andreas are responsible for much of the Pliocene through Quaternary uplift and may form considerable seismic hazards.

Parts of Chapter 5, *Post-seismic strain following the 1989 Loma Prieta earthquake from repeated GPS measurements and leveling*, have been submitted to the *U.S. Geological Survey Professional Paper 1550* on the 1989 Loma Prieta, California, earthquake. The research project was initiated by Paul Segall and the Crustal Deformation group at the U.S. Geological Survey. Mike Lisowski and Jerry Svarc, who are coauthors of

the manuscript, provided GPS results from the Loma Prieta profile across the epicentral area. GPS measurements along the Black Mountain profile were collected by a large number of Stanford students and faculty. Paul Segall helped with the GPS data processing and Grant Marshall and Ross Stein cooperated in the acquisition of leveling data across the Loma Prieta area. A second manuscript is in preparation for submission to *Nature*. GPS measurements and leveling data show that post-seismic displacement rates within about 20 km of the 1989 Loma Prieta earthquake epicenter exceed pre-seismic velocities. These post-seismic strain transients can be explained by a model of aseismic slip on the San Andreas fault and a thrust fault northeast of the San Andreas fault. The results suggest possible seismic hazards associated with the Foothills thrust system

1. Influence Of The State Of Stress On The Brittle-Ductile Transition In Granitic Rock: Evidence From Fault Steps In The Sierra Nevada, California

ABSTRACT

Left-lateral strike-slip faults in the Lake Edison granodiorite (central Sierra Nevada, California) are composed of en échelon segments. Relative displacements across the faults apparently are transferred between segments by ductile shearing at right steps, and by extensional fracturing at left steps. The granodiorite within right steps displays mylonitic foliation, and thin sections show textures in quartz associated with dislocation glide, recovery processes, and dynamic recrystallization, whereas textures in feldspar are related to fracturing. Only centimetres outside the right steps, the rock fabric is approximately isotropic and deformation is accommodated by mineralized opening-mode fractures. The stress field calculated for the right-step geometry, using a boundary element model, shows an increase of up to 25 MPa mean compressive stress within the step relative to that outside. Apparently this difference in stress produced the contrasting behaviors of the granitic rock. Experimentally derived power-law flow laws do not predict these behaviors.

INTRODUCTION

Brittle fracture and/or ductile flow result when rocks are subjected to stresses that exceed their compressional or tensile strength, thereby forming an upper bound on stresses in the Earth's crust. At relatively low temperatures and low confining pressures brittle faulting occurs, and rock strength increases linearly with depth in the upper crust (Byerlee, 1968). With increasing confining pressure fault localization is suppressed by friction, and cataclastic flow results with microfracturing spreading throughout the rock (Byerlee, 1968). Crystal plasticity is the dominant deformation mechanism at higher temperatures and pressures (Paterson, 1978). Diffusive mass transfer (pressure solution) occurs over a wide range of conditions.

Rheological models based on experimentally derived flow laws predict that the earth's crust can be divided into an upper brittle zone and a lower ductile zone. The brittle-ductile transition zone is thought to exist at depths from 5-15 km, chiefly as a function of the crustal lithology, the geothermal gradient, and the lithostatic load. This is often idealized as the intersection of a pressure-dependent Coulomb failure law and a temperature-dependent creep law, but probably involves a broad region of semibrittle behavior in which both brittle and crystal plastic processes occur. This transition is thought to correspond to the approximate depth above which most accurately determined earthquake foci occur (Sibson, 1983; Smith and Bruhn, 1984). Care has to be taken when using the concept of a brittle-ductile transition (Rutter, 1986), as it can represent the transition from brittle faulting to distributed cataclastic flow, or the transition to flow dominated by intracrystalline plasticity (Scholz, 1988; Shimamoto, 1989). The transition between brittle and plastic regimes in a polycrystalline material involves a broad region of semibrittle behavior in which both brittle and crystal plastic processes occur to accommodate non-localized, ductile (meaning here capacity for distributed flow) strain (Carter and Kirby, 1978; Shimamoto, 1989). Consequently, both

temperature and pressure are thought to affect rock strength in this region (Scholz, 1988).

Most of our knowledge of the rheology of crustal rocks comes from cm-scale laboratory samples, often deformed at strain rates and temperatures well beyond those occurring in nature (e.g., Tullis, 1990). We document a change from brittle to ductile deformation over distances as short as 1 cm from deformation mechanisms observed on metre-scale discontinuities along strike-slip faults in the Sierra Nevada (Fig. 1.1). An analysis of the microstructural fabrics within and outside of compressional fault steps, in combination with models of the associated stress field, shows the influence of the state of stress on the ductile yield strength in this natural example.

FAULT ZONES IN THE MT. ABBOTT QUADRANGLE: PREVIOUS WORK

In the medium-to fine-grained biotite-hornblende granodiorite of Lake Edison (Stern and others, 1981); Fig. 1.1), an episode of extensional fracturing resulted in joints filled with epidote, chlorite, and other hydrothermal constituents soon after the emplacement of the Late Cretaceous pluton (Segall and Pollard, 1983a). Left-lateral strike-slip faulting subsequently (75-79 Ma) nucleated on these mineral-filled planes of weakness (Segall and others, 1990; Segall and Pollard, 1983b). Estimates of temperature and pressure for the faulting event are 300-350 °C and 100-200 MPa, respectively, based on micro structural evidence and the inferred crystallization pressures in the area (Ague and Brimhall, 1988; Martel and others, 1988). Offsets along the faulted joints are in the range of centimetres to 2 m, and fault segments range from a few metres to several tens of metres in length.

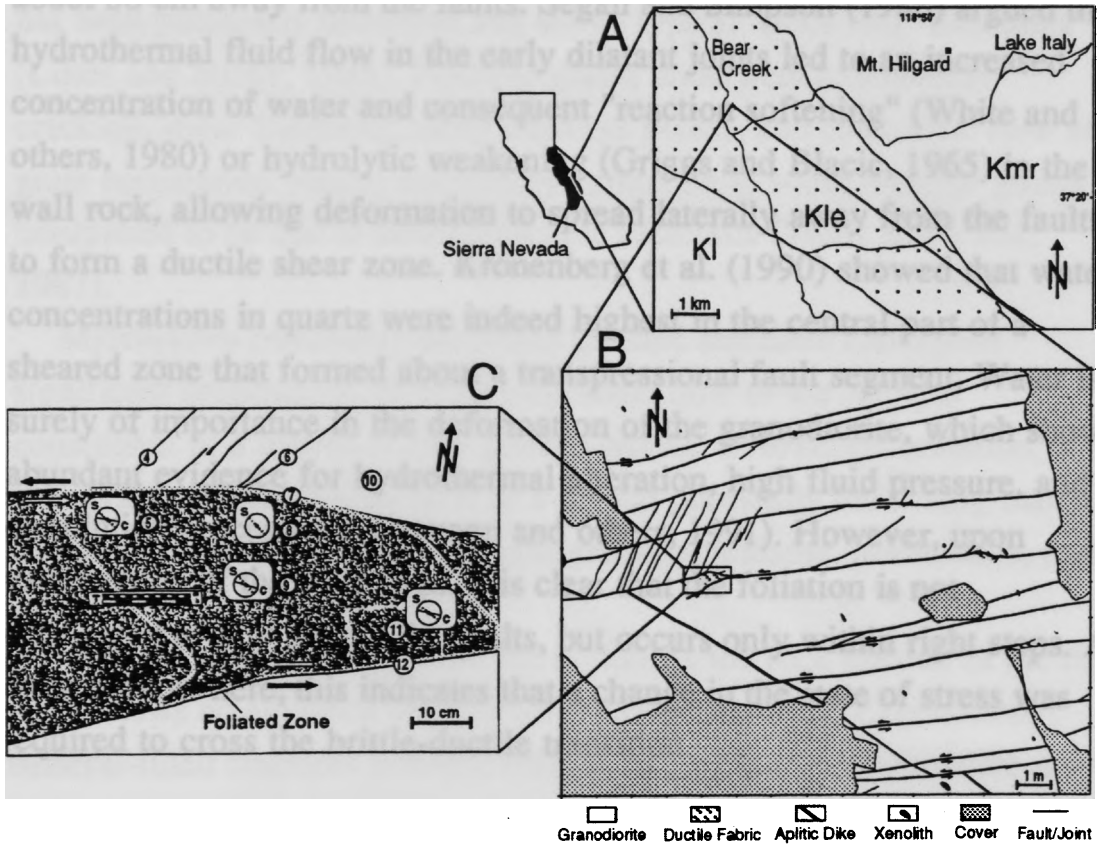


Figure 1.1. A: Map showing Bear Creek region of Mt. Abbot quadrangle. Pluton contacts are shown in heavy lines. KI-Lamarck granodiorite, Kle-granodiorite of Lake Edison, Kmr-Quartz monzonite of Mono Recesses. B: Outcrop map of faults, fractures and right steps. C: Detailed map of step analyzed here. Fabric orientations (S and C planes) from four cores are indicated in boxed diagrams. Circled numbers indicate locations of cored samples.

Conditions during faulting were close to the brittle-ductile transition (Segall and Simpson, 1986). Extensional brittle fracturing accompanied faulting as evidenced by oblique mineralized opening-mode fractures (splay cracks) at fault ends and within left steps of overlapping en échelon fault segments. Mylonitic fabrics in the granodiorite are mostly localized within right steps (Fig. 1.1B and C).

A few faults show evidence for distributed mylonitic textures up to about 50 cm away from the faults. Segall and Simpson (1986) argued that hydrothermal fluid flow in the early dilatant joints led to an increased concentration of water and consequent "reaction softening" (White and others, 1980) or hydrolytic weakening (Griggs and Blacic, 1965) in the wall rock, allowing deformation to spread laterally away from the faults to form a ductile shear zone. Kronenberg et al. (1990) showed that water concentrations in quartz were indeed highest in the central part of a sheared zone that formed about a transpressional fault segment. Water is surely of importance in the deformation of the granodiorite, which shows abundant evidence for hydrothermal alteration, high fluid pressure, and dissolution processes (Bürgmann and others, 1991). However, upon examination of the fault steps, it is clear that the foliation is not distributed evenly around the faults, but occurs only within right steps. As we will show here, this indicates that a change in the state of stress was required to cross the brittle-ductile transition.

DEFORMATION ASSOCIATED WITH FAULT STEPS

Whereas deformation within left steps is accommodated by extensional jointing and fractures, the right steps display S-C mylonitic fabrics (Lister and Snoke, 1984) indicating a component of noncoaxial flow. Distinct shear surfaces (C planes), rich in fine-grained mica and finely recrystallized quartz, separate zones of mostly undeformed feldspars and plastically deformed quartz and mica. The latter show a preferred grain orientation (S planes), oblique to the shears and the step-bounding faults,

that defines the observed foliation. Foliation is oriented at angles of 25° to 35° close to the faults and shows higher angles of 40° to 55° in the center of the fault steps, whereas the C planes deviate from the fault strike by up to 15°, also in a clockwise sense (Fig. 1.1 C).

Figure 1.2A (from core 5 in Fig. 1.1C) shows the typical microstructures developed in the ductilely deformed granodiorite in the right steps. Quartz is dynamically recrystallized and there is a strong preferred orientation of the new grains. Biotite (often altered to chlorite) has been plastically deformed and shows typical "mica fish" structures (Lister and Snoke, 1984). Feldspar grains underwent extensional cracking, shear fracturing along cleavage planes, and cataclastic flow at grain boundaries. Patchy undulatory extinction in some feldspar grains is interpreted to be due to submicroscopic cataclasis (Tullis and Yund, 1987).

Myrmekites commonly are found crushed and have undergone significant deformation through cataclastic flow of the feldspar constituent in a matrix of fine-grained quartz. Overall, deformation is semibrittle, dominated by flow of a crystal plastically deforming matrix of quartz and mica enveloping rigid grains of feldspar, hornblende, and opaques.

Only millimetres away from the mylonites the rock outside of the right steps shows no evidence of significant ductile straining. Extensional, mineral-filled fractures oriented oblique to the faults accommodate some deformation outside of the steps, but the magnitude of strain is significantly lower than that accommodated by flow within the steps. Approximately 60 opening-mode fractures northwest of the fault step shown in Figure 1.1B accommodate about 2% extension. Figure 1.2B (from core 4 in Fig. 1.1C) shows an extensional fracture breaking the approximately isotropic granodiorite. Quartz exhibits undulatory extinction, but we see no evidence for recrystallization. Grain scale shear and opening mode fractures are common in feldspars, and cracks are filled with fine-grained quartz and chlorite.

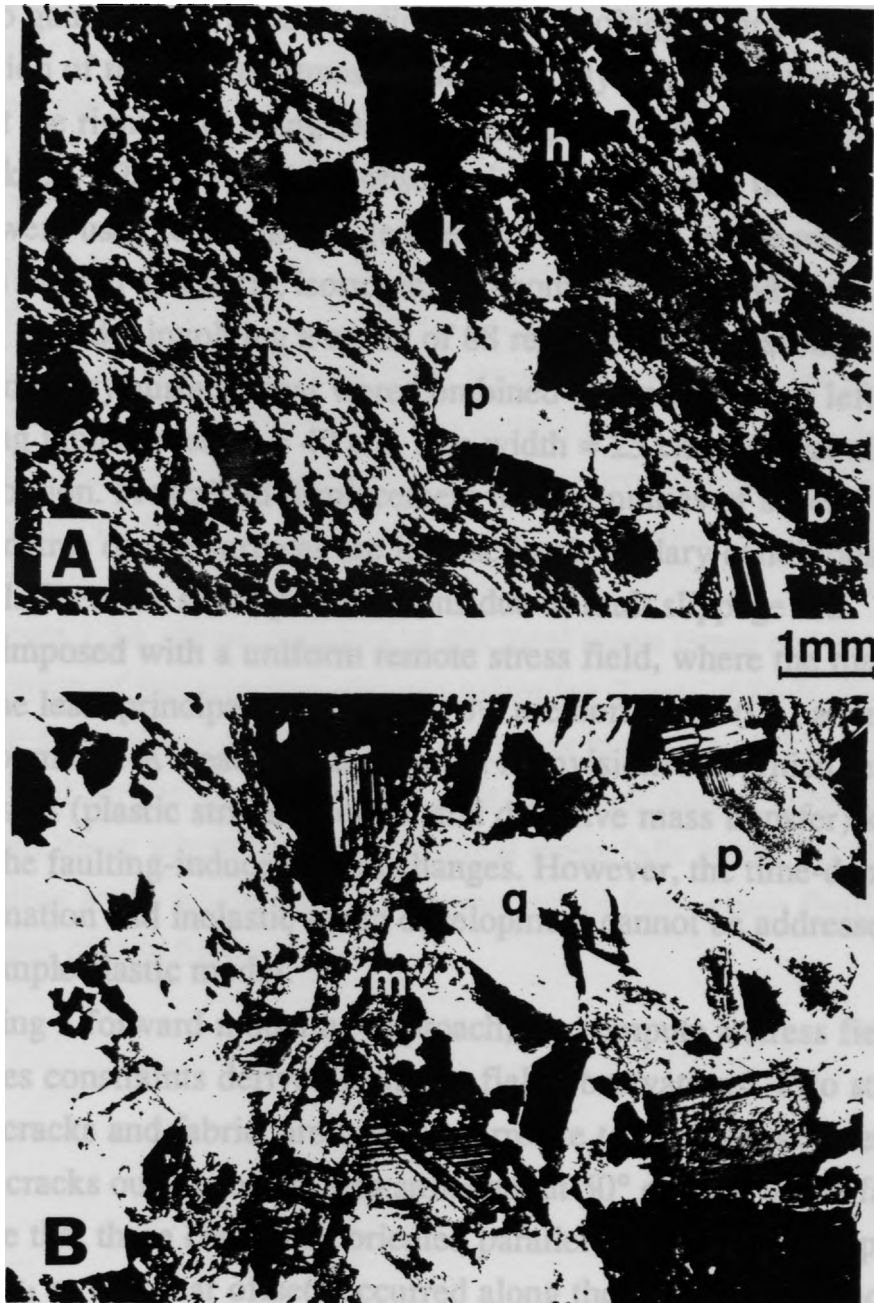


Figure 1.2. Microscopic images of thin sections under crossed Nichols. A: Core 5 (Fig. 1.1C) from ductilely deformed step showing recrystallized quartz, fractured feldspars, and fabrics related to non-coaxial flow. B: Core 4 located 10 cm away from core 5 showing brittle fractures and no fabric development. C-mylonitic C-surface, b-biotite, h-hornblende, k-potassium feldspar, m-myrmekite, p-plagioclase, q-quartz.

STRESS FIELD ASSOCIATED WITH FAULT STEPS

To gain a better understanding of the rheology of granitic rock as a function of the state of stress, we numerically calculated the stress field about the right steps using DIS3D, a program based on dislocation theory (Erickson, 1987). Structural observations from one of the fault steps (Fig. 1.1) were used to define the geometric parameters of the model. The stress field in an elastic, isotropic, and homogeneous body was computed using a model involving a series of 88 rectangular displacement-discontinuity surfaces that were combined to represent two left-lateral 20-m-long faults (overlap = 40 cm, step width = 25 cm) with an elliptical slip distribution. Prescribed displacement discontinuities of several millimetres on the surfaces are imposed as boundary conditions of the model. Then the stress perturbations due to fault slippage are superimposed with a uniform remote stress field, where the maximum and the least principal stresses (σ_1 , σ_3) are horizontal (i.e., a strike-slip environment). A steady-state situation is envisioned in which relaxation processes (plastic strain, fracture, and diffusive mass transfer) keep pace with the faulting-induced stress changes. However, the time-dependent deformation and inelastic strain development cannot be addressed with this simple elastic model.

Using a forward-modeling approach, we compute a stress field that satisfies constraints derived from the field observations. Two structures, splay cracks and fabric, are used to correlate to local stress orientations. Splay cracks outside of the step strike about 50° oblique to the faults. We assume that these cracks are oriented parallel to the maximum principal stress σ_1 as no shear offsets occurred along them. For splay cracks to form, the effective tensile stress, $\sigma_3(\text{eff})$ must have been larger than the tensile strength of the rock. Shear surfaces (C planes) within the plastically deformed mylonite of the right steps are inferred to be oriented at an angle of between 30° and 45° to the local σ_1 . Elongated mineral grains that define the foliation (S planes) are thought to indicate the direction of the long axis of the finite strain ellipse (Ramsay, 1980).

The angle between S and C surfaces varies from about 30° to 40° across the fault step, suggesting that σ_1 is oriented approximately perpendicular to the foliation. Some rotation of the S and C orientations may occur as finite strain develops, but, in light of the observed shear strain magnitudes ($\gamma < 1$), the difference between the estimated and true stress directions is thought to be less than 10°. Remote mean stress ($P = [\sigma_1 + \sigma_2 + \sigma_3]/3$) is assumed to be 100 MPa. The larger the imposed offset on the faults, the greater the remote maximum shear stress ($(\sigma_1 - \sigma_3)/2$) for the model results to be consistent with the inferred principal stress directions. At lower remote shear stresses, the model predicts approximately fault-parallel shortening in the right step, not the strongly oblique orientations observed.

Figure 1.3A shows contours of the local mean stress and the orientation of the principal stresses assuming 2 mm of fault slip and a remote shear stress of 25 MPa. Mean stress increases of 10 to 25 MPa are calculated for the area within the fault step. The shaded regions in Figure 1.3A are areas where the least principal stress falls below 70 MPa, indicating areas where tensile fractures might form given fluid pressure in excess of this figure.

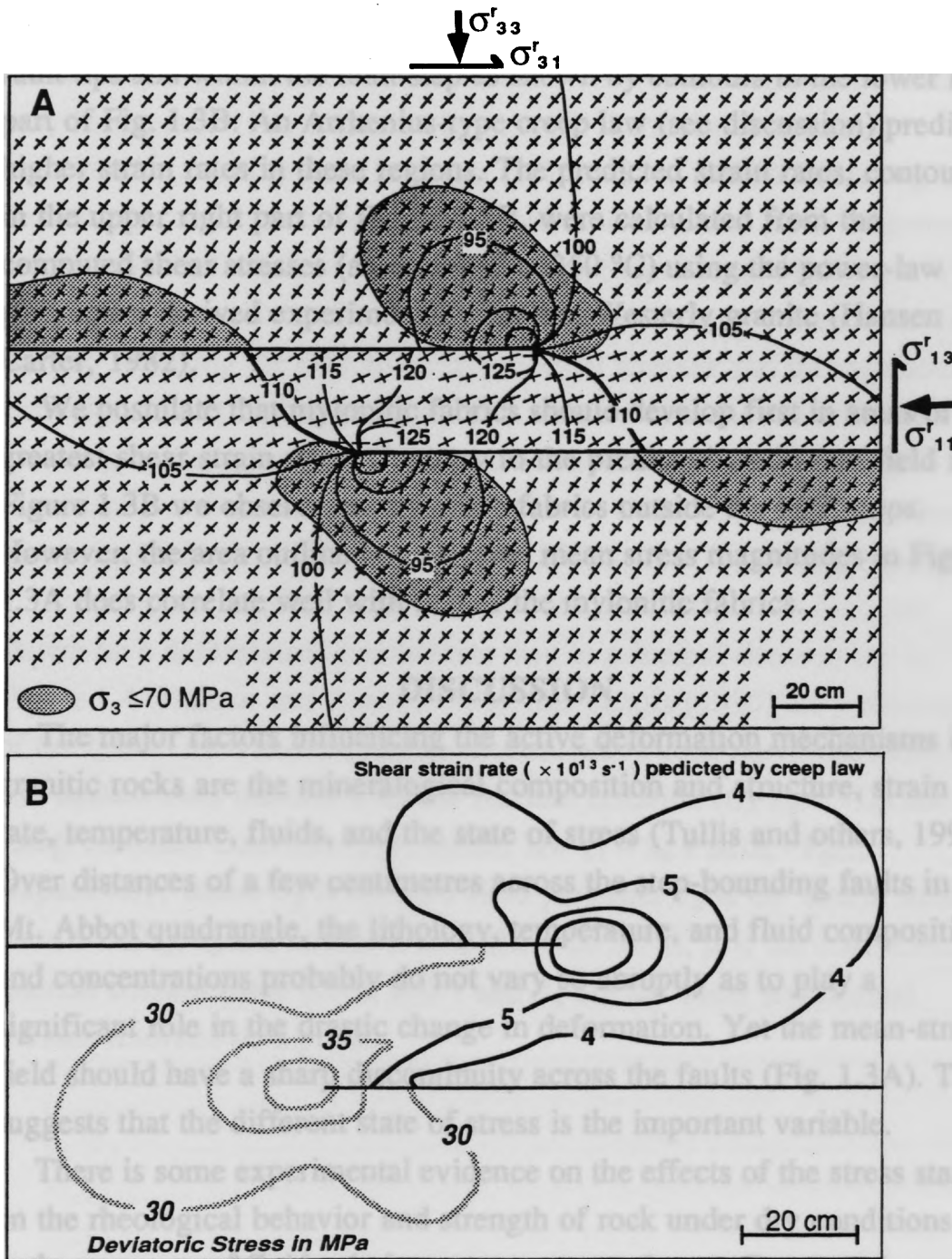


Figure 1.3. A: Mean stress distribution and trajectories of principal stress directions near right step. Maximum slip on two faults was 2 mm at center of fault segments diminishing toward fault ends in elliptical distribution. B: Contours of maximum shear-stress magnitudes (lower left) and shear-strain rates predicted by power-law creep law (upper right).

Magnitudes of the local maximum shear stress are elevated around the fault tips and within the fault step as shown by contours in the lower left part of Fig. 1.3B. An Arrhenius-type creep law (see discussion) predicts higher strain rates in these regions. The predicted strain rates, contoured in the upper right part of Figure 1.3B, were calculated from the computed shear stresses (assuming $T = 350\text{ }^{\circ}\text{C}$) using the power-law parameters derived experimentally for wet Westerly granite (Hansen and Carter, 1982).

We postulate that mylonitic fabrics should develop first in areas of greatest shear strain rates. Contrary to the predicted strain-rate field in Figure 1.3B we observe no mylonitic fabrics outside the fault steps. However, the area outlined by elevated mean stress magnitudes in Figure 1.3A does correlate well with that of the mylonitic fabrics.

DISCUSSION

The major factors influencing the active deformation mechanisms in granitic rocks are the mineralogical composition and structure, strain rate, temperature, fluids, and the state of stress (Tullis and others, 1990). Over distances of a few centimetres across the step-bounding faults in the Mt. Abbot quadrangle, the lithology, temperature, and fluid compositions and concentrations probably do not vary so abruptly as to play a significant role in the drastic change in deformation. Yet the mean-stress field should have a sharp discontinuity across the faults (Fig. 1.3A). This suggests that the different state of stress is the important variable.

There is some experimental evidence on the effects of the stress state on the rheological behavior and strength of rock under dry conditions and in the presence of fluids. At low temperatures, the tensile strength can be several orders of magnitude lower than the compressive strength at high confining pressures (Scholz, 1990). At higher temperatures, when the flow stress is less strongly influenced by the confining pressure, experimenters infer that crystal plasticity, a constant-volume process, is the dominant mechanism of deformation. However, to attain crystal

plastic behavior in rocks at high temperatures, it is necessary to apply some confining pressure (Paterson, 1978). Increased confining pressure may be needed (1) to offset the anisotropic thermal expansion of individual mineral grains (Paterson, 1978), (2) to inhibit fracturing by increasing crack-normal stresses (Paterson, 1978), and (3) it is known to enhance the hydrolytic weakening effect in experiments (Tullis and Yund, 1989). The immediate effect of introducing fluids is to enhance fracture, both by lowering the effective crack-normal stresses and through stress corrosion, but at higher pressures and temperatures the net effect is a lowering of the temperature of the transition from microcracking (cataclasis) to dislocation glide and climb by about 150-200 °C for both quartz and feldspar (Tullis and others, 1979).

The stresses required for brittle fracture and for plastic flow are shown on a deformation-mechanism map in principal stress space in Figure 1.4 (Hallam and Ashby, 1990). See Scholz (1990) for a discussion of the failure laws and the choice of parameters used here. The shaded and dashed lines indicate a tensile fracture criterion ($\sigma_3 - P_p = -T_o$) and a compressional, Coulomb-type, failure law ($\tau = \tau_o + \mu[\sigma_n - P_p]$), respectively; where P_p is the pore fluid pressure, T_o is the tensile strength (here 5 MPa), τ_o is a cohesive term (here 10 MPa), μ is the coefficient of internal friction (here 0.75), and τ and σ_n are the shear and normal stresses resolved on a plane.

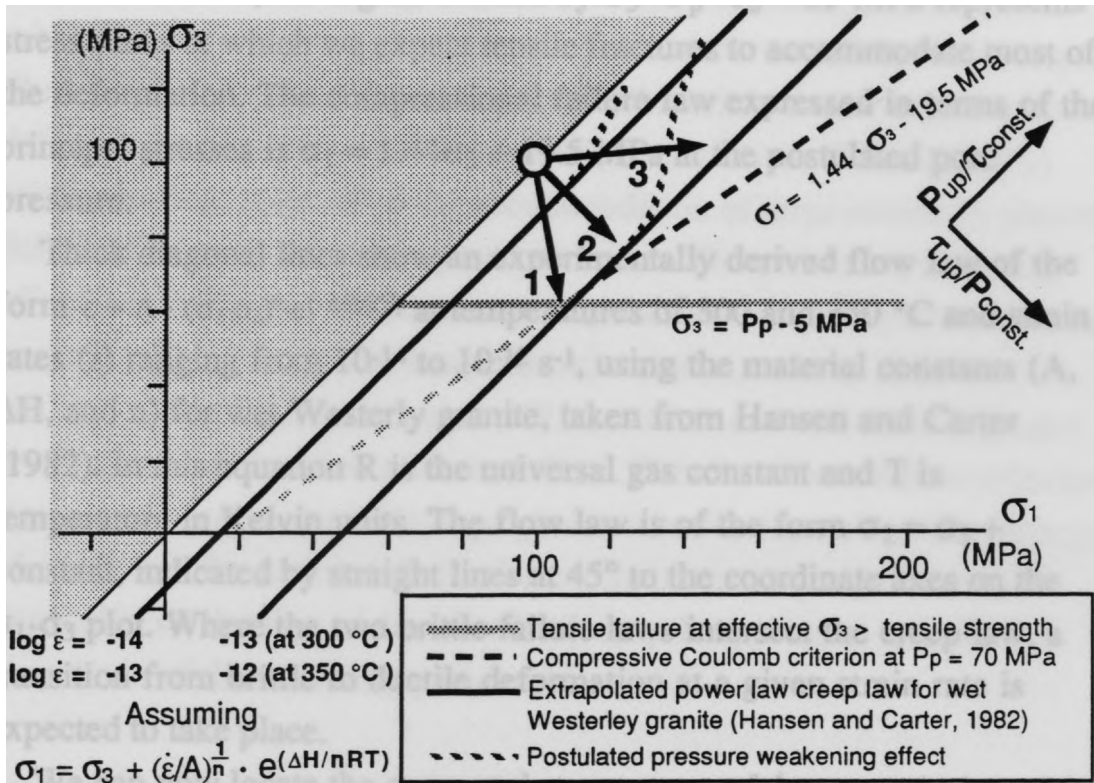


Figure 1.4. Deformation-mechanism map in principal-stress space based on brittle and ductile deformation laws in strike-slip environment ($\sigma_2 = [\sigma_1 + \sigma_3]/2$ is vertical). If pore pressure exceeds least principal stress by more than tensile strength (ca. 5 MPa), tensile failure is predicted. Coulomb-Navier criteria delineates area where brittle failure is to be expected, and flow-law lines indicate stress states at which ductile flow (at strain rates ranging from 10^{-14} to 10^{-12} s^{-1}) occurs in wet Westerley granite at 300 °C and 350 °C (Hansen and Carter, 1982). Pressure-weakening effect is schematically drawn as deviation from (inherently pressure independent) power-law flow law, leading to lower strength and increased strain rates at elevated pressures. Starting out from confining pressure of 100 MPa at pore pressure of 70 MPa, response of granitic rock under different loading conditions encountered around Sierran fault steps can be considered. As we change shear-stress τ and/or confining pressure P to values predicted in model, different deformation processes will dominate. This is schematically illustrated by three arrows indicating stress states in zones of (1) splay cracks, (2) undeformed rock away from faults, and (3) right steps.

Under the assumption that the pore pressure is 70% of the lithostatic load of 100 MPa, the region defined by $\sigma_3 \leq P_p - T_o = 65$ MPa represents stress states at which we expect tensile fractures to accommodate most of the deformation. The compressional failure law expressed in terms of the principal stresses is $\sigma_1 = 1.44\sigma_3 + 19.5$ MPa at the postulated pore pressure.

Thick diagonal lines show an experimentally derived flow law of the form $\dot{\epsilon} = A \cdot (\sigma_1 - \sigma_3)^n \cdot e^{(-\Delta H/RT)}$ at temperatures of 300 and 350 °C and strain rates ($\dot{\epsilon}$) ranging from 10^{-14} to 10^{-12} s⁻¹, using the material constants (A, ΔH , and n) for wet Westerly granite, taken from Hansen and Carter (1982). In this equation R is the universal gas constant and T is temperature in Kelvin units. The flow law is of the form $\sigma_1 = \sigma_3 + \text{constant}$, indicated by straight lines at 45° to the coordinate axes on the $\sigma_1 - \sigma_3$ plot. Where the two brittle failure laws intersect the creep law, a transition from brittle to ductile deformation at a given strain rate is expected to take place.

We can now locate the computed stress states of the numerical model on the deformation-mechanism map in principal-stress space as indicated by the arrows labeled 1, 2, and 3 in Figure 1.4. The occurrence of tensile fracturing adjacent to the Sierra Nevadan fault steps indicates that the effective least principal stress ($\sigma_3 - P_p$) exceeded the tensile strength of the rock leading to brittle fracturing. In our numerical fault-step model, the least principal stress in the region of tension cracks is <70 MPa (Fig. 1.3A) indicating that fluid pressures may have been as high as 75 MPa, assuming a tensile strength of 5 MPa. A dependence of the flow strength on the mean stress has been described in the previous section. This pressure-dependent (hydrolytic?) weakening effect is indicated in schematic form in Figure 1.4 by a dashed deviation from the straight power-law flow law at higher pressures.

CONCLUSIONS

Field observations along faults in the Sierra Nevada, in combination with numerical modeling of the stress fields about en échelon fault steps, illustrate the effects of the stress state on the brittle and/or crystal plastic deformation of granitic rock. Increased mean stresses (10 to 25 MPa) within the fault steps allow the accommodation of large strains by plastic deformation mechanisms in quartz and mica. The pressure-weakening effect is possibly due to the pressure dependence of hydrolytic weakening in quartz. Thus, at a given temperature, rocks in zones of fluid infiltration *and* high mean stress will be weaker and will show a greater proportion of dislocation glide and climb. Tensile effective least-principal stresses adjacent to the fault steps promote tensile fracturing. The strength of a rock and the acting deformation mechanisms vary significantly depending on the sign of the effective least principal stress and the magnitude of the confining pressure.

ACKNOWLEDGMENTS

This research was supported by the Geological Society of America, Sigma Xi, the McGee research fund, and the Rock Fracture Project. Ramón Arrowsmith, Peter Christiansen, Steve Martel, Michael Pollard, and Betty Suh helped with the field work. We thank Jan Tullis and Ben van der Pluijm for helpful reviews.

REFERENCES

- Ague, J. J. and Brimhall, G. H., 1988, Magmatic arc asymmetry and distribution of anomalous plutonic belts in the batholiths of California: Effects of assimilation, crustal thickness, and depth of crystallization: Geological Society of America Bulletin, v. 100, p. 912-927.
- Bürgmann, R., Martel, S. J. and Pollard, D. D., 1991, Volume strain and mass transport in en échelon fault steps accommodated by pressure solution in granitic rock, Sierra Nevada, California: Geological Society of America Abstracts with Programs, v. 23, p. 427.
- Byerlee, J. D., 1968, Brittle-ductile transition in rocks: Journal of Geophysical Research, v. 73, p. 4741-4750.
- Carter, N. L. and Kirby, S. H., 1978, Transient creep and semi-brittle behavior of crystalline rocks: Pure and Applied Geophysics, v. 116, p. 807-839.
- Erickson, L. L., 1987, User's Manual for DIS3D: A three dimensional dislocation program with applications to faulting in the earth: v. p.
- Griggs, D. T. and Blacic, J. D., 1965, Quartz: Anomalous weakness of synthetic crystals: Science, v. 147, p. 292-295.
- Hallam, S. D. and Ashby, M. F., 1990, Compressive brittle fracture and the construction of multi-axial failure maps, *in* Barber, D. J. and Meredith, P. G., ed., Deformation processes in minerals, ceramics and rocks: London, The Mineralogical Society of Great Britain and Ireland, Unwin Hyman, p. 84-108
- Hansen, F. D. and Carter, N. L., 1982, Creep of selected crustal rocks at 1000 MPa: EOS (American Geophysical Union Transactions), v. 63, p. 437.
- Kronenberg, A. K., Segall, P. and Wolf, G. H., 1990, Hydrolytic weakening and penetrative deformation within a natural shear zone, ed., The Brittle-Ductile Transition -- The Heard Volume: AGU, Washington, D.C., p. 21-36
- Lister, G. S. and Snoke, A. W., 1984, S-C mylonites: Journal of Structural Geology, v. 6, p. 617-638.

- Martel, S. J., Pollard, D. D. and Segall, P., 1988, Development of simple strike-slip fault zones in granitic rock, Mount Abbot quadrangle, Sierra Nevada, California: Geological Society of America Bulletin, v. 99, p. 1451-1465.
- Paterson, M. S., 1978, Experimental Rock Deformation - The Brittle Field: Berlin, Springer-Verlag, 254 p.
- Ramsay, J. G., 1980, Shear zone geometry: A review: Journal of Structural Geology, v. 2, p. 83-99.
- Rutter, E. H., 1986, On the nomenclature of models of failure transitions in rocks: Tectonophysics, v. 122, p. 381-387.
- Scholz, C. H., 1988, The brittle-plastic transition and the depth of seismic faulting: Geologische Rundschau, v. 77, p. 319-328.
- Scholz, C. H., 1990, The Mechanics of Earthquakes and Faulting: Cambridge, Cambridge University Press, 439 p.
- Segall, P., McKee, E. H., Martel, S. J. and Turrin, B. D., 1990, Late Cretaceous age of fractures in the Sierra Nevada batholith, California: Geology, v. 18, p. 1248-1251.
- Segall, P. and Pollard, D. D., 1983a, Joint formation in granitic rock of the Sierra Nevada: Geological Society of America Bulletin, v. 94, p. 563-575.
- Segall, P. and Pollard, D. D., 1983b, Nucleation and growth of strike-slip faults in granite: Journal of Geophysical Research, v. 88, p. 555-568.
- Segall, P. and Simpson, C., 1986, Nucleation of ductile shear zones on dilatant fractures: Geology, v. 14, p. 56-59.
- Shimamoto, T., 1989, The origin of S-C mylonites and a new fault-zone model: Journal of Structural Geology, v. 11, p. 51-64.
- Sibson, R. H., 1983, Continental fault structure and the shallow earthquake source: Journal of the Geological Society of London, v. 140, p. 741-767.
- Smith, R. B. and Bruhn, R. L., 1984, Intraplate extensional tectonics of the eastern basin-range: Inferences on structural style from seismic reflection data, regional tectonics, and thermal-mechanical models of

- brittle-ductile deformation.: *Journal of Geophysical Research*, v. 89, p. 5733-5762.
- Stern, T. W., Bateman, P. C., Morgan, B. A., Newall, m. F. and Peck, D. L., 1981, Isotopic U-Pb ages of zircon from the granitoids of the central Sierra Nevada, California: U.S. Geological Survey Professional Paper, v. 1185, p. 17 p.
- Tullis, J., Dell'Angelo, L. and Yund, R. A., 1990, Ductile shear zones from brittle precursors in feldspathic rocks: The role of dynamic recrystallization, *in* Duba, A. G. et. al., ed., *Geophysical Monograph: American Geophysical Union*, p. 67-82
- Tullis, J. and Yund, R. A., 1987, Transition from cataclastic flow to dislocation creep of feldspar: mechanisms and microstructures: *Geology*, v. 15, p. 606-609.
- Tullis, J. and Yund, R. A., 1989, Hydrolytic weakening of quartz aggregates: The effects of water and pressure on recovery: *Geophysical Research Letters*, v. 16, p. 1343-1346.
- Tullis, J. A., 1990, Experimental studies of deformation mechanisms and microstructures in quartzo-feldspathic rocks, *in* Barber, D. J. and Meredith, P. G., ed., *Deformation processes in minerals, ceramics and rocks: London, The Mineralogical Society of Great Britain and Ireland, Unwin Hyman*, p. 190-226
- Tullis, J. A., Shelton, G. L. and Yund, R. A., 1979, Pressure dependences of rock strength: Implications for hydrolytic weakening: *Bulletin Minéralogique*, v. 102, p. 110-114.
- White, S. H., Burrows, S. E., Carreras, J., Shaw, N. D. and Humphreys, F. J., 1980, On mylonites in ductile shear zones: *Journal of Structural Geology*, v. 2, p. 175-187.

2. Strain Accommodation About Strike-Slip Fault Discontinuities In Granitic Rock Under Brittle-To-Ductile Conditions

ABSTRACT

Brittle and ductile structures adjacent to fault terminations and echelon fault steps of left-lateral strike-slip faults in the Lake Edison Granodiorite of the central Sierra Nevada, California, are related to stress perturbations caused by fault slip. The structures associated with fault terminations change from dilatant splay fractures only, to splay fractures and ductile fabrics on opposing sides of the fault, to ductile fabrics ahead of the fault, with decreasing distance from a younger neighboring pluton and, presumably, with increased temperatures. The local magnitudes and spatial distributions of the maximum tensile stress, the mean stress, and the maximum shear stress correlate with the distributions of different deformation mechanisms. Displacements along the faults are transferred across echelon stepovers by mineralized dilatant fractures in extensional steps. To accommodate slip transfer across contractional steps, rock apparently was squeezed vertically out of the step by ductile flow; concentrations of mobile and immobile elements indicate that mass solution transfer was not significant. Increased mean stress in contractional steps apparently enhances crystal-plastic flow of quartz. A flow law that includes a pressure effect through correlation with pressure-dependent solidus temperatures appears to be more successful than other experimentally derived flow laws in predicting the observed distribution of ductile fabrics.

INTRODUCTION

Discontinuities (steps, bends, and breaks) along crustal strike-slip faults are potential initiation and arrest zones of earthquake ruptures (King & Nabelek 1985, Sibson 1986b, Harris & Day 1993). Earthquakes commonly initiate at the base of the seismically active fault zones where conditions are thought to be close to the brittle-to-ductile transition of crustal rocks (Sibson 1984). Therefore the study of fault stepovers that were active at transition conditions may offer insight into the processes related to initiation of fault ruptures and the mechanics of slip transfer across discontinuities.

We describe fault terminations and fault stepovers in granitic rock in the central Sierra Nevada, California (Fig. 2.1), that formed under conditions close to the brittle-ductile transition (Segall & Simpson 1986, Bürgmann & Pollard 1992). After describing the observed structures and the history of their development, we evaluate the effects of the stress field at fault terminations on the constitutive behavior of granitic rock at varying temperatures. We compare and contrast the field observations of fault steps with the stress field predicted by mechanical models. Our analysis suggests that deformation laws for granitic rock should include a pressure weakening effect (Bürgmann & Pollard 1992).

Experimental studies of rock deformation involving crystal-plastic deformation mechanisms are carried out at temperatures and stresses greatly exceeding those in natural settings to achieve measurable deformation rates. Therefore flow laws established in such experiments have to be extrapolated over a wide range of temperatures and deformation rates when applied to the earth (e.g., Paterson 1987). The Sierran faults described in this paper can be considered natural experiments that give us further insight into the mechanics of rock deformation at hydrothermal conditions and geological deformation rates.

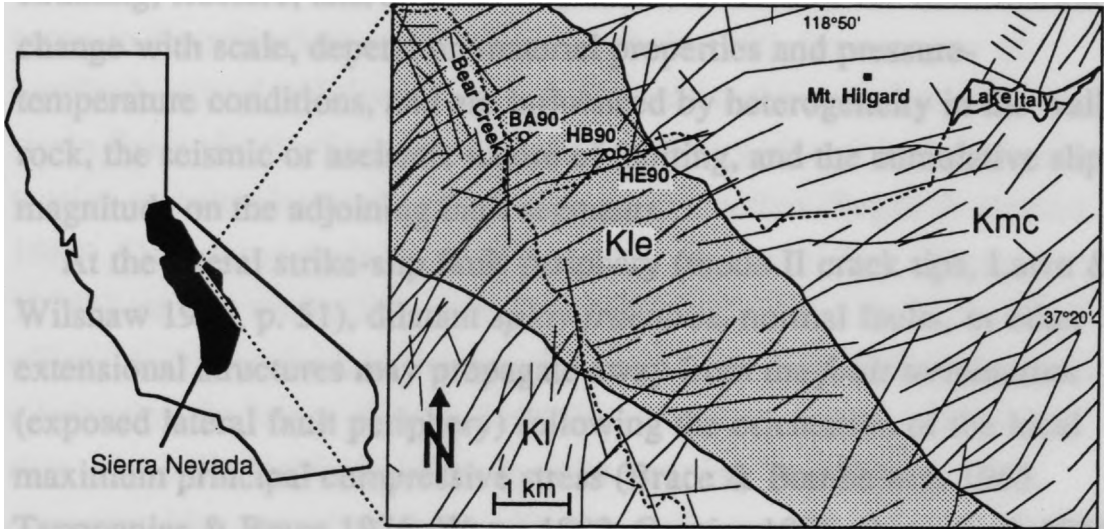


Fig. 2.1. Map showing Bear Creek region of Mt. Abbot quadrangle and the location of the numbered outcrops described in this paper. Pluton contacts are shown in heavy lines and major stream valleys are dashed. KI-Lamarck Granodiorite, Kle-Lake Edison Granodiorite, Kmc-Mono Creek Granite. The plutons intruded sequentially from W to E in the Late Cretaceous. Thin lines are photo lineaments marked by vegetation lines and small drainages that apparently follow strike-slip fault zones that developed along previously formed joints in the area.

Deformation along discontinuous faults

Deformation along faults is concentrated at their *peripheries* and around discontinuities, over a wide range of length scales and geologic settings (Chinnery 1965, Rodgers 1980, Segall & Pollard 1980, Aydin & Nur 1982). Where faults terminate or deviate from their trace, strain from fault slip must be distributed in the surrounding rock by elastic straining, fracture, and/or flow. The characteristics of the deformation change with scale, depend on material properties and pressure-temperature conditions, and are influenced by heterogeneity in the wall rock, the seismic or aseismic nature of faulting, and the cumulative slip magnitude on the adjoining fault segments.

At the lateral strike-slip fault periphery (mode II crack tips, Lawn & Wilshaw 1975, p. 51), dilatant *splay fractures*, normal faults, or other extensional structures may propagate away from the *fault termination* (exposed lateral fault periphery) following the orientation of the local maximum principal compressive stress (Brace & Bombolakis 1963, Tapponnier & Brace 1976, Wong 1982, Granier 1985, Deng *et al.* 1986). Contractional structures such as pressure solution seams (Fletcher & Pollard 1981), folds, and thrust faults (Deng *et al.* 1986) may form on the opposite side of the fault termination and trend in the orientation of the local minimum principal stress. At a crustal scale, subsidence in the extensional quadrants and uplift in the antisymmetric contractional quadrants (Chinnery 1965, Bilham & King 1989) occurs near the termination of faults. Near the upper or lower periphery of a strike-slip fault (mode III crack tips), echelon fracture arrays may develop (Pollard *et al.* 1982, Cox & Scholz 1988, Jackson *et al.* 1992). A wide range of 'mixed-mode' conditions along the periphery of a fault is expected to lead to a more complex pattern of deformation (Pollard & Segall 1987). This study addresses lateral (mode II) fault terminations and stepovers that show no evidence of significant mode III deformation.

Individual fault segments typically are arranged in a left- or right-stepping echelon geometry. Echelon geometries may stem from pre-

existing arrangements of weak surfaces (e.g., joints, bedding planes, and older faults) or may develop during shearing (Gamond 1987, Swanson 1988). The interaction of fault segments leads to characteristic stress fields and resulting deformation patterns, depending on the left- or right-stepping character of fault stepovers for a given sense of faulting (Segall & Pollard 1980).

We would prefer to refrain from the common usage of stress or strain terms to describe fault stepovers (see Scholz 1990, for a review of terminology and additional references), because the complex stress and strain fields about a fault step of either geometry always include zones of tension or extension and compression or contraction (Segall & Pollard 1980). Describing fault steps as 'releasing' or 'restraining' (Crowell 1974b) may be misleading as well, considering, for instance, poroelastic effects during earthquake rupture that may delay or stop faulting through a 'releasing' fault step (Sibson 1985, Harris & Day 1993). Also, in the case of the Sierran faults, flow in right-stepping 'restraining' discontinuities appears to be as effective a slip-transfer process as brittle fracture is in the left-steps (see below). However, to avoid cumbersome geometric phrases such as "left step on left-lateral fault" we adopt the use of *extensional step* for left steps along left-lateral faults and right steps along right-lateral faults, and *contractional step* for the contrasting cases.

Structures such as joints, veins, dilation breccias, extensional faults, or regions of stretched rock typically link fault segments adjoining an extensional step. Such extensional fault steps have been observed along millimeter-scale shear zones in felsic gneiss (Gibson 1990), in outcrops in a variety of rock types (e.g., Granier 1985, Gamond 1987, Swanson 1988, Cruikshank *et al.* 1991), along mine-induced meter-scale faults (McGarr *et al.* 1979, Sibson 1987), and along large strike-slip fault zones, such as the San Andreas fault, where sag ponds and basins mark the fault stepovers (e.g., Crowell 1974b, 1974a, Christie-Blick & Biddle 1985, Woodcock & Fischer 1986). Analogue models of echelon faults in a variety of materials produce similar structures (Brace & Bombolakis

1963, Tschalenko 1970, Hempton & Neher 1986, Naylor *et al.* 1986, Lin & Logan 1991). In all cases mass is being removed from the fault step as slip on the bounding faults continues. The resulting mass loss may be compensated by the emplacement of mineral precipitates into veins or rhombochasms (Sibson 1987), by contraction across the step perpendicular to the faults (Woodcock & Fischer 1986), or by vertical contraction commonly leading to basin formation along crustal fault systems (Crowell 1974a, Dibblee 1977).

Contractional steps are characterized by shortening sub-parallel to the fault planes within the step. As material is pushed into the step, possible accommodating mechanisms include mass solution transfer (Gamond 1987, Martel *et al.* 1990), extension perpendicular to the step-bounding faults and distortion of the fault planes (Woodcock & Fischer 1986), or extension in the vertical direction. The latter commonly results in uplift along crustal-scale strike-slip faults (Sharp & Clark 1972, Dibblee 1977, Woodcock & Fischer 1986).

Brittle-to-ductile deformation

The 'brittle-to-ductile transition' is a somewhat vague concept, and it does not directly imply the deformation mechanisms involved (Paterson 1978, Rutter 1986, Ross & Lewis 1989). Therefore, seismologists, structural geologists, and rock mechanicians commonly have different views as to the nature of this transition (e.g., Byerlee 1968, Smith & Bruhn 1984, Simpson 1985, Sibson 1986a, Scholz 1988, Tullis 1990). Here, we consider the brittle-to-ductile transition to reflect the material state (range of temperature, deformation rate, and stress conditions) beyond which the activation of crystal-plastic dislocation creep, dynamic recrystallization, and/or mass solution transfer of one or more mineral constituents allows the rock to flow macroscopically. Below the transition a material will fail predominantly by brittle fracture if its strength is exceeded.

We infer past 'ductility' in deformed rock if we observe abundant microstructures such as undulatory extinction, preferred c-axes orientation, recrystallized grains, or pressure solution seams (Simpson 1985). We infer past 'brittle' behavior if we observe few of the above microstructures and instead find evidence of fracture as the dominant deformation mechanism. However, both brittle and ductile structures can form over a wide range of conditions (e.g., Scholz 1988, Swanson 1992). The transition to crystal-plastic deformation in experiments can be achieved by increasing temperatures, by the addition of water, by applying high confining pressures, and by decreasing strain rates (e.g., Tullis & Yund 1977, Tullis & Yund 1980); it is furthermore dependent in a more complex fashion on the state of stress, as will be discussed below.

STRUCTURAL DEVELOPMENT OF FAULT ZONES IN THE LAKE EDISON GRANODIORITE

Left-lateral strike-slip faults

Left-lateral strike-slip faults in the Late Cretaceous, fine- to medium-grained biotite-hornblende Lake Edison Granodiorite (Bateman 1992) reactivated and are restricted to pre-existing, steeply-dipping, subparallel joint surfaces (Fig. 2.2). Therefore, the initial geometry, spacing, and orientation of faults is not related to the later shearing event. The early ENE-striking joints are mineralized with epidote, chlorite \pm quartz \pm biotite \pm sphene \pm calcite \pm zeolites (Segall & Pollard 1983a, Segall *et al.* 1990). Strike-slip faulting subsequently nucleated on these pre-existing planes of weakness (Fig. 2.2b, Segall & Pollard 1983b). Offsets along the faulted joints range from millimeters to two meters, and fault segments range from a few meters to several tens of meters in length. The coexistence of parallel faulted and unfaulted mineralized joints shows that the fault surfaces did not form as shear but as dilatant fractures (Segall & Pollard 1983b). A microscopic examination of the fine-grained fault material (chlorite, epidote, and quartz) shows that deformation was

dominantly crystal-plastic, evidenced by a strong mylonitic fabric. Sharp boundaries commonly separate the ductile shear zones from the undeformed wall rock. Single fault planes did not grow beyond the terminations of the older joints on which slip developed.

Some single faults interact to form fault zones (Fig. 2.2c) about one meter in width that accommodate up to several tens of meters of slip on their bounding surfaces (Segall & Pollard 1983b, Martel *et al.* 1988, Martel & Pollard 1989). In these boundary faults the mylonitic fabric has been overprinted by cataclastic processes. Martel *et al.* (1988) postulated that the transition from mylonitic fabrics in smaller faults to cataclastic textures in boundary faults that accommodated larger displacements resulted from an increase in the shear strain rate across the boundary faults as adjacent faults became inactive. Alternatively, the cataclastic deformation maybe be related to cooling of the pluton as deformation progressed (Christiansen *et al.* 1992).

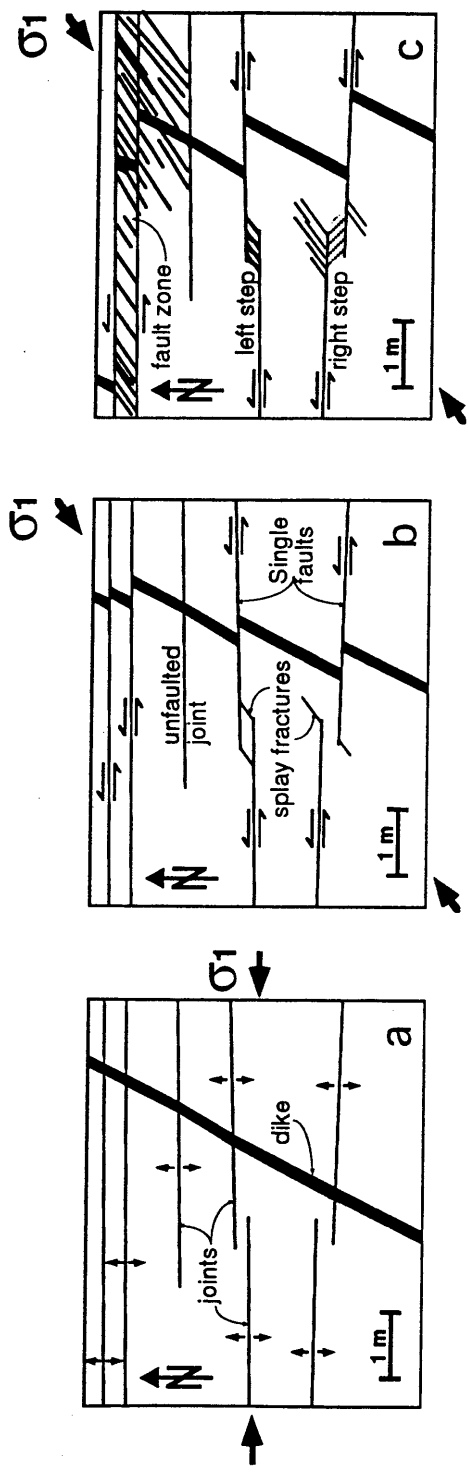


Fig. 2.2. Map views of Late Cretaceous development of joints and faults in the Mt. Abbot quadrangle. (a) Joints formed soon after emplacement of the Lake Edison Granodiorite. (b) Stress reorientation subsequently caused left-lateral fault slip along the joint planes and splay fractures form near fault terminations. (c) Individual faults interact across left and right steps and form brittle fault zones. Ductile deformation occurs in right steps and dilatant fracturing in left steps and in the fault zones (after Segall & Pollard, 1983a,b; Martel et al., 1989).

Timing

A minimum age of motion along two ENE-trending, left-lateral fault zones in the Lake Edison Granodiorite has been determined to be 75-79 Ma based on $^{40}\text{Ar}/^{39}\text{Ar}$ and K-Ar dating of muscovites formed as a product of hydrothermal alteration in the fractured fault-zone interior (Segall *et al.* 1990). The early jointing and slip on isolated faults must have occurred between intrusion (~85-90 Ma, Stern *et al.* 1981) and fault-zone development 75-79 Ma (Segall *et al.* 1990).

Jointing presumably occurred during the initial cooling and dewatering phase (Best 1982, p. 290) of the Lake Edison Granodiorite. Subsequent stress reorientation and faulting may be related to the intrusion of the neighboring, somewhat younger Mono Creek Granite to the east (Bateman 1992, Fig. 2.1). This is supported by the increased development of ductile fabrics along the faults near the younger pluton, indicating that faulting occurred during or soon after intrusion of the Mono Creek Granite (Segall *et al.* 1990). However, the abundance of similarly oriented fracture sets throughout the central Sierra Nevada (Mayo 1941, Lockwood & Moore 1979) and evidence of significant margin-parallel right-lateral shear in the Late Cretaceous (Page & Engebretson 1984, Busby-Spera & Saleeby 1990, Tikoff & Teyssier 1992) suggest a relationship to regional tectonism (Davies & Pollard 1986, Segall *et al.* 1990).

Fluid flow

Fluid flow is evident at all stages of fracturing, from jointing to faulting, producing hydrothermal mineralization and extensive wall-rock alteration. The wall rock adjoining some joints was altered by interaction with circulating fluids, resulting in albitization of calcic plagioclase and potassium feldspar over a width of several centimeters. Sericitization of feldspar, removal of mafic minerals and an abundance of fluid inclusions give the altered rock a bleached appearance (Segall *et al.* 1990). These

alteration halos increase in width where joints intersect (Segall & Pollard 1983a).

Faults and fault zones in the study area show evidence of continued fluid flow in the form of quartz veins and associated wall-rock alteration at fault terminations, in extensional fault steps and bends, and in fault zones. Rock permeability is strongly dependent on the availability of fluid pathways in the form of open fractures that form in different geometries at different stages of the structural development in the area (Bürgmann *et al.* 1992). Therefore the deformation style, the cooling history of the plutons, and fluid flow are linked in a complex pattern (Pollard *et al.* 1992).

Brittle fracture and ductile flow

Structures formed during faulting in the Lake Edison Granodiorite were both brittle and ductile in nature (Segall & Simpson 1986, Bürgmann & Pollard 1992). The opening of brittle fractures accompanied ductile shearing as evidenced by oblique mineralized splay fractures that developed near fault terminations and fault discontinuities (Fig. 2.2b). Locally, ductile shear as evidenced by the development of mylonitic fabrics occurs on either side of the faults. Ductile fabrics are localized in contractional stepovers and along bends of the strike-slip faults (Segall & Simpson 1986, Martel *et al.* 1988, Bürgmann & Pollard 1992). Kronenberg *et al.* (1990) described the first natural example of localized hydrolytic weakening where ductile shearing spreads from a fault segment in the Lake Edison Granodiorite. They observed a correspondence of water concentrations in quartz (mostly in fluid inclusions) and ductilely accommodated shear strain in the rock adjacent to the fault. This suggests that water infiltration through open microcracks during initial jointing may have induced a reduction in ductile strength of the wall rock (Kronenberg *et al.* 1990). Bürgmann & Pollard (1992) showed that there is a transition from brittle deformation processes to crystal-plastic deformation in quartz and mica within right

stepovers where the mean stress increases by less than 25 MPa. This weakening effect is possibly due to the pressure dependence of hydrolytic weakening in quartz (Tullis & Yund 1989).

FAULT TERMINATIONS

Three fundamentally different types of fault-termination structures in the Lake Edison Granodiorite developed at different distances from the neighboring Mono Creek Granite (Fig. 2.6). These are fault terminations with splay fractures (Fig. 2.6a,b), with splay fractures and mylonitic fabrics juxtaposed on either side of the fault (Fig. 2.6c), and with mylonitic fabrics ahead of the fault terminations (Fig. 2.6d). We hypothesize that these structures reflect the material response of the granodiorite at different temperatures, as the neighboring pluton reheated the Lake Edison Granodiorite. Later we present model results that help explain the variety of fault-termination structures observed.

The first type of fault-termination structure can be observed throughout the pluton and is characterized by the development of dilatant splay fractures in the NE and SW quadrants oblique to the left-lateral faults (Fig. 2.6a, b). Little or no shear offset is observed on the splay fractures that form at angles ranging from about 30° to 60° to the faults. Commonly a set of fractures spaced several centimeters apart forms near the fault termination. Continued opening of splay fractures in the presence of hydrothermal fluids allows the formation of thick wedges filled with precipitates, primarily quartz (Fig. 2.6a). There is no evidence of ductility in the granodiorite. However, mylonitic fabrics in the fine-grained fault material and deposition of quartz, epidote, and chlorite in the splay fractures, indicate that deformation occurred during hydrothermal activity. Splay fractures provided efficient conduits for fluid flow during the faulting stage of deformation.

Closer to the Mono Creek Granite we find examples of a similar type of fault termination, however, in the quadrant opposite to the splay fractures mylonitic fabrics appear (Fig. 2.6c). The example in Fig. 2.6c

shows that the slip gradient near the fault termination is very steep; slip decreases from about 0.8 m to 0 m in <2 m. Significant strain occurs in the granodiorite to accommodate the slip gradient along the fault.

Within about 100 m of the contact with the Mono Creek Granite, some faults terminate in localized zones of mylonitic fabrics, up to a meter in width, that do not extend more than a few meters from the fault ends. Whereas a dike is offset by ~1.2 m across the fault about 1.5 m from the fault termination, a second dike is strongly sheared and thinned ahead of the fault shown in Fig. 2.6d. As slip on the sheared joint decreases rapidly towards the termination, the zone of deformation broadens from a few millimeters into a continuous shear zone about 70 cm across.

In summary, depending on their distance from the neighboring Mono Creek Granite, faults develop just splay fractures, splay fractures and ductile fabrics on opposed sides of the fault termination, or localized symmetric zones of ductile fabrics extending from the fault termination, as one approaches the pluton contact.

LEFT STEPOVERS

Where two faults are arranged in an echelon geometry, the brittle and/or ductile strain intensifies due to fault interaction. We mapped several left and right steps in detail to determine the geometries of the structures and to examine the deformation mechanisms accommodating the strain.

Slip transfer through extensional left stepovers was accommodated through the dilation of fractures as evidenced by veins filled with quartz, epidote, and chlorite. Vein fillings and alterations in the wall rock close to the stepovers indicate the abundance of fluids during the deformation event. The size of fractured left steps ranges from a few centimeters to ~1 m in width and up to 2 m of overlap. Vein thicknesses of up to 10 cm can be found in some steps.

Figure 2.3 shows a map of a left stepover at site HE90 (see Fig. 2.1). The 7 cm offset of an aplitic dike across one of the stepover-bounding

faults compares well with the combined opening of 5 to 6 cm within the stepover that was determined from the vein widths measured at varying distances from the faults. This comparison demonstrates that macroscopic dilatant fractures have transferred at least 70% of the slip across the stepover. Even though the fracture of the eastern fault segment continues for 2 m to the W of the stepover it shows no evidence of fault slip past the stepping region. Two NE-striking mineralized fractures initiate on the eastern fault segment outside of the fault stepover. These fractures are splay fractures from the western segment that cut across the eastern segment, suggesting that slip on the latter was of lesser magnitude. Several NS-striking joints with no mineral fill or associated alteration zones are not related to the faulting event. There is no evidence of ductile fabrics associated with left steps; deformation is purely brittle by dilatant fracture between the fault stepovers.

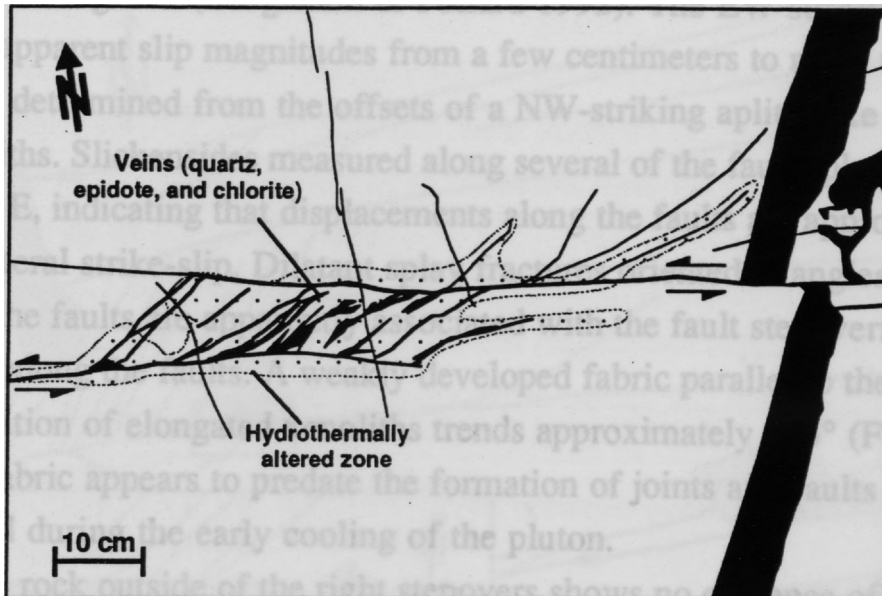


Fig. 2.3. Outcrop map of two left-stepping echelon fault segments at site HE90 linked by dilatant fractures that transfer 5-6 cm of slip between the faults. Note bleached halo of altered granodiorite indicating active fluid circulation through the step. The fault-linking veins are filled with quartz and minor chlorite and epidote.

RIGHT STEPOVERS

Macroscale structure

Figure 2.4a shows an outcrop map from the Bear Creek area labeled BA90 in Fig. 2.1 (Bürgmann & Pollard 1992). The EW-striking fractures have apparent slip magnitudes from a few centimeters to more than a meter determined from the offsets of a NW-striking aplite dike and mafic xenoliths. Slickensides measured along several of the faults plunge $< 10^\circ$ to the E, indicating that displacements along the faults are approximately left-lateral strike-slip. Dilatant splay fractures oriented at angles of $30-60^\circ$ from the faults are apparently associated with the fault stepovers and bends along the faults. A weakly developed fabric parallel to the orientation of elongated xenoliths trends approximately 315° (Fig. 2.4a). This fabric appears to predate the formation of joints and faults and formed during the early cooling of the pluton.

The rock outside of the right stepovers shows no evidence of significant ductile strain. A zone of NE-striking fractures in the middle left of Fig. 2.4a is spatially related to the fault stepover labeled BA90, forming a large splay fracture array. The mineral-filled fractures oriented $50-60^\circ$ to the faults accommodate some extension. The 1.2 m offset of the aplite dike located 3-4 m to the W of the fault stepover, is reduced by about 6-8 cm by the combined dilation of about 60 mineralized splay fractures between the offset dike and the fault termination.

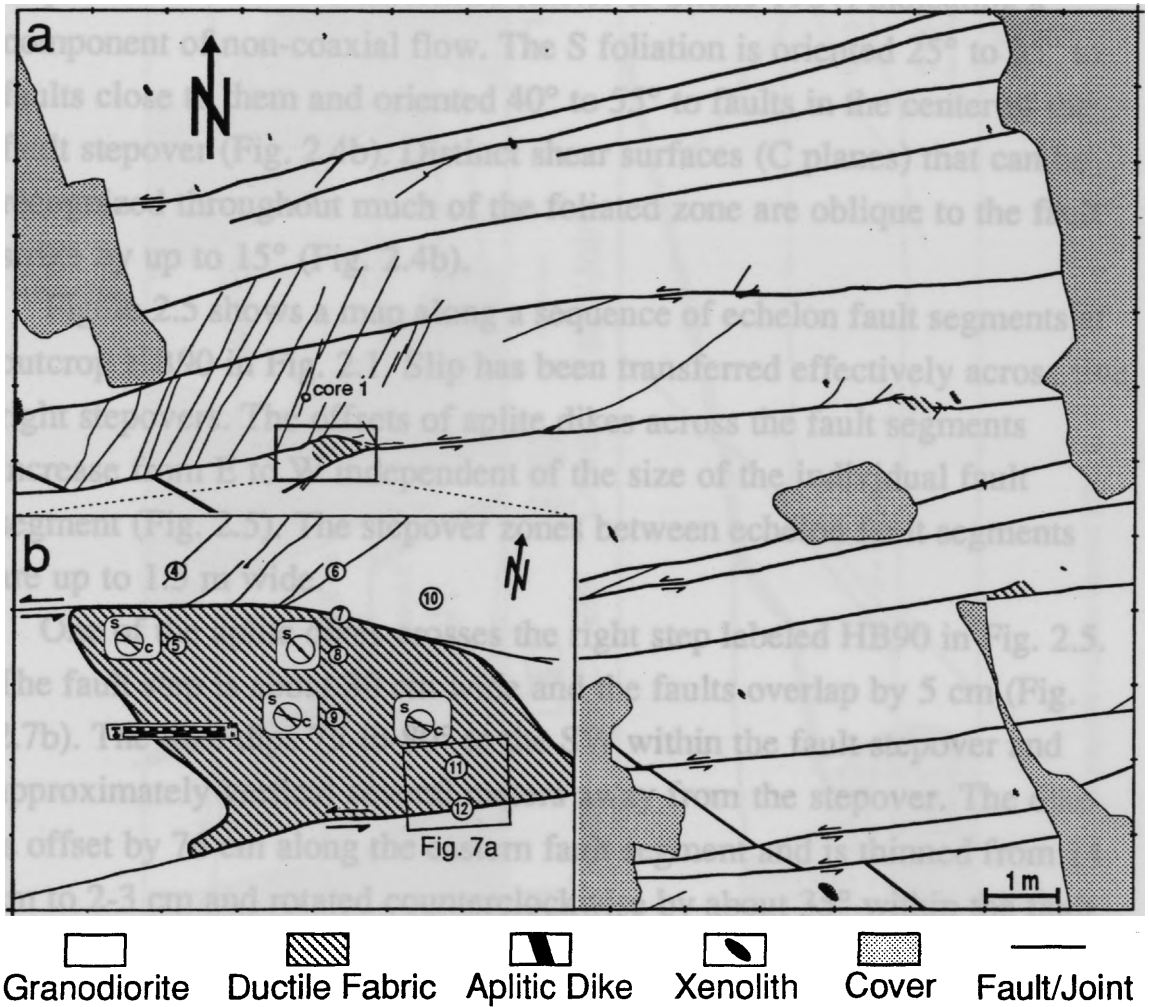


Fig. 2.4. (a) Outcrop map of faults, fractures and right steps at location BA90 in Fig. 2.1. Left-lateral offsets on some of the faults are indicated by a displaced aplite dike. Oblique fractures near the boxed right stepover appear to be related to stress perturbations near the fault step. (b) Detailed map of boxed right step. Circled numbers indicate core sample locations. Diagrams show the orientation of S and C planes in thin sections from cores.

Well-developed ductile fabrics, shown as hachured areas, are restricted to right stepovers along the faults. Only millimeters outside the steps, the granodiorite appears isotropic (Fig. 2.7a). The textures in the fault stepover resemble S-C mylonites (Lister & Snoke 1984) indicating a component of non-coaxial flow. The S foliation is oriented 25° to 35° to faults close to them and oriented 40° to 55° to faults in the center of the fault stepover (Fig. 2.4b). Distinct shear surfaces (C planes) that can be recognized throughout much of the foliated zone are oblique to the fault strike by up to 15° (Fig. 2.4b).

Figure 2.5 shows a map along a sequence of echelon fault segments at outcrop HB90 in Fig. 2.1. Slip has been transferred effectively across five right stepovers. The offsets of aplite dikes across the fault segments increase from E to W independent of the size of the individual fault segment (Fig. 2.5). The stepover zones between echelon fault segments are up to 1.5 m wide.

One of the aplite dikes crosses the right step labeled HB90 in Fig. 2.5. The fault step is about 30 cm wide and the faults overlap by 5 cm (Fig. 2.7b). The dike dips 75° -to- 80° to the SW within the fault stepover and approximately vertical several meters away from the stepover. The dike is offset by 76 cm along the eastern fault segment and is thinned from 14 cm to 2-3 cm and rotated counterclockwise by about 35° within the fault stepover (Fig. 2.7b). This corresponds to an offset of 1.15 m of a second dike on the western fault segment, indicating that slip was transferred almost in full across the stepover. Both faults curve outward adjacent to the right step, indicating an outward bending of the faults as material is pushed into the stepover. However, the widening of the stepping region can not accommodate the horizontal shortening of about 1 m we infer from the fault offsets. The thinning of the aplite dike in the step indicates that up to 80% of the rock originally located within the fault step had to be removed to accommodate slip transfer.

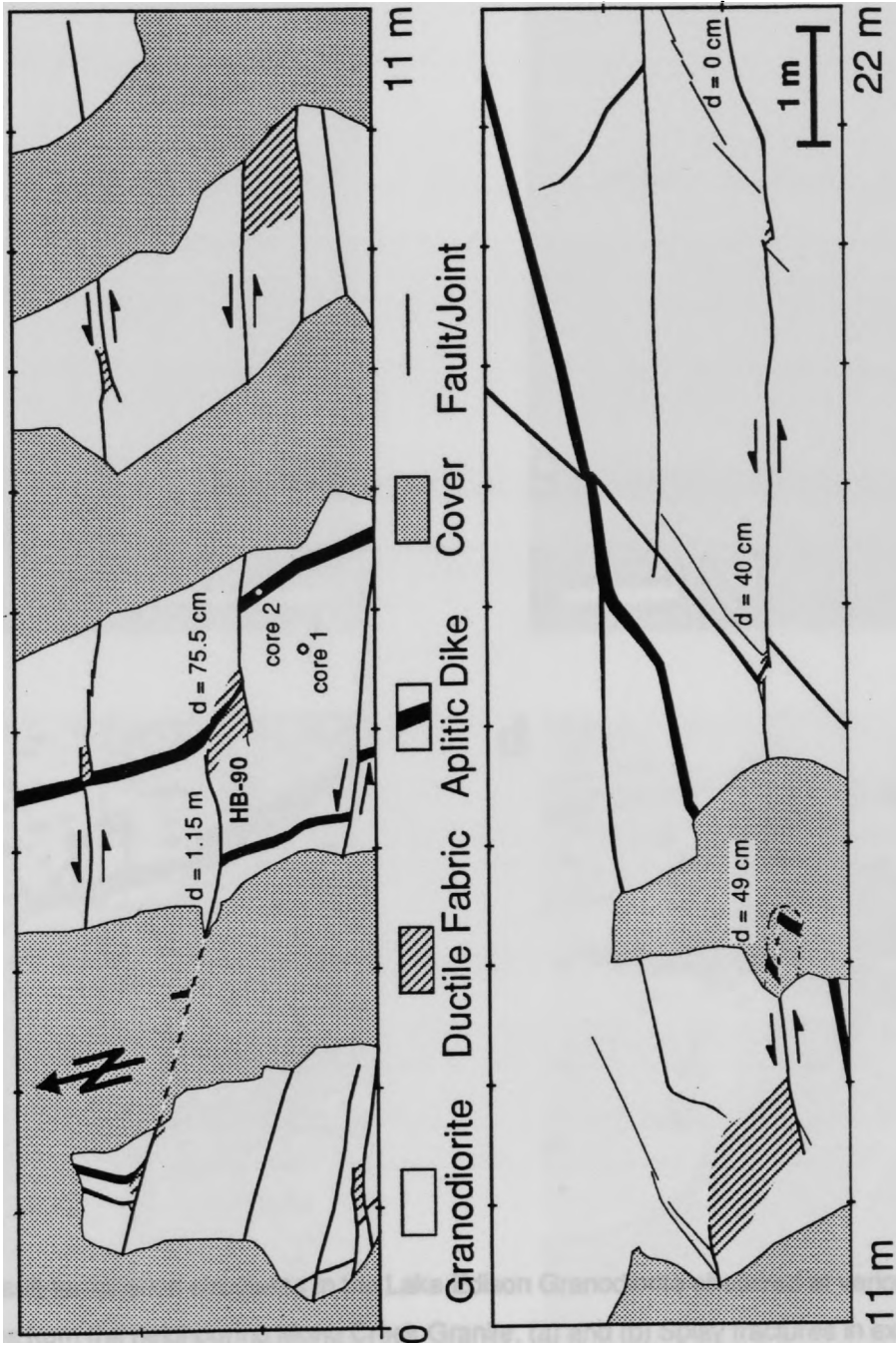


Fig. 2.5. Outcrop map of faults, fractures and right steps at location labeled HB90 in Fig. 2.1. Fault-slip measurements are from offset aplite dikes.

Fig. 2.6. Fault-termination structures in the Lake Edison Granodiorite observed at various distances from the neighboring Mono Creek Granite. (a) and (b) Splay fractures in extensional quadrant; the wedge near the fault termination in (a) is filled with quartz. (c) Splay fractures in extensional quadrant and mylonitic fabric in the contractional quadrant. (d) Symmetric mylonitic shear zone spreading from fault termination. Arrows in (c) and (d) point to offset aplite dikes indicating m-scale slip magnitudes near fault terminations. Scale bars are 20 cm.

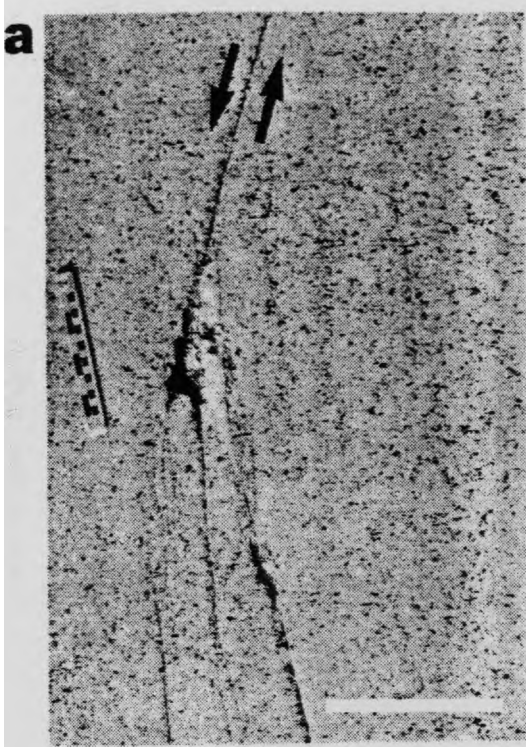
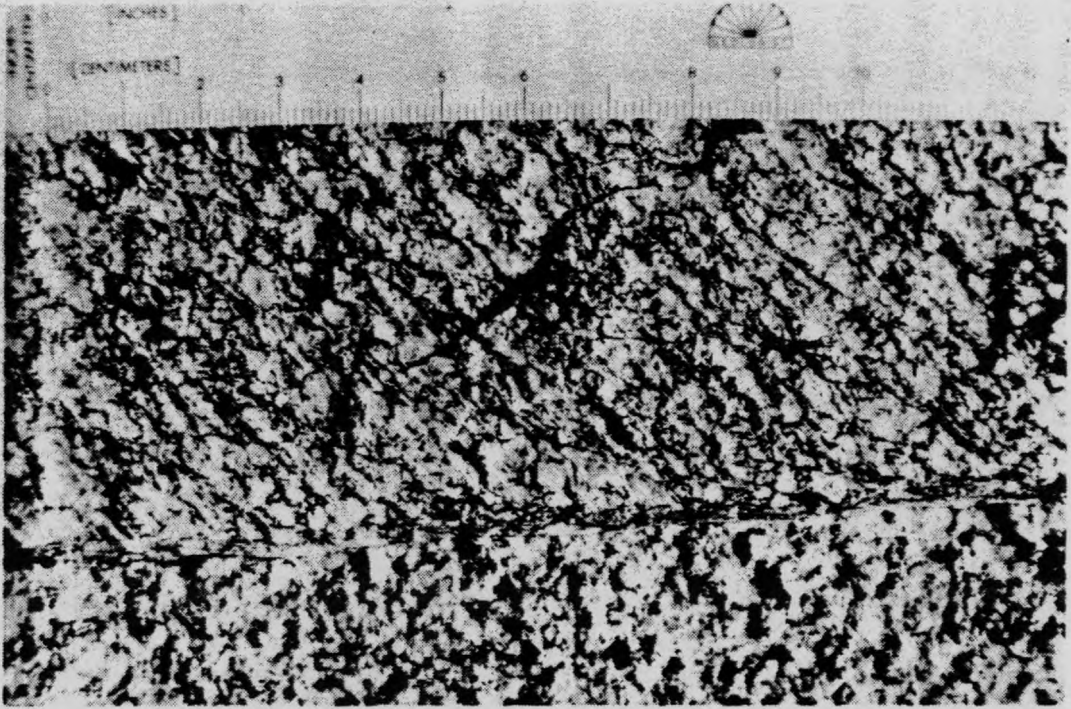


Fig. 2.7. (a) Close-up photograph of fabric contrast across the step-bounding fault in boxed region near core 12 in Fig. 2.4. (b) Close-up photograph of right step in upper panel of Fig. 2.5 showing a marked textural change (isotropic to foliated) across the step-bounding faults. The aplite dike is thinned to 2-3 cm in the stepover from an original thickness of 14 cm and reoriented by counterclockwise rotation of $\sim 35^\circ$. The numbered circles mark the location of core samples taken for microstructural and geochemical analyses.

a

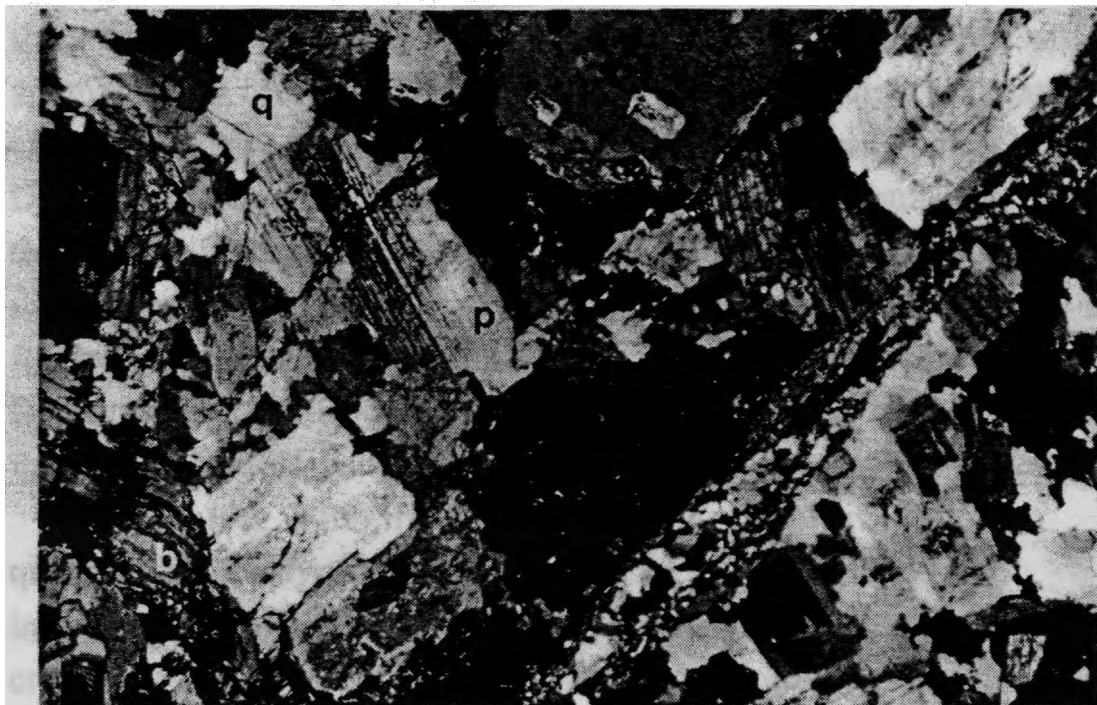


b



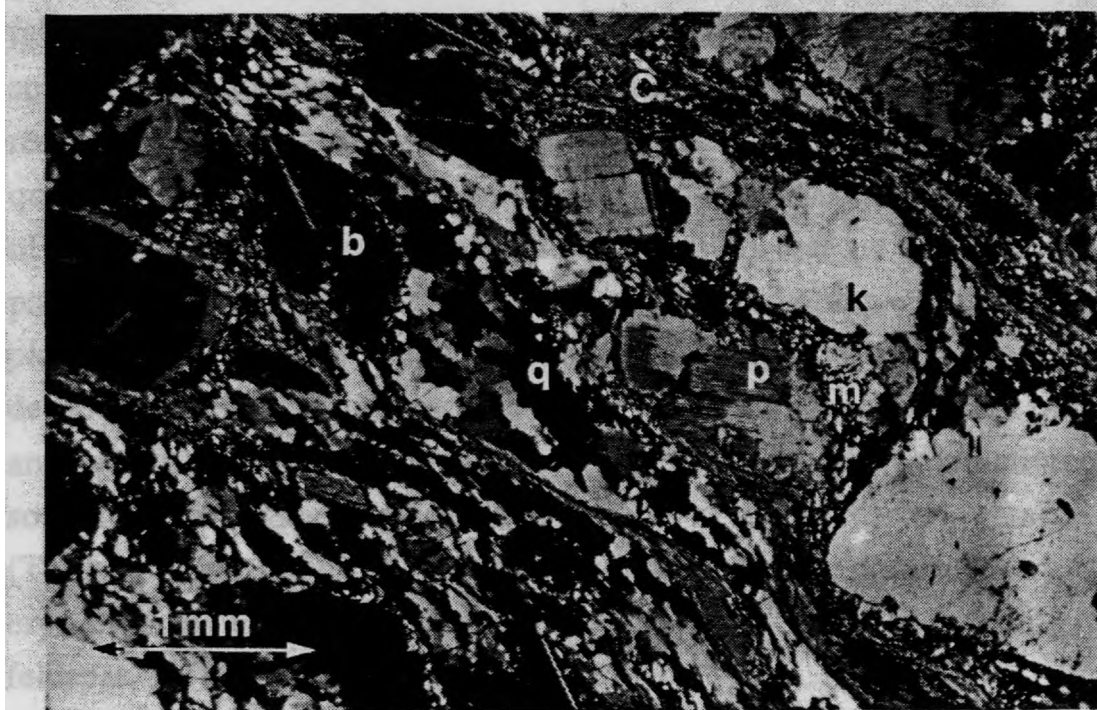
Fig. 2.8. Photo micrographs of thin sections from cores 6 and 8 under crossed nichols (see Fig. 2.4 for core locations). Both photographs are at the same magnification. (a) Core 6 (located 10 cm away from the step) showing dilatant fractures filled with quartz and no fabric development. (b) Core 8 from ductilely deformed step area showing recrystallized quartz, fractured feldspars, mica fish textures, and S-C type fabrics indicative of non-coaxial flow. C-mylonitic C-surface, b-biotite, k-potassium feldspar, m-myrmekite, p-plagioclase, q-quartz.

a



Since 1943, Myrmecolites are common in the undeformed
slates are often crushed and deformed by cataclastic flow of the

b



Microscale structure

We analyzed several thin sections to characterize the deformation of the granite around the stepover. Core 6 (see location in Fig. 2.4b) has an approximately isotropic fabric and quartz shows only slight undulatory extinction (Fig. 2.8a). Grain sizes are typically in the range of 1-3 mm. One of the fractures emanating from the step-bounding fault crosses the thin section in the lower right of the photograph. Grain-scale shear and dilatant fractures subparallel to the splay fracture are common in feldspars, and fractures are filled with fine-grained quartz and chlorite. Deformation is brittle, dominated by dilatant fracturing of an interconnected feldspar framework.

In core 8 (Fig. 2.8b), from within the right stepover (Fig. 2.4b), quartz grains are dynamically recrystallized and strongly elongate, indicating crystal-plastic flow. Biotite, often altered to chlorite, is also crystal-plastically deformed and shows typical "mica fish" textures (Lister & Snoke 1984). Myrmekites that are common in the undeformed granodiorite are often crushed and deformed by cataclastic flow of the feldspar constituent in a matrix of fine-grained quartz. Distinct, EW-striking shear surfaces (C-planes), rich in fine-grained mica and finely recrystallized quartz, separate zones of feldspars and plastically deformed quartz and biotite. The quartz and biotite domains anastomose in and out of the C-planes and wrap around feldspar clusters that are elongate parallel to the macroscopic foliation (S-planes) and oblique to the C-planes and the stepover-bounding faults. Feldspar grains are commonly deformed by extensional cracking, shear fracturing along cleavage planes, and cataclastic flow at grain boundaries. Patchy undulatory extinction in some feldspar grains is interpreted to be due to submicroscopic cataclasis (Tullis & Yund 1987). Overall, deformation is ductile, dominated by crystal-plastic flow of quartz and mica enveloping grains of broken feldspar, hornblende, and opaques.

Figure 2.9 shows maps of plagioclase, K-feldspar, quartz, and opaque minerals of cores 1 and 9 (see Fig. 2.4 for core locations). Both feldspars

were stained on the thin sections to allow easy recognition on an image projected onto a digitizing table. We were able to accurately calculate the area percentage of the individual mineral constituents. Individual grain boundaries between neighboring grains of the same mineral species, however, could not be mapped.

The textures in the horizontal section from core 1, located about 1 m N of the fault step, indicate that the little-deformed granodiorite is characterized by an interconnected framework of feldspar interspersed with approximately equant-shaped quartz, amphibole, and biotite grains (Fig. 2.9a). A weakly developed, approximately NS-oriented elongation of feldspar and quartz grain aggregates follows the trace of the regional foliation.

The foliated granodiorite from core 9, taken from the middle of the step, shows drastically different textures (Fig. 2.9b). Feldspar grains are aligned and slightly elongated in a NW-SE orientation. The feldspar framework apparent in core 1 appears to be broken and thin bands of elongated and sheared quartz and mica domains envelop the feldspar grains. The quartz and mica domains curve into two EW-striking shear surfaces in the middle and upper half of the section.

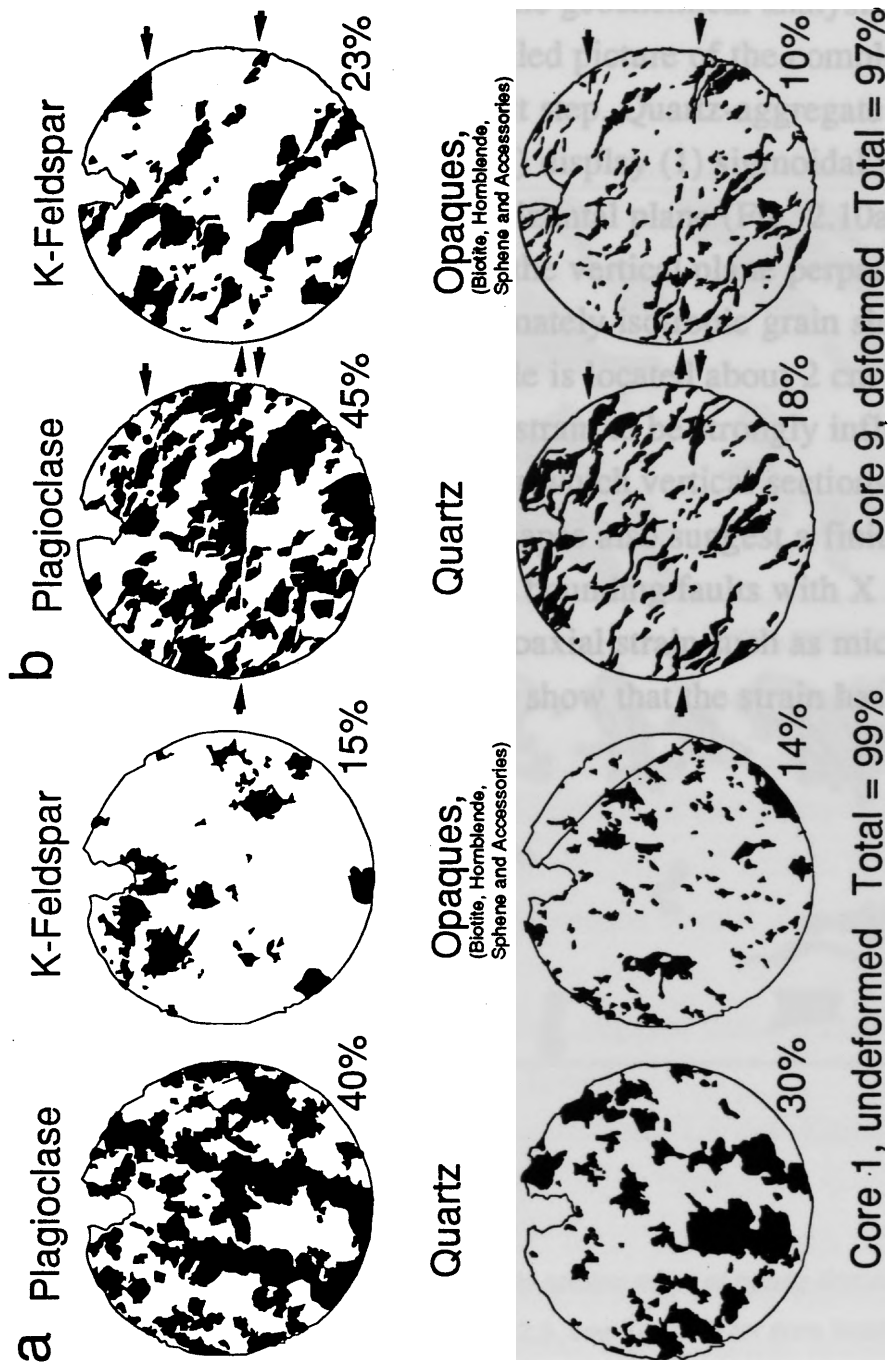


Fig. 2.9. Thin section maps of quartz, feldspars, and opaques in cores 1 & 9 (see Fig. 2.4 for core location). The diameter of the cores is 2.54 cm, the notches at the tops of the sections are oriented towards the N. (a) The fabric in core 1 is approximately isotropic. (b) The granodiorite in core 9 is strongly sheared; grains are elongated in the NW-SE direction and are dragged along EW-striking C-planes. Note the reduced quartz content of core 9 compared to core 1.

Thin sections were cut along three mutually perpendicular planes, parallel and perpendicular to the foliation plane, to evaluate the three-dimensional strain and the distribution of strain within a fault stepover (Fig. 2.10). Most cores were used for the geochemical analysis (see below), so we do not have a very detailed picture of the complete range of textural changes throughout the fault step. Quartz-aggregate shapes from core 8 (see Fig. 2.7b for location) display (1) sigmoidal patterns indicating non-coaxial shear in the horizontal plane (Fig. 2.10a), (2) strongly stretched grain aggregates in the vertical plane perpendicular to foliation (Fig. 2.10b), and (3) approximately isotropic grain shapes in the foliation plane (Fig. 2.10c). This sample is located about 2 cm from the step-bounding fault and we expect the strain to be strongly influenced by the nearby fault. In a second sample for which vertical sections could be prepared (core 4 in Fig. 2.7b), grain shapes also suggest a finite strain ellipsoid that is flattened oblique to the bounding faults with X and Y axes of subequal length. Indicators of non-coaxial strain such as mica fish, sigmoidal grain shapes, and SC-fabrics show that the strain has a strong simple-shear component.

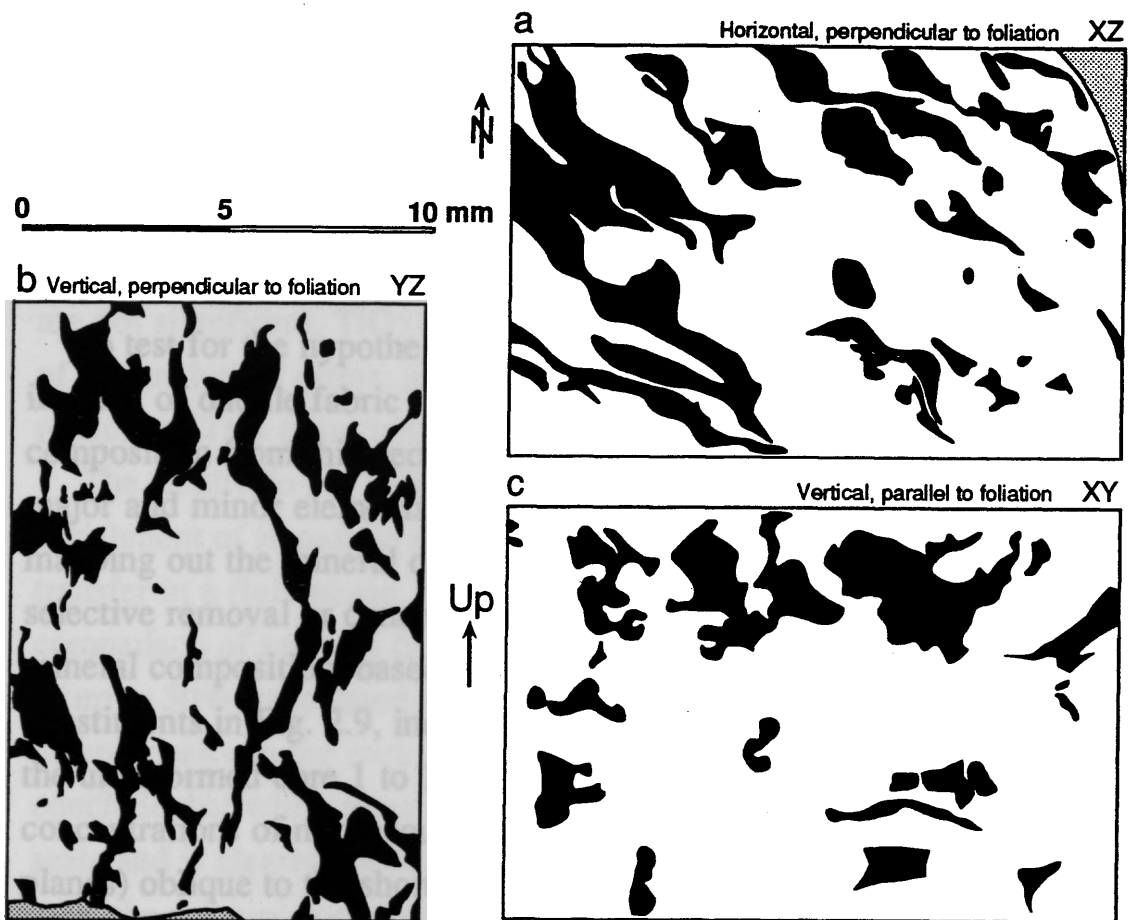


Fig. 2.10. (a) - (c) Three mutually perpendicular thin section maps of quartz domains for core 8 from within the stepover at outcrop HB90 (Fig. 2.5, see Fig. 2.7b for core location). The foliation is defined by deformed elongate quartz aggregates. Note that the quartz domain shapes in the foliation plane in (c) are approximately equant.

Mass solution transfer: mineralogic and geochemical analyses

While the evidence of mineralization in dilatant fractures associated with the faults is clear, the source of the precipitating material is not obvious. Mass solution transfer may have occurred only over short distances at the grain scale, however, the large volume of some of the vein fillings suggests otherwise. Fluids may have been derived from a magmatic source, possibly from the newly intruded, cooling Mono Creek Granite to the E. Mass solution transfer may also have occurred locally, possibly involving mass removal from the deformed right steps. As the mineralizations in splay fractures and along some fault segments are mostly quartz, we would expect a reduction of silica content in the deformed rock.

To test for the hypothesis of local mass removal by pressure solution in areas of ductile fabric development, we determined the mineral composition from thin sections and carried out a geochemical analysis of major and minor elements of deformed and undeformed granodiorite. By mapping out the mineral distribution in a thin section we can test for selective removal or concentration of individual mineral species. The mineral composition, based on area percentage of the mapped mineral constituents in Fig. 2.9, indicates a large decrease of quartz from 30% in the undeformed core 1 to 18% in the deformed core 9. Increased concentrations of micaceous material along discrete shear surfaces (C-planes) oblique to the shortening direction suggest that pressure solution may have occurred in these high strain zones.

However, mineral composition deduced from 2.5 cm-diameter thin sections are based on a very small sample size. Therefore, we undertook major-element analyses of cored samples from the two fault stepovers at BA90, HB90 and a third site, HC90 (about 200 m NE of HB90), as well as trace-element analyses for BA90 and HB90. Geochemical analyses of cored samples can determine if bulk chemical differences exist between deformed and undeformed samples and can test for the removal or residual enrichment of mobile and immobile elements, respectively. Table

2.1 indicates which cores were used in the X-ray fluorescence spectroscopy analyses and shows the results and the associated uncertainties. Experimental errors were calculated from repeated results of G-2 standard granite samples over a week-long time period, as well as from our own repeated sample runs (Table 2.1).

To determine the extent of mass solution transfer or pressure solution, we compare the concentration of SiO_2 , a mobile and easily dissolved element, and the immobile elements TiO_2 and Zr (e.g. Ague 1991). Figure 2.11 shows the ratios of the concentrations in the deformed samples (C_s) and the approximately undeformed cores (C_o). While the concentration of SiO_2 in the fault stepovers is less than or equal to that of the undeformed rock in each example, the differences of less than 1.5% are not significant. TiO_2 -concentration differences are also in the range of the analytical errors, and show no consistent trend of enrichment or reduction. This trend holds true for Zr as well.

The results do not indicate any significant decrease of mobile phases or enrichment of immobile elements due to mass removal by mass solution transfer in a fluid phase. It is interesting to note, however, that a comparison of samples from the individual sites suggests volume strains of up to 30% (calculated after Ague, 1991), indicating significant heterogeneity in the rock composition over few hundred meters. We conclude that while mass solution transfer may have occurred at the grain scale and is clearly implicated in the abundant mineral precipitation in the area, the mineral constituents were not derived from ductilely deforming stepover zones along the faults. The quartz-content change observed in the thin sections in Fig. 2.9 reflects the natural heterogeneity of the rock at the thin-section scale and not mass-solution transfer.

In summary, we find that strain in mylonitically deformed right stepovers in the Lake Edison Granodiorite apparently was accommodated by ductile flow, including a vertical flow component. Mass solution transfer was not responsible for the significant mass transport out of the contractional steps required by their kinematics.

Cores:	BA90-1&3 Undef.	BA90-4,6&10 Undef. nearby	BA90-8,9&11 Def.	HB90-1,3&5 Undef.	HB90-7,4&8 Def.	HC90-1,2,7&9 Undef.	HC90-6&10 Def.	1Sigma (G-2)*	Precision (%)**
Major Elements (%)									
SiO2	65.86	66.22	65.94	70.48	69.15	66.76	66.29	0.35	0.13
TiO2	0.55	0.53	0.51	0.36	0.39	0.54	0.53	0.01	0.00
Al2O3	16.07	15.82	15.71	15.01	14.89	15.71	16.01	0.11	0.06
Fe2O3	4.25	4.23	4.11	2.97	2.98	4.05	3.99	0.02	0.02
MnO	0.08	0.08	0.08	0.07	0.07	0.08	0.08	0.00	0.00
MgO	1.83	1.81	1.80	1.14	1.15	1.52	1.53	0.01	0.01
CaO	4.38	4.28	4.09	2.98	3.07	3.84	3.85	0.01	0.00
Na2O	3.59	3.49	3.46	3.45	3.67	3.77	4.07	0.06	0.03
K2O	3.04	3.17	3.36	4.08	3.41	3.18	2.87	0.03	0.01
P2O5	0.18	0.17	0.17	0.12	0.13	0.20	0.20	0.00	0.00
TOTAL	99.83	99.79	99.22	100.66	98.92	99.65	99.41	0.40	0.56
Trace Elements (ppm)								1Sigma (G-2)**	Precision (ppm)***
Zr	111.7		114.0	97.4	95.4			1.99	3.34
Y	10.3		9.5	6.8	7.5			0.64	0.36
Nb	9.4		9.7	6.9	8.7			0.26	0.14
Sr	540.4		532.6	443.4	447.2			2.14	2.52
U	6.4		7.1	3.2	4.0			0.67	0.35
Rb	132.3		137.0	147.0	164.2			0.55	0.79
Th	17.4		16.1	15.5	16.9			0.65	0.63
Pb	18.4		18.8	22.8	22.4			0.94	0.26
Ga	17.8		16.6	16.2	17.3			0.29	0.38

* Standard deviation of 14 G-2 standard analyses over 5 days

** Standard deviation of 4 G-2 standard analyses over 8 days

*** Mean of standard deviations of own repeated samples

Table 2.1. Major and trace element concentrations of undeformed and deformed samples (from outside and within contractional steps) from XRF analyses.

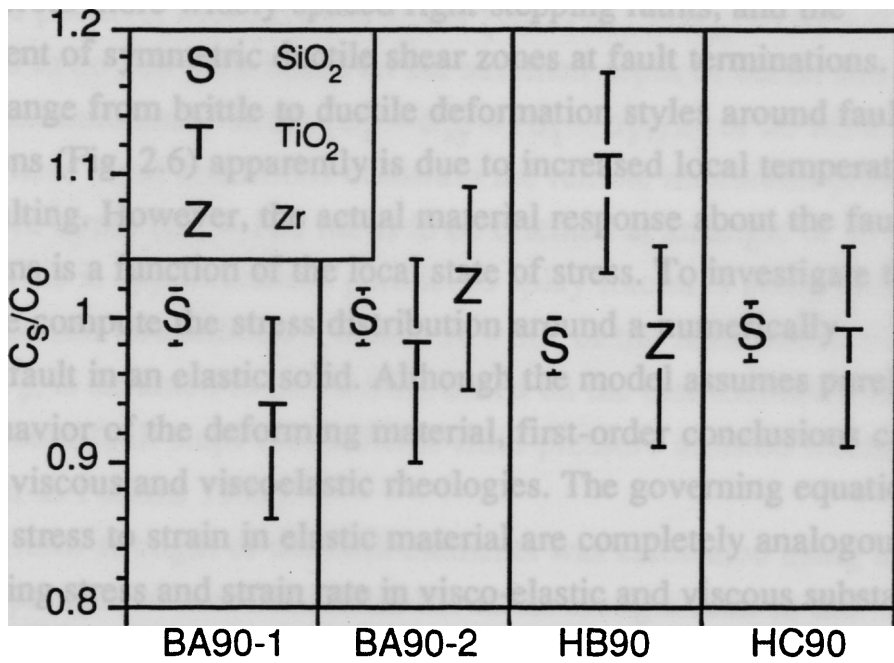


Fig. 2.11. Concentration ratios of SiO₂, TiO₂ and Zr between undeformed and deformed samples derived from Table 2.1. (See Fig. 2.1 for sample locations, HC90 is located ~ 200 m NE of HB90). Significant differences in concentrations of mobile or immobile elements between deformed and undeformed samples are not apparent.

TEMPERATURE DEPENDENT DEFORMATION STYLE AT FAULT TERMINATIONS

Deformation was increasingly accommodated by ductile mechanisms as the contact to the neighboring Mono Creek Granite is approached. This pluton is younger than the Lake Edison Granodiorite and apparently intruded during faulting. The enhanced ductility near the contact is evidenced by steep slip gradients near fault terminations, ductile slip transfer across more widely-spaced right-stepping faults, and the development of symmetric ductile shear zones at fault terminations.

The change from brittle to ductile deformation styles around fault terminations (Fig. 2.6) apparently is due to increased local temperatures during faulting. However, the actual material response about the fault terminations is a function of the local state of stress. To investigate this further, we compute the stress distribution around a numerically generated fault in an elastic solid. Although the model assumes purely elastic behavior of the deforming material, first-order conclusions can be drawn for viscous and viscoelastic rheologies. The governing equations that relate stress to strain in elastic material are completely analogous to those relating stress and strain rate in visco-elastic and viscous substances (Johnson 1970, p. 272). In particular solutions for stresses in plane strain of an elastic body are solutions for stresses in incompressible, viscous bodies with the same boundary conditions (Johnson 1970, p. 278). However, the development of large strains and anisotropic fabrics, and non-linear rheologies, clearly are not addressed in our models. Instead, we model the stress field caused by a few millimeters displacements along the faults. Inelastic deformation continuously relaxes these stresses. Furthermore, we do not address the three-dimensional character of the deformation. Models of equidimensional faults in three dimensions do not differ significantly from the plane strain models except for very near the upper and lower fault peripheries (Bürgmann & Pollard 1992).

The stress field around a fault termination was determined using the boundary element method (Crouch & Starfield 1983) implemented as the

program Frac2D by Thomas & Pollard (1993). The model assumes a homogeneous, isotropic, linear elastic solid under conditions of two-dimensional elastostatic plane strain. The vertical dimension of the fault is assumed to be much greater than its length and we postulate that no vertical variations in geometry or boundary conditions occur.

A 20-m long left-lateral fault is divided into 80 displacement-discontinuity boundary elements, each 25-cm long . Compressive stress is taken to be positive. Mean remote stress ($\sigma_m^r = \sigma_{xx}^r = \sigma_{yy}^r = (\sigma_1^r + \sigma_3^r)/2$) is assumed to be 100 MPa based on the assumed depth of burial and a remote maximum shear stress ($\sigma_s^r = \sigma_{xy}^r = (\sigma_1^r - \sigma_3^r)/2$) of 20 MPa is applied. These input conditions constrain the remote maximum principal compressive stress ($\sigma_{r1} = 120$ MPa) to be oriented at an angle of 45° to the fault. This is approximately parallel to splay fractures along faults in the Lake Edison Granodiorite (within $30 - 60^\circ$ of the fault trace). Fluid pressure, P_p , is assumed to be 70 MPa based on the distribution of dilatant fractures about fault steps that indicate fluid-pressure assisted fracture (Bürgmann & Pollard 1992).

The uniform strength of the fault elements was calculated using a Byerlee-type friction law that relates the stress along a fault to the effective normal stress, the coefficient of friction, and the inherent cohesion of the fault zone:

$$\tau = \sigma_n \mu + C \quad (1)$$

With an effective fault-normal stress, $\sigma_n = \sigma_n^{\text{lith}} - P_p = 100 - 70$ MPa (Bürgmann & Pollard 1992), a coefficient of friction, $\mu = 0.4$, suggested for faults at hydrothermal conditions (Blanpied *et al.* 1992), and cohesion, C of 5 MPa, we find the frictional strength τ of the fault to be 17 MPa. These values are only approximations of the conditions during faulting; they are constrained by observations of abundant veining indicating high fluid pressures and estimates of shear strength of the ductilely deforming fault gouge based on the orientation of secondary splay fractures and fabrics about fault steps that indicate that faults had significant strength (Bürgmann & Pollard 1992).

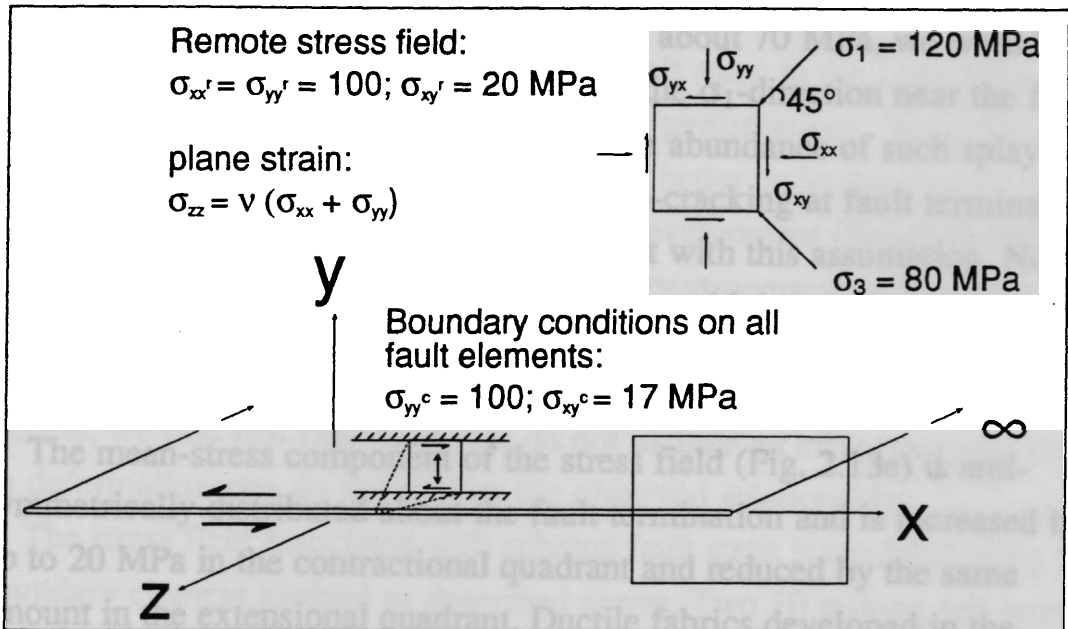


Fig. 2.12. Boundary conditions and model geometry of a fault surface in an elastic, isotropic, and homogeneous material. Compressional stresses are positive and shear stresses are positive as shown. The fault is idealized to extend infinitely in the out-of-plane z-direction (two-dimensional plane strain).

The lower panels in Fig. 2.13 (d-f) show the magnitudes of key components of the stress field and the orientation of the principal stresses at one fault termination, all from the same model calculation. Least principal stress (σ_3 , Fig. 2.13d) is at a minimum (least compressive) in the extensional quadrants (the NE and SW quadrants of the EW-trending, left-lateral fault) and is slightly increased from its remote magnitude (80 MPa) in the contractional quadrant. For splay fractures to form, the effective tensile stress, $\sigma_3(\text{eff}) = \sigma_3 - P_p$, must be larger than the tensile strength of the rock. If the fluid pressure is about 70 MPa, we would expect to find dilatant fractures parallel to the σ_1 -direction near the fault termination in the extensional quadrant. The abundance of such splay fractures (Fig. 2.6a,b) and associated micro-cracking at fault terminations throughout the Bear Creek area is consistent with this assumption. Note that the splay fractures in Fig. 2.6b initiate at a higher angle and then propagate towards a lower angle, indicating a variable stress field due to stress perturbations near the fault termination.

The mean-stress component of the stress field (Fig. 2.13e) is anti-symmetrically distributed about the fault termination and is increased by up to 20 MPa in the contractional quadrant and reduced by the same amount in the extensional quadrant. Ductile fabrics developed in the contractional quadrant of fault terminations, while splay fractures formed in the extensional quadrant at intermediate distances from the Mono Creek Granite (Fig. 2.6c). This is consistent with the pressure-weakening effect proposed by Bürgmann & Pollard (1992) that occurs under conditions close to the brittle-ductile transition. Apparently the side-by-side occurrence of brittle and ductile structures is caused by this difference in the mean stress component across the fault trace.

The maximum shear stress component of the stress field (Fig. 2.13f) shows a symmetrical distribution around the fault termination. Shear stress magnitudes are increased to 35 MPa immediately in front of the fault termination. Deformation laws involving viscous flow (e.g., by power-law creep) predict that deformation rates and resultant finite strain

correlate with high shear-stress magnitudes. In the Lake Edison Granodiorite this is the case in a narrow region at the margin of the Mono Creek Granite where symmetric shear zones spread from the fault terminations (Fig. 2.6d). This indicates that temperatures in the immediate vicinity of the Mono Creek Granite were high enough to cause viscous deformation at fault terminations despite mean-stress differences.

STRESS-DEPENDENT DEFORMATION ABOUT ECHELON FAULTS

Brittle and/or ductile structures about fault steps in the Lake Edison Granodiorite formed because of local stress perturbations. We evaluate elastic models of echelon fault steps to gain better understanding of the effects of the stress field on the structural development (Segall & Pollard 1980, Bürgmann & Pollard 1992). Secondary structures such as splay fractures may partially relax the stress perturbations. Even though permanent strains by viscous flow can not be computed from elastic models, we find that flow laws that do not include an effect of mean stress on deformation rate do not predict the observed relationships.

The stress field associated with echelon fault steps is modeled using the boundary element method as described above. Two 10 m-long left-lateral faults are arranged echelon with a left or right step of 45 cm width and 50 cm overlap. The amounts of separation and overlap of the echelon fault segments determine details of the perturbed stress field. However, the general conclusions drawn from the presented models apply to other geometries as well. Boundary conditions are the same as for the fault-termination models (Fig. 2.12). Figure 2.14 shows the stress fields associated with deformation about left steps (Fig. 2.14a-c), left steps with splay fractures (Fig. 2.14d-f), and right steps (Fig. 2.14g-i).

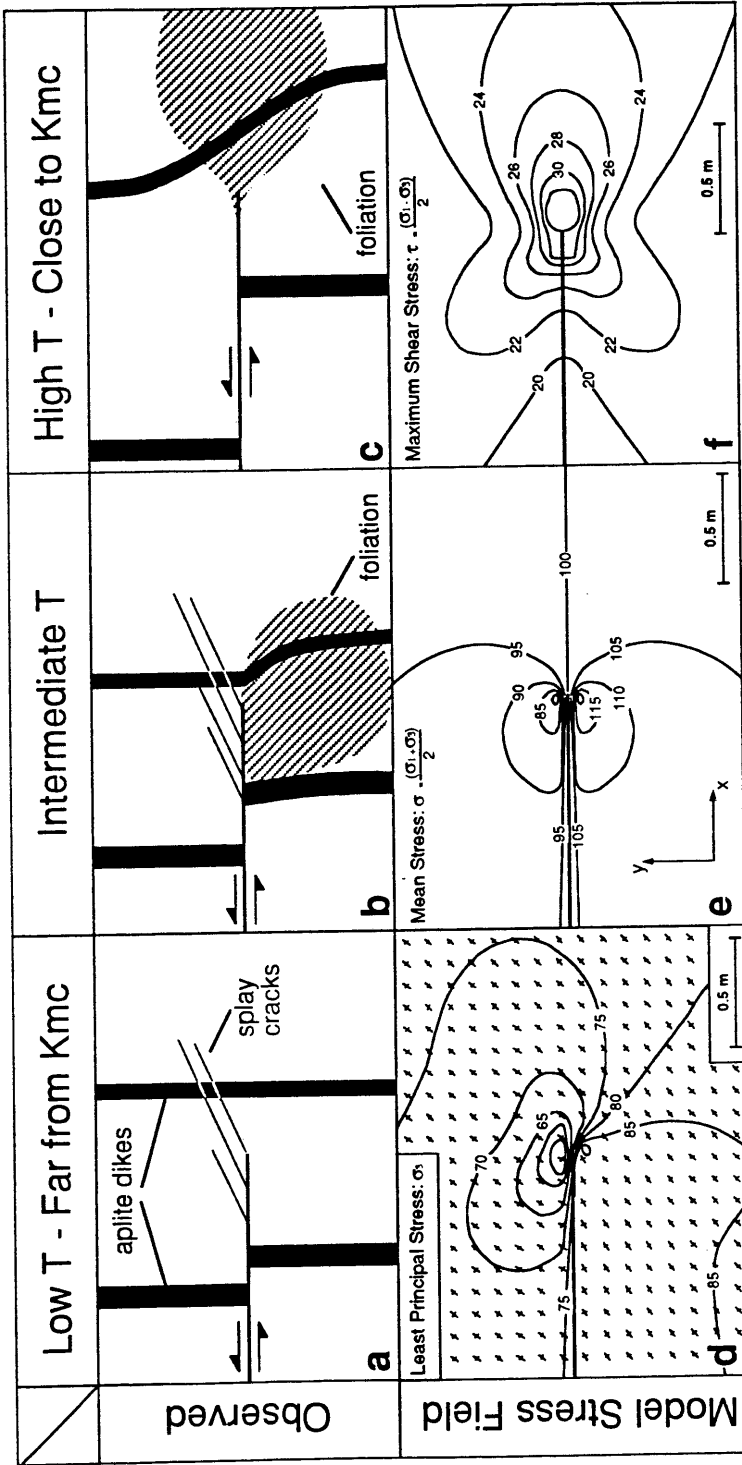


Fig. 2.13. (a-c) Schematic illustrations of fault-termination structures observed at various distances from the Mono Creek Granite (Fig. 2.4). (d-f) Components of the stress field that appear to control the deformation processes about the fault terminations.

Left steps

Dilatant fractures form where the fluid pressure exceeds the applied least compressive stress, σ_3 . Veins and fractures near fault terminations and fault discontinuities indicate that stress perturbations due to faulting may sufficiently reduce σ_3 to cause rock to break by dilatant fracture. The modeled stress fields associated with fault terminations and steps suggest that under the given boundary conditions such fractures form if σ_3 is less than ~ 70 MPa (Fig. 2.13d and 2.14 a, d, & g).

Where two strike-slip fault segments are arranged in an echelon geometry, stress perturbations may favor the development of inelastic deformation around the stepover (Segall & Pollard 1980). We investigate the effects of inelastic deformation at fault discontinuities by allowing dilatant fractures to grow from the fault terminations of a left step between two left-lateral faults (Fig. 2.14d-f). Fracture growth is introduced in our two-dimensional models with a fracture criterion at the crack tip (e.g., Hallam & Ashby 1990). The fractures are prescribed to grow by a 0.5-cm increment if the stress intensity factor, K_I , exceeds a critical stress intensity factor $K_{Ic} = 1.5 \text{ MPa m}^{1/2}$ (Atkinson & Meredith 1987, p. 492). The newly formed elements are specified to have zero shear traction and normal tractions equivalent to the assumed fluid pressure of 70 MPa. The fractures propagate in a direction parallel to the local σ_3 -orientation.

Figure 2.14d-f shows the stress fields and the fracture geometry about a left step with two splay fractures. The effective stresses within the step and the shear stress perturbations at the fault terminations are partly relaxed due to crack opening (Fig. 2.14d). Cracks in the fault step transfer slip between the two faults and reduce the stress perturbations at the fault discontinuity.

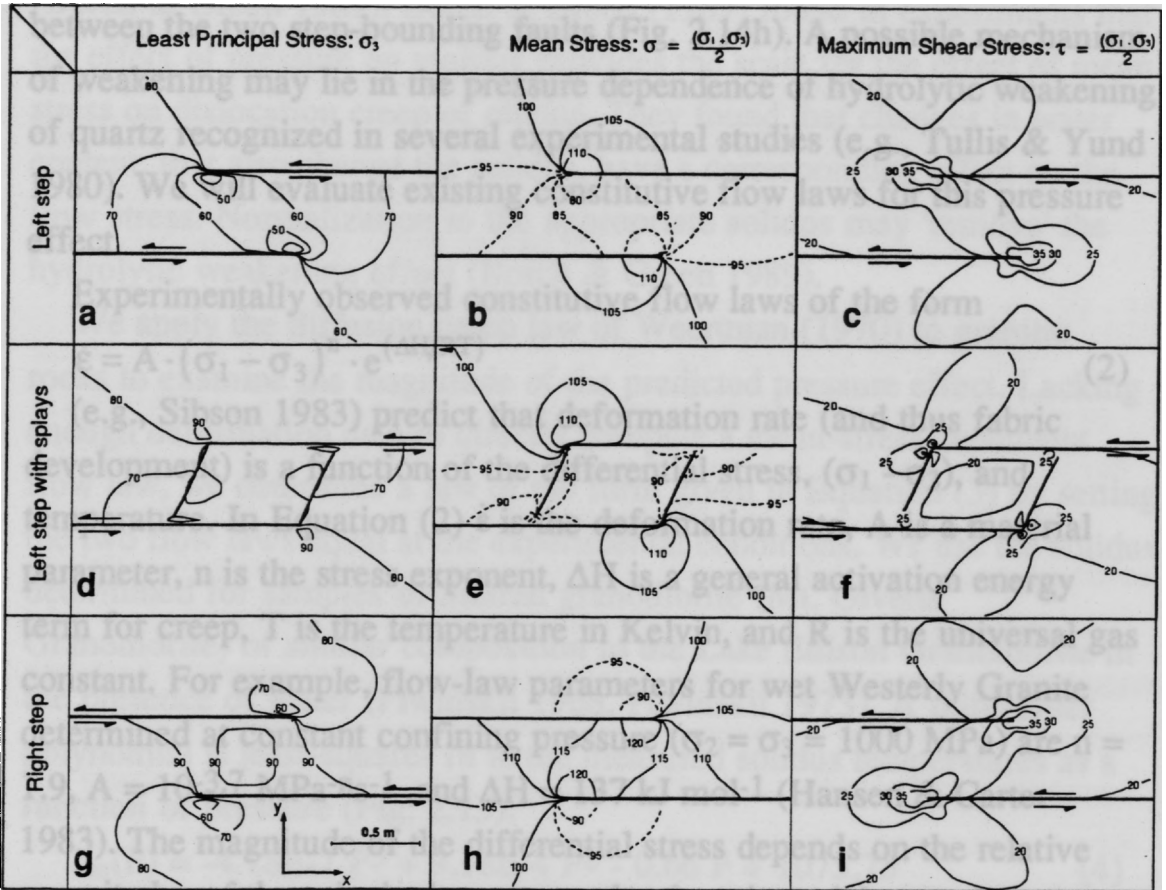


Fig. 2.14. Components of the stress field about two faults in left and right-stepping geometry. (a-c) Left step, (d-f) left step with dilatant fractures growing within the fault step, (g-i) right step.

Right steps

Bürgmann & Pollard (1992) suggest that a mean-stress dependent flow strength of granitic rock at brittle-to-ductile conditions is responsible for the observed localization of mylonitic fabrics within the right stepovers in the Lake Edison Granodiorite. Whereas shear stress is increased within and around a right step (Fig. 2.14i), the mean stress is elevated only between the two step-bounding faults (Fig. 2.14h). A possible mechanism of weakening may lie in the pressure dependence of hydrolytic weakening of quartz recognized in several experimental studies (e.g., Tullis & Yund 1980). We will evaluate existing constitutive flow laws for this pressure effect.

Experimentally observed constitutive flow laws of the form

$$\dot{\epsilon} = A \cdot (\sigma_1 - \sigma_3)^n \cdot e^{(\Delta H/RT)} \quad (2)$$

(e.g., Sibson 1983) predict that deformation rate (and thus fabric development) is a function of the differential stress, $(\sigma_1 - \sigma_3)$, and temperature. In Equation (2) $\dot{\epsilon}$ is the deformation rate, A is a material parameter, n is the stress exponent, ΔH is a general activation energy term for creep, T is the temperature in Kelvin, and R is the universal gas constant. For example, flow-law parameters for wet Westerly Granite determined at constant confining pressure ($\sigma_2 = \sigma_3 = 1000$ MPa) are $n = 1.9$, $A = 10^{-3.7} \text{ MPa}^{-n}\text{s}^{-1}$, and $\Delta H = 137 \text{ kJ mol}^{-1}$ (Hansen & Carter 1983). The magnitude of the differential stress depends on the relative magnitudes of the principal stresses only; there is no inherent pressure effect, except for a weak pressure dependence of ΔH . Equation (2) therefore predicts increased deformation rates and resultant larger permanent strains in zones of increased maximum shear stress (e.g., Fig. 2.13f and 2.14c,f, and i).

Weertman (1970) suggested a different flow law for creep by diffusion mechanisms,

$$\dot{\epsilon} = C \cdot (\sigma_1 - \sigma_3)^m \cdot e^{\left(-g \frac{T_m}{T}\right)}, \quad (3)$$

where C and g are empirically derived constants, m is the stress exponent, and T_m is the melting temperature of the same rock at the current pressure. This relationship suggests that, at a constant fraction of the rock's solidus temperature, the strength of the rock is constant. The effect of pressure, composition changes, and the chemical environment on the solidus can be used to quantify the effect of these parameters on creep (Borch & Green 1989). Borch & Green (1989) found in experiments that the effect of pressure on melting provides the scale for the effect of mean stress on dislocation creep of olivine. They found that changes in water content, that also change the solidus, have a corresponding effect on the flow stress. Normalization to the appropriate solidus may 'remove' the hydrolytic weakening effect (Borch & Green 1989).

We apply the diffusion creep law of Weertman (1970) to granitic rocks to examine the magnitude of the predicted pressure effect. Lacking enough deformation data to directly compute a mean-stress dependent flow law, we determine a law of the form given in Equation (3) by setting the two flow laws equal at the experimental conditions. We use the solidus determined for samples of Sierran granodiorite (Mt. Givens Granodiorite) of similar composition to the Lake Edison Granodiorite in the presence of water (Piwinskii 1968, Piwinskii 1973). A third-order polynomial is least-squares fit to the measured solidus temperatures as a function of pressure (Fig. 2.15).

$$T_m(P) = -4.18E-7 P^3 + 9.18E-4 P^2 - 0.66 P + 1075.75 \quad (4)$$

Assuming that the solidus of Westerly granite is not significantly different from that of Mt Givens Granodiorite we can set $C = A = 10^{-3.7} \text{ MPa}^{-n} \text{ s}^{-1}$, $m = n = 1.9$, and $g = \Delta H / (R T_m) = 137 \text{ kJ mol}^{-1} / (8.3144 \text{ J K}^{-1} \text{ mol}^{-1} T_m)$,

where $T_m = 915 \text{ K}$ is the experimentally determined temperature of the solidus at 1000 MPa.

Using Equation (3) we determine deformation rates for a range of pressures and differential stress' at 350 °C (Fig. 2.16). The pressure-independent deformation rates extrapolated from Equation (2) are shown

below the contoured deformation rates calculated from Equation (3). The flow law of Hansen & Carter (1983) predicts higher deformation rates at lower pressures than those extrapolated from Equation (3) because the solidus temperature at 1000 MPa (915 K) is significantly lower than at 100 MPa (1018 K). Figure 2.16 shows that the predicted pressure effect becomes more significant at lower pressures due to the larger gradient of the solidus at lower pressures (Fig. 2.15). The predicted pressure effect is less pronounced at higher temperatures. From Equations (3) and (4) we find that an increase of pressure from 100 MPa to 120 MPa at a differential stress of 40 MPa (dashed line) causes an increase of deformation rates by ~30% at 350 °C.

Temperatures of 300-350 °C are thought to occur at depths of ~10 - 15 km in seismically active areas such as the San Andreas fault system (Lachenbruch & Sass 1980). An increase of pressure from 400 MPa to 420 MPa (~ 15 km) at 350 °C would be expected to result in an increase of deformation rate of only ~7%. We may therefore not expect the pressure-weakening effect we observe in the Lake Edison Granodiorite to play an important role where geothermal gradients are not significantly elevated. Constitutive models of inelastic rheologies and rock deformation experiments at a variety of pressures to test pressure-dependent flow laws are needed to better constrain the proposed relationships. The diffusion creep law of Weertman (1970) appears to be qualitatively consistent with the observed relationships of localized fabric development in the Lake Edison Granodiorite and model stress field.

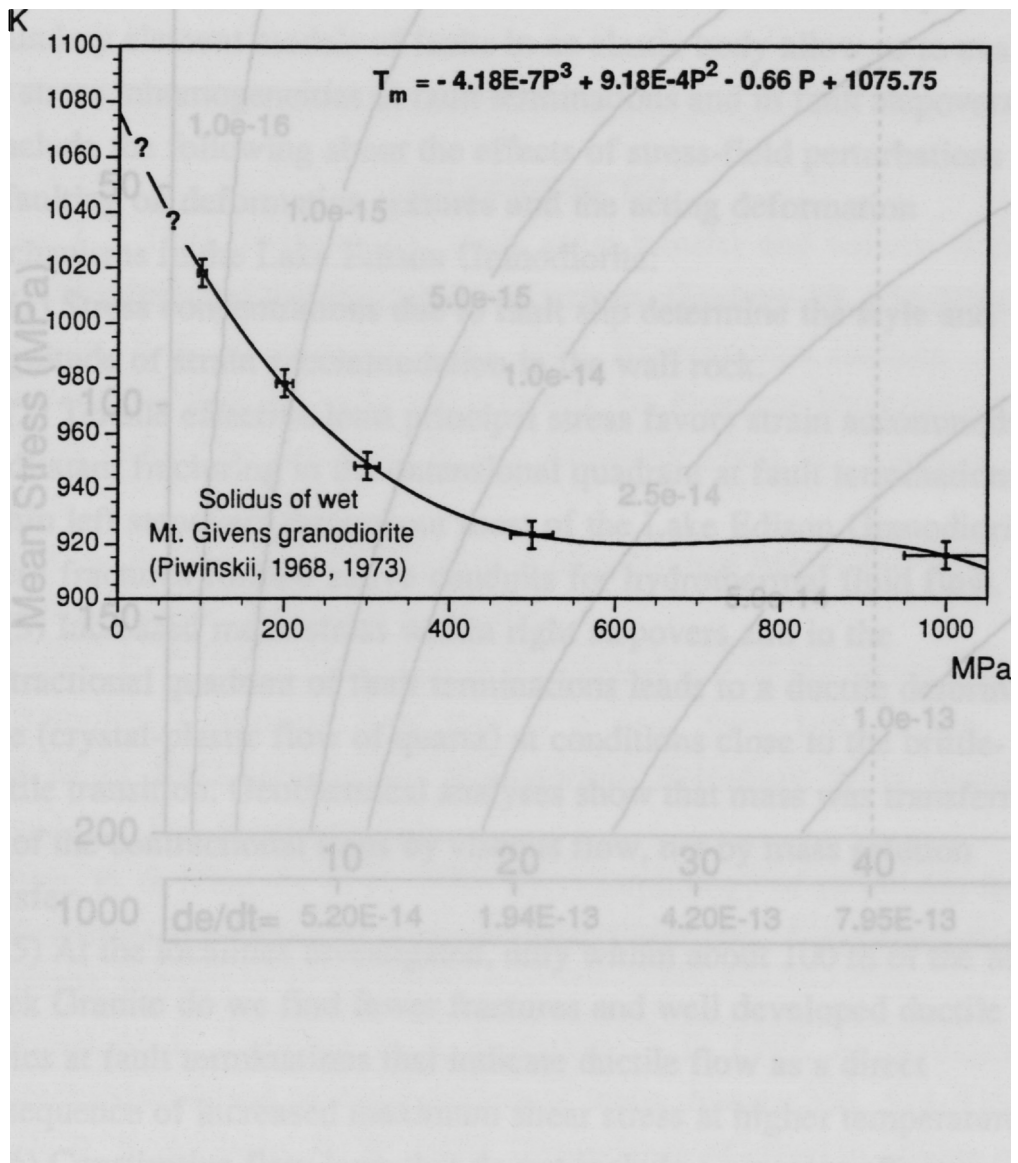


Fig. 2.15. Experimentally determined solidus for Mt. Givens Granodiorite with excess water from 100 - 1000 MPa (Piwinskii 1968, 1973).

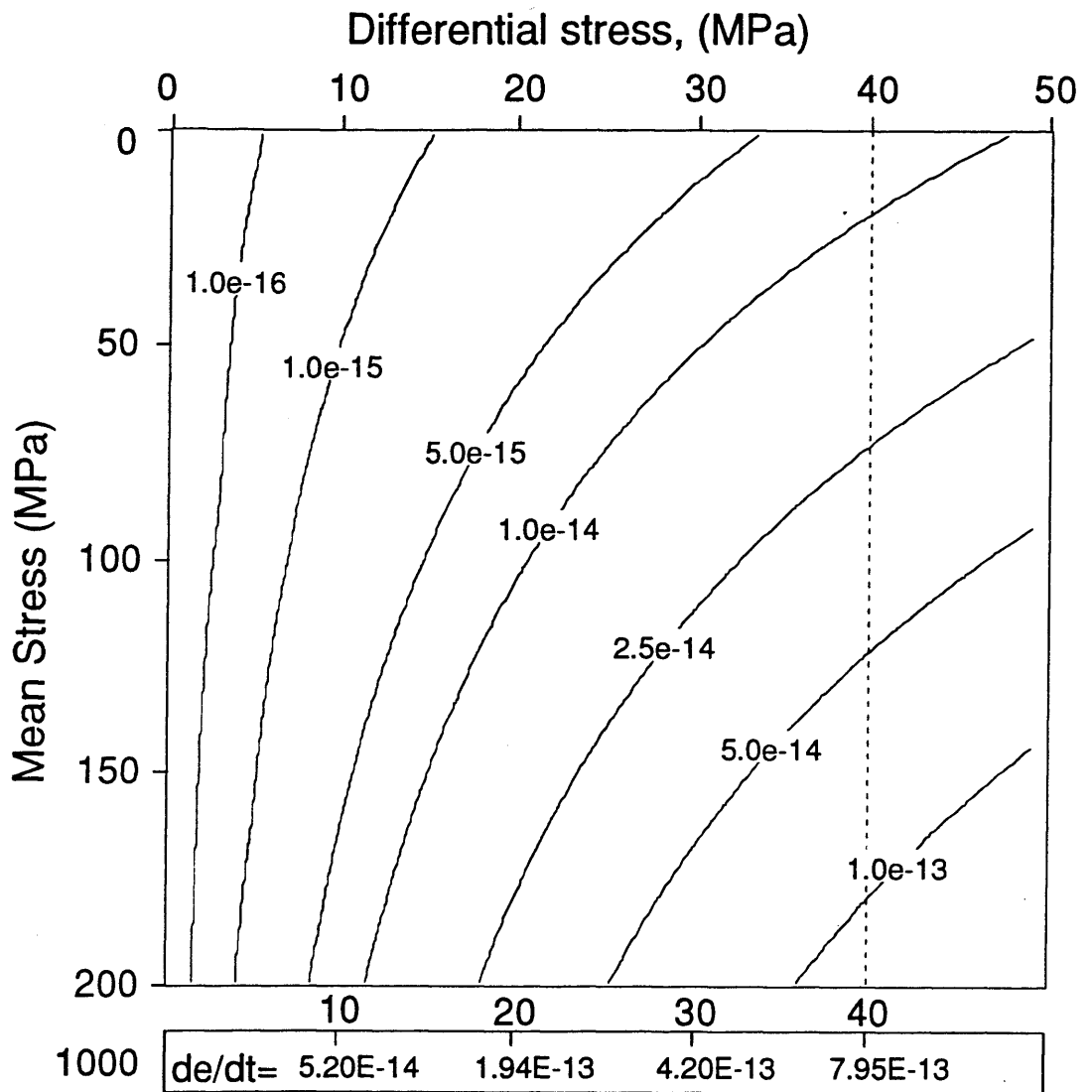


Fig. 2.16. Contour plot of deformation rates at 350 °C as a function of pressure and differential stress calculated from Equations 3 and 4. Flow law parameters for wet Westerly granite at 1000 MPa are from Hansen and Carter (1982).

CONCLUSIONS

This research suggests that, in the brittle-to-ductile deformation regime at a given temperature and in the presence of hydrothermal fluids, the local state of stress can determine the locally active deformation mechanisms in granitic rock. Detailed field and microscopic observations show that brittle and ductile deformation features in the Lake Edison Granodiorite are localized near fault terminations and fault steps. Boundary element models of faults in an elastic body allow us to evaluate the stress inhomogeneities at fault terminations and in fault stepovers. We conclude the following about the effects of stress-field perturbations due to faulting on deformation textures and the acting deformation mechanisms in the Lake Edison Granodiorite:

(1) Stress concentrations due to fault slip determine the style and magnitude of strain accommodation in the wall rock.

(2) Tensile effective least principal stress favors strain accommodation by dilatant fracturing in the extensional quadrant at fault terminations and within left stepovers throughout most of the Lake Edison Granodiorite. These fractures formed active conduits for hydrothermal fluid flow.

(3) Increased mean stress within right stepovers and in the contractional quadrant of fault terminations leads to a ductile deformation style (crystal-plastic flow of quartz) at conditions close to the brittle-ductile transition. Geochemical analyses show that mass was transferred out of the contractional steps by viscous flow, not by mass solution transfer.

(5) At the localities investigated, only within about 100 m of the Mono Creek Granite do we find fewer fractures and well developed ductile fabrics at fault terminations that indicate ductile flow as a direct consequence of increased maximum shear stress at higher temperatures.

(6) Constitutive flow laws that do not include a pressure effect on deformation rate fail to predict the observed distribution of ductile fabrics.

ACKNOWLEDGMENTS

This research was supported by the Geological Society of America, Sigma Xi, the McGee research fund of the Geology Department, and the Rock Fracture Project of Stanford University. Ramón Arrowsmith, Peter Christiansen, Steve Martel, Michael Pollard, and Betty Suh helped with the field work. Joel Sparks gave advice on the geochemical analyses. We thank Pamela Burnley for pointing out pressure-dependent flow laws. Elizabeth Miller, Mark Swanson, Jan Tullis, Steven Wojtal, and an anonymous reviewer provided very helpful comments and suggestions.

REFERENCES

- Ague, J. J. 1991. Evidence for major mass transfer and volume strain during regional metamorphism of pelites. *Geology* **19**, 855-858.
- Atkinson, B. K. & Meredith, P. G. 1987. Experimental fracture mechanics data for rocks and minerals. In: *Fracture Mechanics of Rock* (edited by Atkinson, B. K.). Academic Press Inc. London, 477-525.
- Aydin, A. & Nur, A. 1982. Evolution of pull-apart basins and their scale independence. *Tectonics* **1**, 91-105.
- Bateman, P. C. 1992. Plutonism in the central part of the Sierra Nevada Batholith, California. *Prof. Pap. U. S. geol. Surv.* **1483**, 1-186.
- Best, M. G. 1982. *Igneous and Metamorphic Petrology*. W. H. Freeman and Co., San Francisco, CA.
- Bilham, R. & King, G. P. C. 1989. The morphology of strike-slip faults: Examples from the San Andreas fault, California. *J. geophys. Res.* **94**, 10204-10216.
- Blanpied, M. L., Lockner, D. A. & Byerlee, J. D. 1992. An earthquake mechanism based on rapid sealing of faults. *Nature* **358**, 574-576.
- Borch, R. S. & Green, H. W. 1989. Dependence of creep in olivine on the homologous temperature and its implications for flow in the mantle. *Nature* **330**, 345-348.

- Brace, W. F. & Bombolakis, E. G. 1963. A note on brittle crack growth in compression. *J. geophys. Res.* **68**, 3709-3713.
- Bürgmann, R., Christiansen, P. & Pollard, D. D. 1992. Hydrothermal fluid pathways along fracture systems in granitic rock; evidence from the Mt. Abbot Quadrangle, Sierra Nevada. *Geol. Soc. Am. Abstr. w. Prog.* **24**, 11-12.
- Bürgmann, R. & Pollard, D. D. 1992. Influence of the state of stress on the brittle-ductile transition in granitic rock: Evidence from fault steps in the Sierra Nevada, California. *Geology* **20**, 645-648.
- Busby-Spera, C. J. & Saleeby, J. B. 1990. Intra-arc strike-slip fault exposed at batholithic levels in the southern Sierra Nevada, California. *Geology* **18**, 255-259.
- Byerlee, J. D. 1968. Brittle-ductile transition in rocks. *J. geophys. Res.* **73**, 4741-4750.
- Chinnery, M. A. 1965. The vertical displacement associated with transcurrent faulting. *J. geophys. Res.* **70**, 4627-4632.
- Christiansen, P., Bürgmann, R. & Pollard, D. D. 1992. Relationship between faulting and hydrothermal circulation during cooling of granitoid plutons. *Geol. Soc. Am. Abstr. w. Prog.* **24**, 15.
- Christie-Blick, N. & Biddle, K. T. 1985. Deformation and basin formation along strike-slip faults. In: *Strike-slip Deformation, Basin Formation, and Sedimentation* (edited by Biddle, K. T. & Christie-Blick, N.). *Soc. econ. Paleont. Mineral. Spec. Pub.* **37**, 1-34.
- Cox, S. J. D. & Scholz, C. H. 1988. On the formation and growth of faults: An experimental study. *J. Struct. Geol.* **10**, 413-430.
- Crouch, S. L. & Starfield, A. M. 1983. *Boundary element methods in solid mechanics*. Unwin Hyman, London.
- Crowell, J. C. 1974a. Origin of late Cenozoic basins in southern California. In: *Tectonics and Sedimentation* (edited by Dickinson, W. R.). *Soc. econ. Paleont. Mineral. Spec. Pub.* **22**, 190-204.
- Crowell, J. C. 1974b. Sedimentation along the San Andreas fault, California. In: *Modern and ancient geosynclinal sedimentation* (edited

- by Dott, R. H. & Shaver, R. H.). *Soc. econ. Paleont. Mineral. Spec. Pub.* **19**, 292-303.
- Cruikshank, K. M., Zhao, G. & Johnson, A. M. 1991. Duplex structures connecting fault segments in Entrada Sandstone. *J. Struct. Geol.* **13**, 1185-1196.
- Davies, R. K. & Pollard, D. D. 1986. Relations between left-lateral strike-slip faults and right-lateral monoclinial kink bands in granodiorite, Sierra Nevada, California. *Pageoph* **124**, 177-201.
- Deng, Q., Wu, D., Zhang, P. & Chen, S. 1986. Structure and deformational character of strike-slip fault zones. *Pageoph* **124**, 203-224.
- Dibblee, T. W., Jr. 1977. Strike-slip tectonics of the San Andreas fault and its role in Cenozoic basin evolution. In: *Late Mesozoic and Cenozoic sedimentation and tectonics in California* (edited by Nilsen, T. H.). San Joaquin Geological Society Bakersfield, California, 26-38.
- Fletcher, R. & Pollard, D. D. 1981. An anticrack mechanism for stylolites. *Geology* **9**, 419-424.
- Gamond, J. F. 1987. Bridge structures as sense of displacement criteria in brittle fault zones. *J. Struct. Geol.* **9**, 609-620.
- Gibson, R. G. 1990. Nucleation and growth of retrograde shear zones: an example from the Needle Mountains, Colorado, U.S.A. *J. Struct. Geol.* **12**, 339-350.
- Granier, T. 1985. Origin, damping and pattern of development of faults in granite. *Tectonics* **4**, 721-737.
- Hallam, S. D. & Ashby, M. F. 1990. Compressive brittle fracture and the construction of multi-axial failure maps. In: *Deformation processes in minerals, ceramics and rocks* (edited by Barber, D. J. & Meredith, P. G.). The Mineralogical Society of Great Britain and Ireland, Unwin Hyman London, 84-108.
- Hansen, F. D. & Carter, N. L. 1983. Semibrittle creep of dry and wet Westerly granite at 1000 MPa. *Proc. U. S. Symp. on Rock Mechanics* **24**, 429-447.

- Harris, R. A. & Day, S. M. 1993. Dynamics of fault interaction: Parallel strike-slip faults. *J. geophys. Res.* **98**, 4461-4472.
- Hempton, M. R. & Neher, K. 1986. Experimental fracture, strain and subsidence patterns over en-échelon strike-slip faults. *J. Struct. Geol.* **8**, 597-605.
- Jackson, M. D., Endo, E. T., Delaney, P. T., Amadottir, T. & Rubin, A. M. 1992. Ground ruptures of the 1974 and 1983 Koaiki earthquakes, Mauna Loa volcano, Hawaii. *J. geophys. Res.* **97**, 8775-8798.
- Johnson, A. M. 1970. *Physical Processes in Geology*. Freeman, Cooper, San Francisco, Calif.
- King, G. C. P. & Nabelek, J. 1985. Role of fault bends in the initiation and termination of earthquake rupture. *Science* **228**, 984-987.
- Kronenberg, A. K., Segall, P. & Wolf, G. H. 1990. Hydrolytic weakening and penetrative deformation within a natural shear zone. In: *The Brittle-Ductile Transition in Rocks -- The Heard Volume* (edited by Duba, A. G., Durham, W. B., Handin, J. W. & Wang, H. F.). *Am. Geophys. Un.Geophys. Monogr.* **56**, 21-36.
- Lachenbruch, A. H. & Sass, J. H. 1980. Heat flow and energetics of the San Andreas fault zone. *J. geophys. Res.* **85**, 6185-6223.
- Lawn, B. R. & Wilshaw, T. R. 1975. *Fracture of Brittle Solids*. Cambridge University Press, Cambridge.
- Lin, P. & Logan, J. M. 1991. The interaction of two closely spaced cracks: A rock model study. *J. geophys. Res.* **96**, 21667-21675.
- Lister, G. S. & Snoke, A. W. 1984. S-C mylonites. *J. Struct. Geol.* **6**, 617-638.
- Lockwood, J. P. & Moore, J. G. 1979. Regional deformation of the Sierra Nevada, California, on conjugate microfault sets. *J. geophys. Res.* **84**, 6041-6049.
- Martel, S. J., Bürgmann, R. & Pollard, D. D. 1990. Ductile deformation associated with brittle faulting in granitic rock, Sierra Nevada, California. *EOS Trans. Am. Geophys. Un.* **71**, 1558.

- Martel, S. J. & Pollard, D. D. 1989. Mechanics of slip and fracture along small faults and simple strike-slip fault zones in granitic rock. *J. geophys. Res.* **94**, 9417-9428.
- Martel, S. J., Pollard, D. D. & Segall, P. 1988. Development of simple strike-slip fault zones in granitic rock, Mount Abbot quadrangle, Sierra Nevada, California. *Bull. geol. Soc. Am.* **99**, 1451-1465.
- Mayo, E. B. 1941. Deformation in the interval Mt. Lyell-Mt. Whitney, California. *Bull. geol. Soc. Am.* **52**, 1001-1084.
- McGarr, A., Pollard, D. D., Gay, N. C. & Ortlepp, W. D. 1979. Observations and analysis of structures in exhumed mine-induced faults. *U. S. Geol. Surv. Open-file Rept.* 79-1239, 101-120.
- Naylor, M. A., Mandl, G. & Sijpensteijn, C. H. K. 1986. Fault geometries in basement-induced wrench faulting under different initial stress states. *J. Struct. Geol.* **8**, 737-752.
- Page, B. M. & Engebretson, D. C. 1984. Correlation between the geologic record and computed plate motions for central California. *Tectonics* **3**, 133-155.
- Paterson, M. S. 1978. *Experimental Rock Deformation - The Brittle Field*. Springer Verlag, New York.
- Paterson, M. S. 1987. Problems in the extrapolation of laboratory rheological data. *Tectonophysics* **133**, 33-43.
- Piwinskii, A. J. 1968. Experimental studies of igneous rock series central Sierra Nevada batholith, California. *J. Geol.* **76**, 548-570.
- Piwinskii, A. J. 1973. Experimental studies of igneous rock series, central Sierra Nevada batholith, California: Part II. *Neues Jahrb. Mineral., Monatsh.* **5**, 193-215.
- Pollard, D. D., Bürgmann, R. & Christiansen, P. 1992. Deformation and fluid flow during fault zone development in granitic rock. *Geol. Soc. Am. Abstr. w. Prog.* **24**, 157.
- Pollard, D. D. & Segall, P. 1987. Theoretical displacements and stresses near fractures in rocks: With applications to faults, joints, veins, dikes,

- and solution surfaces. In: *Fracture Mechanics of Rock* (edited by Atkinson, B. K.). Academic Press Inc. London, 277-349.
- Pollard, D. D., Segall, P. & Delaney, P. T. 1982. Formation and interpretation of dilatant echelon cracks. *Bull. geol. Soc. Am.* **93**, 1291-1303.
- Rodgers, D. A. 1980. Analysis of pull-apart basin development produced by en echelon strike-slip faults. In: *Sedimentation in Oblique-slip Mobile Zones* (edited by Ballance, P. F. & Reading, H. G.). *Int. Assoc. Sedimentol. Spec. Publ.* **4**, 27-41.
- Ross, J. V. & Lewis, P. D. 1989. Brittle-ductile transition. Semi-brittle behavior. *Tectonophysics* **167**, 75-79.
- Rutter, E. H. 1986. On the nomenclature of model of failure transitions in rocks. *Tectonophysics* **122**, 381-387.
- Scholz, C. H. 1988. The brittle-plastic transition and the depth of seismic faulting. *Geol.Rdsch.* **77**, 319-328.
- Scholz, C. H. 1990. *The mechanics of earthquakes and faulting*. Cambridge University Press, Cambridge.
- Segall, P., McKee, E. H., Martel, S. J. & Turrin, B. D. 1990. Late Cretaceous age of fractures in the Sierra Nevada batholith, California. *Geology* **18**, 1248-1251.
- Segall, P. & Pollard, D. D. 1980. Mechanics of discontinuous faults. *J. geophys. Res.* **85**, 4337-4350.
- Segall, P. & Pollard, D. D. 1983a. Joint formation in granitic rock of the Sierra Nevada. *Bull. geol. Soc. Am.* **94**, 563-575.
- Segall, P. & Pollard, D. D. 1983b. Nucleation and growth of strike-slip faults in granite. *J. geophys. Res.* **88**, 555-568.
- Segall, P. & Simpson, C. 1986. Nucleation of ductile shear zones on dilatant fractures. *Geology* **14**, 56-59.
- Sharp, R. V. & Clark, M. 1972. Geologic evidence of previous faulting near the 1968 rupture on the Coyote Creek fault. *Prof. Pap. U. S. geol. Surv.* **787**, 131-140.

- Sibson, R. H. 1983. Continental fault structure and the shallow earthquake source. *J. geol. Soc. London* **140**, 741-767.
- Sibson, R. H. 1984. Roughness at the base of the seismogenic zone: Contributing factors. *J. geophys. Res.* **89**, 5791-5800.
- Sibson, R. H. 1985. Stopping of earthquake ruptures at dilational steps. *Nature* **316**, 248-251.
- Sibson, R. H. 1986a. Earthquakes and rock deformation in crustal fault zones. *Ann. Rev. Earth Planet. Sci.* **14**, 149-175.
- Sibson, R. H. 1986b. Rupture interaction with fault jogs. In: *Earthquake Source Mechanics* (edited by Das, S., Boatwright, J. & Scholz, C.). *Am. Geophys. Un. Geophys. Monogr.* **37**, 157-168.
- Sibson, R. H. 1987. Earthquake rupturing as a mineralizing agent in hydrothermal systems. *Geology* **15**, 701-704.
- Simpson, C. 1985. Deformation of granitic rock across the brittle-ductile transition. *J. Struct. Geol.* **7**, 503-511.
- Smith, R. B. & Bruhn, R. L. 1984. Intraplate extensional tectonics of the eastern basin-range: Inferences on structural style from seismic reflection data, regional tectonics, and thermal-mechanical models of brittle-ductile deformation. *J. geophys. Res.* **89**, 5733-5762.
- Stern, T. W., Bateman, P. C., Morgan, B. A., Newall, m. F. & Peck, D. L. 1981. Isotopic U-Pb ages of zircon from the granitoids of the central Sierra Nevada, California. *Prof. Pap. U. S. geol. Surv.* **1185**, 1-17.
- Swanson, M. T. 1988. Pseudotachylyte-bearing strike-slip duplex structures in the Fort Foster Brittle Zone of southern Maine. *J. Struct. Geol.* **10**, 813-828.
- Swanson, M. T. 1992. Fault structure, wear mechanisms and rupture processes in pseudotachylyte generation. *Tectonophysics* **204**, 223-242.
- Tapponnier, P. & Brace, W. F. 1976. Development of stress-induced microcracks in Westerly granite. *Int. J. Rock Mech. Mining Sci.* **13**, 103-112.

- Thomas, A. L. & Pollard, D. D. 1993. The geometry of echelon fractures in rock: Implications from laboratory and numerical experiments. *J. Struct. Geol.* **15**, 323-334.
- Tikoff, B. & Teyssier, C. 1992. Crustal-scale, en echelon "P-shear" tensional bridges; a possible solution to the batholithic room problem. *Geology* **20**, 927-930.
- Tschalenko, J. S. 1970. Similarities between shear zones of different magnitudes. *Bull. geol. Soc. Am.* **81**, 1625-1640.
- Tullis, J. A. 1990. Experimental studies of deformation mechanisms and microstructures in quartzo-feldspathic rocks. In: *Deformation processes in minerals, ceramics and rocks* (edited by Barber, D. J. & Meredith, P. G.). The Mineralogical Society of Great Britain and Ireland, Unwin Hyman London, 190-226.
- Tullis, J. A. & Yund, R. A. 1977. Experimental deformation of dry Westerly granite. *J. geophys. Res.* **82**, 5705-5718.
- Tullis, J. A. & Yund, R. A. 1980. Hydrolytic weakening of experimentally deformed Westerly granite and Hale albite rock. *J. Struct. Geol.* **2**, 439-451.
- Tullis, J. A. & Yund, R. A. 1987. Transition from cataclastic flow to dislocation creep of feldspar: Mechanisms and microstructures. *Geology* **15**, 606-609.
- Tullis, J. A. & Yund, R. A. 1989. Hydrolytic weakening of quartz aggregates: The effects of water and pressure on recovery. *Geophys. Res. Lett.* **16**, 1343-1346.
- Weertman, J. 1970. The creep strength of the earth's mantle. *Rev. geophys. Space Physics* **8**, 145-168.
- Wong, T. F. 1982. Micromechanics of faulting in Westerly granite. **19**, 49-64.
- Woodcock, N. H. & Fischer, M. 1986. Strike-slip duplexes. *J. Struct. Geol.* **8**, 725-735.

3. Slip Distributions On Faults: Effects Of Stress Gradients, Inelastic Deformation And Fault Interaction

ABSTRACT

Fault slip distributions are commonly assumed to be symmetrical about a central slip maximum. However, slip distributions in nature are often asymmetric. While slip along a fault is expected to follow an elliptical distribution after a single slip event in an elastic material, the slip distribution may be modified if the fault propagates or if additional slip events occur. Various factors exist that cause slip to be asymmetrical even along single-slip event faults in an elastic medium. Analytically and numerically computed fault-slip distributions indicate that (1) changes in the (frictional) strength along a fault, (2) spatial gradients in the stress field, and (3) inelastic deformation near fault terminations can cause strong deviations from idealized symmetrical distributions. In particular, the interaction of faults that are located within about one fault radius of one another, is expected to strongly influence slip gradients. Inelastic processes, caused by stress perturbations in the stepover region of echelon faults, will effectively link individual segments along a fault zone whose slip distribution resembles that of a single fault of the combined segment lengths.

INTRODUCTION

Structural discontinuities, such as joints, dikes, solution surfaces, and faults, separate points (e.g., P and Q that initially were arbitrarily close to one another) by the difference of their individual displacement vectors ($\mathbf{u}[P]$, $\mathbf{u}[Q]$). This difference is defined as the *displacement discontinuity* (Fig. 3.1a):

$$\mathbf{D} = \mathbf{u}[P] - \mathbf{u}[Q].$$

If all such differentially displaced points lie on two planar surfaces that are bounded in extent at a common periphery, and the relative motions of the points are small compared to the in-plane dimension of the surfaces, the structure can be idealized as a simple crack, for example in an elastic solid (Pollard & Segall 1987).

In two dimensions the components of the displacement discontinuity are,

$$D_x = u_x(|x| \leq a, y = 0^+) - u_x(|x| \leq a, y = 0^-),$$

$$D_y = u_y(|x| \leq a, y = 0^+) - u_y(|x| \leq a, y = 0^-).$$

If the displacement components parallel to the fracture surface are much larger than the out-of-plane displacement components ($u_x \gg u_y$ and $u_z \gg u_y$), the resulting structural discontinuity is referred to as a *fault* and the in-plane displacement discontinuity is referred to as the *slip*.

It should be noted that relative motions of originally adjacent points on the opposing surfaces of a fault commonly include a small fault-perpendicular component, manifest in fault gouge zone formation and dilation or compaction features (Aydin 1978, Antonellini et al. 1993). This relative motion perpendicular to the fault has been overlooked by most geologists, but may play an important role in fault development and propagation. Nevertheless we focus here on the in-plane discontinuity or slip.

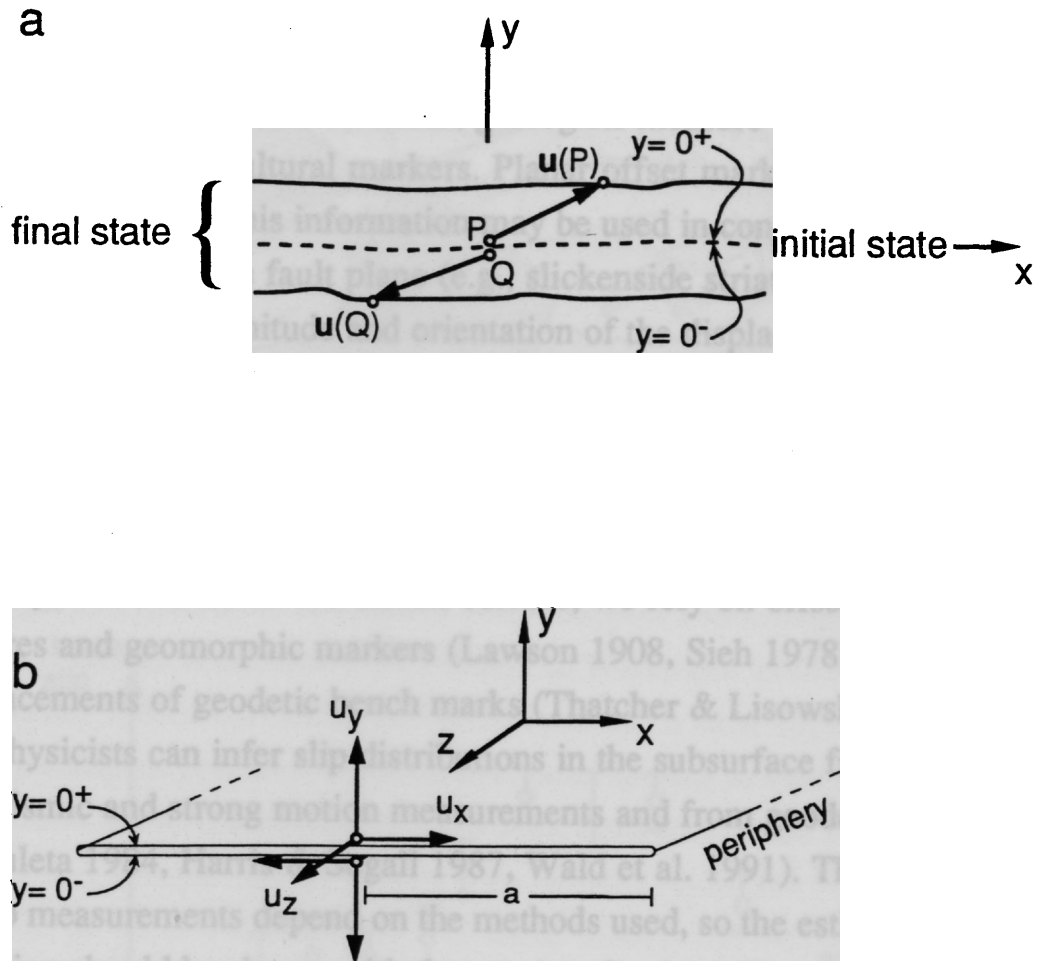


Fig. 3.1. Schematic illustration of a structural discontinuity. (a) The difference between displacement vectors of two originally adjacent points, $\mathbf{u}[P] - \mathbf{u}[Q]$, serves to define the vector displacement discontinuity, \mathbf{D} . (b) Displacement components on faces of a two-dimensional crack of half-length a shown in the initial state.

Measurements of slip along the exposed trace of a fault usually provide limited information about the slip distribution over the three-dimensional fault surface (Fig. 3.2a). Only in a few cases, such as multiple exposures of faults on several mine levels (Rippon 1985) or the seismic imaging of many offset marker beds (Barnett et al. 1987, Bouvier et al. 1989), can one determine the slip distribution over much of a fault plane. To determine the slip vector on faults, geologists measure the offsets of linear geologic or cultural markers. Planar offset markers provide only the *separation*, but this information may be used in conjunction with linear features on the fault plane (e.g., slickenside striations; Petit 1987) to constrain the magnitude and orientation of the displacement discontinuity vector (Fig. 3.2a).

Measurements of slip distributions depend on abundant displaced markers such as sedimentary structures, igneous intrusions or flows, xenoliths, and inactive faults. When measuring slip gradients along recently active faults at the earth's surface, we rely on offset cultural features and geomorphic markers (Lawson 1908, Sieh 1978), and on displacements of geodetic bench marks (Thatcher & Lisowski 1987). Geophysicists can infer slip distributions in the subsurface from teleseismic and strong motion measurements and from geodetic data (e.g., Archuleta 1984, Harris & Segall 1987, Wald et al. 1991). The precision of slip measurements depend on the methods used, so the estimated precision should be shown with the measured values (Fig. 3.2b).

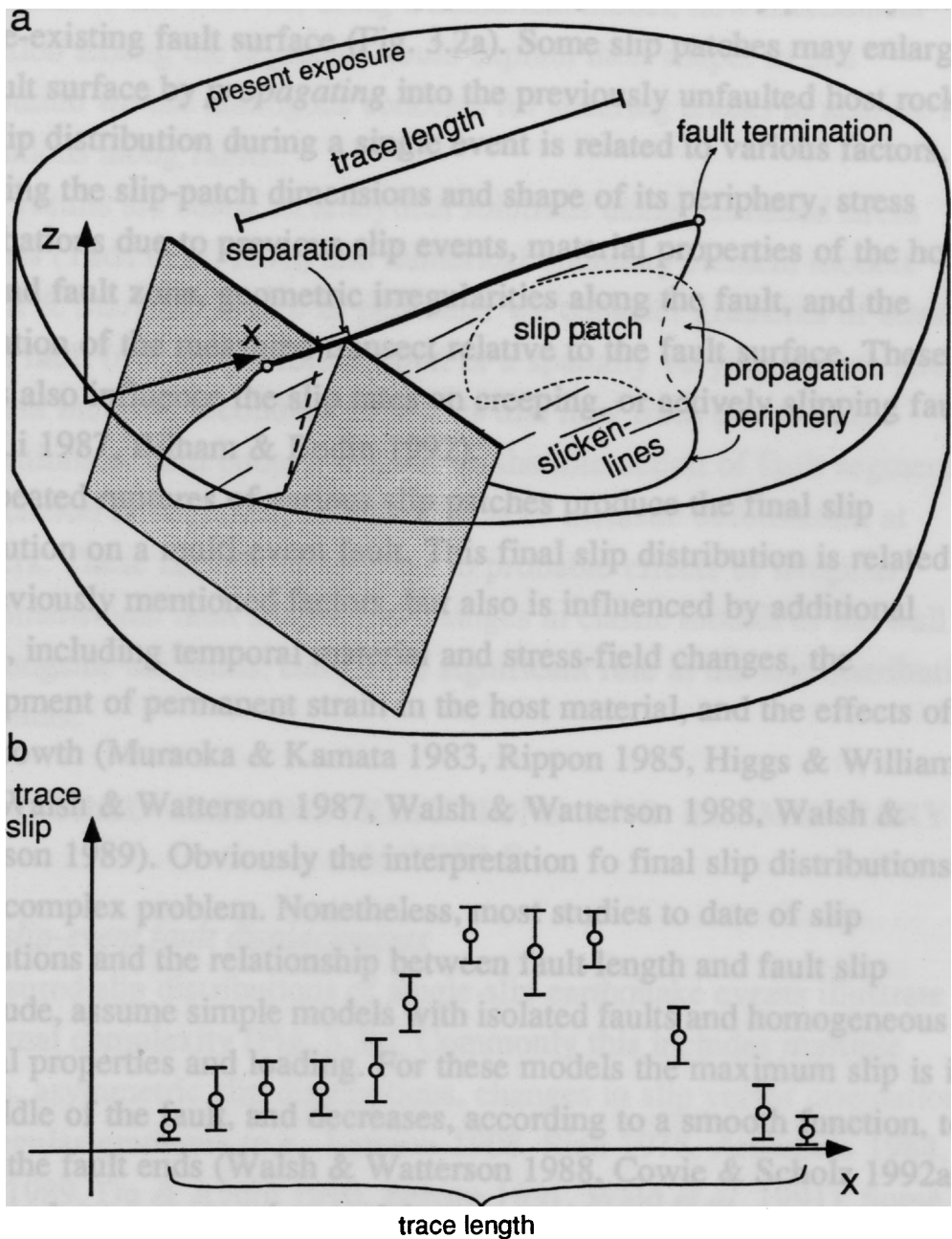


Fig. 3.2 (a) Schematic illustration of a three-dimensional fault with irregular periphery. The orientation of the slip vector is indicated by slickenslines or offset linear markers; the slip magnitude can be determined from offset linear or planar markers. (b) The quality of observed slip distributions along a fault trace depends strongly on the exposure, the number of markers, and the measurement method. Error bars indicate one standard deviation from mean value (circle).

During a single slip event, a slip patch may extend only partially along the pre-existing fault surface (Fig. 3.2a). Some slip patches may enlarge the fault surface by *propagating* into the previously unfaulted host rock. The slip distribution during a single event is related to various factors, including the slip-patch dimensions and shape of its periphery, stress perturbations due to previous slip events, material properties of the host rock and fault zone, geometric irregularities along the fault, and the orientation of the measured transect relative to the fault surface. These factors also influence the slip rates on creeping, or actively slipping faults (e.g., Li 1987, Bilham & Bodin 1992).

Repeated ruptures of various slip patches produce the final slip distribution on a multi-event fault. This final slip distribution is related to the previously mentioned factors, but also is influenced by additional factors, including temporal material and stress-field changes, the development of permanent strain in the host material, and the effects of fault growth (Muraoka & Kamata 1983, Rippon 1985, Higgs & Williams 1987, Walsh & Watterson 1987, Walsh & Watterson 1988, Walsh & Watterson 1989). Obviously the interpretation of final slip distributions is a very complex problem. Nonetheless, most studies to date of slip distributions and the relationship between fault length and fault slip magnitude, assume simple models with isolated faults and homogeneous material properties and loading. For these models the maximum slip is in the middle of the fault, and decreases, according to a smooth function, to zero at the fault ends (Walsh & Watterson 1988, Cowie & Scholz 1992a).

Somewhat more complex models were developed by Pollard and Muller (1976) who used analytical solutions for an opening crack subject to linear stress gradients to explain the teardrop shape of some igneous dikes and sills. They pointed out that the commonly observed asymmetrical shapes of sheet intrusions may be related to (1) regional stress gradients, (2) magma pressure gradients, (3) changes in host rock stiffness along the intrusions, and (4) their irregular three-dimensional geometry. Delaney and Pollard (1981) studied the opening of echelon

dike segments and showed, using a numerical model, how mechanical interaction among the segments could explain their shape. In this contribution we use analogous concepts for shearing cracks to analyze slip distributions along faults.

Our results are based on analytical solutions using published stress functions (Tada et al. 1973) and numerical boundary element models (Crouch & Starfield 1983). In particular we consider gradients of stress along a fault (due to variable friction or a spatially varying remote stress field) and inelastic secondary structures that may form due to stress perturbations at fault ends. We focus on the interaction of fault segments in an echelon arrangement and the effects of inelastic deformation at stepovers. These factors, in addition to probable effects of irregular three-dimensional fault shapes and changes in elastic moduli of the wall rock alongside the faults, can play a significant role in the slip distribution along faults.

MEASURED SLIP DISTRIBUTIONS AND ELEMENTARY MODELS

Single-slip-event fault displacements

Measured slip distributions of single-slip earthquake events illustrate their actual complexity (Fig. 3.3a). Commonly this includes multiple maxima, asymmetric slip distributions, changes in slip vector orientation, and irregular gradients (e.g., Lawson 1908, Sieh 1978, Archuleta 1984, Rymer 1989, Du & Aydin 1990, Beroza 1991, Wald *et al.* 1991). Some of this complexity in slip distributions can be correlated to fault geometry. For example, active fault zones are known to be made up of an array of individual fault segments, often arranged in an echelon fashion, with associated conjugate faults and fault discontinuities at all scales (Tschalenko 1970, Vedder & Wallace 1970, Wallace 1973, Bilham & Williams 1985, Bilham & King 1989, Bilham & Bodin 1992).

Figure 3.3 shows the measured surface offsets and calculated subsurface slip distributions of the 1987 Superstition Hills earthquake (Rymer 1989, Wald *et al.* 1991). Three slip events can be distinguished, only the third broke the whole length of the fault about 8 s after the first event. We note that an early slip patch near the northern termination of the fault may have ruptured in response to a previous event on the left-lateral Elmore Ranch fault oriented perpendicular to the Superstition Hills fault (Fig. 3.3a inset) that reduced the fault normal compressive stress acting on the northern Superstition Hills fault about 11 hours earlier. The subsequent rupture of the two major fault segments resulted in a slip distribution with two distinctive peaks.

Perhaps the most elementary model of a single slip event on a fault predicts an elliptical distribution in a linear elastic, homogeneous, isotropic, and isothermal material (Pollard & Segall 1987). This two-dimensional model assumes that the regional stress field is uniform, that shear tractions on the fault surfaces are constant, and that no fault propagation occurs.

The displacement discontinuity (slip) along such a model fault (Fig. 3.4 inset) may be derived utilizing Westergaard's (1939) simplification of Muskhelishvili's general solution for an elliptical cavity in an infinite elastic body (Muskhelishvili 1954, p. 347-358). The method uses functions of a complex variable ($z = x + iy$) to find an analytical stress function $Z(z)$ that satisfies the equilibrium and compatibility equations and stress-strain relations for an elastic material (Hooke's law), as well as the boundary conditions of a given problem. Using the appropriate Westergaard stress function one can calculate the stress and displacement fields in the body surrounding a crack (the model fault, Fig. 3.4 inset) occupying a straight segment on the x -axis from $x = -a$ to $x = +a$. For example, the two-dimensional, plane strain displacement components in the (x, y) -plane for any loading that produces a displacement discontinuity in the u_x -component across the crack are:

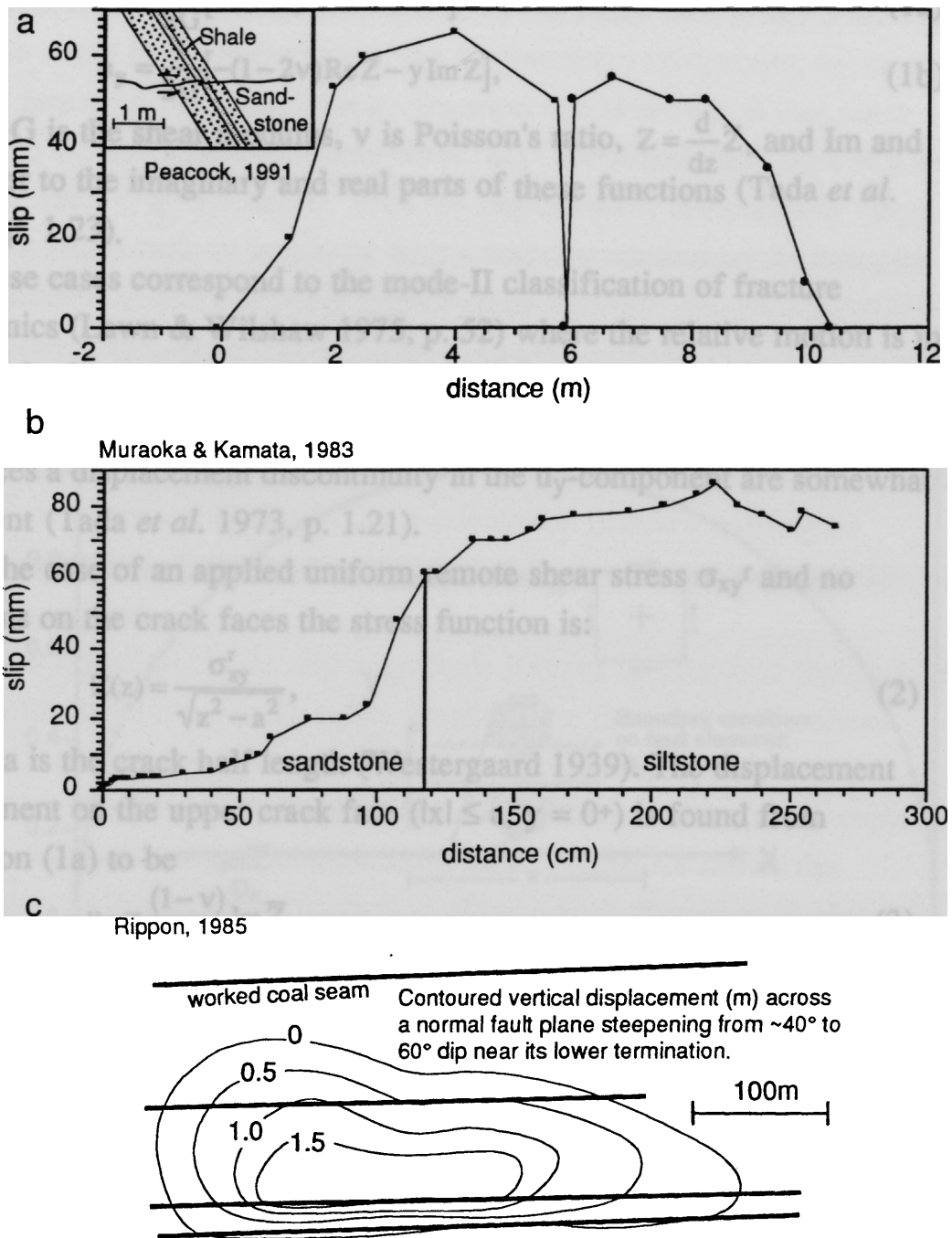


Fig. 3.3 (a) Slip distribution from single-slip events measured along the 1987 Superstition Hills earthquake rupture (SSH) at the earth's surface immediately following (squares) and two years after (triangles) the earthquake (Rymer 1989). Aseismic afterslip approximately doubled the surficial offsets to magnitudes near those that occurred at depth. (ER, Elmore Ranch fault) (b) The slip distribution of the 1987 Superstition Hills earthquake determined from seismologic strong motion data (Wald *et al.* 1991), contours are slip in centimeters.

$$u_x = \frac{1}{2G} [2(1-\nu)\text{Im}\bar{Z} + \text{Re}Z] \quad (1a)$$

$$u_y = \frac{1}{2G} [-(1-2\nu)\text{Re}\bar{Z} - y\text{Im}Z], \quad (1b)$$

where G is the shear modulus, ν is Poisson's ratio, $Z = \frac{d}{dz}\bar{Z}$, and Im and Re refer to the imaginary and real parts of these functions (Tada *et al.* 1973, p. 1.23).

These cases correspond to the mode-II classification of fracture mechanics (Lawn & Wilshaw 1975, p. 52) where the relative motion is in the crack plane and perpendicular to the crack periphery. The displacement field equations for opening cracks (mode I) where loading produces a displacement discontinuity in the u_y -component are somewhat different (Tada *et al.* 1973, p. 1.21).

In the case of an applied uniform remote shear stress σ_{xy}^r and no tractions on the crack faces the stress function is:

$$Z(z) = \frac{\sigma_{xy}^r}{\sqrt{z^2 - a^2}}, \quad (2)$$

where a is the crack half length (Westergaard 1939). The displacement component on the upper crack face ($|x| \leq a$, $y = 0^+$) is found from Equation (1a) to be

$$u_x = \frac{(1-\nu)}{G} \text{Im}\bar{Z} \quad (3)$$

Substituting Equation (2) into Equation (3) we find:

$$u_x(|x| \leq a, y = 0^+) = \sigma_{yx}^r \cdot \frac{(1-\nu)}{G} \cdot \sqrt{a^2 - x^2}. \quad (4)$$

On the opposite crack face u_x is equal in magnitude but opposite in sign, thus producing a displacement discontinuity, D given by twice the value of u_x in Equation (4). A positive σ_{yx}^r produces right-lateral slip on the model fault.

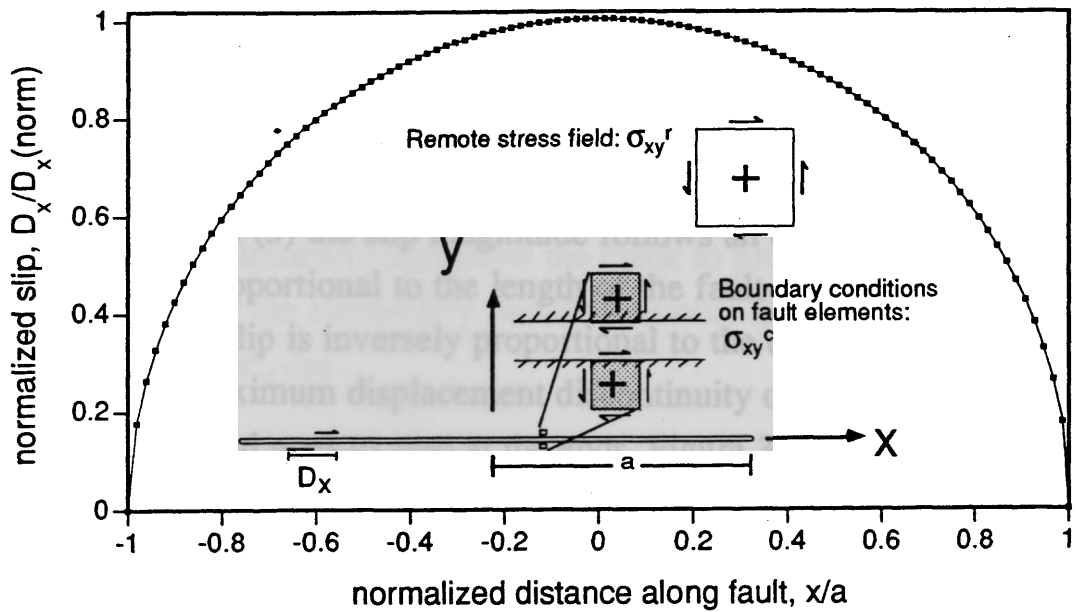


Fig. 3.4 The analytically (solid curve) and numerically (squares) computed displacement discontinuity D along an isolated fault in an infinite body after a unit shear-stress drop. The boundary element numerical model consists of 100 uniform slip elements with prescribed stress boundary condition. Inset shows boundary conditions and geometry for a crack, the model fault surface, in an elastic, isotropic, and homogeneous material. The coordinates are aligned with the crack and the origin is at the crack center.

For a uniform shear traction acting on the crack face in the x-direction and no stress in the remote field, the displacement component, u_x , on the crack face is of the same form as Equation (4). However, if this shear traction induces a positive shear stress, σ_{yx}^c , the model fault slips in a left-lateral sense (Fig. 3.4, inset). Thus the displacement discontinuity (slip) along a single fault of length $2a$ with a uniform traction on the faces of magnitude σ_{yx}^c and a uniform remote stress σ_{yx}^r is

$$D_x = 2(\sigma_{yx}^r - \sigma_{yx}^c) \cdot \frac{(1-\nu)}{G} \cdot \sqrt{a^2 - x^2}, \quad (5)$$

where $(\sigma_{yx}^r - \sigma_{yx}^c)$ is the constant shear-stress drop along the model fault (Fig. 3.4). A positive D_x refers to a right-lateral sense of slip. The displacement discontinuity in the y-orientation (mode-I opening or interpenetration of the crack walls) and in the z-orientation (mode-III sliding) are zero.

From Equation (5) the slip magnitude follows an elliptical distribution and is linearly proportional to the length of the fault and to the shear-stress drop. The slip is inversely proportional to the elastic shear modulus. The maximum displacement discontinuity occurs at the center of the model fault and goes to zero at the ends. Figure 3.4 shows the normalized elliptical slip distribution along a fault. Distance, x , along the fault trace is normalized by fault half length, a . Following the result in Equation (5), we normalize all the plotted slip distributions for our models by the maximum for this base case, where

$$D_x(x=0; \sigma_{yx}^c = 0) = D_x(\text{norm}) = 2(\sigma_{yx}^r) \frac{(1-\nu)}{G} a.$$

In the case of a three-dimensional fault the slip distribution has an elliptical form if the fault has an elliptical periphery and one of the axes is parallel to the direction of shear-stress drop (Eshelby 1957);

$$D_x = \frac{8b}{\pi} (\sigma_{yx}^r - \sigma_{yx}^c) \cdot \left(\frac{(1-\nu)}{G(2-\nu)} \right) \cdot \sqrt{1 - \frac{x^2}{a^2} - \frac{z^2}{b^2}}. \quad (6)$$

The displacement discontinuity in the z-direction, D_z is zero (here z refers to the other coordinate in the crack plane (Fig. 3.2a), and has no relation to the complex z). Faults of a more complex shape, or elliptical

faults whose axes are oriented oblique to the shear stress drop, will have more complex slip distributions. The simple two- and three-dimensional models provide a standard against which more complex cases can be judged. We will restrict our attention to two-dimensional plane-strain examples.

Fault slip results in stress concentrations around the fault termination. The stress intensity factors K_I , K_{II} , and K_{III} represent the strength of the stress field surrounding a crack tip in opening, in-plane shearing, and tearing displacement discontinuity modes respectively (Lawn & Wilshaw 1975, p. 51). The stress intensity factors are proportional to the applied stresses and are determined by the stress boundary conditions and the geometry of a given problem. Only if all three stress intensity factors are zero do we not find a stress singularity at a crack tip. If any stress intensity factors are not zero, the stress concentration may cause the material to fail inelastically and allow the crack to propagate. The stress intensity factor for the elementary two-dimensional fault model is

$$K_{II} = \sigma_{yx}^r \sqrt{\pi a} .$$

Cumulative fault displacements

Measured cumulative slip distributions along faults are often distinctly non-elliptical and consequently a number of researchers have developed fault models to explain and categorize such distributions (Muraoka & Kamata 1983, Higgs & Williams 1987, Walsh & Watterson 1987, Walsh & Watterson 1988, Walsh & Watterson 1989, Peacock 1991, Cowie & Scholz 1992a). In these studies, non-elliptical distributions have been attributed to the effects of fault growth, fault interaction, and ductile drag adjacent to the fault. Some studies implicitly assume a symmetric slip distribution by plotting slip versus distance from the fault center (Higgs & Williams 1987, Walsh & Watterson 1987, Walsh & Watterson 1988). However, where slip distributions reported in the literature extend from one termination to the other (Fig. 3.5) they commonly are asymmetric and irregular (e.g., Muraoka & Kamata 1983, Rippon 1985, Peacock

1991, Cowie & Scholz 1992a). Some appear to be affected by lithologic variations, fault interaction, and bends along the fault trace (Muraoka & Kamata 1983, Peacock 1991).

Figure 3.5a shows slip along two right stepping left-lateral strike-slip faults (Fig. 3.5a inset) mapped by Peacock (1991) near Kirkcudbright, Scotland. Note the high slip gradient where the two fault segments interact. The step is contained in a shale bed. The example by Muraoka, (1983) in Fig. 3.5b indicates that the slip distribution may be influenced by changing host rock properties about a fault. Where the normal fault breaks sandstone, slip is reduced. The contoured three-dimensional distribution of vertical displacements in Fig. 3.5c is derived from measured offsets of coal and sandstone beds on several levels of a mine in north-east Derbyshire presented by Rippon (1985). The slip distribution along this normal fault may be influenced by down-dip and lateral steepening, effects of changing host rock properties, and fault segmentation.

One class of modifications to the elementary elastic models (Fig. 3.4), motivated by non-elliptical slip distributions, involves the introduction of fault propagation with each slip event (Watterson 1986, Walsh & Watterson 1987, Cowie & Scholz 1992a). Slip in the single event models increases linearly with fault length (Equation 5). If each event slips the whole growing fault, the cumulative slip distribution can be considered to be made up of the sum of individual, elliptical, distributions at each growth stage (Watterson 1986). This implies that stress perturbations resulting from slip relax by permanent straining between each slip event. If slip in successive events increases in constant size increments, implying fault growth in constant length increments (Watterson 1986), the resultant slip distribution will be of the form

$$D_x = D_{\max} \cdot 2 \left(1 - \frac{x}{a}\right) \cdot \sqrt{\left(\frac{1 + \frac{x}{a}}{2}\right)^2 - \left(\frac{x}{a}\right)^2}, \quad (7)$$

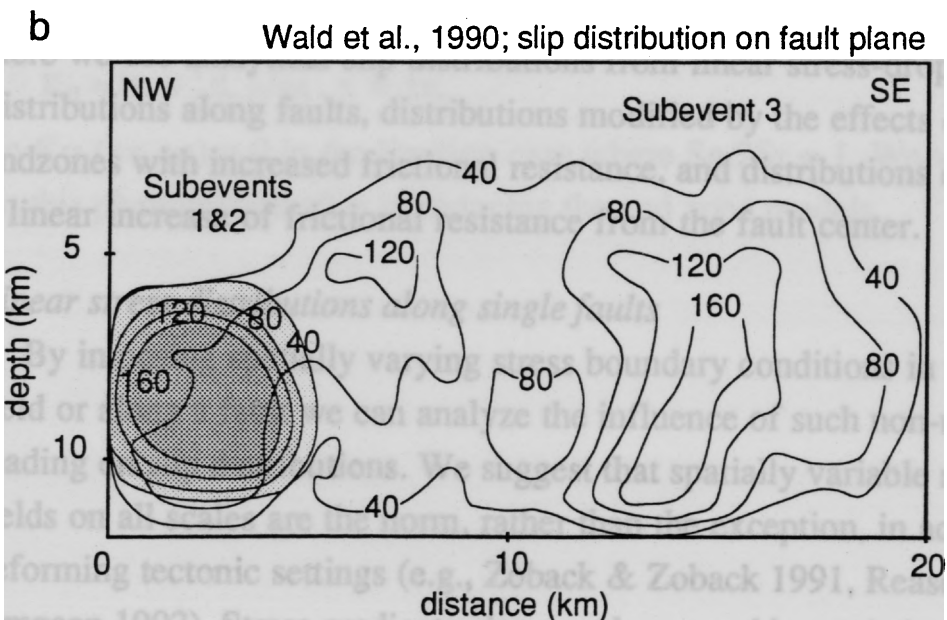
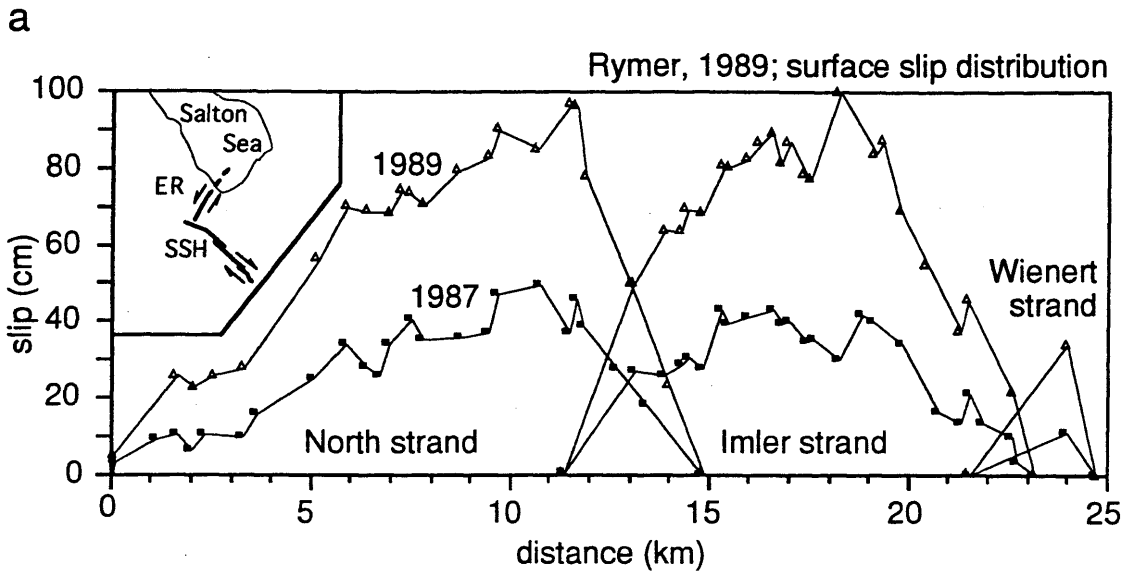


Fig. 3.5 Cumulative slip distributions measured along faults exhumed in mines or along outcrops that provide abundant offset markers. From (a) Peacock (1991), (b) Muraoka (1983), and (c) Rippon (1985). The examples emphasize the effects of fault interaction, host-rock material properties, and fault shape.

where a is the final fault half length and D_{\max} is the accumulated maximum slip (Walsh & Watterson 1987). If the increase in fault length produced by each slip event is some non-constant function of fault length (Cowie & Scholz 1992a, Cowie & Scholz 1992b, Gillespie et al. 1992), the resultant slip distribution becomes more complex.

SLIP DISTRIBUTIONS ON SINGLE FAULTS WITH NON-UNIFORM STRESS DROPS

Measured slip distributions (Figs. 3.3 and 3.5) are commonly more complex than predicted by the elementary elastic model (Fig. 3.4). One mechanism causing deviations from the simple model is related to non-uniform stress drop along faults. The remote stress field may be non-uniform because of stress gradients related to nearby tectonism (e.g., previous slip events on adjacent faults). Traction along faults may be variable due to changing frictional resistance or cohesion along a fault. Here we use analytical slip distributions from linear stress-drop distributions along faults, distributions modified by the effects of fault endzones with increased frictional resistance, and distributions caused by a linear increase of frictional resistance from the fault center.

Linear stress distributions along single faults

By imposing spatially varying stress boundary conditions in the remote field or along a fault we can analyze the influence of such non-uniform loading on slip distributions. We suggest that spatially variable stress fields on all scales are the norm, rather than the exception, in actively deforming tectonic settings (e.g., Zoback & Zoback 1991, Reasenber & Simpson 1992). Stress gradients also may be caused by variations in frictional resistance along a fault plane. First we analyze the effects of a linear stress distribution along a fault. This may approximate conditions where a fault has propagated through materials of varying coefficient of friction. In the remote field $\sigma_{yx}^f(x, y \rightarrow \infty) = \text{const.} = S_r$ and on the fault

surfaces the traction varies linearly such that the stress is $\sigma_{yx}^c(|x| < a, y = 0^\pm) = S_g (x/a)$

The slip distribution is:

$$D_x = \frac{(1-\nu)}{G} \left[2S_r - S_g \left(\frac{x}{a} \right) \right] \cdot \sqrt{a^2 - x^2} . \quad (8)$$

A linear distribution of the shear traction on the fault provides resistance to slip along one side ($x > 0$) and enhances slip on the other side ($x < 0$) relative to the base case of a uniform stress drop. This results in a skewed or tear-drop slip distribution with the maximum slip centered off the middle of the fault (Fig. 3.6). As the ratio $S_g/2S_r$ increases from 0 to 1 the asymmetry in slip becomes more pronounced. In the limiting case for right-lateral slip where $S_g/2S_r = 1$ the slip asymptotically approaches zero at $x = +a$. For greater values of the ratio, the right hand side of the model fault slips in a left-lateral (negative) sense. It is worth noting that the mode II stress intensity is

$$K_{II} = \left(S_r \mp \frac{1}{2} S_g \right) \sqrt{\pi a} , \quad x = \pm a,$$

so $K_{II} (x = +a) = 0$ in the limiting case where $S_g/2S_r = 1$. We will return to this phenomenon after introducing the end zone models.

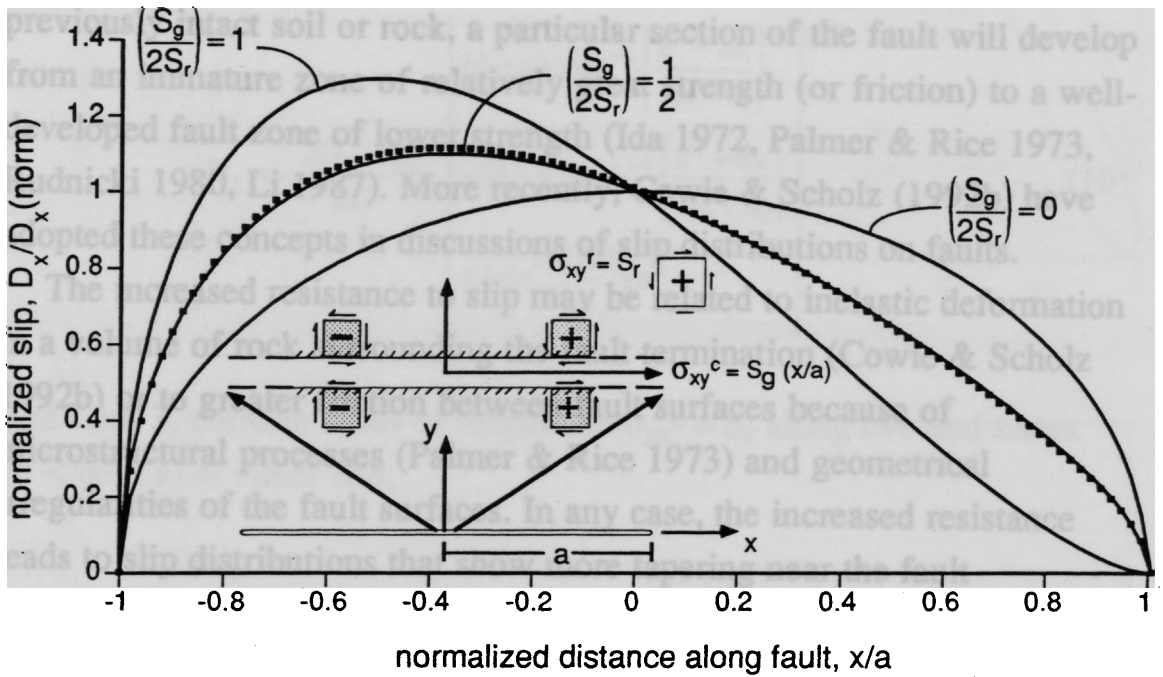


Fig. 3.6. Effects of a linear stress distribution along a model fault. Plot of normalized slip versus normalized distance using Equation (8). The parameter $S_g/2S_r$ controls the relative magnitudes of the linear and uniform stresses loading the model fault. For comparison we plot the numerical (small squares) solution for $S_g/2S_r = 0.5$. Boundary conditions are shown in the inset.

Non-linear stress distributions: an end zone model

Remote shear stress distributions or changes in frictional strength along faults that are more complex than the uniform or linearly varying cases may be justified in particular tectonic settings or by particular mechanisms for fault propagation and frictional resistance to slip. For example it has been suggested that, as a fault propagates through previously intact soil or rock, a particular section of the fault will develop from an immature zone of relatively great strength (or friction) to a well-developed fault zone of lower strength (Ida 1972, Palmer & Rice 1973, Rudnicki 1980, Li 1987). More recently, Cowie & Scholz (1992b) have adopted these concepts in discussions of slip distributions on faults.

The increased resistance to slip may be related to inelastic deformation in a volume of rock surrounding the fault termination (Cowie & Scholz 1992b) or to greater friction between fault surfaces because of microstructural processes (Palmer & Rice 1973) and geometrical irregularities of the fault surfaces. In any case, the increased resistance leads to slip distributions that show more tapering near the fault terminations than predicted for a uniform stress drop (Fig. 3.4).

We consider a simple end-zone fault model with uniform remote shear stress, σ_{yx}^r , uniform shear stress, σ_{yx}^m , over the central portion of the fault, and end zones with uniform shear stress, σ_{yx}^c , (Fig. 3.7a, inset). Cowie & Scholz (1992b) studied a similar distribution of normal stresses using the Barenblatt (1962) opening-mode equations as an analogue for faults. We compute the effects of the non-uniform loading on fault patches using Westergaard stress functions from Tada *et al.* (1973, p. 5.11). Because the linear-elastic stress fields and the related stress functions are additive, solutions for the different loading configurations are superimposed. The displacement discontinuities for the three different applied shear stresses are:

Case 1, stress-free crack of length $2a$ under remote uniform loading, $\sigma_{yx}^r = S_r$;

$$D_x = 2S_r \cdot \frac{(1-\nu)}{G} \sqrt{a^2 - x^2} \quad (9)$$

Case 2, uniform stress of magnitude $\sigma_{yx}^m = S_m$ along the central portion of the fault ($-d \leq x \leq +d$, Fig. 3.7a inset);

$$D_x = -\frac{2(1-\nu)}{\pi G} S_m \left[\begin{array}{l} (d-x) \cosh^{-1} \left\{ \frac{a^2 - dx}{a|x-d|} \right\} \\ +(d+x) \cosh^{-1} \left\{ \frac{a^2 + dx}{a|x+d|} \right\} \\ +2 \sin^{-1} \left(\frac{d}{a} \right) \sqrt{a^2 - x^2} \end{array} \right] \quad (10)$$

and Case 3, uniform stress of magnitude $\sigma_{yx}^c = S_c$ along two end zones ($d < |x| \leq a$) at either end;

$$D_x = -\frac{2(1-\nu)}{\pi G} S_c \left[\begin{array}{l} -(d+x) \cosh^{-1} \left\{ \frac{a^2 + dx}{a|x+d|} \right\} \\ -(d-x) \cosh^{-1} \left\{ \frac{a^2 - dx}{a|x-d|} \right\} \\ +2 \left\{ \frac{\pi}{2} - \sin^{-1} \left(\frac{d}{a} \right) \right\} \sqrt{a^2 - x^2} \end{array} \right]. \quad (11)$$

Adding the three terms we find

$$D_x = \frac{2(1-\nu)}{G} \left[\begin{array}{l} \left\{ (S_r - S_c) - (S_m - S_c) \frac{2}{\pi} \sin^{-1} \left(\frac{d}{a} \right) \right\} \sqrt{a^2 - x^2} \\ -\frac{1}{\pi} (S_m - S_c) \left\{ \begin{array}{l} (d+x) \cosh^{-1} \left(\frac{a^2 + dx}{a|x+d|} \right) \\ +(d-x) \cosh^{-1} \left(\frac{a^2 - dx}{a|x-d|} \right) \end{array} \right\} \end{array} \right]. \quad (12)$$

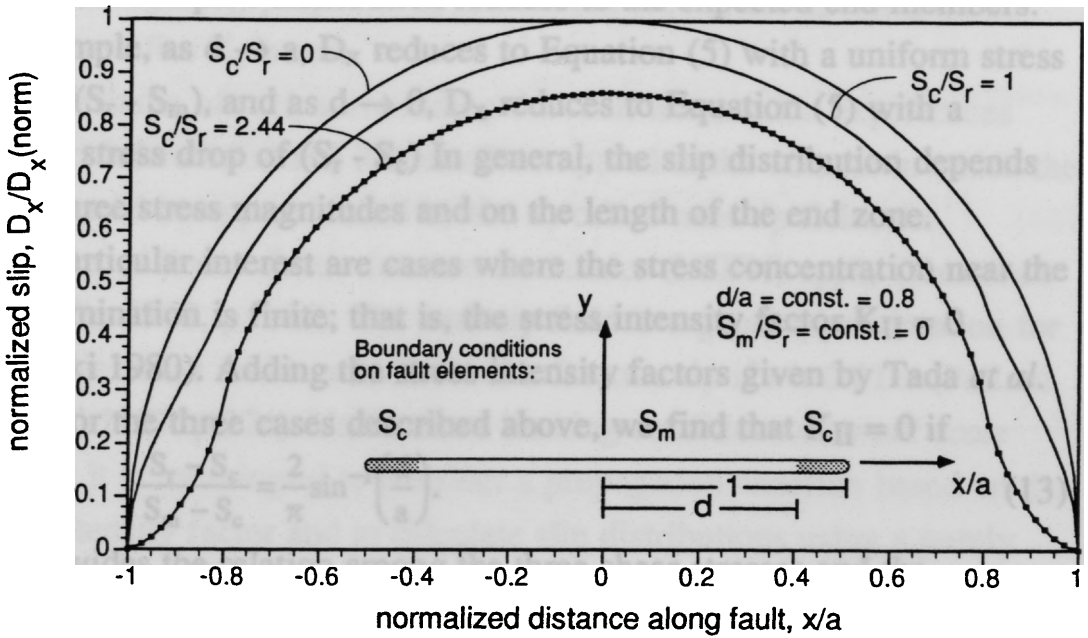
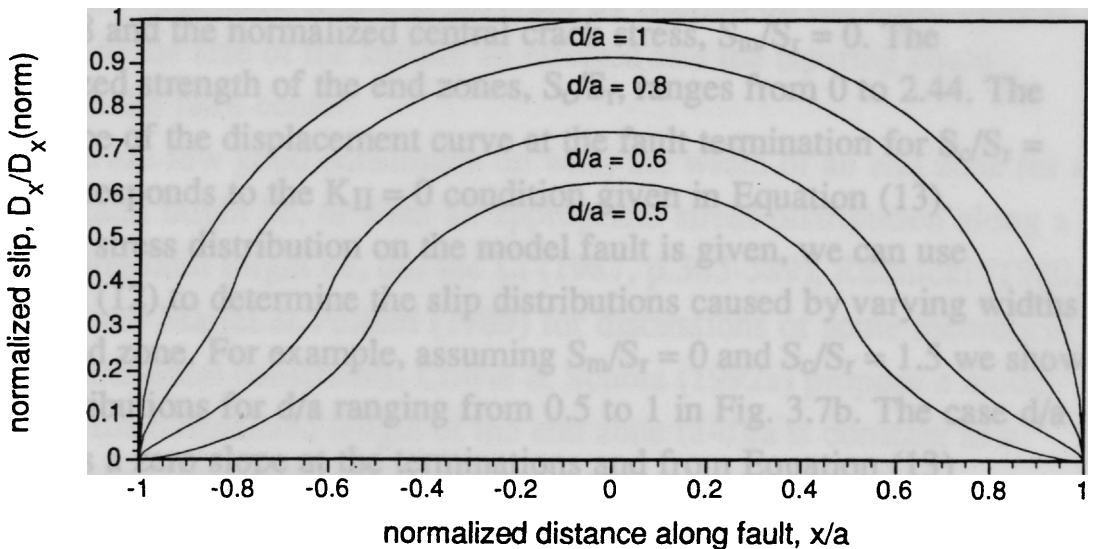
a**b**

Fig. 3.7. Effects of non-linear stress distributions along a model fault with a weak center portion and stronger end zones. (a) Normalized slip distributions with $d/a = 0.8$ and $S_m/S_r = 0$ for a range of end-zone stresses $0 \leq S_c/S_r \leq 2.44$. The numerical model for $S_c/S_r = 2.44$ (squares) closely reproduces the analytical result. The boundary conditions and geometry are shown in the inset. (b) Normalized slip distributions with $S_m/S_r = 0$ and $S_c/S_r = 1.5$ for end zone widths, $0.5 \leq d/a \leq 1$.

This rather complex distribution reduces to the expected end-members. For example, as $d \rightarrow a$, D_x reduces to Equation (5) with a uniform stress drop of $(S_r - S_m)$, and as $d \rightarrow 0$, D_x reduces to Equation (5) with a uniform stress drop of $(S_r - S_c)$. In general, the slip distribution depends on the three stress magnitudes and on the length of the end zone.

Of particular interest are cases where the stress concentration near the fault termination is finite; that is, the stress intensity factor $K_{II} = 0$ (Rudnicki 1980). Adding the stress intensity factors given by Tada *et al.* (1973) for the three cases described above, we find that $K_{II} = 0$ if

$$\frac{S_r - S_c}{S_m - S_c} = \frac{2}{\pi} \sin^{-1} \left(\frac{d}{a} \right). \quad (13)$$

This provides the relation among the three shear stresses and the geometric parameters of the fault for a fault growth criterion $K_{II} > 0$.

Figure 3.7a shows the normalized slip distribution for a model where $d/a = 0.8$ and the normalized central crack stress, $S_m/S_r = 0$. The normalized strength of the end zones, S_c/S_r , ranges from 0 to 2.44. The zero slope of the displacement curve at the fault termination for $S_c/S_r = 2.44$ corresponds to the $K_{II} = 0$ condition given in Equation (13).

If the stress distribution on the model fault is given, we can use equation (12) to determine the slip distributions caused by varying widths of the end zone. For example, assuming $S_m/S_r = 0$ and $S_c/S_r = 1.5$ we show slip distributions for d/a ranging from 0.5 to 1 in Fig. 3.7b. The case $d/a = 0.5$ has a zero slope at the terminations and from Equation (13) corresponds to the $K_{II} = 0$ condition. If $d/a < 0.5$, the positive stress on the end zones will cause left lateral slip near the fault terminations.

A special case stems from the work on *cohesive* end zones near the terminations of opening-mode cracks by Barenblatt (1962) and on plastic end zones for opening cracks by Dugdale (1960). By analogy to their results, certain distributions of shear stress in the cohesive zone of a shearing-mode crack will oppose the action of the remotely applied load so as to eliminate the stress singularity at the model fault termination. For these cases the stress intensity factor K_{II} is zero (Rudnicki 1980). The

criterion originally proposed by Barenblatt (1962) for opening-mode cracks specifies K_I is zero.

If a volume of rock surrounding the fault termination experiences inelastic deformation and it is small compared to the volume in which the stress would be approximated by the so-called near-tip field, the principles of linear elastic fracture mechanics (LEFM) apply (Kanninen & Popelar 1985, p. 146). The near-tip field is a good approximation for the elastic stress within a radius r of a fracture tip if $r < 0.01 a$ (Pollard & Segall 1987, p.324). Under these limiting conditions of *small scale yielding* it is meaningful to consider a propagation criterion based on the stress intensity factor and to calculate slip distributions using a purely elastic solution. The tapered portion of the slip distribution would be confined to very near the terminations of the fault. On the other hand, if the greater resistance to slip is provided by friction on the fault, there is no limit to the size of the surface so effected and the tapering could extend to the fault center.

There are few good constraints on what the width of an end zone for a natural fault might be, or what an appropriate stress distribution along a developing fault might be, but see Li (1987, p.383-389), Rudnicki (1980, p. 498), and Martel & Pollard (1989) for discussions of some theoretical and experimental constraints. Cowie & Scholz (1992a) propose a model wherein the normalized length of the end zone $(a-d)/a$ is constant as a fault grows. This implies that a critical displacement is required to weaken the breakdown zone which scales with the dimension of the fault.

A symmetric linear stress distribution

Increased strength or friction may be limited to a small zone near the fault terminations or may, in fact, decrease more gradually towards the region of greater displacement near the fault center. To remain in the context of our models this shear strength must not be exceeded except within the fault itself so the surrounding material is elastic. We examine the possible effects of gradual changes in the resistance to slip towards the

fault ends using the Westergaard function for a symmetric linear stress distribution (Tada *et al.* 1973, p. 5.14). In the remote field $\sigma_{yx}^r(x, y \rightarrow \infty) = \text{const.} = S_r$, and $\sigma_{yx}^c(|x| \leq a, y = 0^\pm) = S_g (|x|/a)$ on the fault surfaces. The displacement discontinuity is given by:

$$D_x = \frac{(1-\nu)}{G} 2 \left[S_r \sqrt{a^2 - x^2} - S_g \frac{1}{\pi} \left\{ \sqrt{a^2 - x^2} + \frac{x^2}{a} \cosh^{-1} \left(\frac{a}{x} \right) \right\} \right] \quad (14)$$

The mode II stress intensity factor is:

$$K_{II} = \left(S_r - S_g \frac{2}{\pi} \right) \sqrt{\pi a}. \quad (15)$$

So the condition of Barenblatt, $K_{II}=0$, is obtained at both terminations when

$$\frac{S_g}{\pi S_r} = \frac{1}{2}. \quad (16)$$

If $\sigma_{yx}(x = \pm a, y = 0^+) = S_g$ is a measure of the shear strength of the fault near its termination, then the fault will propagate when $S_r \geq \frac{2}{\pi} S_g$ maintaining $K_{II}=0$. The resulting modified slip distribution is shown as one of the curves in Figure 3.8. This slip distribution shows a reduction of the maximum slip magnitude (~50% of the complete stress-drop model, $S_g = 0$) and a more linear (tapered) decrease towards the fault terminations, ending in a zero slope.

Model faults such as those shown in Figs. 3.7 and 3.8 may explain the tapered form of slip observed along some natural faults (e.g., Cowie & Scholz 1992b, their Fig. 7).

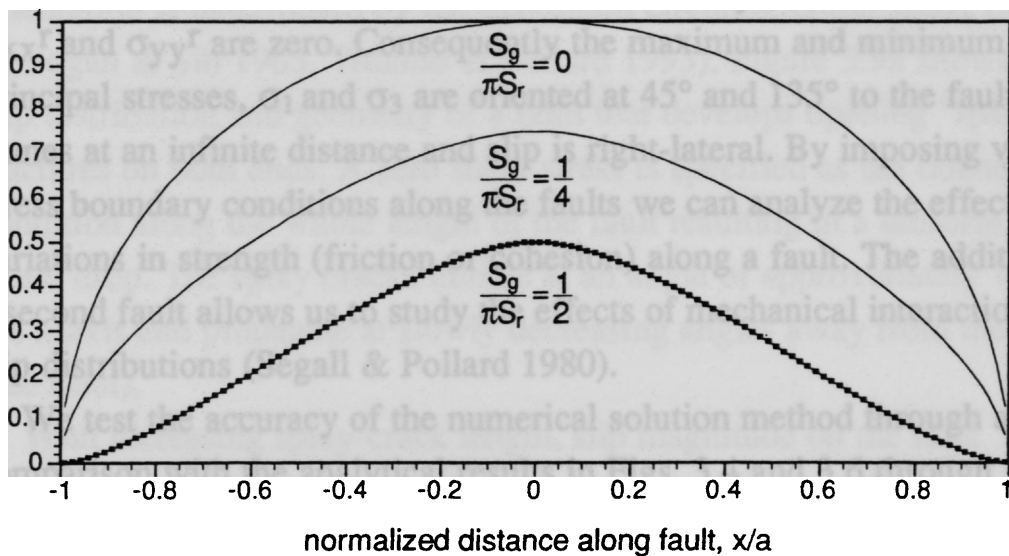


Fig. 3.8. Effects of linear symmetric stress distributions along a model fault. Normalized slip distributions for a range of stress gradients $0 \leq S_g/\pi S_r \leq 0.5$. The numerical model for $S_g/\pi S_r = 0.5$. (squares) closely reproduces the analytical result. If $S_g/\pi S_r > 0.5$, slip will be left-lateral near the fault terminations; if $S_g/\pi S_r < 0$ slip is enhanced towards the fault ends.

EFFECTS OF INELASTIC STRAIN AT FAULT ENDS AND FAULT INTERACTION ON SLIP DISTRIBUTIONS

We utilize the boundary element method (Crouch & Starfield 1983) to study the displacement distributions on faults under boundary conditions that are more complex than those described in the previous section. The program Frac2D (Thomas & Pollard 1993) allows us to study the plane, elastostatic stress and displacement fields about any number of fractures with varying loads and geometries. Each fault is divided into 100 or more individual boundary elements for which we specify shear and normal traction boundary conditions. The faults are parallel to the x-axis and are subjected to a unit remote, uniform shear stress $\sigma_{yx}^f = 1$ MPa, while σ_{xx}^f and σ_{yy}^f are zero. Consequently the maximum and minimum principal stresses, σ_1 and σ_3 are oriented at 45° and 135° to the fault planes at an infinite distance and slip is right-lateral. By imposing varying stress boundary conditions along the faults we can analyze the effects of variations in strength (friction or cohesion) along a fault. The addition of a second fault allows us to study the effects of mechanical interaction on slip distributions (Segall & Pollard 1980).

We test the accuracy of the numerical solution method through a comparison with the analytical results in Figs. 3.4 and 3.6 through 3.8. In each figure, the unbroken line represents the analytical solution, whereas the individual points are the numerical results computed for similar boundary conditions. Slip distributions in the numerical models very closely follow the analytical results. Slight deviations are primarily the result of approximating smoothly varying stress distributions on the fault by constant loads of differing magnitude on each boundary element.

Effects of inelastic deformation at fault ends

Commonly, stress concentrations at fault terminations favor the development of secondary structures: opening cracks, veins and normal faults in the extensional quadrant (Erdogan & Sih 1963, Nemat-Nasser & Horii 1982, Segall & Pollard 1983b, Granier 1985, Deng et al. 1986,

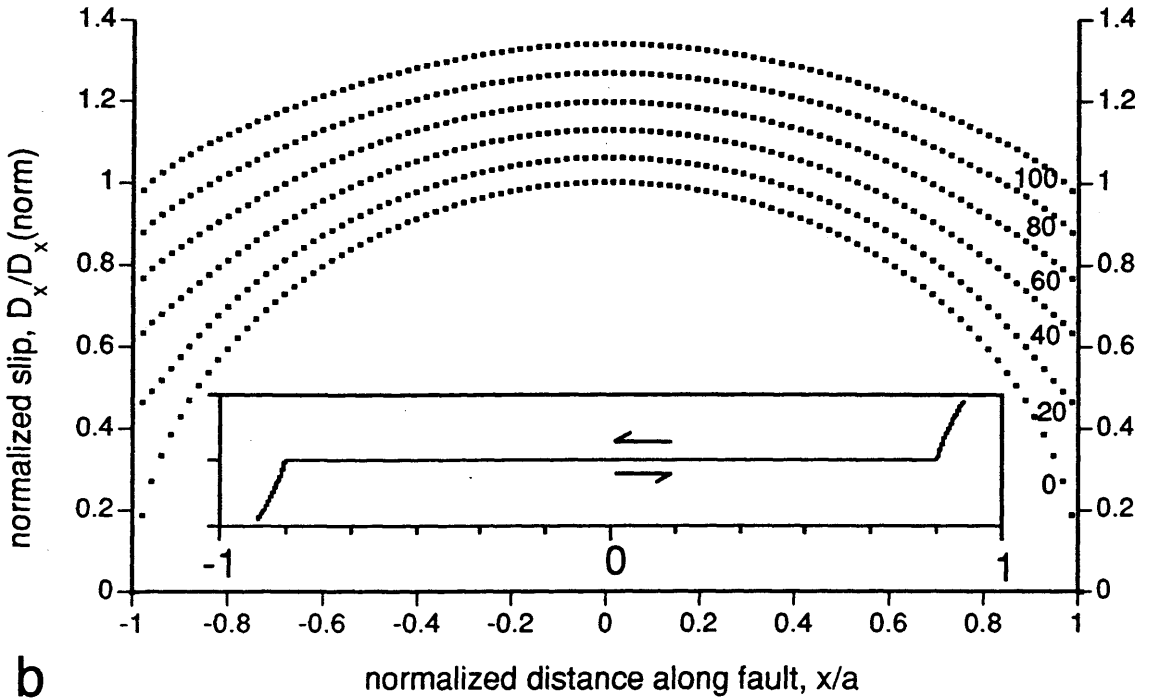
Petit & Barquins 1988, Barquins & Petit 1992), and pressure solution seams, thrust faults, folds, and ductile fabrics in the contractional quadrant (Fletcher & Pollard 1981, Deng *et al.* 1986, Bürgmann & Pollard 1992).

Opening-mode fracture growth is introduced with a fracture criterion at the model fault terminations (e.g., Lawn & Wilshaw 1975). These cracks are prescribed to grow by a small increment ($0.002 \cdot a$) if the mode I stress intensity factor, K_I , exceeds the critical stress intensity factor $K_{Ic} = 1.5 \text{ MPa m}^{1/2}$ (Atkinson & Meredith 1987, p. 492). The newly formed elements are specified to carry zero shear- and normal tractions and their orientation is determined by the maximum circumferential stress criterion (Erdogan & Sih 1963, Thomas & Pollard 1993). Figure 3.9a shows the slip distribution and geometry of a fault that develops opening "splay" fractures on both ends. A zero shear stress is specified as the boundary condition along the whole length of the fault resulting in a uniform 1 MPa stress drop. The splay cracks initiate at an angle of approximately 70° to the x-axis and propagate at slowly decreasing angles away from the fault (see inset).

With increasing splay-crack length, slip magnitude on the fault increases and the slip gradient near the fault terminations decreases. The slip magnitude on boundary elements near the fault termination is approximately equal to the opening displacement on the boundary elements near the base of the splay crack. The maximum slip magnitude near the center of the fault increases approximately linearly with splay crack length (Fig. 3.9b).

This analysis illustrates how inelastic deformation near fault terminations, due to opening fractures increase the slip magnitude along a fault and decrease the gradient in slip elsewhere along the fault. Furthermore, slip is not constrained to be zero at the fault termination, if it is coupled to the inelastic deformation such as splay crack opening. If such inelastic deformation were to occur near one fault termination only, a highly asymmetric slip distribution would result.

a



b

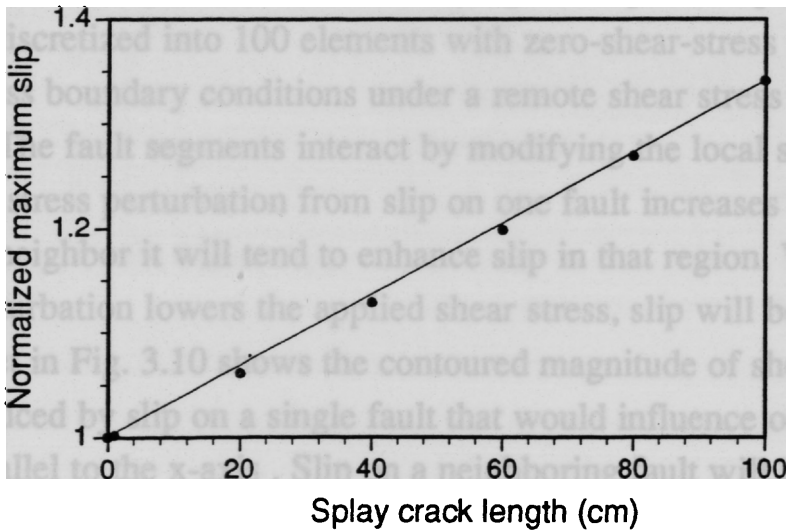


Fig. 3.9. Influence of inelastic deformation (opening splay fractures) at fault terminations on slip. (a) Slip distribution at various stages of splay fracture growth. The inset shows the fracture path through 100 growth increments. (b) Maximum slip magnitude at the center of the fault is approximately linearly related to the length of the splay fractures.

Fault interaction across echelon steps

Faults are typically composed of individual fault segments in a left- or right stepping echelon geometry (Wallace 1973, Crowell 1974, Dibblee 1977, Segall & Pollard 1980, Christie-Blick & Biddle 1985, Aydin & Schultz 1990). The interaction of individual fault segments in an echelon arrangement leads to characteristic stress fields and resulting deformation patterns, depending on the left- or right-stepping character of fault stepovers for a given sense of shear (Rodgers 1980, Segall & Pollard 1980, Bilham & King 1989, Aydin & Schultz 1990, Bürgmann & Pollard 1992). Here we analyze the effects of fault interaction across simple echelon fault steps on the slip distribution.

We model the slip distribution along two stress free, frictionless faults; that is, fault strength is not dependent on the fault-normal stress, as would be the case if faulting is frictional (Aydin & Schultz 1990). We illustrate the effects of fault interaction by calculating the slip distribution along two straight parallel faults of varying overlap and separation. Each fault is discretized into 100 elements with zero-shear-stress and zero-normal-stress boundary conditions under a remote shear stress of 1 MPa.

The fault segments interact by modifying the local stress field. Where the stress perturbation from slip on one fault increases the shear stress on its neighbor it will tend to enhance slip in that region. Where the stress perturbation lowers the applied shear stress, slip will be decreased. The inset in Fig. 3.10 shows the contoured magnitude of shear stress, σ_{yx} , induced by slip on a single fault that would influence other faults oriented parallel to the x-axis. Slip on a neighboring fault will be enhanced where $\sigma_{yx} > 1$ and reduced where $\sigma_{yx} < 1$. The slip distributions will be the same for left- and right-stepping geometries due to the symmetric nature of the shear stress field.

The interaction of the echelon fault segments can cause asymmetric slip distributions along the faults, and the maximum slip magnitude may increase or decrease compared to that for the single fault model. The slip

distribution depends on the amount of overlap of the two fault segments and their separation.

Figure 3.10 shows the slip distribution of the left member of an echelon set of two faults with zero overlap and varying separation. The greatest slip magnitude (two times the base case) is achieved when the two fault segments have zero overlap and separation, thereby forming a single fault of twice the original length. With zero overlap, the slip magnitude on the individual faults decreases with increasing separation and the locus of maximum slip shifts toward the segment centers (Fig. 3.10). Models of the effects of varying overlap (not shown) indicate that slip along the step bounding fault segments is reduced due to a stress shadowing effect if overlap is large. If the two faults overlap completely, the slip distribution is elliptical but of lower magnitude depending on the separation. However, if faults overlap or underlap by only a small fraction of their length, slip is increased at small separations.

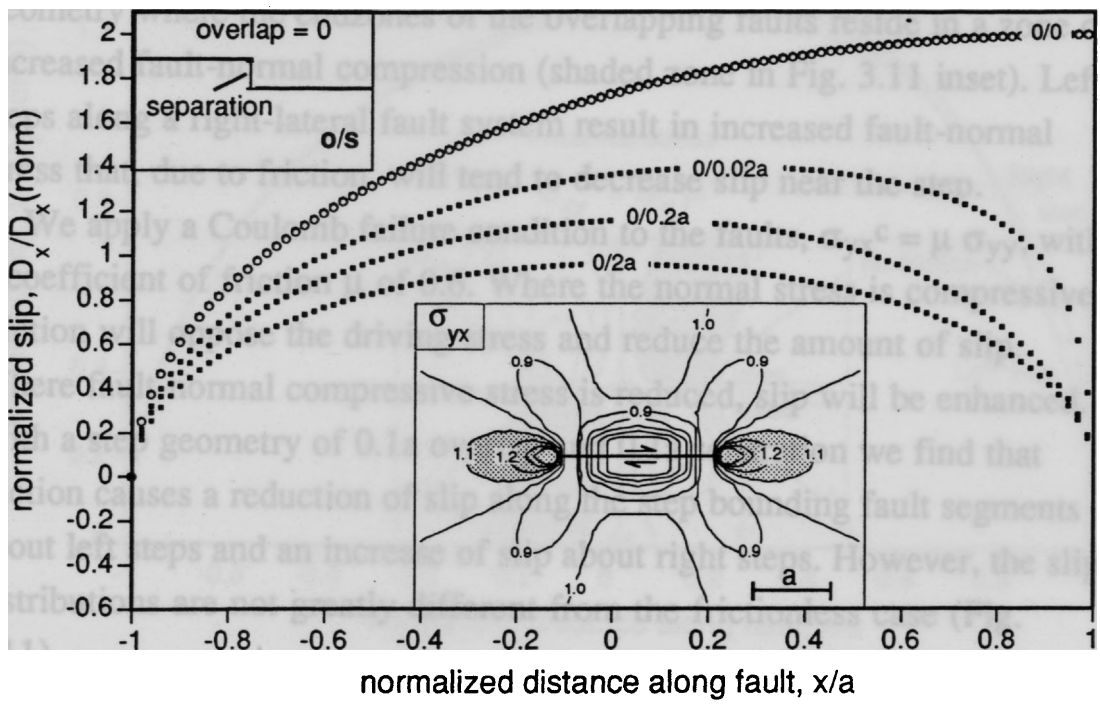


Fig. 3.10. Slip distribution along the left most echelon segment of a pair of faults with zero overlap and various amounts of separation (0 to 2 times the fault half length a). Fault slip is locally enhanced or diminished due to the effects of the local stress field (inset). Both fault segments have zero-stress boundary conditions.

In the previous discussion we neglected the effects of non-uniform fault-normal stresses due to mechanical interaction. The inset in Fig. 3.11 shows the contoured magnitude of the fault-normal stress σ_{yy} about a single fault with the same boundary conditions as in the previous model. In a right-stepping arrangement the adjacent fault will be exposed to fault-normal tensile stress near the overlapping region. If faulting is frictional, the reduced fault-normal compressive stress will reduce frictional stress and increase slip (Segall & Pollard 1980, Aydin & Schultz 1990). The opposite is to be expected for the left-stepping geometry where the endzones of the overlapping faults reside in a zone of increased fault-normal compression (shaded zone in Fig. 3.11 inset). Left steps along a right-lateral fault system result in increased fault-normal stress that, due to friction, will tend to decrease slip near the step.

We apply a Coulomb failure condition to the faults, $\sigma_{yx}^c = \mu \sigma_{yy}$, with a coefficient of friction μ of 0.6. Where the normal stress is compressive, friction will oppose the driving stress and reduce the amount of slip. Where fault-normal compressive stress is reduced, slip will be enhanced. With a step geometry of 0.1a overlap and 0.1a separation we find that friction causes a reduction of slip along the step bounding fault segments about left steps and an increase of slip about right steps. However, the slip distributions are not greatly different from the frictionless case (Fig. 3.11).

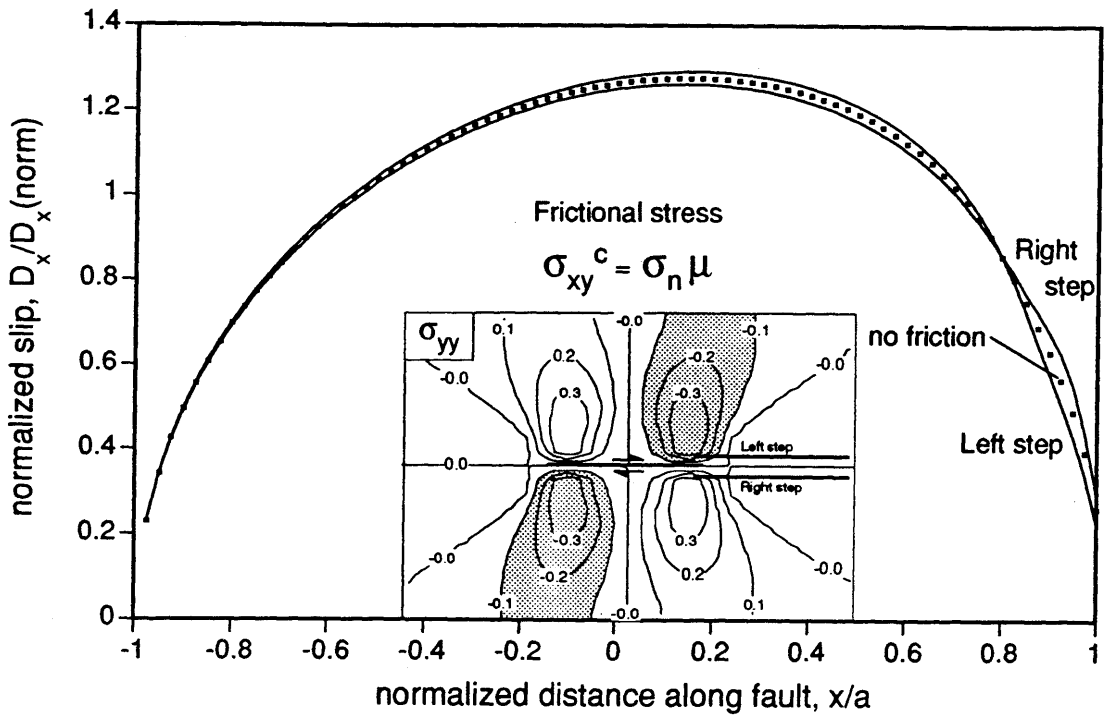


Fig. 3.11. Slip distribution along frictional right-lateral echelon fault segments with $0.1a$ overlap and $0.1a$ separation. Because the stress boundary conditions along the faults depend on the normal stress, σ_{yy} , (inset), the slip distributions of left- and right-stepping echelon faults differ.

Where two strike-slip fault segments are arranged in an echelon geometry, stress perturbations may favor the development of inelastic deformation around the stepover (Segall & Pollard 1980, Sibson 1986, Gamond 1987, Aydin & Schultz 1990, Bürgmann & Pollard 1993). We investigate the effects of inelastic deformation at fault discontinuities by allowing opening fractures to grow from the echelon fault ends of a right step between two right-lateral fault segments (Fig. 3.12). If the opening cracks propagate across the step, they effectively link the segments, and transfer slip. We find that the slip distribution along the faults approaches that of a single fault of the combined length of the two segments as the open fractures approach linkage. Similarly, mass solution transfer out of fault steps through the development of pressure solution seams (Gamond 1987) or pressure enhanced ductile strain accommodation in left steps allows the effective transfer of displacement between echelon faults (Bürgmann & Pollard 1993).

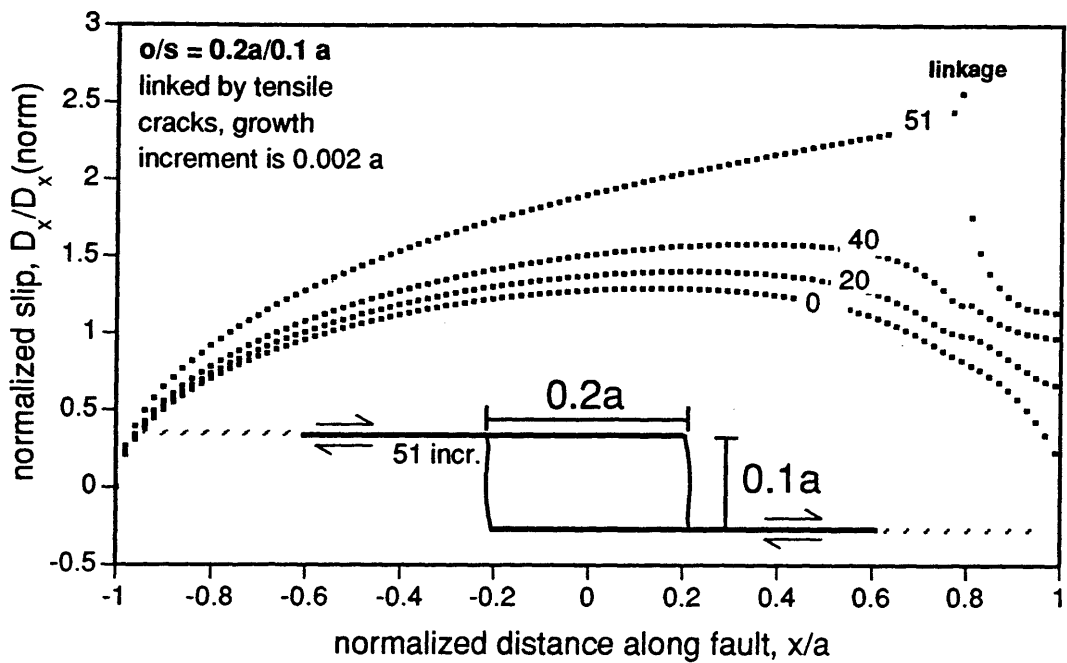


Fig. 3.12. Influence of opening fractures in a right step on fault slip distributions. Inset shows the paths of the fractures emanating from the fault terminations according to a maximum circumferential stress criterion. Remote and crack stress boundary conditions are same as in Fig. 3.10.

DISCUSSION AND CONCLUSIONS

We have identified several factors that are expected to influence the slip distributions along faults. Our model results show that deviations from an idealized symmetrical and elliptical slip distribution can be caused by stress gradients, inelastic deformation processes, and mechanical interaction between adjacent fault segments.

As faults propagate through previously intact rock, the resistance to slip near the fault periphery may be greater than that near the mature center. Similarly, if the friction changes with slip magnitude along a fault, this non-uniform resistance influences the slip distribution. If stress concentrations near fault terminations exceed the strength of the surrounding material, the development of secondary structures (fractures, folds, and fabric) will cause further deviations from slip distributions derived from simple models. Some faults are part of a larger fault zone and are expected to strongly influence slip distributions along their nearest neighbors because of perturbations of the local stress field.

In addition to the effects directly addressed in this contribution, changes in rheological properties of the material alongside faults also can influence on the slip distributions. For example, Muraoka and Kamata (1983) speculated that changes in competence of the host rock may influence the slip distribution of faults breaking through various sedimentary rock types. The less competent (in its current state) sandstone in Fig. 3.5 (middle) is thought to reduce fault slip by ductile drag. Alternatively, a reduction of slip is to be expected if the sandstone were more rigid (higher elastic shear modulus G), as can be deduced from Equation 5. Another possible explanation is that the sandstone has a greater frictional resistance to slip, and that slip was reduced in a high-friction breakdown zone as the fault propagated through the sandstone.

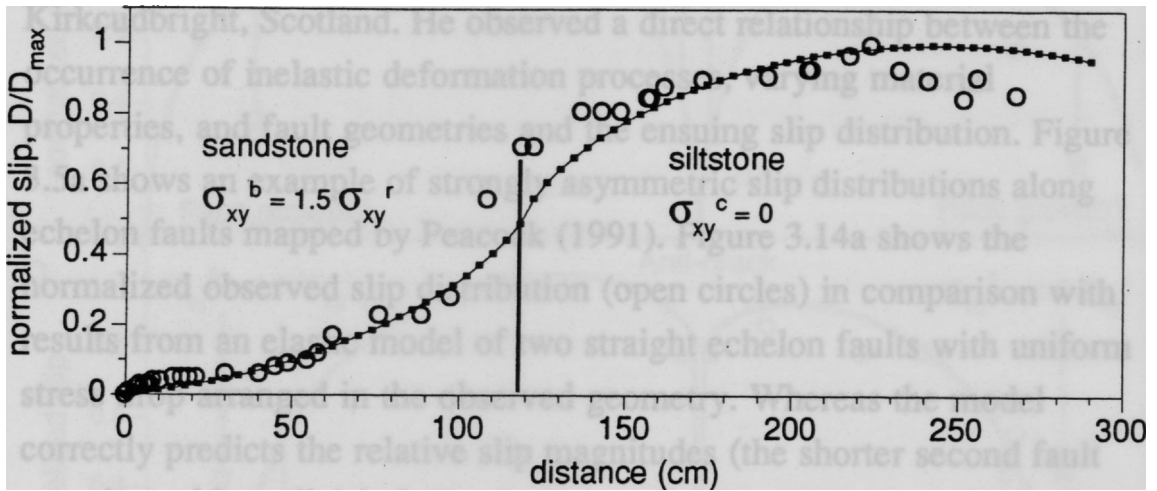


Fig. 3.13. Measured slip distribution (Fig. 3.5b, Muraoka, 1983) in comparison with model of increased frictional resistance of the fault segment in the sandstone bed. Alternatively this effect could be caused by greater stiffness of the sandstone.

We can model these two factors by applying a slip retarding shear stress boundary condition on the fault segment in the sandstone. The modeled slip distribution shown in Fig. 3.13 closely matches the observed slip (open circles). Without further testing of the constitutive and frictional properties of the host rock materials we are not able to discriminate between the different explanations.

Examples of fault interaction across left- and right-stepping echelon strike-slip fault segments have been mapped by Peacock (1991) near Kirkcudbright, Scotland. He observed a direct relationship between the occurrence of inelastic deformation processes, varying material properties, and fault geometries and the ensuing slip distribution. Figure 3.5a shows an example of strongly asymmetric slip distributions along echelon faults mapped by Peacock (1991). Figure 3.14a shows the normalized observed slip distribution (open circles) in comparison with results from an elastic model of two straight echelon faults with uniform stress drop arranged in the observed geometry. Whereas the model correctly predicts the relative slip magnitudes (the shorter second fault experienced less slip) it does not account for the strong asymmetry of the slip distribution and overpredicts slip near the distal fault terminations.

Peacock (1991) pointed out that ductile flow in a shale layer that encloses the fault discontinuity may enhance slip transfer (see inset, Fig. 3.5a). We modify our model by including a fault-perpendicular anticrack between the two model faults (Fletcher & Pollard 1981). Interpenetration of the anticrack walls represents inelastic strain accommodation in the step. We introduce two strong end zones at the distal fault ends where $\sigma_{yx}^b = 1.5 \sigma_{yx}^r$, to model the effects of lateral fault growth. The slip distribution resulting from this model more closely matches the observed pattern (Fig. 3.14b). However, the mechanisms used here are not unique and independent evidence for their application is needed to make this a convincing explanation.

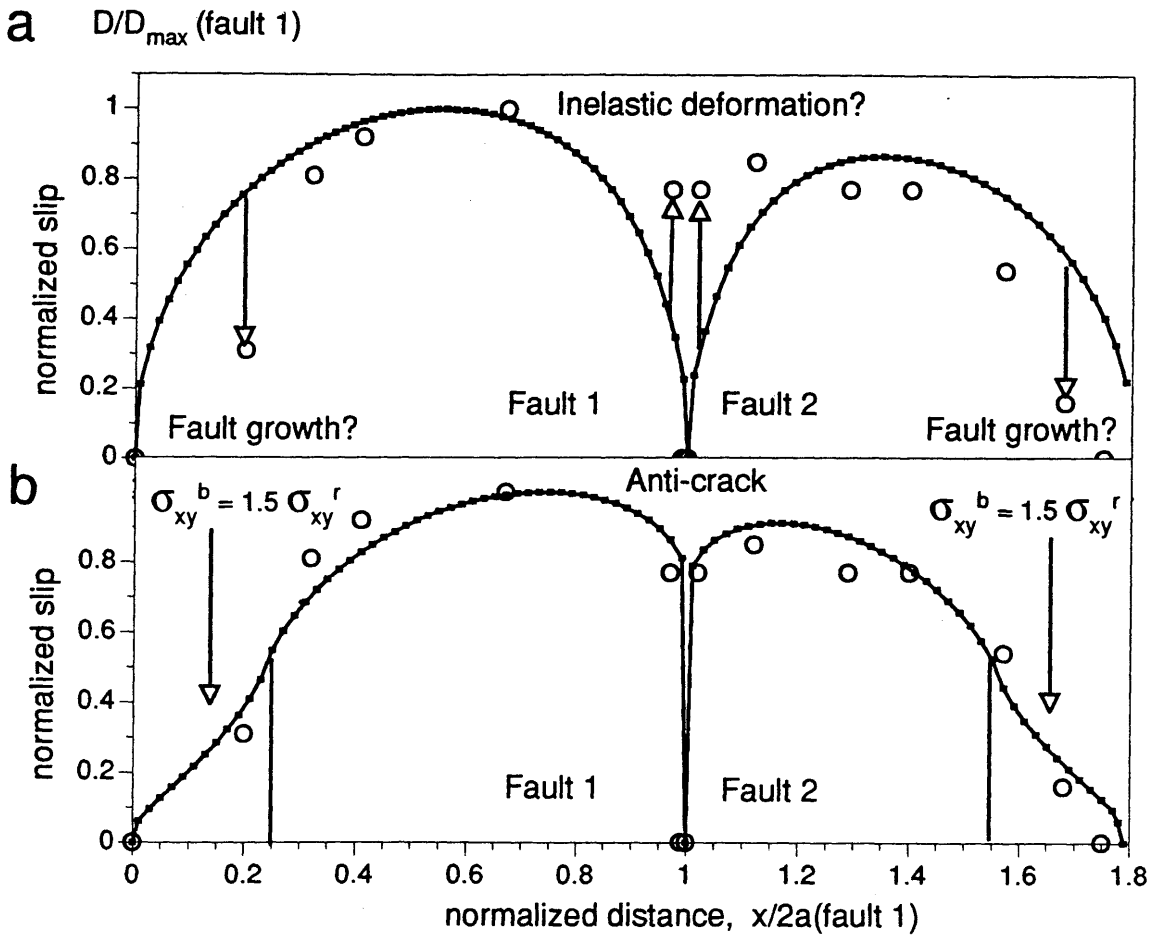


Fig. 3.14. Measured slip distribution along echelon fault segments (Fig. 3.5a, Peacock 1991) in comparison with model of mechanical interaction and inelastic deformation near fault discontinuities. (a) A model of two segments with uniform-stress boundary conditions does not adequately model the observed slip distributions. (b) Inelastic deformation in the fault step, and frictional end zones near the distal fault ends improve the model fit.

Clearly it is important to analyze slip distributions in the context of a fault's three-dimensional geometry, its relationship to nearby structures, the constitutive behavior of the host rock, and the development of secondary structures. Studies that assume that slip is symmetric about a central maximum neglect these important factors. Studies which reduce fault slip distributions from a variety of tectonic settings to single points on log-log plots of maximum slip versus trace length should be viewed with considerable skepticism.

REFERENCES

- Antonellini, M. A., Aydin, A. & Pollard, D. 1993. Microstructure of deformation bands in porous sandstones at Arches National Park, Utah. *J. Struct. Geol.* submitted.
- Archuleta, R. 1984. A faulting model for the 1979 Imperial Valley earthquake. *J. Geophys. Res.* **89**, 4559-4585.
- Atkinson, B. K. & Meredith, P. G. 1987. Experimental fracture mechanics data for rocks and minerals. In: *Fracture Mechanics of Rock* (edited by Atkinson, B. K.). Academic Press Inc. London, 477-525.
- Aydin, A. 1978. Small faults formed as deformation bands in sandstone. *Pageoph* **116**, 913-930.
- Aydin, A. & Schultz, R. A. 1990. Effect of mechanical interaction on the development of strike-slip faults with echelon patterns. *J. Struct. Geol.* **12**, 123-129.
- Barenblatt, G. I. 1962. The mathematical theory of equilibrium cracks in brittle fracture. *Adv. Appl. Mech.* **7**, 55-125.
- Barnett, J. A. M., Mortimer, J., Rippon, J. H., Walsh, J. J. & Watterson, J. 1987. Displacement geometry in the volume containing a single normal fault. *Am. Ass. Petrol. Geol. Bull.* **71**, 925-937.
- Barquins, M. & Petit, J. P. 1992. Kinetic instabilities during the propagation of a branch crack: effects of the loading conditions and internal pressure. *J. Struct. Geol.* **14**, 893-903.

- Beroza, G. C. 1991. Near-source modeling of the Loma Prieta earthquake: Evidence for heterogeneous slip and implications for earthquake hazard. *Bull. Seism. Soc. Am.* **81**, 1603-1621.
- Bilham, R. & Bodin, P. 1992. Fault zone connectivity: Slip rates on faults in the San Francisco Bay area, California. *Science* **258**, 281-284.
- Bilham, R. & King, G. P. C. 1989. The morphology of strike-slip faults: Examples from the San Andreas fault, California. *J. Geophys. Res.* **94**, 10204-10216.
- Bilham, R. & Williams, P. 1985. Sawtooth segmentation and deformation processes on the southern San Andreas fault, California. *Geophys. Res. Lett.* **12**, 557-560.
- Bouvier, J. D., Kaars-Sijpesteijn, C. H., Kluesner, D. F., Onyejekwe, C. C. & van der Pal, R. C. 1989. Three-dimensional seismic interpretation and fault sealing investigations, Nun River Field, Nigeria. *Am. Assoc. Pet. Geol. Bull.* **73**, 1397-1414.
- Bürgmann, R. & Pollard, D. D. 1992. Influence of the state of stress on the brittle-ductile transition in granitic rock: Evidence from fault steps in the Sierra Nevada, California. *Geology* **20**, 645-648.
- Bürgmann, R. & Pollard, D. D. 1993. Strain accommodation about strike-slip fault discontinuities in granitic rock under brittle-to-ductile conditions. *J. Struct. Geol.* submitted. Chapter 2, this Thesis.
- Christie-Blick, N. & Biddle, K. T. 1985. Deformation and basin formation along strike-slip faults. In: *Strike-slip Deformation, Basin Formation, and Sedimentation* (edited by Biddle, K. T. & Christie-Blick, N.). *Soc. econ. Paleont. Mineral. Spec. Pub.* **37**, 1-34.
- Cowie, P. A. & Scholz, C. H. 1992a. Growth of faults by accumulation of seismic slip. *J. Geophys. Res.* **97**, 11085-11095.
- Cowie, P. A. & Scholz, C. H. 1992b. Physical explanation for the displacement-length relationship of faults using a post-yield fracture mechanics model. *J. Struct. Geol.* **14**, 1133-1148.
- Crouch, S. L. & Starfield, A. M. 1983. *Boundary element methods in solid mechanics*. Unwin Hyman, London.

- Crowell, J. C. 1974b. Sedimentation along the San Andreas fault, California. In: *Modern and ancient geosynclinal sedimentation* (edited by Dott, R. H. & Shaver, R. H.). *Soc. econ. Paleont. Mineral. Spec. Pub.* **19**, 292-303.
- Delaney, P. T. & Pollard, D. D. 1981. Deformation of host rocks and flow of magma during growth of minette dikes and breccia-bearing intrusions near Ship Rock, New Mexico. *Prof. Pap. U. S. Geol. Surv.* **1202**, 1-61.
- Deng, Q., Wu, D., Zhang, P. & Chen, S. 1986. Structure and deformational character of strike-slip fault zones. *Pageoph* **124**, 203-224.
- Dibblee, T. W., Jr. 1977. Strike-slip tectonics of the San Andreas fault and its role in Cenozoic basin evolution. In: *Late Mesozoic and Cenozoic sedimentation and tectonics in California* (edited by Nilsen, T. H.). San Joaquin Geological Society Bakersfield, California, 26-38.
- Du, Y. & Aydin, A. 1990. Stress transfer during three sequential moderate earthquakes along the central Calaveras fault. *EOS Trans. Am. Geophys. Un.* **71**, 1652.
- Dugdale, D. S. 1960. Yielding of steel sheets containing slits. *J. Mech. Phys. Solids* **8**, 100-104.
- Erdogan, F. & Sih, G. C. 1963. On the crack extension in plates under plane loading and transverse shear. *J. Basic Engin.* 519-527.
- Eshelby, J. D. 1957. The determinations of the elastic field of an ellipsoidal inclusion and related problems *Proc. Roy. Soc. London* **A241**, 376-396.
- Fletcher, R. & Pollard, D. D. 1981. An anticrack mechanism for stylolites. *Geology* **9**, 419-424.
- Gamond, J. F. 1987. Bridge structures as sense of displacement criteria in brittle fault zones. *J. Struct. Geol.* **9**, 609-620.
- Gillespie, P. A., Walsh, J. J. & Watterson, J. 1992. Limitations of dimension and displacement data from single faults and the

- consequences for data analysis and interpretation. *J. Struct. Geol.* **14**, 1157-1172.
- Granier, T. 1985. Origin, damping and pattern of development of faults in granite. *Tectonics* **4**, 721-737.
- Harris, R. & Segall, P. 1987. Detection of a locked zone at depth on the Parkfield, California segment of the San Andreas fault. *J. Geophys. Res.* **92**, 7945-7962.
- Higgs, W. G. & Williams, G. D. 1987. Displacement efficiency of faults and fractures. *J. Struct. Geol.* **9**, 371-374.
- Ida, Y. 1972. Cohesive force across the tip of a longitudinal-shear crack and Griffith's specific surface energy. *J. Geophys. Res.* **77**, 3796-3805.
- Kanninen, M. F. & Popelar, C. H. 1985. *Advanced fracture mechanics*. Oxford University Press, New York.
- Lawn, B. R. & Wilshaw, T. R. 1975. *Fracture of Brittle Solids*. Cambridge University Press, Cambridge.
- Lawson, J. J. 1908. The California earthquake of April 18, 1906: Report of the State Earthquake Investigation Commission. *Carnegie Institution of Washington Publication* **87**.
- Li, V. C. 1987. Mechanics of shear rupture applied to earthquake zones. In: *Fracture Mechanics of Rock* (edited by Atkinson, B. K.). Academic Press Inc. London, 351-428.
- Martel, S. J. & Pollard, D. D. 1989. Mechanics of slip and fracture along small faults and simple strike-slip fault zones in granitic rock. *J. Geophys. Res.* **94**, 9417-9428.
- Muraoka, H. & Kamata, H. 1983. Displacement distribution along minor fault traces. *J. Struct. Geol.* **5**, 483-495.
- Muskhelishvili, N. E. 1954. *Some Basic Problems of the Mathematical Theory of Elasticity*. P. Noordhof, Leyden, Netherlands.
- Nemat-Nasser, S. & Horii, H. 1982. Compression-induced nonplanar crack extension with application to splitting, exfoliation, and rockburst. *J. Geophys. Res.* **87**, 6805-6821.

- Palmer, A. C. & Rice, J. R. 1973. The growth of slip surfaces in the progressive failure of overconsolidated clay. *Proc. Roy. Soc. London* **A332**, 527-548.
- Peacock, D. C. P. 1991. Displacements and segment linkage in strike-slip fault zones. *J. Struct. Geol.* **13**, 1025-1035.
- Petit, J. P. 1987. Criteria for the sense of movement on fault surfaces in brittle rock. *J. Struct. Geol.* **9**, 597-608.
- Petit, J. P. & Barquins, M. 1988. Can natural faults propagate under mode II conditions. *Tectonics* **7**, 1243-1256.
- Pollard, D. D. & Muller, O. H. 1976. The effect of gradients in regional stress and magma pressure on the form of sheet intrusions in cross-section. *J. Geophys. Res.* **81**, 975-984.
- Pollard, D. D. & Segall, P. 1987. Theoretical displacements and stresses near fractures in rocks: With applications to faults, joints, veins, dikes, and solution surfaces. In: *Fracture Mechanics of Rock* (edited by Atkinson, B. K.). Academic Press Inc. London, 277-349.
- Reasenber, P. A. & Simpson, R. W. 1992. Response of regional seismicity to the static stress change produced by the Loma Prieta earthquake. *Science* **255**, 1687-1690.
- Rippon, J. H. 1985. Contoured patterns of the throw and hade of normal faults in the Coal Measures (Westphalian) of north-east Derbyshire. *Proc. Yorks. Geol. Soc.* **45**, 147-161.
- Rodgers, D. A. 1980. Analysis of pull-apart basin development produced by en echelon strike-slip faults. In: *Sedimentation in Oblique-slip Mobile Zones* (edited by Ballance, P. F. & Reading, H. G.). *Int. Assoc. Sedimentol., Oxford, England, Spec. Publ.* **4**, 27-41.
- Rudnicki, J. W. 1980. Fracture mechanics applied to the Earth's crust. *Annu. Rev. Earth Planet. Sci.* **8**, 489-525.
- Rymer, M. J. 1989. Surface rupture in a fault stepover on the Superstition Hills fault, California. In: *Fault segmentation and controls of rupture initiation and termination* (edited by Schwartz, D. P. & Sibson, R. H.). U.S. Geological Survey Open-File Report 89-315 309-323.

- Segall, P. & Pollard, D. D. 1980. Mechanics of discontinuous faults. *J. Geophys. Res.* **85**, 4337-4350.
- Segall, P. & Pollard, D. D. 1983b. Nucleation and growth of strike-slip faults in granite. *J. Geophys. Res.* **88**, 555-568.
- Sibson, R. H. 1986. Rupture interaction with fault jogs. In: *Earthquake Source Mechanics*, (edited by Das, S., Boatwright, J. & Scholz, C.). *Am. Geophys. Un. Geophys. Monograph, Washington, D.C.* **37**, 157-168.
- Sieh, K. 1978. Slip along the San Andreas fault associated with the great 1857 earthquake. *Bull. Seism. Soc. Am.* **68**, 1421-1428.
- Tada, H., Paris, P. C. & Irwin, G. R. 1973. *The Stress Analysis of Cracks Handbook*. Del Research Corporation, Hellertown, Pennsylvania.
- Thatcher, W. & Lisowski, M. 1987. Long-term seismic potential of the San Andreas fault southeast of San Francisco, California. *J. Geophys. Res.* **92**, 4771-4784.
- Thomas, A. L. & Pollard, D. D. 1993. The geometry of echelon fractures in rock: Implications from laboratory and numerical experiments. *J. Struct. Geol.* **15**, 323-334.
- Tschalenko, J. S. 1970. Similarities between shear zones of different magnitudes. *Bull. geol. Soc. Am.* **81**, 1625-1640.
- Vedder, J. G. & Wallace, R. E. 1970. Map showing recently active breaks along the San Andreas and related faults between Cholame Valley and Tejon Pass, California. *U.S.G.S. Misc. Field Investig. Map I-574*.
- Wald, D. J., Helmberger, D. V. & Heaton, T. H. 1991. Rupture model of the 1989 Loma Prieta earthquake from the inversion of strong-motion and broadband teleseismic data. *Bull. Seism. Soc. Am.* **81**, 1540-1572.
- Wallace, R. E. 1973. Surface fracture patterns along the San Andreas Fault. In: *Conference on tectonic problems of the San Andreas Fault system, Proceedings* (edited by Kovach, R. L. & Nur, A.). Stanford University Publications, Stanford **13**, 248-250.

- Walsh, J. J. & Watterson, J. 1987. Distribution of cumulative displacement and of seismic slip on a single normal fault surface. *J. Struct. Geol.* **9**, 1039-1046.
- Walsh, J. J. & Watterson, J. 1988. Analysis of the relationship between displacements and dimensions of faults. *J. Struct. Geol.* **10**, 239-247.
- Walsh, J. J. & Watterson, J. 1989. Displacement gradients on fault surfaces. *J. Struct. Geol.* **11**, 307-316.
- Watterson, J. 1986. Fault dimensions, displacements and growth. *Pageoph* **124**, 365-373.
- Westergaard, H. M. 1939. Bearing pressures and cracks. *J. Appl. Mech.* **66**, A49-A53.
- Zoback, M. D. & Zoback, M. L. 1991. Tectonic stress field of North America and relative plate motions. In: *Neotectonics of North America, The Decade of North American Geology Project series* (edited by Slemmons, D. B., Engdahl, E. R., Zoback, M. D. & Blackwell, D. D.). Geol. Soc. Am. Boulder, Colorado, 339-366.

4. Rise and Fall of the Southern Santa Cruz Mountains, California, From Fission Tracks, Geomorphology, and Geodesy

ABSTRACT

The southern Santa Cruz Mountains are closely associated with a left bend along the right-lateral San Andreas fault. The Loma Prieta area on the northeast side of the San Andreas consists of fault-bounded blocks that rise along active, deeply rooted, reverse and oblique-slip faults. Six samples from a transect across this area yield concordant apatite fission track ages averaging 4.6 ± 0.5 Ma. These ages date the time of cooling below ≈ 110 °C and suggest that about 3 km of unroofing has occurred over the last 4.6 m.y. Allowing for current elevations of ≈ 1 km, this suggests an average uplift rate on the order of 1 mm/yr over the last ≈ 4.6 m.y. To further define the extent and distribution of this young uplift, we used morphometric analyses of the youthful topography of the area. Steep drainage slopes and high local relief indicate that the area northeast of the San Andreas forms a well defined zone of high uplift bounded on the northeast by the southwest-dipping Foothills thrust system. In contrast, the region on the southwest side of the San Andreas is characterized by a broad upwarping and folding, more subdued topography, old fission track ages, and mean Quaternary uplift rates of ≈ 0.1 - 0.4 mm/yr. Geodetic data from the 1906 San Francisco earthquake, 20 years of interseismic deformation, 1970-1989, the 1989 Loma Prieta earthquake and post-seismic strain show that the southern Santa Cruz Mountains repeatedly rise and subside through the complex Bay Area deformation cycle. An additional deformation element that involves reverse slip averaging 2-3 mm/yr on the Foothills thrust system must occur to explain the longer-term uplift pattern in the Loma Prieta area since the re-initiation of deformation in the Late Pliocene. The asymmetry in deformation on opposite sides of the San Andreas reflects the contrasting rock types on opposite sides of the fault, the influence of preexisting structures, and the interaction with neighboring faults of the San Andreas system.

INTRODUCTION

Along strike-slip faults, the permanent deformation associated with restraining steps and bends is manifest in the development of folded and uplifted terrain (e.g., Crowell, 1974, Segall and Pollard, 1980, Bilham and King, 1989b, Bürgmann, 1991). The Santa Cruz Mountains in the San Francisco Bay area are closely associated with a left bend in the San Andreas fault (Fig. 4.1). Since the M_s 7.1 1989 Loma Prieta earthquake, attention has focused on the seismotectonics of this area and the relationship between the apparently youthful uplift and seismically active structures. Geodetic field observations, seismological data, the mapped fault-trace geometry, the topographic expression of deformation, and the structural geology of the area all reflect various aspects of the current and past deformation processes and history.

The northern Santa Cruz Mountains on the southwest side of the San Andreas are characterized by broad warping and folding, possibly related to advection of the range past the fault bend. Zones of more intense deformation are associated with the Zayante fault zone and other approximately NW-trending faults. Anderson (1990; and 1993, submitted to JGR) and Valensise and Ward (1991) proposed that repeated Loma Prieta-type events are responsible for much of the apparent uplift in this area. Their findings are based on comparisons of modeled coseismic uplift patterns during the earthquake with the elevations of raised marine terraces along the Pacific coast, the overall topographic expression of the mountain range, and the uplift and deformation of the 6-3 Ma Purísima formation (Valensise, 1993). Anderson and Menking (1993) find that oblique slip on the San Gregorio fault is required to explain a zone of uplifted terraces north of Santa Cruz.

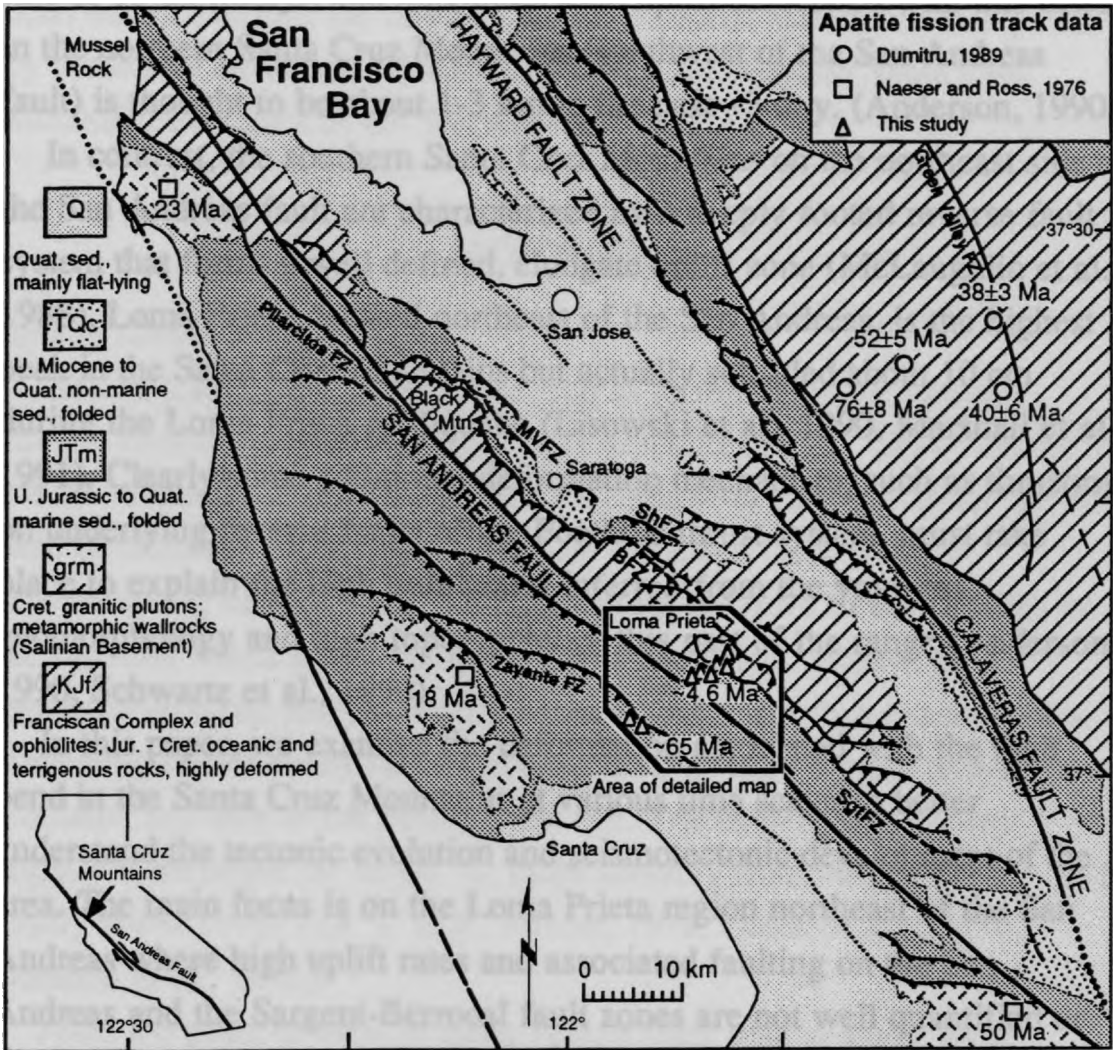


Fig. 4.1 Geologic and fault map of the San Francisco Bay area with existing and new fission track ages. Fault abbreviations: MVFZ, Monte Vista Fault Zone; ShFZ, Shannon Fault Zone; BFZ, Berrocal Fault Zone; SgtFZ, Sargent Fault Zone; the Foothills thrust belt consists of the MVFZ, the BFZ, and the ShFZ. Modified from Aydin and Page (1984).

Over the last 3 Ma, rock uplift rates were apparently as high as 0.5 mm/yr near the epicentral area southwest of the San Andreas (Valensise, 1993, Anderson, 1990). The Pacific plate moves northwestward relative to North America through the fault bend and its associated uplift zone at a rate of 10-20 mm/yr, and maximum total uplift associated with this bend in the northern Santa Cruz Mountains (southwest of the San Andreas fault) is thought to be about 1-3 km in the past ~3 m.y. (Anderson, 1990).

In contrast, the southern Santa Cruz Mountains on the northeast side of the San Andreas fault are characterized by a deeply rooted reverse fault system that forms a well defined, elongate uplift zone (McLaughlin et al., 1988). Loma Prieta, located northeast of the San Andreas, is the highest peak in the Santa Cruz Mountains but actually subsided about 10 cm during the Loma Prieta earthquake (Lisowski et al., 1990, Marshall et al., 1991). Clearly some additional deformation mechanism, such as thrusting on underlying reverse faults of the Foothills thrust system, must take place to explain the high uplift rates inferred from the youthful geomorphology and high topography of this part of the range (Anderson, 1990, Schwartz et al., 1990).

In this paper, we examine the deformation associated with the fault bend in the Santa Cruz Mountains at various time scales to better understand the tectonic evolution and seismotectonic development of the area. The main focus is on the Loma Prieta region northeast of the San Andreas where high uplift rates and associated faulting on the San Andreas and the Sargent-Berrocal fault zones are not well quantified or understood at present. We (1) evaluate apatite-fission-track data from exhumed rocks to determine the longer-term (Plio-Pleistocene) exhumation and uplift history; (2) analyze the structural geology of the area to estimate late Cenozoic fault displacements and to identify active structures causing uplift; (3) describe the topographic expression and associated geomorphic parameters to identify regions of high surface uplift rates and tectonic activity in the Quaternary; and (4) examine the historic neotectonic deformation related to fault slip and interseismic

strain in the area to investigate the individual elements of the current deformation cycle. The assessment of long-term, as well as short-term expressions of deformation along the San Andreas fault bend allows us to better understand the kinematic development of the San Andreas fault bend and to evaluate the importance and potential earthquake risk posed by secondary structures related to the uplifting southern Santa Cruz Mountains northeast of the San Andreas fault.

METHODS

Apatite fission-track dating

Fission tracks form in minerals such as apatite from the natural nuclear fission decay of dispersed trace amounts of ^{238}U . Decay occurs at a well-defined rate, so numbers of tracks and ^{238}U concentrations can be used to calculate fission track ages. Use of fission track data for reconstructing cooling, uplift, and unroofing histories of rocks relies on the fact that tracks are partially or entirely annealed (erased) by thermally-induced recrystallization at elevated subsurface temperatures. Annealing causes easily measured reductions in track lengths and apparent numbers, and thus in the fission track age. Tracks in apatite anneal slightly from about 20° to 60 °C, more severely from ≈ 60 to 125 °C, and totally above about 125 °C (e.g., Naeser, 1979, Green et al., 1989b, Dumitru et al., 1991).

From the point of view of using fission track data to study latest Cenozoic uplift along the San Andreas, three interpretive approaches may be applicable (Fig. 4.2). If samples have resided in the total annealing zone ($>\approx 110$ -135 °C), all tracks existing before uplift and unroofing are totally erased. Tracks begin to accumulate during uplift, unroofing, and resulting cooling, and ages of these samples will generally date the time of cooling below about 105-115 °C. Assuming geothermal gradients of about 30-35 °C/km (discussed below) this dates unroofing (exhumation) up through about the 3 km depth level. For samples that yield latest Cenozoic

ages, the number of tracks is small and useful track length data can seldom be collected.

In samples that resided in the partial annealing zone ($\approx 60-115$ °C) before uplift and unroofing, fission tracks will be partially annealed and fission track ages will be only partially reset. The sample fission track age will therefore generally be much older than the time of uplift and will be a mixed (partially reset) age that does not directly date a specific geologic event. However, in this case large numbers of tracks are generally present so useful track length data can be collected. These data allow estimation of the paleotemperatures and paleodepths of the samples before uplift, and thus the magnitudes of uplift and unroofing (e.g., Green et al., 1989b, Dumitru et al., 1991). Often it is possible to extrapolate the time of uplift from adjacent, totally annealed samples and conclude that the partially annealed samples were at slightly shallower depths (slightly lower temperatures) before the uplift.

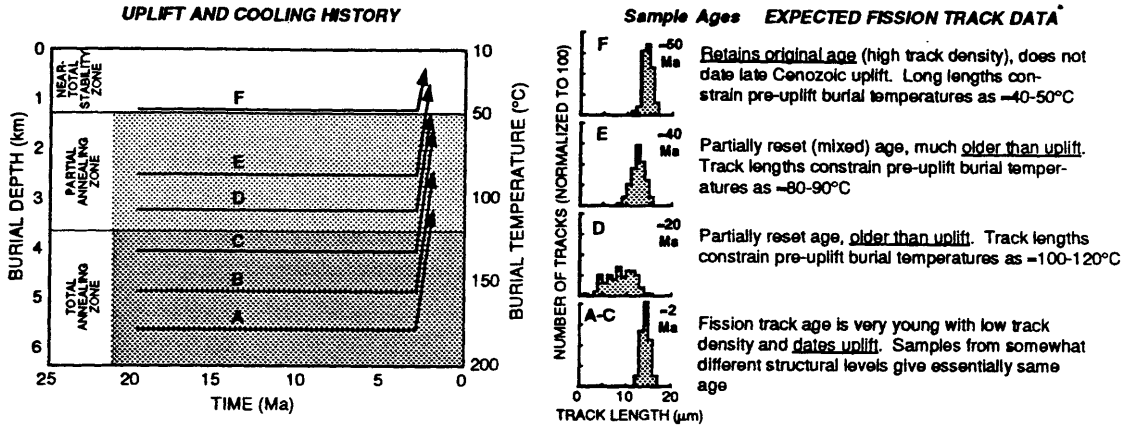


Fig. 4.2 Schematic illustration of fission track data patterns expected from latest Cenozoic uplift along the San Andreas. Samples that formerly resided in the total annealing zone (A-C) will give ages that date their time of cooling below about 110°C. Samples that resided in the partial annealing zone will yield older, mixed (partially reset ages) that do not directly date a cooling event. Track length data from these samples allow estimation of paleoburial temperatures and thus paleodepths before uplift.

A third approach relies on the fact that the thermal structure of the crust is subhorizontal, with temperature increasing with depth. This imposes a set of depth-varying fission track parameters on rocks in the upper 4 km or so of the crust. Samples below 3.5 km will have zero ages, with ages and track lengths increasing toward the surface. Such a layered paleothermal structure can serve as a crude stratigraphy for revealing later deformation of the crust by faulting or folding. Discontinuities in fission track age and length data then may reveal major fault offsets that may not be well constrained from other data (e.g., Dumitru et al., 1991).

It is important not to overstate the resolution of apatite fission track techniques as applied to studies of very recent uplift. Apatite uplift ages as young as those reported here are unusual and have previously been reported only in a few areas along parts of the Himalayas (e.g., Zeitler, 1985), the Alpine fault (e.g., Kamp et al., 1989, Kamp et al., 1993), the Papuan fold belt (Hill and Gleadow, 1989), the Denali massif (Fitzgerald et al., 1993), and other local areas along the San Andreas (White, 1991, Dumitru, 1991). Relative precisions of ages are a function of the number of tracks counted (Green, 1981) and with young ages, few tracks are present. Therefore uncertainties are often large as is illustrated by the one sigma uncertainties of $\pm 15\text{-}60\%$ for individual samples in this study. By pooling data from multiple samples, we can reduce these uncertainties to $\pm 10\text{-}20\%$. When uncertainties in ages, annealing temperatures (probably about $\pm 10^\circ\text{C}$), and geothermal gradients are taken into account, estimates of uplift amounts and rates probably have $\pm 1\sigma$ uncertainties on the general order of $\pm 25\text{-}35\%$.

In order to calculate amounts of unroofing from fission track data, it is necessary to estimate the geothermal gradient. Lachenbruch and Sass (1980) compiled heat flow data from the California Coast Ranges. In the San Francisco Bay area, the mean heat flow is 86 mW m^{-2} with a narrow standard deviation of the determinations of $\pm 10\%$. Lachenbruch and Sass (1980) developed a model for heat flow along the San Andreas that suggests that similar heat flows apply since soon after passage of the

Mendocino triple junction, which may have occurred about 18 Ma at the reconstructed latitude of the Sierra Azul block (based on stratigraphic evidence see McLaughlin and Clark, 1993). The geothermal gradient is expected to change through time in response to regional tectonism.

However, we do not address temporal heat flow changes due to crustal thickening and other factors. Using a nominal rock thermal conductivity of $2.5 \text{ W m}^{-1} \text{ }^{\circ}\text{C}^{-1}$, this suggests that a thermal gradient of around 30-35 $^{\circ}\text{C}/\text{km}$ is appropriate for interpreting the fission track data in this study (e.g., Dumitru, 1989). Lachenbruch and Sass (1980, p. 6195-6198) also concluded that frictional heating and fluid-mediated heat transfer were minimal along the San Andreas fault system.

Geomorphic analysis

Detailed evaluation of topography, drainage patterns, and other geomorphic features can identify areas of rapid uplift in the Quaternary (e.g., Schumm, 1986, Keller, 1986, Merritts and Vincent, 1989).

However, quantitative determination of uplift rates from geomorphic analysis is generally not possible. Here, we use geomorphic analysis to define qualitatively zones of strong neotectonic activity.

Localized surface uplift (or base-level lowering) increases the stream gradient and thus the ability of a stream to erode. The principal effect of uplift on the geomorphic expression of an area is to increase the slope of streams, increase channel erosion rates, and thus increase the relief of drainage basins relative to the surrounding ridge crests (e.g., Merritts and Vincent, 1989). In addition, warping or tilting of a region will tend to increase drainage slopes away from the zone of highest uplift. Locally, the interaction of streams with earthquake fault scarps or actively deforming folds may lead to the development of offsets, knickpoints, and stream-gradient modifications.

Large, higher-order streams often have sufficient stream power to adjust their gradient to base-level changes and will effectively propagate the effects of base-level lowering upstream (Merritts and Vincent, 1989).

Lower-order streams, however, may lack sufficient power to diminish the increased gradient. Therefore, stream-gradient increases are commonly most pronounced among second and first-order streams. However, if an area with lower-order streams is uplifted as a crustal block without significant tilting, slope increases may occur only near the margins of the block, because the streams lack sufficient time or power to propagate the base-level change into the area. Drainage slopes of equilibrated streams (no tectonic effects) increase with distance from base-level. Methods used to normalize stream gradients to remove this effect will be discussed and applied in a separate paper. In this paper, stream slopes are described in the form of a contoured surface of stream bottom elevations (see below).

High stream erosion increases the difference between the stream incision rate and the concurrent erosion rate of adjacent ridge crests, leading to higher relief of the drainage basin. Therefore, areas of high relief may indicate tectonically active zones of high uplift rates and stream downcutting. Topographic residual maps display the incision of drainages into the surrounding landscape and may be constructed by subtracting the contoured elevations of drainage bottoms (subenvelope map) from the elevations of the surrounding ridge crests (envelope map; Stearns, 1967, Bullard and Lettis, 1993). Stream incision depends on tectonic activity, bedrock lithology, bedding attitude, base level, vegetation cover, and climate. If all factors but tectonic uplift are accounted for, or can be assumed constant over the area, the residual map reflects the relative magnitude of stream downcutting in response to uplift.

An envelope map can be envisioned as the contoured topography of the elevated terrain reduced by ridge-crest erosion only. It is therefore thought to reflect more accurately the total uplift pattern that would be observed if no erosion had occurred. However, the exposure of rocks at the surface that were buried several kilometers indicates that the envelope surface can not be directly correlated with the total uplift distribution. The subenvelope-map elevations are, by definition, strongly influenced by

the effectiveness of fluvial erosion in the drainage system. The slope of the subenvelope surface corresponds to the slope of individual drainages. As in the case of individual river profiles, the subenvelope slopes correlate naturally with elevation and are affected by various other parameters. The tectonic component may therefore be difficult to separate from the remaining factors.

Geodetic analysis

We use 20 years of trilateration measurements and more recent Global Positioning System (GPS) and Very Long Baseline Interferometry (VLBI) high precision measurements of the relative and absolute locations of benchmarks to determine the horizontal and vertical displacement and velocity fields in the San Francisco Bay area. The details of this analysis are presented in Bürgmann and others, (1993, and Chapter 5 this thesis).

We utilize boundary element models of faults idealized as rectangular surfaces of displacement discontinuity in an elastic, isotropic, and homogeneous halfspace (Erickson, 1987) to calculate the horizontal and vertical surface displacements associated with historic earthquakes and interseismic strain accumulation from geodetic measurements. This approach is similar to elastic models of strike-slip related deformation presented by other authors (Rodgers, 1980, Segall and Pollard, 1980, Bilham and King, 1989b), but extends the analysis into the third dimension. This allows us to model buried fault planes, faults that slip only to certain depths, and dipping faults with reverse-slip components. The models do not account for isostatic compensation or inelastic deformation processes.

TECTONICS OF THE SANTA CRUZ MOUNTAINS

A record of the late Cenozoic deformation in the San Francisco Bay area exists in the structural geology of the area, and the distribution, provenance, stratigraphy, and deformation of Late Pliocene through Quaternary marine and non-marine sediments.

The latest contractional tectonic event involving the southern Santa Cruz Mountains apparently began several million years ago (Page and Engebretson, 1984), and was related to a change in relative plate motion at the Pacific - North American plate boundary approximately 3.5 Ma (Harbert and Cox, 1989). The plate-motion change resulted in contraction of about 2-7 mm/yr across the San Andreas fault system that resulted in renewed uplift of the central California Coast Ranges (Page, 1990, Montgomery, 1993). Rock uplift along the Coast Ranges since the Late Pliocene averages about 300 to 1000 m assuming erosion rates of ~0.1 mm/yr (Christensen, 1965, Montgomery, 1993). In the San Francisco Bay area, the changing plate motion vector appears to have led to (1) transfer of slip from the Pilarcitos fault to the currently active trace of the San Andreas fault on the northern San Francisco Peninsula; (2) increased slip along the East Bay strike-slip system (initiation of slip on Calaveras fault); and (3) the activation of reverse faults oriented subparallel to the San Andreas and the rise of the ancestral Santa Cruz Mountains (Page, 1990; Fig. 4.1).

Late Cenozoic slip on the newly formed San Andreas fault is estimated at 25-30 km based on the offsets of (1) the Corte Madera facies of the Santa Clara formation (Cummings, 1968); (2) the Franciscan Calero limestone (Page, 1990); and (3) the correlative late Pliocene marine units found at Mussel Rock and north of Black Mountain (Addicott, 1969).

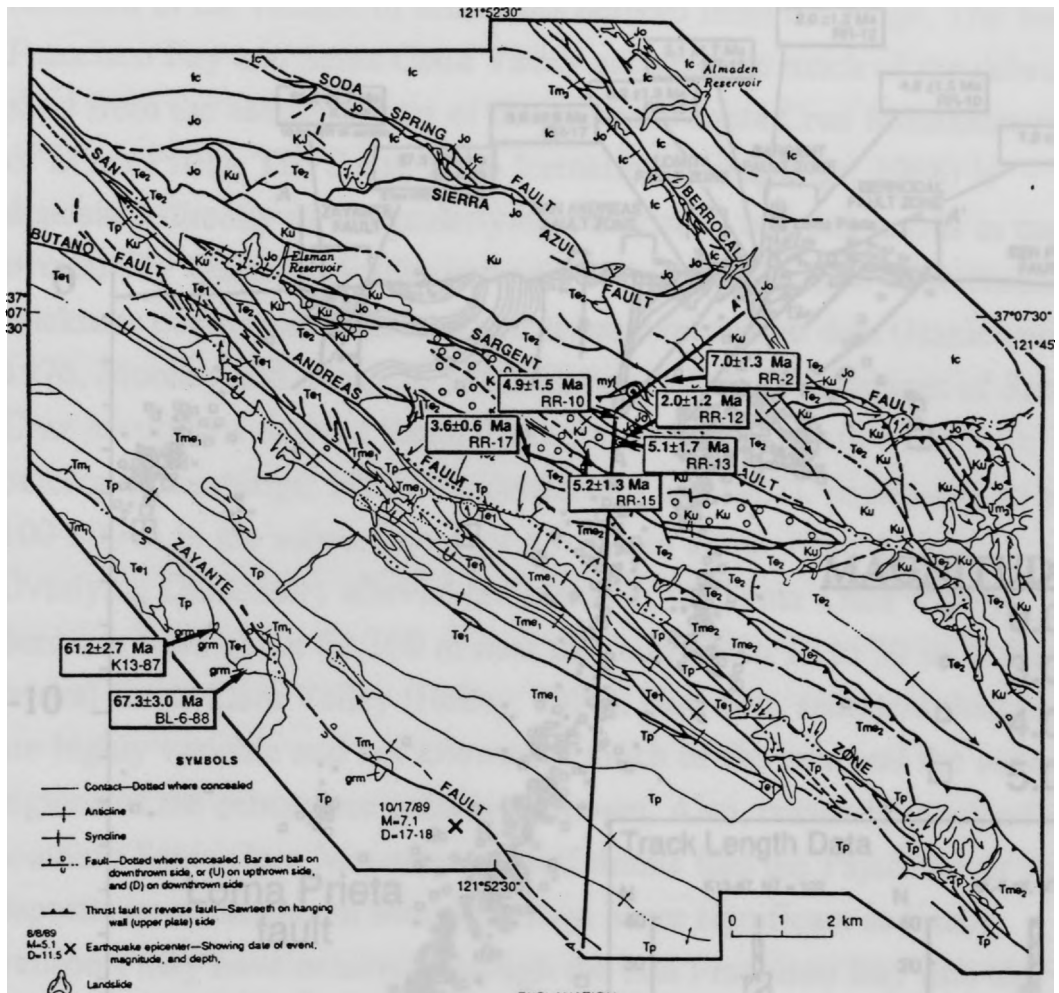
Northeast of the San Andreas fault, several fault-bounded blocks contain Jurassic to Eocene(?) rocks of the Franciscan Complex, Coast Range ophiolite, and Great Valley forearc basin overlain by Miocene to Pleistocene marine and non-marine deposits (Fig. 4.3). The tectonic events of the last 3 Ma follow a complex history of deformation, with

earliest activity on the major faults in the southern Santa Cruz Mountains possibly related to the passage of the Mendocino triple junction. McLaughlin and Clark (1990) suggest that the rocks in the southern Santa Cruz Mountains were juxtaposed with the triple-junction at their restored latitude as early as 18 Ma which agrees with 17 Ma ages of hydrothermal mineralizations in the Sargent fault zone. The age of the Page Mill basalt to the NE of the San Andreas puts the passage of the triple junction at about 15 Ma (e.g., Stanley, 1987). Because of this evidence of pre-3 Ma contractional tectonism in the area, it is difficult to quantify the amount of deformation in the late Cenozoic based on structural data only.

The uplift of the ancestral mountains in the area may have begun in the middle Miocene, as indicated by ~12 Ma eastward shedding of the Orinda formation fluvial clastic wedge from the site of the present San Francisco Bay (Graham et al., 1984). However, the formation of the present southern Santa Cruz Mountains range as a topographic high appears to have begun in the (Late?) Pliocene; bracketed by the youngest preserved marine cover sediments (Miocene Margaritan molluscan stage of ~10 Ma) and the oldest fluvial sediments shed from the range (Pliocene and Pleistocene synorogenic Santa Clara Formation; Cummings, 1968, Sorg and McLaughlin, 1975, Adam et al., 1982). This event coincides with the onset of uplift southwest of the San Andreas fault marked by the end of marine conditions (shallow marine Purisima and Merced formations) in the Late Pliocene (Addicott, 1969, Clark, 1981, Madrid et al., 1986, Gavigan, 1984, Valensise, 1993).

The age, distribution, and provenance of the non-marine Santa Clara formation presents additional constraints on the timing of uplift. Cummings, (1968) recognized eight lithofacies on the San Francisco Peninsula that reveal different depositional environments and source material. The (Late?) Pliocene, braided-stream Arastradero facies that outcrops between Saratoga and Black Mountain is primarily derived from sources to the east and south with a possible minor contribution from source rocks near Loma Prieta (Vanderhurst et al., 1982). The

Arastradero unit grades laterally into the Los Gatos facies south of Saratoga (Fig. 4.1) that is derived from the southern Santa Cruz Mountains near the head waters of Los Gatos Creek (Cummings, 1968). Overlying the Arastradero facies is the early Pleistocene Stevens Creek unit that is clearly derived from the Franciscan rocks to the west, marking the initiation of Neogene uplift of the Monte Bello ridge near Black Mountain (Vanderhurst et al., 1982). Between the Pilarcitos and San Andreas faults, conglomerates that are strikingly similar to the Los Gatos facies near Loma Prieta, overlay the Purisima formation and indicate that about 28 km of offset occurred along the San Andreas fault since deposition ~3-1 Ma (Cummings, 1968).



SOUTHWEST OF THE SAN ANDREAS FAULT ZONE

- TP** Purissima Formation (Pliocene)—Marine sandstone and siltstone.
- Tm₁** (Upper and Middle Miocene)—Marine sandstone, siltstone, shale and mudstone.
- Tme₁** (Lower Miocene, Oligocene, and Upper Eocene)—Marine sandstone, siltstone and shale.
- Te₁** (Upper and Lower Eocene)—Marine sandstone, shale, and conglomerate.
- gm** (Pre-Tertiary)—Granitic and metamorphic rocks (Salinian Basement).

NORTHEAST OF THE SAN ANDREAS FAULT ZONE

- Tme₂** (Lower Miocene, Oligocene, and Upper to Lower Eocene)—Marine siliceous to carbonaceous shale and quartzfeldspathic sandstone.
- Te₂** (Middle to Lower Eocene)—Marine quartzfeldspathic sandstone, siltstone, shale and mudstone.
- Ku** (Upper Cretaceous-Campanian)—Marine sandstone, siltstone and shale.
- KJ** (Lower Cretaceous to Upper Jurassic)—Marine shale, and minor sandstone, conglomerate and tuff.
- Jo** (Upper and Middle Jurassic)—Ultramafic and mafic rocks of Coast Range Ophiolite.

- M₁** (Mesozoic?)—Mylonitic rocks of Sargent thrust zone on Loma Prieta.
- Tm₃** (Lower and Middle Miocene)—Marine sandstone and siliceous shale.
- lc** (Pre-Tertiary)—Central belt of the Franciscan Complex.

Fig. 4.3 Apatite fission track ages shown on geologic map and cross-section of the Loma Prieta area (base map from (McLaughlin, 1990)). (a) The two samples near the Zayante fault indicate possible 2-3 km total exhumation in the last 10 Ma near the epicenter and the zone of highest uplift of the Loma Prieta earthquake. The remaining samples, with young ages indicating high uplift rates, are located near the zone of greatest subsidence during the earthquake.

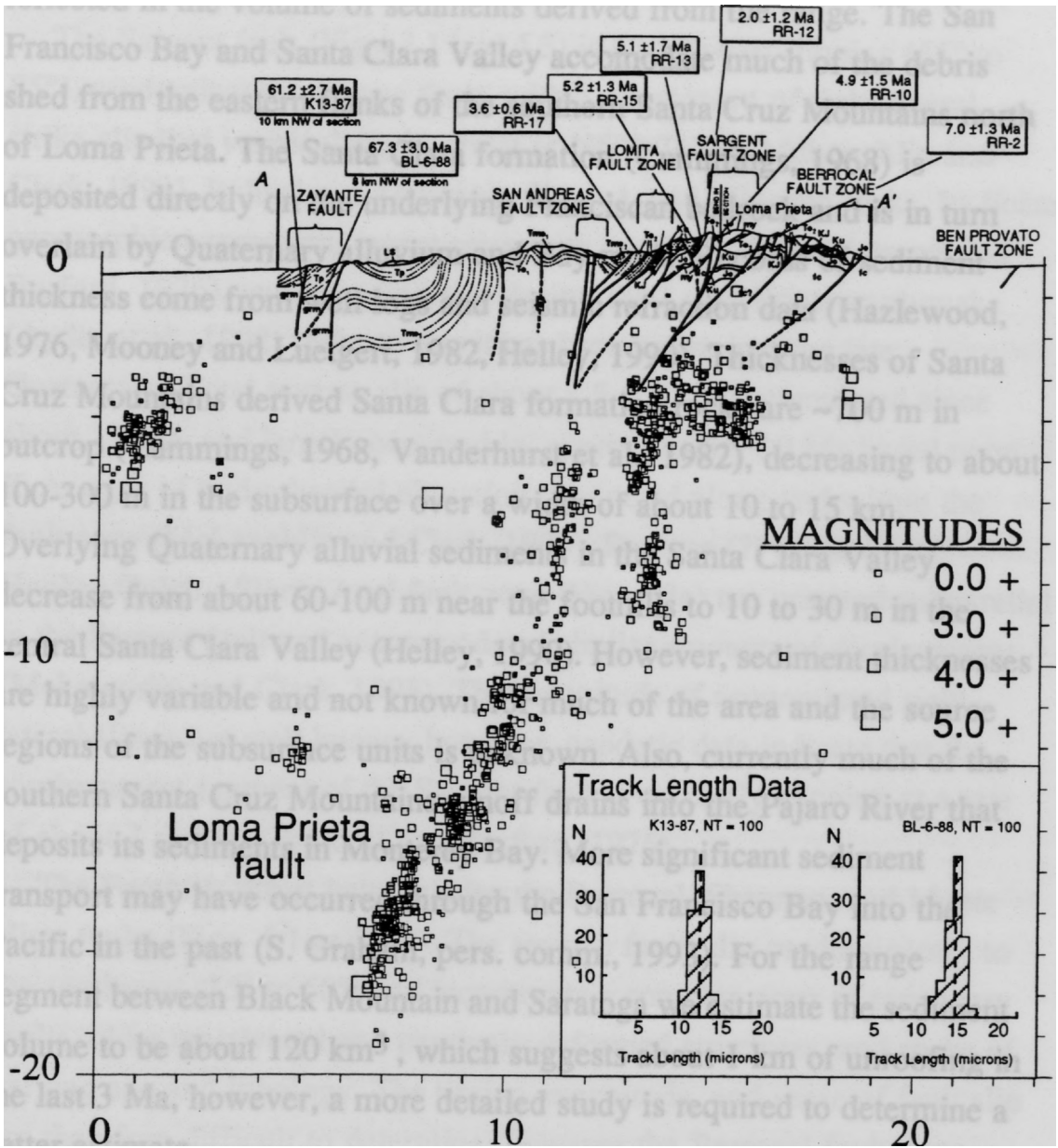


Fig. 4.3 cont. (b) The cross-section shows the fault geometry inferred from geologic mapping (McLaughlin et al., 1988) together with the aftershocks over 3 years following the Loma Prieta earthquake. Seismicity near the Berrocal fault zone has been at a heightened level since the earthquake and may indicate a rapidly deforming region.

The amount of unroofing from the rising mountains should be reflected in the volume of sediments derived from the range. The San Francisco Bay and Santa Clara Valley accommodate much of the debris shed from the eastern flanks of the southern Santa Cruz Mountains north of Loma Prieta. The Santa Clara formation (Cummings, 1968) is deposited directly on the underlying Franciscan bedrock and is in turn overlain by Quaternary alluvium and Bay muds. Records of sediment thickness come from well logs and seismic refraction data (Hazlewood, 1976, Mooney and Luetgert, 1982, Helley, 1990). Thicknesses of Santa Cruz Mountains derived Santa Clara formation rocks are ~700 m in outcrop (Cummings, 1968, Vanderhurst et al., 1982), decreasing to about 100-300 m in the subsurface over a width of about 10 to 15 km. Overlying Quaternary alluvial sediments in the Santa Clara Valley decrease from about 60-100 m near the foothills to 10 to 30 m in the central Santa Clara Valley (Helley, 1990). However, sediment thicknesses are highly variable and not known for much of the area and the source regions of the subsurface units is unknown. Also, currently much of the southern Santa Cruz Mountains runoff drains into the Pajaro River that deposits its sediments in Monterey Bay. More significant sediment transport may have occurred through the San Francisco Bay into the Pacific in the past (S. Graham, pers. comm., 1993). For the range segment between Black Mountain and Saratoga we estimate the sediment volume to be about 120 km^3 , which suggests about 1 km of unroofing in the last 3 Ma, however, a more detailed study is required to determine a better estimate.

We will briefly discuss the individual block-bounding faults to the northeast of the San Andreas fault based on geologic (McLaughlin and Clark, 1993), aeromagnetic, gravity, (Jachens and Griscom, 1993, in press), and seismological information. McLaughlin and Clark (1993) estimate that about 6 km of uplift occurred across the southern Santa Cruz Mountains northeast of the San Andreas fault since the Miocene (possibly mostly since about 3 Ma). Uplift is related to slip on northeast-vergent

(oblique-) reverse faults, most of which have clearly been active into late Pleistocene and possibly Recent times.

The Sargent fault (Figs. 4.1 and 4.3) is a southwest-dipping (55° to 85°), predominantly reverse fault, with a component of right-lateral strike-slip that varies along its strike of $N60^\circ$ - 74° W (McLaughlin and Clark, 1993). It displaces Mesozoic, Eocene, and Miocene rocks. Its linear geomorphic expression, recent seismicity and fault creep (Prescott and Burford, 1976), and triggered slip during the Loma Prieta earthquake (Aydin et al., 1992) indicate that it has been active into the late Quaternary. Total reverse slip of about 1.5-1.8 km accumulated since about 18 Ma, and largely occurred by approximately 10 Ma based upon K-Ar ages of hydrothermal alteration channeled along and within the fault zone (McLaughlin and Clark, 1993). Reverse (?) faults of the Hooker Gulch - Sierra Azul fault zone (Fig. 4.3a) are oriented subparallel to the Sargent fault and accommodated similar amounts of displacement (McLaughlin and Clark, 1993). The magnitude of accumulated right-lateral slip is not well known; however, geodetic data indicate that the southernmost segment of the Sargent fault is currently slipping at a rate of about 3 mm/yr (Prescott and Burford, 1976).

The Foothills thrust belt includes the Berrocal, Shannon, and Monte Vista faults (Figs. 4.1 and 4.3). The reverse faults dip predominantly to the southwest (35° to 60°) and incorporate a complex zone of secondary faults, older reactivated and passively deformed structures, and rocks of varying age and lithology. The timing, magnitude, and sense of fault slip are therefore difficult to determine; however the Berrocal fault zone exhibits evidence for major displacements since the Miocene (≈ 10 Ma). Structural relations and gravity data suggest that up to 4.2 km of reverse slip have been accommodated across the thrust belt (Fig. 4.3), leading to 3 km of uplift since as long ago as 10 Ma, but more likely within the last 3 m.y (McLaughlin and Clark, 1993).

The Berrocal, Shannon, and Monte Vista faults offset and deform the Plio-Pleistocene Santa Clara formation that was derived, in part, from the

actively rising Santa Cruz Mountains (Page, 1992). A major pulse of faulting may have occurred along the entire Foothills thrust belt in the late Pleistocene (500-120 ka; McLaughlin and Clark, 1993). Several of the faults exposed at the surface appear to have been inactive in the Holocene based upon evidence of colluvial draping of Pleistocene fault scarps. However, the Shannon fault offsets a latest Pleistocene paleosol by (12 to 20 ka; McLaughlin and Clark, 1993) and the whole thrust belt displays relatively clear evidence of Quaternary displacements (McLaughlin and Clark, 1993). Many of the thrust faults deform Miocene to Pleistocene hanging wall rocks into open to tight folds whose axes trend parallel to the thrusts. These thrust faults may propagate from depth as blind thrusts that ultimately breach the folds and therefore estimates of fault slip and timing based on offset markers may be minimum estimates of the shortening in the area and provide maximum ages for deformation.

Oblique contraction across the southern Santa Cruz Mountains since 18 Ma has generated about 5 km of cumulative shortening, 6 km of cumulative uplift, and as much as 7.8 km of cumulative reverse slip across faults between the San Andreas fault and the Foothills thrust belt (McLaughlin and Clark, 1993). The shortening is accommodated by 1) exposed faults of the Foothills thrust belt; 2) blind thrusts rooting into the thrust zone and the San Andreas fault; 3) folds above the blind thrusts; 4) and deeper blind thrusts possibly accommodating the more broadly distributed northeast-southwest shortening of the Coast Ranges (Page, 1992, McLaughlin and Clark, 1993). Because of the unknown amount of strike-slip deformation within the thrust belt and the difficulty of estimating the Late Cenozoic displacements based on structural data, additional information in the form of apatite fission track data become especially useful.

Following the Loma Prieta earthquake, northeast-southwest shortening of curbs and sidewalks was observed along the Monte Vista and Berrocal-Shannon thrust zones (Haugerud and Ellen, 1990). Parts of these fault zones have been seismically active in recent years (McEvelly, 1966, Bakun

and McLaren, 1984, Kovach and Beroza, 1993) and experienced increased seismicity (Reasenberg and Simpson, 1992), and possibly accelerated aseismic creep at depth (Bürgmann et al., 1992, Bürgmann et al., 1993, and Chapter 5 this thesis), in the aftermath of the Loma Prieta earthquake.

RESULTS

Fission track dating

Six fission-track samples were collected from various sedimentary units in a 6-km transect on the northeast side of the San Andreas fault across the Loma Prieta area (Fig. 4.3). They yielded statistically concordant ages with a weighted mean age of 4.6 ± 0.5 Ma (Fig. 4.3, Table 4.1). As mentioned previously, apatite uplift ages this young are unusual and have previously been reported only in areas of intense tectonic activity. Allowing for the uncertainties in the individual sample ages, there is no evidence of an age discontinuity across the Sargent fault zone or a gradient in ages along the transect (Table 4.1). These data are the initial results from a larger fission track survey of the Santa Cruz Mountains region.

The apatite ages date the passage of samples through the ≈ 110 °C isotherm, probably during an early stage in the uplift of the southern Santa Cruz Mountains. Continued uplift and erosion of overlying rocks brought the rocks to the surface where they are exposed today at elevations of about 1000 m. The fission track ages constrain exhumation rates and, if surface uplift rates are known, can be used to estimate rock uplift rates (England and Molnar, 1990). Assuming a geothermal gradient of 30 to 35°C/km (Lachenbruch and Sass, 1980), the rocks were buried at depths of about 3.5-4 km, ≈ 4.6 m.y. ago. The exhumation rate was therefore approximately 0.8 mm/yr. The topographic expression of the southern Santa Cruz Mountains developed since about 3-1 Ma (Vanderhurst et al., 1982), therefore rock uplift rates may be $\sim 20\%$

higher than exhumation rates. It is important to emphasize that this is a rate averaged from 4.6 Ma to the present and the current fission-track data cannot resolve temporal variation in the uplift rate over this period.

The rock uplift rate represents the cumulative uplift associated with slip along all of the reverse faults in the Foothills thrust belt, since the sampling area is structurally high in the uppermost hanging wall (Fig. 4.3b). The lack of a detectable age discontinuity across the Sargent fault does not imply that there has been minimal dip-slip offset across the fault in the last 4.6 m.y. Rather, samples on both sides of the fault were uplifted from within the total annealing zone (e.g., juxtaposition of sample A against sample C in Fig. 4.2). Further sampling along strike northwest and southeast of the Loma Prieta area may reveal discontinuities in data across the Sargent fault as shallower structural levels are sampled.

We also analyzed two samples of Salinian granodiorite emplaced 91-103 Ma (James, 1992) from near the Zayante fault southwest of the San Andreas (Fig. 4.3; Table 4.1). They have 61 and 67 Ma apatite ages and narrow, unimodal track length distributions with significantly shortened mean track lengths of 12.5 and 12.2 μm . Very few tracks longer than 14 μm are present. These data indicate that these samples have not experienced temperatures hotter than about 90-100°C at any time in the mid or late Cenozoic (to permit the old ages), and experienced burial temperatures of about 70-90°C sometime within the last 10 m.y. to shorten virtually all the tracks (c.f., Green et al., 1989a, Green et al., 1989b, Dumitru, 1988). This may suggest that about 2-3 km of unroofing has occurred sometime within the last 10 m.y.

Sample	Rho-S tracks/cm ²	NS	Rho-I tracks/cm ²	NI	Rho-D tracks/cm ²	ND	NG	P(χ^2)	Pooled Age (Ma, $\pm 1\sigma$)	Mean Length (μm , $\pm 1\sigma$)	S.D. (μm)	NT
NORTHEAST OF SAN ANDREAS												
RR-2	3.255E+04	30	1.439E+06	1326	1.595E+06	3634	25	44.7%	7.0 \pm 1.3			0
RR-10	3.747E+04	10	2.337E+06	686	1.583E+06	3634	11	20.4%	4.9 \pm 1.5			0
RR-12	1.297E+04	3	1.975E+06	457	1.580E+06	3634	7	94.1%	2.0 \pm 1.2			0
RR-13	9.920E+03	10	0.592E+06	597	1.577E+06	3634	25	63.2%	5.1 \pm 1.7			0
RR-15	1.107E+05	17	6.413E+06	985	1.574E+06	3634	4	32.3%	5.2 \pm 1.3			0
RR-17	4.986E+04	30	4.203E+06	2529	1.568E+06	3634	20	15.9%	3.6 \pm 0.6			0
Pooled*	3.115E+04	100	2.050E+06	6580	1.580E+06	3634	92	10.3%	4.6 \pm 0.5			0
SOUTHWEST OF SAN ANDREAS												
BL-6-88	3.156E+06	1037	1.406E+07	4620	1.562E+06	3634	20	13.5%	67.3 \pm 3.0	12.200 \pm 0.100	1.000	100
K13-87	1.168E+06	1106	5.709E+06	5406	1.559E+06	3634	19	6.3%	61.2 \pm 2.7	12.478 \pm 0.099	0.995	100

Sample, sample number; Rho-S, spontaneous track density; NS, number of spontaneous tracks counted; Rho-I, induced track density; NI, number of induced tracks counted; Rho-D, track density in CN5 neutron dosimetry glass; ND, number of tracks counted in determining Rho-D; NG, number of grains dated; P(χ^2) chi-square probability (Galbraith, 1988); Pooled Age, pooled fission track age (Green, 1981) calculated using a zeta calibration factor (Hurford and Green, 1983) of 385.9 \pm 6.9 for CN5 glass; Mean Length, mean fission track length with one standard error of the mean (the samples from NE of the San Andreas are too young to allow significant track length analysis); S.D., standard deviation of the track length distribution; NT, number of track lengths measured.

All uncertainties quoted at the one standard error level. Data reduction done with program by Paul Green (slightly modified). Analyst: Trevor Dumitru.

* Pooled track counts of all six samples on the northeast side of the San Andreas.

TABLE 4.1: Fission-track counting, age, and track length data.

Naeser and Ross (1976) reported apatite ages of 18 Ma and 23 Ma from the Cretaceous Ben Lomond and Montara granites in the northern Santa Cruz Mountains (Fig. 4.1), indicating that late Cenozoic uplift magnitudes were insufficient to exhume rocks with young ages. Track length data were not collected. Possible explanations for these ages include a thermal pulse related to Miocene volcanic activity (Naeser, 1976), an uplift event that initiated in the Miocene, or incomplete resetting of the ages in the partial annealing zone such that the ages are mixed ages that predate a post-20 Ma exhumation event.

The Salinian basement on the San Francisco Peninsula is overlain by Paleocene to Pliocene sedimentary rocks with a composite thickness of more than 10000m (Clark & Brabb, 1978). Repeated uplift and subsidence events throughout the Tertiary are recorded in the sedimentary record. Our results indicate that in the vicinity of our sample sites near the Olive Springs quarry, burial was not more than 2-3 km since the Late Cretaceous. A more detailed description could be derived from more detailed sedimentological and fission track studies in the northern Santa Cruz Mountains.

Geomorphic analysis

We undertook a tectonic geomorphologic analysis to extend our results from the fission-track transect across Loma Prieta to a larger part of the southern Santa Cruz Mountains and to examine the distribution of Quaternary uplift. We constructed drainage-network maps and contour maps of drainage elevations and relief. The geomorphic data do not independently constrain uplift rates, but allow us to outline high-uplift zones on the San Francisco Peninsula. A more detailed quantitative analysis of the geomorphology of the southern Santa Cruz Mountains will be presented elsewhere.

The tectonically controlled slope and relief patterns help outline high-uplift zones; however, care must be taken to distinguish tectonic effects from variations in other parameters such as the local precipitation rates,

vegetation cover, and rock types in a given area. As we do not quantify such variations in this analysis, these parameters may mask the effects of tectonic uplift. For instance, drainage slopes and overall topography in the northern Santa Cruz Mountains are clearly strongly influenced by rock type where the Salinian Montara and Ben Lomond granitic bodies are exposed. Further, precipitation drops drastically from west to east with an accompanying change in vegetation cover. Depending on climate, rock type, and vegetation cover, land sliding, downslope creep, or fluvial erosion may be the dominant degrading mechanisms (e.g., Anderson, 1993).

The drainage network map (Fig. 4.4) shows that the drainage divide between the Pacific Ocean and San Francisco Bay runs sub-parallel to and a few kilometers west of the San Andreas fault north of the intersection of the San Andreas with the Sargent fault zone. Further to the southeast, streams originating in the southern Santa Cruz Mountains drain southwest to the Pacific, north to San Francisco Bay, or southeast to the Pajaro River basin that then flows into the Pacific. The map shows that some streams tend to follow major fault traces that may form easily erodable pathways for drainages and that juxtaposed topography along active faults may deflect and dam drainages.

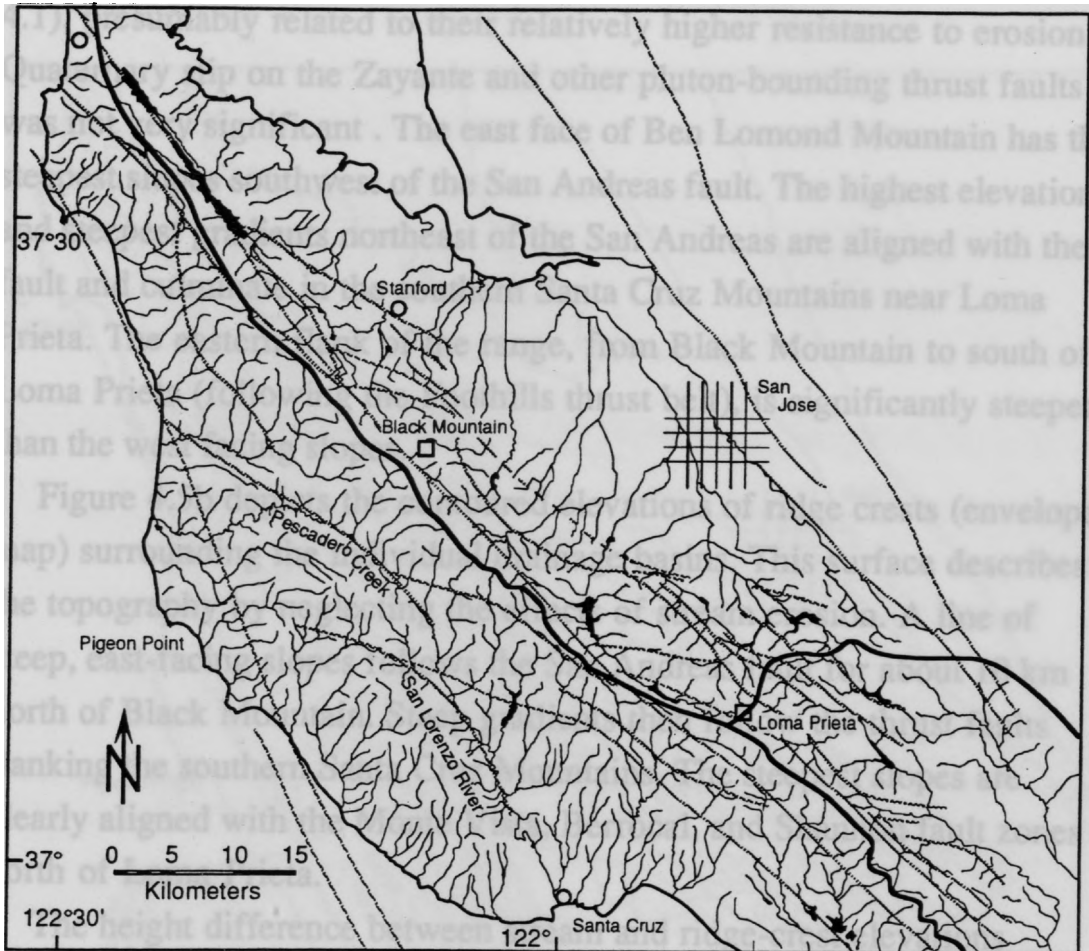


Fig. 4.4 Drainage network map of the San Francisco Peninsula digitized from 1:125,000 scale topographic map. Thicker black lines follow the drainage divides between the Pacific Ocean, San Francisco Bay, and Pajaro River basin southeast of Loma Prieta. Drainage patterns are structurally controlled and streams are commonly affected where they cross major faults. Light gray lines are major faults from Aydin and Page (1984).

The subenvelope map (contoured elevations of stream bottoms; Fig. 4.5a) summarizes information about the distribution and shape of source areas and the slope of drainages. Local highs southwest of the San Andreas are associated with the Ben Lomond and Montara plutons (Fig. 4.1), presumably related to their relatively higher resistance to erosion. Quaternary slip on the Zayante and other pluton-bounding thrust faults was not very significant. The east face of Ben Lomond Mountain has the steepest slopes southwest of the San Andreas fault. The highest elevations and steepest gradients northeast of the San Andreas are aligned with the fault and culminate in the southern Santa Cruz Mountains near Loma Prieta. The eastern flank of the range, from Black Mountain to south of Loma Prieta (following the Foothills thrust belt), is significantly steeper than the west facing slopes.

Figure 4.5b depicts the contoured elevations of ridge crests (envelope map) surrounding the individual drainage basins. This surface describes the topography by neglecting the effects of stream erosion. A line of steep, east-facing slopes follows the San Andreas fault for about 10 km north of Black Mountain. Steep gradients then follow the thrust faults flanking the southern Santa Cruz Mountains. The steepest slopes are clearly aligned with the Monte Vista, Berrocal, and Shannon fault zones north of Loma Prieta.

The height difference between stream and ridge-crest elevations defines local relief which can be analyzed in the form of contoured topographic residual maps (Fig. 4.6). Regional residual maps allow the identification of zones of high stream incision rates that may delineate high uplift-rate zones. Relief highs are associated with the two largest basins of the northern Santa Cruz Mountains (Pescadero and San Lorenzo rivers) because we did not include crests surrounding their relatively large sub basins (Fig. 4.4). High local relief occurs along an elongate zone aligned with the Berrocal fault zone north of Loma Prieta. Geomorphic analyses indicate that the southern Santa Cruz Mountains form a zone of relatively rapid in the Quaternary.

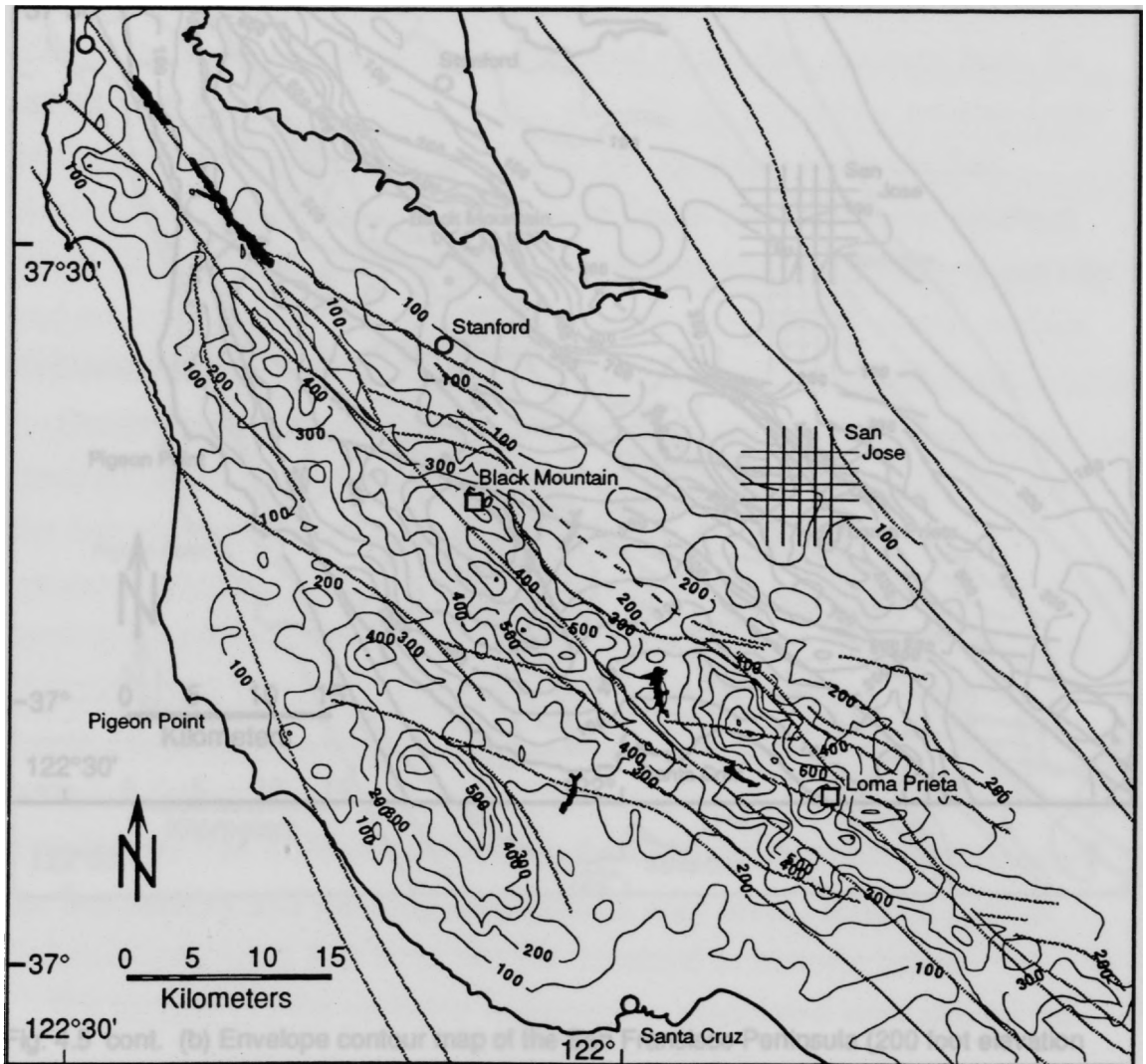


Fig. 4.5 (a) Subenvelope contour map of the San Francisco Peninsula determined from elevations of streams shown in Fig. 4.4.

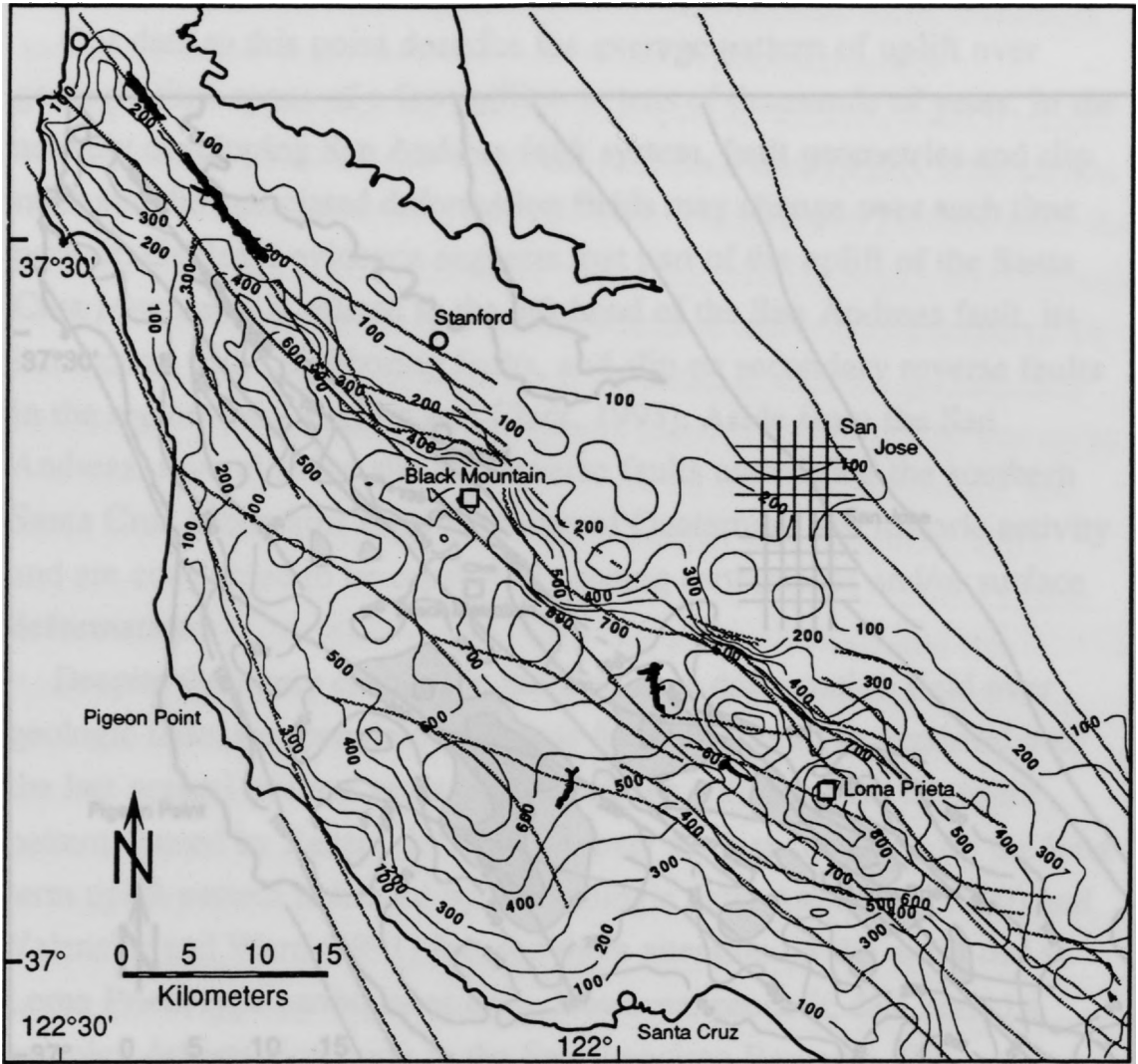


Fig. 4.5 cont. (b) Envelope contour map of the San Francisco Peninsula (200 foot elevation contours converted to meters). The envelope map is essentially a surface draped over the highpoints of the topography at the scale of ridge crests surrounding the major drainage basins. Whereas the northern Santa Cruz Mountains to southwest of the San Andreas fault appear as broad regional highs, the Sierra Azul range surrounding Loma Prieta is more localized. Steepest slopes in the area are associated with the northeast front of the southern Santa Cruz Mountains, coincident with location of the Foothills thrust belt.

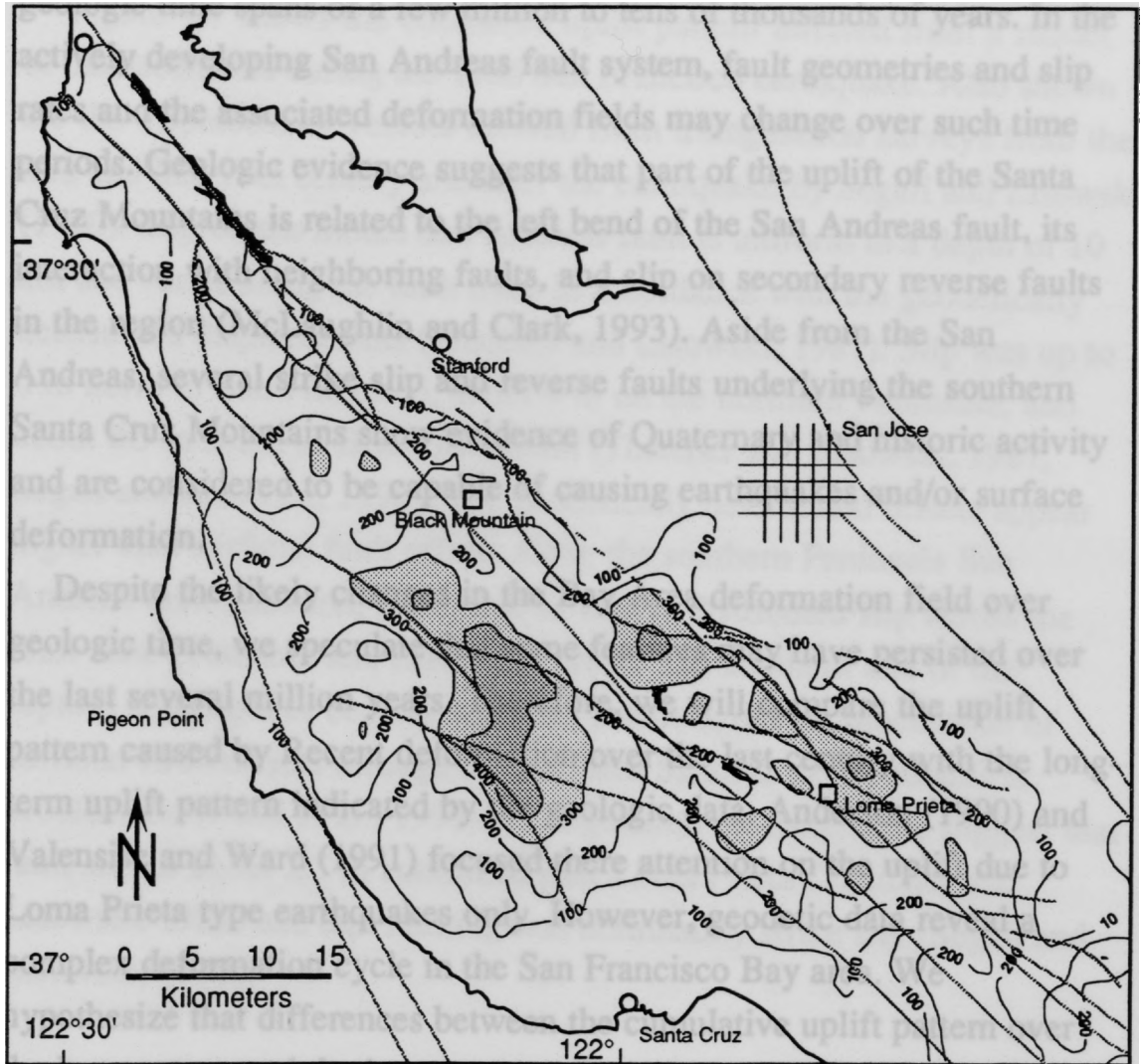


Fig. 4.6 Residual map (envelope elevations minus subenvelope elevations) showing the distribution of local relief. Highs are associated with the largest drainage basins southwest of the San Andreas (Pescadero and San Lorenzo in Fig. 4.4) and with the eastern slopes of the southern Santa Cruz Mountains where we infer significant Quaternary uplift.

Recent Crustal Deformation

Our data to this point describe the average pattern of uplift over geologic time spans of a few million to tens of thousands of years. In the actively developing San Andreas fault system, fault geometries and slip rates and the associated deformation fields may change over such time periods. Geologic evidence suggests that part of the uplift of the Santa Cruz Mountains is related to the left bend of the San Andreas fault, its interaction with neighboring faults, and slip on secondary reverse faults in the region (McLaughlin and Clark, 1993). Aside from the San Andreas, several strike slip and reverse faults underlying the southern Santa Cruz Mountains show evidence of Quaternary and historic activity and are considered to be capable of causing earthquakes and/or surface deformation.

Despite the likely changes in the Bay Area deformation field over geologic time, we speculate that some features may have persisted over the last several million years. Therefore, we will compare the uplift pattern caused by Recent deformation over the last century with the long-term uplift pattern indicated by the geologic data. Anderson (1990) and Valensise and Ward (1991) focused their attention on the uplift due to Loma Prieta type earthquakes only. However, geodetic data reveal a complex deformation cycle in the San Francisco Bay area. We hypothesize that differences between the cumulative uplift pattern over the last century and the long-term pattern may reveal seismic gaps or deformation events that have not yet occurred in historic times.

We include (1) the probable deformation associated with slip on the San Andreas fault at the time of the M 8.3 1906 San Francisco earthquake; (2) interseismic strain accumulation from trilateration and GPS measurements in the two decades before the Loma Prieta earthquake; (3) effects of fault slip at the time of the M 7.1 1989 Loma Prieta earthquake; (4) creep and coseismic faulting on the Hayward and Calaveras fault zones, the southern Sargent fault, and the creeping

segment of the San Andreas fault; and (5) post-seismic strain transients measured in the years following the Loma Prieta earthquake.

Figure 4.7 shows the contoured uplift pattern inferred from a model of displacements during the 1906 San Francisco earthquake. Also shown are the displacement vectors derived from triangulation surveys from the mid and late 19th century and after the earthquake by Segall and Lisowski (1990). Slip on the model San Andreas fault is uniform to a depth of 10 km and varies along the fault trace in accordance with the geodetically determined displacements (Thatcher and Lisowski, 1987). Slip was up to 6 m north of San Francisco, about 4 m on the northern Peninsula, and about 2.5 m south of Black Mountain (Thatcher and Lisowski, 1987, Segall and Lisowski, 1990). The geodetically determined offsets appear higher than surficial fault offsets along the southern Peninsula San Andreas fault (Lawson, 1908) due to widely distributed slip across the fault zone (Thatcher and Lisowski, 1987). The southern end of the rupture is thought to be near San Juan Bautista, but documentation of surficial 1906 offsets through the southern Santa Cruz Mountains is problematic (Ponti et al., 1990). Triangulation measurements suggest that fault slip of about 2.5 m continued past Loma Prieta (Thatcher and Lisowski, 1987) and that faulting was dominantly strike slip (Segall and Lisowski, 1990).

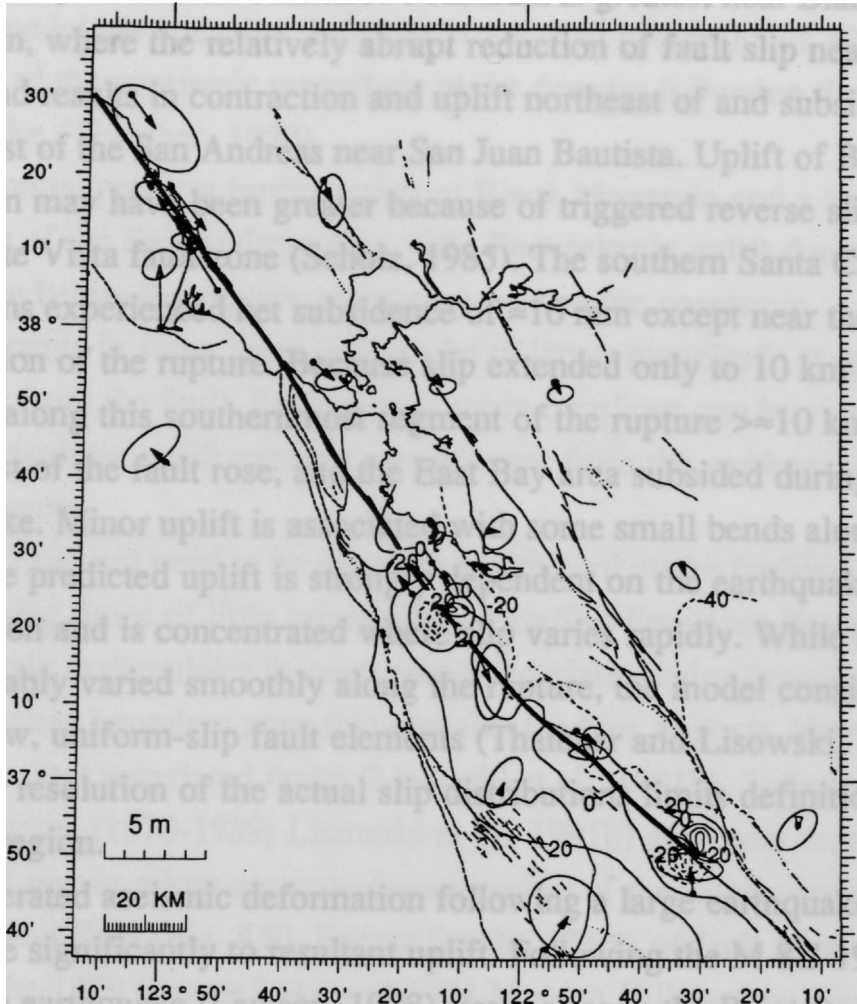


Fig. 4.7 Modeled uplift magnitudes in the San Francisco Bay area associated with slip on the San Andreas fault at the time of the M 8.3 1906 San Francisco earthquake. The contoured vertical displacements (mm) are computed from a numerical model of uniform-slip boundary elements embedded within an elastic halfspace that represent coseismic fault slip to a depth of 10 km. Slip was geodetically determined from triangulation measurements (Thatcher and Lisowski, 1987). The displacement vectors are from Segall and Lisowski, 1990.

The theoretical 1906 coseismic surface uplift (derived from the above-cited model) on the San Francisco Peninsula is greatest near Black Mountain, where the relatively abrupt reduction of fault slip near a $\approx 10^\circ$ fault bend results in contraction and uplift northeast of and subsidence southwest of the San Andreas near San Juan Bautista. Uplift of Black Mountain may have been greater because of triggered reverse slip along the Monte Vista fault zone (Scholz, 1985). The southern Santa Cruz Mountains experienced net subsidence of ≈ 10 mm except near the termination of the rupture. Because slip extended only to 10 km depth, the area along this southernmost segment of the rupture $> \approx 10$ km southwest of the fault rose, and the East Bay area subsided during the earthquake. Minor uplift is associated with some small bends along the fault. The predicted uplift is strongly dependent on the earthquake slip distribution and is concentrated where slip varies rapidly. While seismic slip probably varied smoothly along the rupture, the model consists of only a few, uniform-slip fault elements (Thatcher and Lisowski, 1987). The poor resolution of the actual slip distributions limits definition of the uplifted region.

Accelerated aseismic deformation following a large earthquake may contribute significantly to resultant uplift. Following the M 8.3 1906 San Francisco earthquake (Lawson, 1908) strain rates in the Point Reyes and Point Arena triangulation networks northwest of San Francisco were about 2-3 times the rates measured in the 1970's (Thatcher, 1974). This indicates a variation in deformation rates through the seismic cycle due to time-dependent deformation processes at depth. The data can be explained by either viscous relaxation of a ductile (asthenospheric) layer underlying an elastic (lithospheric) plate, or by downward propagation of aseismic slip along a lower crustal extension of the fault zone induced by the coseismic stress perturbations (Thatcher, 1983). Even though post-seismic deformation may be due to viscous flow below the rupture plane, the displacement pattern is similar to that predicted by a dislocation model (Thatcher, 1983). Post-seismic processes effectively extend the fault break

to greater depths and will significantly modify the associated displacement field. The magnitude and depth of aseismic slip are not well constrained, but the model assumes that fault slip propagated to a depth of 30 km and was half of the coseismic magnitude in the decades following the earthquake (Thatcher, 1983).

The model predicts further uplift of Black Mountain and a broad zone northeast of the San Andreas (Fig. 4.8). Post-seismic uplift due to relaxation below the rupture plane may reverse the coseismic displacements in some areas and can be of larger magnitude at greater distances from the fault. Post-seismic strain transients can be significant and the resulting uplift patterns are different from the earthquake displacements.

Uplift does not need to be associated with earthquake faulting and may occur during times of little seismicity. In the San Francisco Bay area, elastic strain accumulates through continued plate motion across a ≈ 100 -km wide plate boundary zone that contains the San Andreas, Hayward, Calaveras, and associated faults (Lisowski et al., 1991b). Trilateration measurements (1970-1989; Lisowski et al., 1991b) and more recent GPS and VLBI results allow accurate determination of the interseismic displacement field (Fig. 4.9). Except for the effects of fault slippage at the times of the 1979 Coyote Lake and 1984 Morgan Hill earthquakes, the velocity field appears to have been constant over that period.

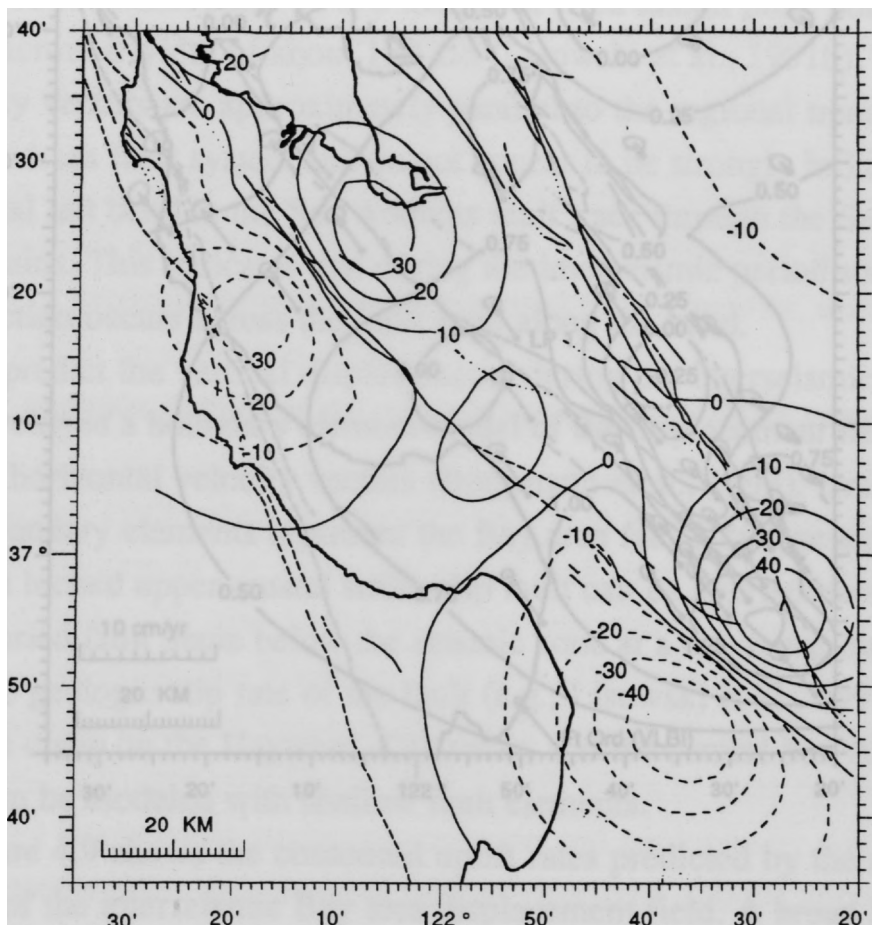


Fig. 4.8 Modeled uplift magnitudes (in mm) in the San Francisco Bay area associated with post-seismic relaxation following the 1906 earthquake. In this model it is assumed that the down-dip extension of the fault is 50% relaxed to a depth of 30 km, which may have occurred over several decades following the earthquake (e.g. Thatcher, 1983). Note the broadening of the vertical displacement zones near Black Mountain and San Juan Bautista, and a reversal of the regional coseismic uplift pattern in the far field southwest of the fault and in the East Bay area.

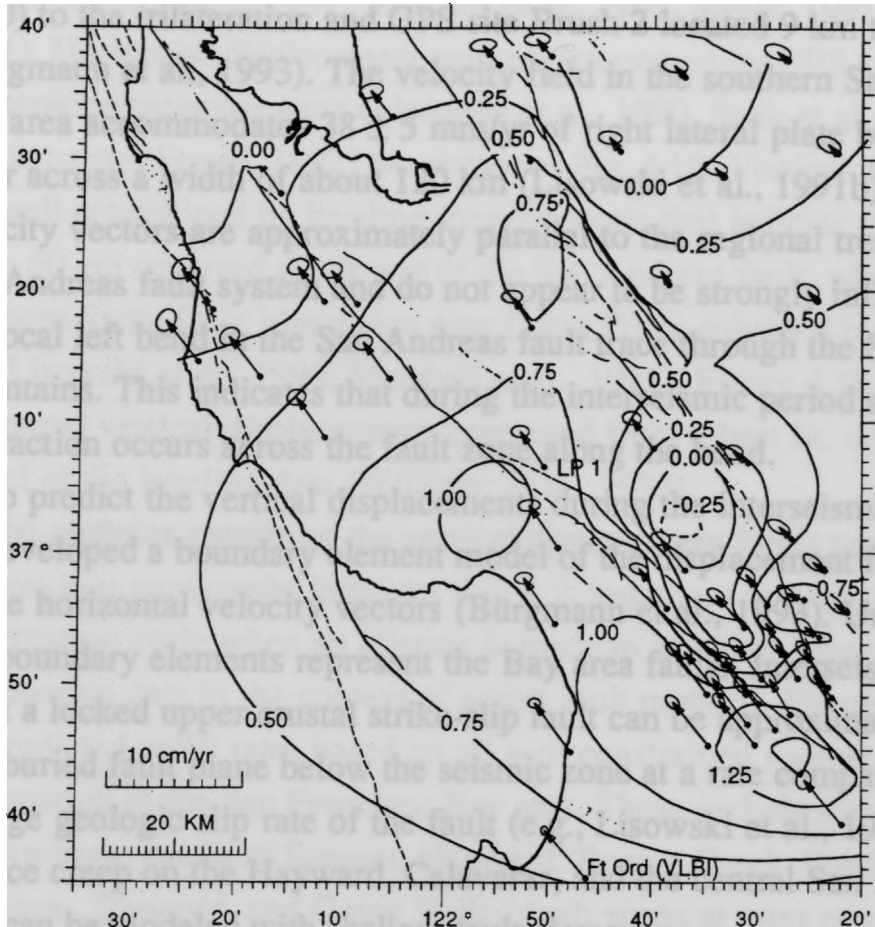


Fig. 4.9 Horizontal displacement rates based on 20 years of trilateration measurements and more recent GPS and VLBI results. Displacement rate vectors and 95% confidence ellipses are shown relative to a North American reference frame (modified from Bürgmann and others, 1993; Chapter 5, this thesis). Predicted uplift is derived from a numerical model that includes deep shear below locked faults, and shallow slipping faults where creep occurs. Uplift southwest of the San Andreas and north of Loma Prieta, and subsidence east of Loma Prieta are caused by the left bend of the San Andreas fault, end effects of the rapidly slipping creeping central section of the San Andreas to the southeast of the mapped region, and complex interaction of all Bay Area faults.

The velocities were computed relative to a North American reference frame by applying the velocity of the VLBI site at Fort Ord (Clark et al., 1990) to the trilateration and GPS site Brush 2 located 9 km to the north (Bürgmann et al., 1993). The velocity field in the southern San Francisco Bay area accommodates 38 ± 5 mm/yr of right lateral plate boundary shear across a width of about 120 km (Lisowski et al., 1991b). The velocity vectors are approximately parallel to the regional trend of the San Andreas fault system and do not appear to be strongly influenced by the local left bend in the San Andreas fault trace through the Santa Cruz Mountains. This indicates that during the interseismic period some contraction occurs across the fault zone along the bend.

To predict the vertical displacements during the interseismic period, we developed a boundary element model of the displacement field based on the horizontal velocity vectors (Bürgmann et al., 1993). Uniform-slip rate boundary elements represent the Bay area faults. Interseismic shear about a locked upper crustal strike-slip fault can be approximated by slip on a buried fault plane below the seismic zone at a rate comparable to the average geologic slip rate of the fault (e.g., Lisowski et al., 1991b). Surface creep on the Hayward, Calaveras, and the central San Andreas fault can be modeled with shallow fault elements.

Figure 4.9 shows the contoured uplift rates predicted by the numerical model of the interseismic Bay area displacement field. A broad high uplift zone is associated with the left bend of the San Andreas fault through the Santa Cruz Mountains. North of San Juan Bautista, about 15 mm/yr of slip are transferred from the San Andreas fault to the Hayward and Calaveras faults which causes further contraction and uplift southwest of the San Andreas and localized subsidence southeast of Loma Prieta. Uplift also occurs in the left-stepping transfer zone between the Calaveras and the Hayward faults.

Next, we analyze uplift associated with the M 7.1 1989 Loma Prieta earthquake. Fault slip occurred on a previously unrecognized, 35-km-long fault dipping 70° southwest from about 8 km to 18 km depth with

comparable amounts of strike slip and reverse slip. Slip of up to 5 m occurred on two fault patches to the northwest and southeast of the hypocenter (Beroza, 1991, Hartzell et al., 1991, Steidl, 1991, Wald et al., 1991). Horizontal displacement vectors determined by GPS and trilateration measurements (Lisowski et al., 1990, Snay et al., 1991, Williams and Segall, 1992) are shown in Fig. 4.10. Vertical displacements are well constrained by leveling measurements that indicate that uplift of up to 50 cm occurred southwest of the San Andreas fault, while the southern Santa Cruz Mountains near Loma Prieta subsided by about 10 cm (Lisowski et al., 1990, Marshall et al., 1991). Figure 4.10 shows the contoured vertical displacements computed from a best fit, uniform slip model of the leveling data (Williams et al., 1993).

The complex pattern of the vertical displacement fields presented in the previous paragraphs indicates that it is important to recognize the full deformation cycle when an attempt is made to interpret long-term deformation data in the context of active fault motions. Figure 4.11 shows the predicted uplift rates based on all well constrained sources of active deformation in the San Francisco Bay area. These include slip along the San Andreas, southern Sargent, Hayward, Rogers Creek, Paicines, Calaveras, Concord, and Green Valley fault zones at rates constrained by measured interseismic strain accumulation and geologically determined displacement rates, and repeated Loma Prieta-type oblique slip events at ≈ 1000 year intervals. Shorter repeat times of Loma Prieta earthquakes predict uplift rates that exceed those determined from terrace uplifts and other geologic data (Anderson, 1990, Valensise and Ward, 1991).

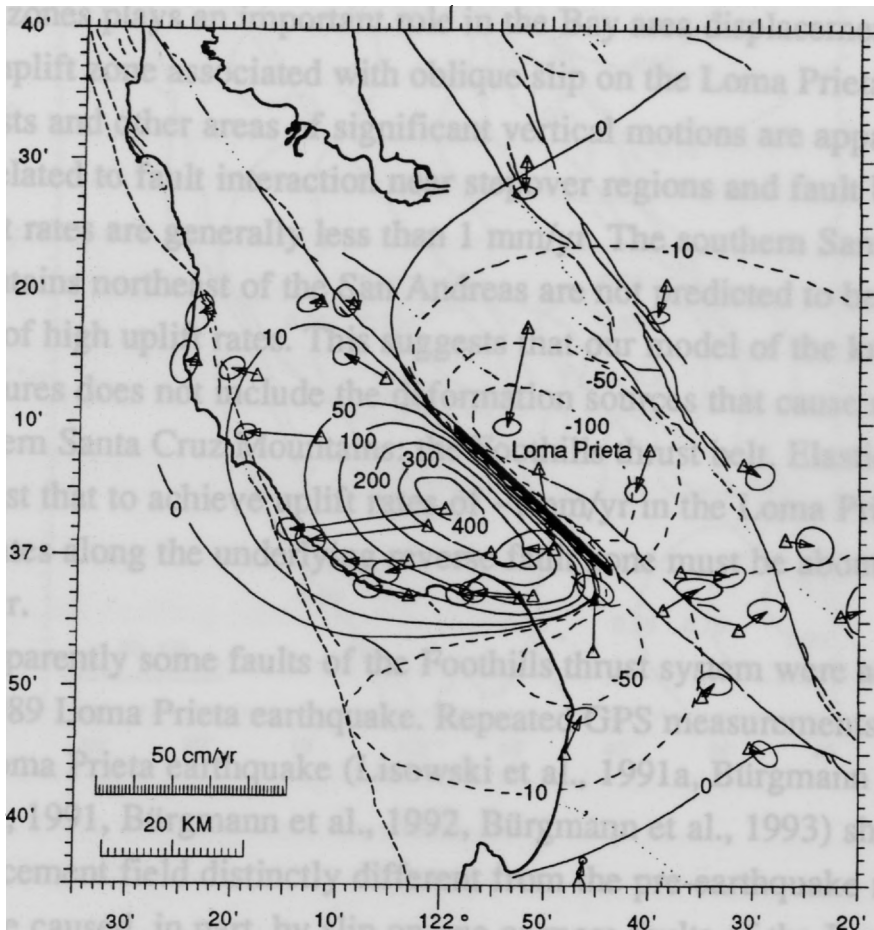


Fig. 4.10 Horizontal displacements derived from GPS, VLBI, and trilateration measurements (Williams et al., 1993) and modeled uplift magnitudes (in mm) in the Bay Area associated with the M 7.1 1989 Loma Prieta earthquake. The fault model was determined from a non-linear inversion (Williams et al., 1993) of the leveling uplift measurements (Marshall et al., 1991). Anderson (1990) and Valensise and Ward (1991) recognized the similarity of the coseismic uplift pattern with raised terrace elevation along the Pacific coast. Note that Loma Prieta subsided about 10 cm during the event.

Clearly most of the secondary strike-slip faults of the East Bay area do not have any noticeable effect on the uplift of the Santa Cruz Mountains. However, interaction of the San Andreas with the Hayward and Calaveras fault zones plays an important role in the Bay area displacement field. The uplift zone associated with oblique slip on the Loma Prieta fault persists and other areas of significant vertical motions are apparent that are related to fault interaction near stepover regions and fault bends. Uplift rates are generally less than 1 mm/yr. The southern Santa Cruz Mountains northeast of the San Andreas are not predicted to be a localized zone of high uplift rates. This suggests that our model of the known active structures does not include the deformation sources that cause uplift of the southern Santa Cruz Mountains: the Foothills thrust belt. Elastic models suggest that to achieve uplift rates of ~ 1 mm/yr in the Loma Prieta area, slip rates along the underlying reverse fault zone must be about 2-3 mm/yr.

Apparently some faults of the Foothills thrust system were activated by the 1989 Loma Prieta earthquake. Repeated GPS measurements following the Loma Prieta earthquake (Lisowski et al., 1991a, Bürgmann and Segall, 1991, Bürgmann et al., 1992, Bürgmann et al., 1993) show a displacement field distinctly different from the pre-earthquake rates that may be caused, in part, by slip on one or more faults of the Berrocal and Shannon fault zones (Fig. 4.12; Chapter 5, this thesis). Sites near Loma Prieta within 20 km of the San Andreas fault show significant deviations in magnitude and orientation of velocity vectors from pre-seismic values (Figs. 4.9 and 4.12). Fault-parallel velocities increased to the southwest of the San Andreas. There has also been a large fault-normal contraction, centered northeast of the San Andreas.

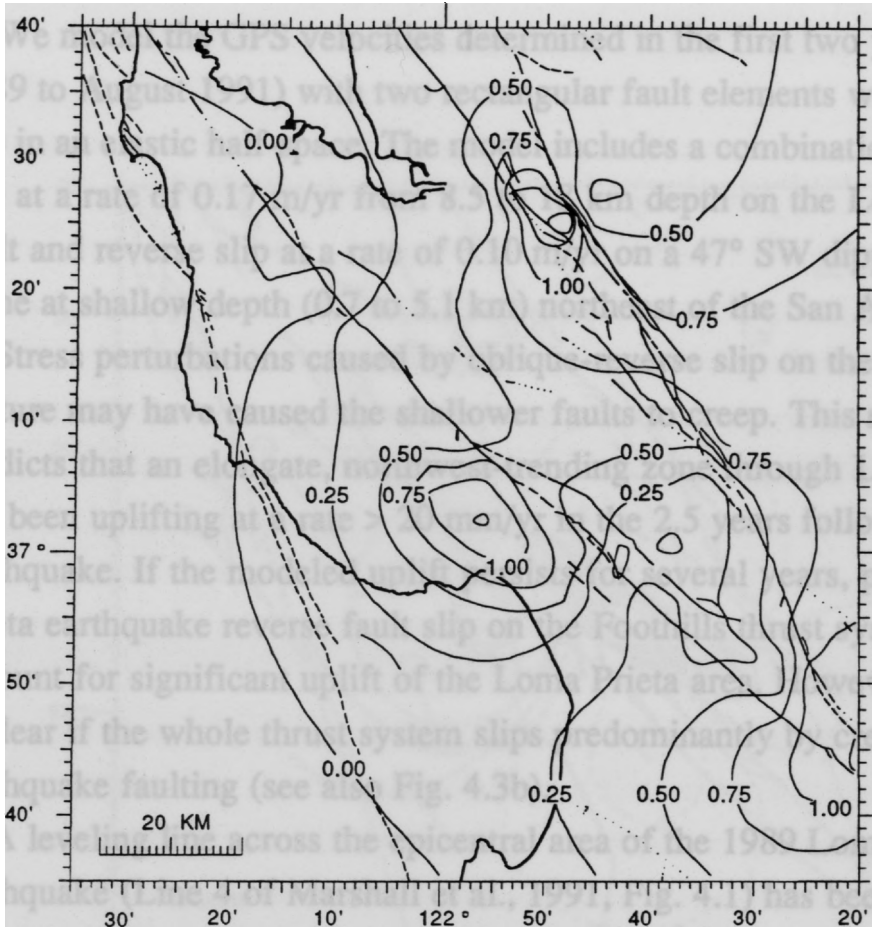


Fig. 4.11 Vertical displacement rates in mm/yr computed from a model of the known components of the Bay Area displacement cycle. The combined effects on uplift rates of (1) slip on the San Andreas, Hayward, and Calaveras fault zones including creep and earthquake faulting, (2) full relaxation (deep slip) below the Bay area faults, and (3) 1989 Loma Prieta type events assuming a repeat time of 1000 yrs. Two uplift zones southwest of the San Andreas fault are related to end effects of the rapidly slipping creeping section and the obliquely slipping Loma Prieta fault. Rapid uplift between the Hayward and Calaveras faults is caused by the transfer of ≈ 8 mm of slip across a left stepping discontinuity between the faults. Note that several topographic features, including the high-uplift zone northeast of the San Andreas, are not predicted by this model. Slip on the reverse faults of the Foothills thrust belt at 2-3 mm/yr could produce the geologic uplift rates.

We model the GPS velocities determined in the first two years (Oct. 1989 to August 1991) with two rectangular fault elements with uniform slip in an elastic half-space. The model includes a combination of strike-slip at a rate of 0.17 m/yr from 8.5 to 18 km depth on the Loma Prieta fault and reverse slip at a rate of 0.10 m/yr on a 47° SW dipping thrust plane at shallow depth (0.7 to 5.1 km) northeast of the San Andreas.

Stress perturbations caused by oblique-reverse slip on the Loma Prieta rupture may have caused the shallower faults to creep. This model predicts that an elongate, northwest-trending zone through Loma Prieta has been uplifting at a rate > 20 mm/yr in the 2.5 years following the earthquake. If the modeled uplift persists for several years, post-Loma Prieta earthquake reverse fault slip on the Foothills thrust system may account for significant uplift of the Loma Prieta area. However, it is unclear if the whole thrust system slips predominantly by creep or by earthquake faulting (see also Fig. 4.3b).

A leveling line across the epicentral area of the 1989 Loma Prieta earthquake (Line 4 of Marshall et al., 1991, Fig. 4.1) has been resurveyed to measure elevation changes associated with the apparently accelerated post-seismic velocity field (see Chapter 5, this thesis). This line is part of a larger leveling network that was last occupied in the spring of 1990 to determine coseismic elevation changes (Marshall et al., 1991). The line extends from Capitola at the Pacific coast via Loma Prieta to Coyote in the central Santa Clara Valley, roughly parallel to the Loma Prieta GPS profile. The leveling survey recorded several centimetres uplift across the southern Santa Cruz Mountains (Fig. 5.7?). We note that the steepest displacement gradient occurs directly in the hanging wall of the Berrocal fault zone. However, the uplift magnitude is somewhat less than that derived from the GPS data. Chapter 5 presents a new model derived from more than 3 years of GPS data and the leveling survey.

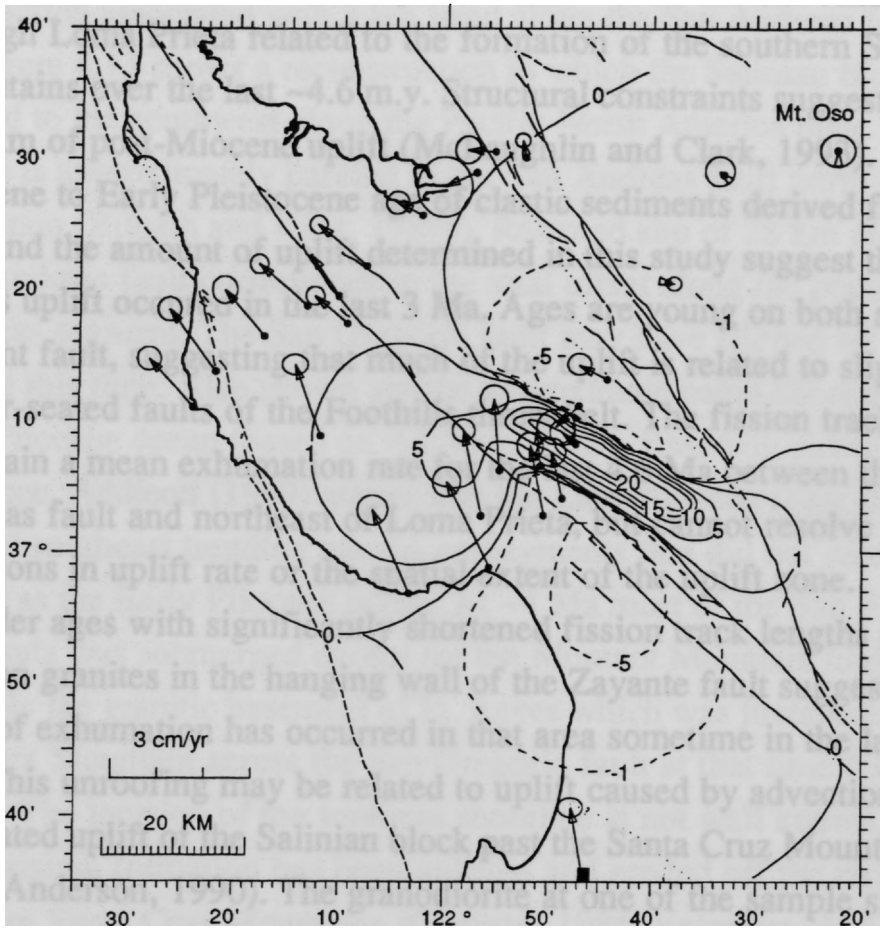


Fig. 4.12 Horizontal displacement rates based on 2 years of post-Loma Prieta-earthquake GPS measurements. Displacements are shown relative to a 'fixed' site, Mt. Oso (modified from Bürgmann et al., 1993). The contoured uplift rates (in mm/yr) are computed from a numerical model of two uniform-slip boundary elements, embedded in an elastic halfspace with 17 cm/yr post-seismic strike-slip shear on the Loma Prieta fault, and 10 cm/yr reverse slip on the Berrocal fault zone. This preliminary model of post-seismic deformation predicts uplift northeast of the San Andreas fault at a > 2 cm/yr rate.

INTERPRETATION AND CONCLUSIONS

The apatite fission-track ages indicate about 3-4 km of unroofing at average rates of about 0.8 mm/yr in the area from the San Andreas fault through Loma Prieta related to the formation of the southern Santa Cruz Mountains over the last ~4.6 m.y. Structural constraints suggest as much as 6 km of post-Miocene uplift (McLaughlin and Clark, 1993). The Late Pliocene to Early Pleistocene age of clastic sediments derived from the area and the amount of uplift determined in this study suggest that much of this uplift occurred in the last 3 Ma. Ages are young on both sides of the Sargent fault, suggesting that much of the uplift is related to slip on deeper-seated faults of the Foothills thrust belt. The fission track data constrain a mean exhumation rate for the last 4.6 Ma between the San Andreas fault and northeast of Loma Prieta, but cannot resolve temporal variations in uplift rate or the spatial extent of the uplift zone.

Older ages with significantly shortened fission track lengths from Salinian granites in the hanging wall of the Zayante fault suggest about 2-3 km of exhumation has occurred in that area sometime in the last 10 m.y. This unroofing may be related to uplift caused by advection and associated uplift of the Salinian block past the Santa Cruz Mountains fault bend (Anderson, 1990). The granodiorite at one of the sample sites (BL-6-88, Olive Springs Quarry) is in contact with Pliocene to lower Pleistocene, shallow marine Purisima formation rocks (Coppersmith, 1990). The Purisima formation is offset vertically by the Zayante fault by about 400 m. If we accept the 2-3 km uplift estimate, this suggests that either the Purisima formation has been eroded by several kilometers or that some of the uplift occurred before its deposition. Known formation thicknesses and other evidence for pre-Pliocene tectonism in the area suggests that some of the uplift did in fact occur before juxtaposition with the San Andreas fault bend.

The localized late Cenozoic uplift associated with the Santa Cruz Mountains fault bend occurred concurrently with regional uplift of the California Coast Ranges caused by a component of margin-perpendicular

plate motion since about 3.5 Ma (Page and Engebretson, 1984, Harbert and Cox, 1989). However, uplift of the southern Santa Cruz Mountains greatly exceeds these background values and is related to localized contraction associated with a left bend along the San Andreas fault.

Figure 4.13 shows a reconstruction in which the Salinian block was moved to the southwest along the Pacific-North America plate vector which is approximately parallel to the San Andreas fault north of Black Mountain (Bilham and King, 1989a). Restored slip of 28 km along the San Andreas fault corresponds to the total offset along the peninsular San Andreas segment. The San Gregorio fault may have slipped by 10-20 km during this time. Also shown are the approximate paleo-shorelines of the Late Pliocene ocean (based on Addicott, 1969). Based on paleontologic evidence, Addicott (1969) argues that the Late Pliocene coast line formed several southeast trending narrow embayments that did not reach as far inland as the Early Pliocene ocean. At ~4 Ma most of the San Francisco Peninsula was submerged except for the Montara Mountain high and possibly the granitic basement of Pt. Reyes which was juxtaposed with Montara Mountain across the San Gregorio fault at that time (Gavigan, 1984). The location of the southern shoreline is not well known, because the Purisima formation has been uplifted and eroded off the rising northern Santa Cruz Mountains (Gavigan, 1984, Valensise, 1993).

The gap between the Salinian and San Francisco Bay blocks in Fig. 4.13 indicates the total amount of shortening (~ 5 km) required to accommodate plate motion about the bend. The northern Santa Cruz Mountains (southwest of the San Andreas fault) are uplifted over a broad region as they advect past the fault bend (Anderson, 1990). Up to about a kilometer of the bend related shortening appears to have been accommodated to the southwest of the San Andreas fault as indicated by the late Cenozoic surface uplift, and deformation of the Pliocene Purisima formation. Southwest-dipping reverse faults of the Foothills thrust system to the northeast of the San Andreas apparently accommodate most of the shortening across the range. The Late Cenozoic uplift and associated

shortening of ~3–4 km estimated from geologic (McLaughlin and Clark, 1993) and fission track data can account for much of the required contraction. However, we find no evidence for significant uplift and contraction to the southeast of San Juan Bautista where the San Andreas fault bend continues for almost 20 km. Interaction with other Bay area faults may account for some of the discrepancies from the simple bend model, as indicated by the mechanical models shown in Figs. 4.7–4.11.

Material properties may also play an important role in tectonic development of the San Francisco Bay area. The San Andreas fault bend appears to have been stationary relative to the zone of maximum uplift in the southern Santa Cruz Mountains since the Late Pliocene. This may indicate that the fault bend is related to a contrast in lithology and rock stiffness across the fault.

The geomorphic expression of the southern Santa Cruz Mountains clearly indicates that the range is a zone of relatively high Quaternary surface uplift rates. High relief and steep, east-facing slopes are concentrated along a ≈30-km-long 1–3 km wide band. Quaternary reverse fault displacement is apparently concentrated along the Foothills thrust system that underlies the uplift zone. The uplift zone and associated thrust faults extend northwest towards the Black Mountain area that is associated with a distinct local bend along the San Andreas (Scholz, 1985). The uplift pattern expressed in the geomorphology of the area is similar to that suggested by the geologic evidence of late Cenozoic deformation. The Foothills thrust faults have been active into Late Pleistocene and Recent times as indicated by offsets of <20 ka fluvial terraces (McLaughlin and Clark, 1993) and historic fault slip (Haugerud and Ellen, 1990, Prescott and Burford, 1976).

The long-term record revealed by geologic data indicates high uplift rates in the southern Santa Cruz Mountains. Recent uplift patterns, based on mechanical models of historic deformation events, do not show significant uplift of the mountain range. Considering Recent activity of the Foothills thrust system that accommodates the geologic uplift, this

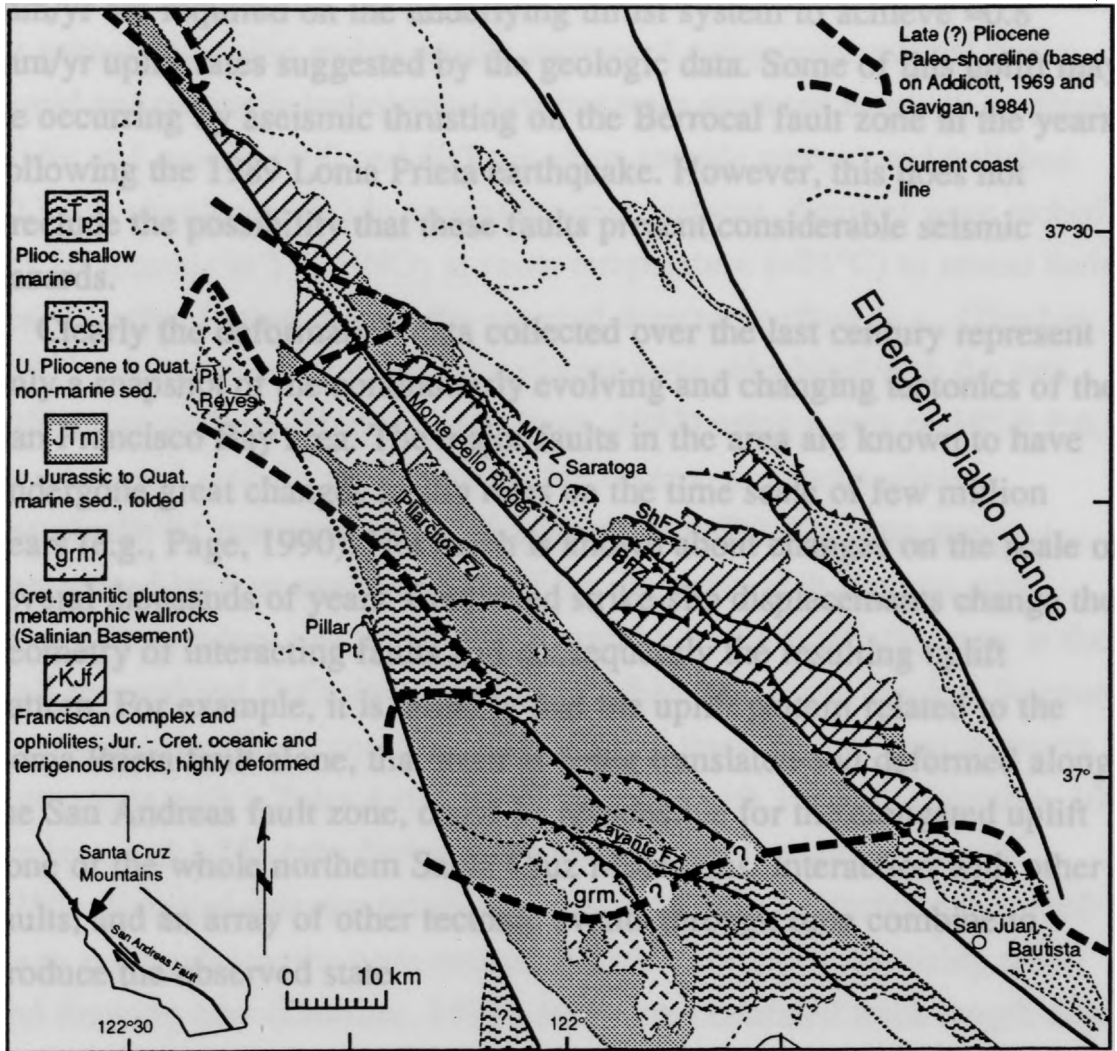


Fig. 4.13 Reconstruction of Late Pliocene configuration of crustal blocks bounding the San Andreas and San Gregorio faults. The Salinian block was moved to the southwest along the Pacific-North America plate vector which is approximately parallel to the San Andreas fault north of Black Mountain. Also shown are the approximate Late Pliocene paleo-shorelines based on Addicott, 1969 and Gavigan, 1984.

suggests that the Monte Vista, Shannon, and Berrocal fault zones will eventually slip again to produce the predicted uplift field. Slip rates of 2-3 mm/yr are required on the underlying thrust system to achieve ≈ 0.8 mm/yr uplift rates suggested by the geologic data. Some of this uplift may be occurring by aseismic thrusting on the Berrocal fault zone in the years following the 1989 Loma Prieta earthquake. However, this does not preclude the possibility that these faults present considerable seismic hazards.

Clearly the deformation data collected over the last century represent only a snapshot of the continuously evolving and changing tectonics of the San Francisco Bay area. The major faults in the area are known to have undergone great changes in slip rates on the time scale of few million years (e.g., Page, 1990). Not much is known about changes on the scale of several thousands of years. Continued strike-slip displacements change the geometry of interacting faults and consequently the resulting uplift pattern. For example, it is unlikely that the uplift pattern related to the Loma Prieta fault alone, that itself is being translated and deformed along the San Andreas fault zone, could be responsible for the elongated uplift zone of the whole northern Santa Cruz Mountains. Interaction with other faults, and an array of other tectonic events through time combine to produce the observed state.

ACKNOWLEDGMENTS

Thanks to Ron Kistler for providing samples K13-87 and BL-6-88, the Texas A&M University Nuclear Science Center for sample irradiation, the Department of Energy Reactor Sharing Program for irradiation costs, Kevin Crowley for advice on irradiation procedures, and ARCO Exploration and Production Technology for support of the fission track laboratory. Thanks to Mike Ellis and Dorothy Merritts for their interest, encouragement, and invitation to attend the Chapman Tectonics and Topography Conference.

APPENDIX: FISSION TRACK LABORATORY METHODS

Samples consisting of a few kilograms of sandstone or a few hundred grams of granitic rock were crushed and ground, and detrital (sandstones) or primary (granitic rocks) apatite recovered using conventional heavy liquid and magnetic techniques. Apatites were mounted in epoxy on glass slides and ground (400 and 600 grit silica carbide papers) and polished (0.3 μm alumina oxide) to expose internal surfaces. Apatites were etched for 20 seconds in 5 N HNO_3 at room temperature ($\approx 21^\circ\text{C}$) to reveal their fossil tracks. Dating was by the external detector method (e.g., Gleadow, 1981) using muscovite detectors and ages were calculated with the zeta calibration method (Hurford and Green, 1983) using a zeta of 385.9 ± 6.9 years track⁻¹ cm² for the Corning CN5 neutron dosimetry glass (nominally 11 ppm undepleted U, insignificant Th). The zeta was determined by four analyses each of the Durango, Fish Canyon, and Mount Dromodary age standards. Thermal neutron irradiation was at the well-thermalized D₂O site in the Texas A&M University Nuclear Science Center reactor. Track counting and confined track length measurements were made with a Zeiss Axioplan microscope with 100x air objective, 10x oculars, and 1.25x tube factor, for a total nominal magnification of 1250x. External detector prints were located with a Kinetek automated-stage and track lengths were measured with a computer digitizing tablet and drawing tube (Dumitru, 1993). Horizontal confined track length data were collected following the protocols of Laslett and others (1982). Uncertainties in ages were calculated using the conventional analysis (Green, 1981, Galbraith, 1981).

REFERENCES

- Adam, D. P., McLaughlin, R. J., Sorg, D. H., Adams, D. B., Forester, R. M., and Repenning, C. A., 1982, An animal and plant-fossil assemblage from the Santa Clara Formation (Pliocene and Pleistocene), Saratoga, California *in* Ingersoll, R. V., and Woodburne, M. O., ed., *Cenozoic non-marine deposits of California and Arizona: Society of Economic Paleontologists and Mineralogists, Pacific Section*, p. 105-110.
- Addicott, W. O., 1969, Late Pliocene mollusks from San Francisco Peninsula, California, and their paleogeographic significance: *Proceedings of the California Academy of Sciences, 4th Ser.*, v. 27, p. 57-93.
- Anderson, R. S., 1990, Evolution of the northern Santa Cruz mountains by advection of crust past a San Andreas fault bend: *Science*, v. 249, p. 397-401.
- Anderson, R. S., 1993, Evolution of the Santa Cruz Mountains, California, through tectonic growth and geomorphic decay: *Journal of Geophysical Research*, submitted.
- Anderson, R. S. and Menking, K. M., 1993, The Santa Cruz marine terraces: Evidence for two coseismic uplift mechanisms: *Geological Society of America Bulletin*, submitted.
- Aydin, A., Johnson, A. M., and Fleming, R. W., 1992, Right-lateral-reverse surface rupture along the San Andreas and Sargent faults associated with the October 17, 1989, Loma Prieta, California, earthquake: *Geology*, v. 20, p. 1063-1067.
- Aydin, A., and Page, B. M., 1984, Diverse Pliocene-Quaternary tectonics in a transform environment, San Francisco Bay region, California: *Geological Society of America Bulletin*, v. 95, p. 1303-1317.
- Bakun, W. H., and McLaren, M., 1984, Microearthquakes and the nature of the creeping-to-locked transition of the San Andreas fault zone near San Juan Bautista, California: *Bulletin of the Seismological Society of America*, v. 74, p. 235-254.

- Beroza, G. C., 1991, Near-source modeling of the Loma Prieta earthquake: Evidence for heterogeneous slip and implications for earthquake hazard: *Bulletin of the Seismological Society of America*, v. 81, p. 1603-1621.
- Bilham, R., and King, G. C. P., 1989a, Slip distribution and oblique segments of the San Andreas fault, California: observations and theory *in* *Fault Segmentation and Controls on Fault Rupture*: U.S. Geological Survey Open File Report, 89-315, p. 80-93.
- Bilham, R., and King, G. P. C., 1989b, The morphology of strike-slip faults: Examples from the San Andreas fault, California: *Journal of Geophysical Research*, v. 94, p. 10204-10216.
- Bullard, T. F., and Lettis, W. R., 1993, Quaternary fold deformation associated with blind thrust faulting, Los Angeles Basin, California: *Journal of Geophysical Research*, v. 98, p. 8349-8369.
- Bürgmann, R., 1991, Transpression along the southern San Andreas Fault, Durmid Hill, California: *Tectonics*, v. 10, p. 1152-1163.
- Bürgmann, R., and Segall, P., 1991, Postseismic GPS monitoring NW of the 1989 Loma Prieta rupture zone: *EOS Transactions American Geophysical Union*, v. 72, p. 119.
- Bürgmann, R., Segall, P., Lisowski, M., and Svarc, J. P., 1992, Rapid aseismic slip on the Berrocal fault zone following the Loma Prieta earthquake: *EOS Transactions American Geophysical Union*, v. 73, p. 119.
- Bürgmann, R., Segall, P., Lisowski, M., and Svarc, J. P., 1993, Post-seismic strain following the 1989 Loma Prieta earthquake from repeated GPS measurements *in* Reasenberg, P., ed., *The Loma Prieta, California Earthquake of October 17, 1989*, U.S. Geological Survey Professional Paper, 1550, in review.
- Christensen, M. N., 1965, Late Cenozoic deformation in the central Coast Ranges of California: *Geological Society of America Bulletin*, v. 76, p. 1105-1124.

- Clark, J. C., 1981, Stratigraphy, paleontology and geology of the central Santa Cruz Mountains, California Coast Ranges: U.S. Geological Survey, Professional Paper 1168, p. 51.
- Clark, J. C. and Brabb, E. E., 1978, Stratigraphic contrasts across the San Gregorio fault, Santa Cruz Mountains, west central California: California Division of Mines and Geology Special Report, v. 137, p. 3-12.
- Clark, T. A., Ma, C., Sauber, J. M., Ryan, J. W., Gordon, D., Shaffer, D. B., Caprette, D. S., and Vandenberg, N. R., 1990, Geodetic measurements of deformation in the Loma Prieta, California earthquake with Very Long Baseline Interferometry: Geophysical Research Letters, v. 17, p. 1215-1218.
- Coppersmith, K. J., 1990, Stop 2. The Zayante-Vergeles fault zone *in* Schwartz, D. D., and Ponti, D. J., ed., Field guide to neotectonics of the San Andreas fault system, Santa Cruz Mountains, in light of the 1989 Loma Prieta earthquake: Menlo Park, U.S. Geological Survey Open File Report 90-274, p. 14-15.
- Crowell, J. C., 1974, Origin of late Cenozoic basins in southern California: in Tectonics and Sedimentation: Society Economic Paleontologists and Mineralogists Special Publication, v. 22, p. 190-204.
- Cummings, J. C., 1968, The Santa Clara formation and possible post-Pliocene slip on the San Andreas fault in Central California *in* Proceedings of the Conference on Geologic Problems of the San Andreas Fault System, Stanford University, 14-16 September: Stanford, CA, p. 191-207.
- Dumitru, T. A., 1988, Subnormal geothermal gradients in the Great Valley forearc basin, California, during Franciscan subduction: A fission track study: Tectonics, v. 7, p. 1201-1221.
- Dumitru, T. A., 1991, Major Quaternary uplift along the northernmost San Andreas fault, King Range, northwestern California: Geology, v. 19, p. 526-529.

- Dumitru, T. A., 1993, A new computer-automated microscope stage system for fission track analysis: *Nuclear Tracks*, in press.
- Dumitru, T. A., Hill, K. C., Coyle, D. A., Duddy, I. R., Foster, D. A., Gleadow, A. J. W., Green, P. F., Kohn, B. P., Laslett, G. M., and O'Sullivan, A. J., 1991, Fission track thermochronology: Application to continental rifting of south-eastern Australia: *Australian Petroleum Exploration Association Journal*, v. 31, p. 131-142.
- Dumitru, T. A. D., 1989, Constraints on uplift in the Franciscan subduction complex from apatite fission track analysis: *Tectonics*, v. 8, p. 197-220.
- England, P., and Molnar, P., 1990, Surface uplift, uplift of rocks, and exhumation of rock: *Geology*, v. 18, p. 1173-1177.
- Erickson, L. L., 1987, User's Manual for DIS3D: A three dimensional dislocation program with applications to faulting in the earth: [M.S. thesis, Stanford University, 167 pp.]
- Fitzgerald, P. G., Stump, E., and Redfield, T. F., 1993, Late Cenozoic uplift of Denali and its relation to relative plate motion and fault morphology: *Science*, v. 259, p. 497-499.
- Galbraith, R. F., 1981, On statistical models for fission track counts: *Mathematical Geology*, v. 13, p. 471-478.
- Gavigan, C. L., 1984, Composition and stratigraphy of the Purisima formation in the central California Coast Ranges: [M.S. thesis, Stanford University, 111 pp.]
- Gleadow, A. J. W., 1981, Fission track dating methods: What are the real alternatives?: *Nucl. Tracks*, v. 5, p. 3-14.
- Graham, S. A., McCloy, C., Hitzman, M., Ward, R., and Turner, R., 1984, Basin evolution during change from convergent to transform continental margin in central California: *American Association of Petroleum Geologists*, v. 68, p. 233-249.
- Green, P. F., 1981, A new look at statistics in fission-track dating: *Nuclear Tracks*, v. 5, p. 77-86.

- Green, P. F., Duddy, I. R., Gleadow, A. J. W., and Lovering, J. F., 1989a, Apatite fission-track analysis as a paleotemperature indicator for hydrocarbon exploration *in* Naeser, N. D., and McCulloh, T. H., ed., *Thermal History of Sedimentary Basins: Methods and Case Histories*: New York, Springer-Verlag, p. 181-195.
- Green, P. F., Duddy, I. R., Laslett, G. M., Hegarty, K. A., Gleadow, A. J. W., and Lovering, J. F., 1989b, Thermal annealing of fission tracks in apatite, 4, Quantitative modelling techniques and extension to geological timescales: *Chem. Geol. (Isot. Geosci.)*, v. 79, p. 155-182.
- Harbert, W., and Cox, A., 1989, Late Neogene motion of the Pacific plate: *Journal of Geophysical Research*, v. 94, p. 3052-3064.
- Hartzell, S. H., Stewart, G. S., and Mendoza, C., 1991, Comparison of L_1 and L_2 norms in a teleseismic waveform inversion for the slip history of the Loma Prieta, California, earthquake: *Bulletin of the Seismological Society of America*, v. 81, p. 1518-1539.
- Haugerud, R. A., and Ellen, S. D., 1990, Coseismic ground deformation along the northeast margin of the Santa Cruz Mountains *in* Schwartz, D. P., and Ponti, D. J., ed., *Field guide to neotectonics of the San Andreas fault system, Santa Cruz Mountains, in light of the Loma Prieta earthquake*: U.S. Geological Survey, Open File Report 90-274, p. 32-37.
- Hazlewood, R. M., 1976, Contour map and interpretive cross sections showing depth and configuration of bedrock surface, South San Francisco Bay region, California: U.S. Geol. Surv., Misc. Field Stud. Map MF-0796.
- Helley, E. J., 1990, Preliminary contour map showing elevation of surface of Pleistocene alluvium under Santa Clara Valley, California: U. S. Geological Survey Open-File Report OF 90-0633,
- Hill, K. C., and Gleadow, A. J. W., 1989, Uplift and thermal history of the Papuan fold belt, Papua New Guinea: Apatite fission track analysis: *Austral. J. Earth Sci.*, v. 36, p. 515-539.

- Hurford, A. J., and Green, P. F., 1983, The zeta age calibration of fission-track dating: *Isotope Geosciences*, v. 1, p. 285-317.
- James, E. W., 1992, Cretaceous metamorphism and plutonism in the Santa Cruz Mountains, Salinian block, California, and correlation with the southernmost Sierra Nevada: *Geological Society of America Bulletin*, v. 104, p. 1326-1339.
- Kamp, P. J. J., Green, P. F., and Tippett, J. M., 1993, Tectonic architecture of the mountain front-foreland basin transition, South Island, New Zealand, assessed by fission track analysis: *Tectonics*, in press.
- Kamp, P. J. J., Green, P. F., and White, S. H., 1989, Fission track analysis reveals character of collisional tectonics in New Zealand: *Tectonics*, v. 8, p. 169-195.
- Keller, E. A., 1986, Investigation of active tectonics: Use of surficial earth processes *in* Wallace, R. E., ed., *Active Tectonics: Studies in Geophysics Series*, Geophysics Research Forum: Washington, D.C., National Academy Press, p. 136-147.
- Kovach, R. L., and Beroza, G. C., 1993, Seismic potential from reverse faulting on the San Francisco Peninsula: *Bulletin of the Seismological Society of America*, in press.
- Lachenbruch, A. H., and Sass, J. H., 1980, Heat flow and energetics of the San Andreas fault zone: *Journal of Geophysical Research*, v. 85, p. 6185-6223.
- Laslett, G. M., Kendal, W. S., Gleadow, A. J. W., I.R., D., and Green, P. F., 1982, Bias in measurement of fission-track length distributions: *Nuclear Tracks*, v. 6, p. 79-85.
- Lawson, J. J., 1908, The California earthquake of April 18, 1906: Report of the State Earthquake Investigation Commission: Carnegie Institution of Washington Publication, v. 87.
- Lisowski, M., Prescott, W. H., Savage, J. C., and Johnston, M. J., 1990, Geodetic estimate of coseismic slip during the 1989 Loma Prieta,

- California earthquake: *Geophysical Research Letters*, v. 17, p. 1437-1440.
- Lisowski, M., Savage, J. C., and Prescott, W. H., 1991a, Surface deformation after the Loma Prieta, California, earthquake: *EOS Transactions American Geophysical Union*, v. 72, p. 119.
- Lisowski, M., Savage, J. C., and Prescott, W. H., 1991b, The velocity field along the San Andreas fault in central and southern California: *Journal of Geophysical Research*, v. 96, p. 8369-8389.
- Madrid, V. M., Stuart, R. M., and Verosub, K. L., 1986, Magnetostratigraphy of the late Neogene Purisima Formation, Santa Cruz County, California: *Earth and Planetary Science Letters*, v. 79, p. 431-440.
- Marshall, G. A., Stein, R. S., and Thatcher, W., 1991, Faulting geometry and slip from co-seismic elevation changes: The October 17, 1989 Loma Prieta, California, earthquake: *Bulletin of the Seismological Society of America*, v. 81, p. 1660-1693.
- McEvelly, T. V., 1966, The earthquake sequence of November 1964 near Corralitos, California: *Bulletin of the Seismological Society of America*, v. 56, p. 755-773.
- McLaughlin, R., 1990, Stop 4. Sargent fault zone at Loma Prieta *in* Schwartz, D. D., and Ponti, D. J., ed., *Field guide to neotectonics of the San Andreas fault system, Santa Cruz Mountains, in light of the 1989 Loma Prieta earthquake*: Menlo Park, U.S. Geological Survey Open File Report, 90-274, p. 19-22.
- McLaughlin, R. J., and Clark, E. E., 1993, Stratigraphy and structure of rocks across the San Andreas fault zone near Loma Prieta, California: Their relation to deformation during the October 17, 1989 earthquake *in* *The Loma Prieta, California Earthquake of October 17, 1989*, U.S. Geological Survey Professional Paper, 1550, in review.
- McLaughlin, R. J., Clark, J. C., and Brabb, E. E., 1988, Geologic map and structure sections of the Loma Prieta 7 1/2' quadrangle, Santa

- Clara and Santa Cruz Counties, California: U.S. Geol. Surv. Open File Map 88-752.
- Merritts, D., and Vincent, K. R., 1989, Geomorphic response of coastal streams to low, intermediate, and high rates of uplift, Mendocino triple junction region, northern California: Geological Society of America Bulletin, v. 101, p. 1373-1388.
- Montgomery, D. R., 1993, Compressional uplift in the central California Coast Ranges: Geology, v. 21, p. 543-546.
- Mooney, W. D., and Luetgert, J. H., 1982, A seismic refraction study of the Santa Clara Valley and southern Santa Cruz Mountains, west-central California: Bulletin of the Seismological Society of America, v. 72, p. 901-909.
- Naeser, C. W., and Ross, D. C., 1976, Fission-track ages of sphene and apatite of granitic rocks of the Salinian block, COast Ranges, California: U. S. Geological Society Journal of Research, v. 4, p. 415-420.
- Naeser, C. W., 1979, Fission track dating and geological annealing of fission tracks *in* Jäger, E., and Hunziker, J. C., ed., Lectures in isotope geology: New York, Springer-Verlag, p. 154-169.
- Page, B. M., 1990, Evolution and complexities of the transform system in California, U.S.A.: Annales Tectonicae, v. 4, p. 53-69.
- Page, B. M., 1992, Tectonic setting of the San Francisco Bay region: California Division of Mines and Geology Special Publication, v. 113.
- Page, B. M., and Engebretson, D. C., 1984, Correlation between the geologic record and computed plate motions for central California: Tectonics, v. 3, p. 133-155.
- Ponti, D. J., Prentice, C. S., Schwartz, D. P., and Wells, R. E., 1990, Surface Fractures associated with the 1906 and 1989 earthquakes *in* Schwartz, D. D., and Ponti, D. J., ed., Field guide to neotectonics of the San Andreas fault system, Santa Cruz Mountains, in light of the 1989 Loma Prieta earthquake, same as McL[Ponti et al., 1990,: Menlo Park, U.S. Geological Survey Open File Report 90-274, p. 23-30.

- Prescott, W. H., and Burford, R. P., 1976, Slip on the Sargent fault: Bulletin of the Seismological Society of America, v. 66, p. 1013-1016.
- Reasenber, P. A., and Simpson, R. W., 1992, Response of regional seismicity to the static stress change produced by the Loma Prieta earthquake: Science, v. 255, p. 1687-1690.
- Rodgers, D. A., 1980, Analysis of pull-apart basin development produced by en echelon strike-slip faults *in* Ballance, P. F., and Reading, H. G., ed., Oxford, England, International Association of Sedimentologists, p. 27-41.
- Scholz, C. H., 1985, The Black Mountain asperity: seismic hazard of the southern San Francisco peninsula, California: Geophysical Research Letters, v. 10, p. 717-719.
- Schumm, S. A., 1986, Alluvial river response to active tectonics *in* Wallace, R. E., ed., Active Tectonics: Studies in Geophysics Series, Geophysics Research Forum: Washington, D.C., National Academy Press, p. 80 - 94.
- Schwartz, S. Y., Orange, D. L., and Anderson, R. S., 1990, Complex fault interactions in a restraining bend on the San Andreas fault, southern Santa Cruz Mountains, California: Geophysical Research Letters, v. 17, p. 1207-1210.
- Segall, P., and Lisowski, M., 1990, Surface displacements in the 1906 San Francisco and 1989 Loma Prieta earthquakes: Science, v. 250, p. 1241-1244.
- Segall, P., and Pollard, D. D., 1980, Mechanics of discontinuous faults: Journal of Geophysical Research, v. 85, p. 4337-4350.
- Snay, R. A., Neugebauer, H. C., and Prescott, W. H., 1991, Horizontal deformation associated with the Loma Prieta earthquake: Bulletin of the Seismological Society of America, v. 81, p. 1647-1659.
- Sorg, D. H., and McLaughlin, R. J., 1975, Geologic map of the Sargent-Berrocal fault zone between Los Gatos and Los Altos Hills, Santa Clara County, California: U. S. Geological Survey Miscellaneous Field Investigations Map MF-643, scale 1:24,000.

- Stanley, R. G., 1987, Implications of the northwestwardly younger age of the volcanic rocks of west-central California alternative interpretation: Geological Society of America Bulletin, v. 98, p. 612-614.
- Stearns, R. G., 1967, Warping on the Western Highland Rim Peneplain in Tennessee by groundwater sapping: Geological Society of America Bulletin, v. 78, p. 1111-1124.
- Thatcher, W., 1974, Strain release mechanism of the 1906 San Francisco earthquake: Science, v. 184, p. 1283-1285.
- Thatcher, W., 1983, Nonlinear strain buildup and the earthquake cycle on the San Andreas fault: Journal of Geophysical Research, v. 88, p. 5893-5902.
- Thatcher, W., and Lisowski, M., 1987, Long-term seismic potential of the San Andreas fault southeast of San Francisco, California: Journal of Geophysical Research, v. 92, p. 4771-4784.
- Valensise, G., 1993, Geological records of combined tectonic processes in the central Santa Cruz mountains *in* The Loma Prieta, California Earthquake of October 17, 1989, U.S. Geological Survey Professional Paper 1550, in press.
- Valensise, G., and Ward, S. N., 1991, Long-term uplift of the Santa Cruz coastline in response to repeated earthquakes along the San Andreas fault: Bulletin of the Seismological Society of America, v. 96, p. 1694-1704.
- Vanderhurst, W. L., Cummings, J. C., and Anderson, D. W., 1982, The Santa Clara Formation as a record of late Cenozoic uplift of the Santa Cruz Mountains, Santa Clara County, California *in* Ingersoll, R. V., and Woodburne, M. O., ed., Cenozoic Nonmarine Deposits of California and Arizona: Los Angeles, California, The Pacific Section, Society of Economic Paleontologists and Mineralogists, p. 23-33.
- Wald, D. J., Helmberger, D. V., and Heaton, T. H., 1991, Rupture model of the 1989 Loma Prieta earthquake from the inversion of strong-motion and broadband teleseismic data: Bulletin of the Seismological Society of America, v. 81, p. 1540-1572.

- White, L. A., 1991, Late Cretaceous to recent unroofing of the western Transverse Ranges: Results from apatite fission track thermochronology: Geological Society of America, Abstracts with Program, v. 23, p. 432-433.
- Williams, C. R., Arnadottir, T. and Segall, P., 1993, Coseismic deformation and dislocation models of the 1989 Loma Prieta earthquake derived from Global Positioning System measurements: Journal of Geophysical Research, v. 98, p. 4567-4578.
- Williams, C. R., and Segall, P., 1992, 1989 Loma Prieta earthquake displacements measured with the Global Positioning System: U.S. Geological Survey Professional Paper 1550, in press.
- Zeitler, P. K., 1985, Cooling history of the NW Himalaya, Pakistan: Tectonics, v. 4, p. 127-151.

5. Post-Seismic Strain Following the 1989 Loma Prieta Earthquake From Repeated GPS Measurements and Leveling

ABSTRACT

Strain transients following large earthquakes may be responsible for clustering of seismic events in space and time. The post-seismic velocity field in the epicentral region of the Loma Prieta earthquake differs significantly from displacement rates measured in the two decades preceding the event. The post-earthquake displacement rates along the Black Mountain profile, crossing the San Andreas fault 40 km northwest of the Loma Prieta epicenter, do not differ significantly from those determined from 20 years of trilateration measurements and more recent GPS and VLBI measurements. However, station velocities along the Loma Prieta profile, through the epicentral region, significantly exceed pre-earthquake rates and changed orientation within 20 km of the Loma Prieta rupture. Aseismic oblique reverse slip at a rate of 8 cm/yr on a sub-vertical fault and reverse slip at a rate of 6 cm/yr on a thrust fault of the Sargent-Berrocal fault zone can explain the observed motions. Rapid post-earthquake fault slip may be a precursory phenomenon to impending rupture, and could influence the timing of future earthquakes on nearby faults affected by the associated stress field.

INTRODUCTION AND MOTIVATION

Observations subsequent to some large earthquakes show accelerated strain rates in the years to decades following the rupture (Thatcher, 1986). Following the M 8.3 1906 San Francisco earthquake that ruptured the San Andreas fault over a length of up to 400 km (Lawson, 1908), strain rates in the Point Reyes and Point Arena triangulation networks N of San Francisco were about 2-3 times the rates measured in the 1970's (Thatcher, 1974). This indicates a variation in deformation rates through the seismic cycle due to time-dependent deformation processes at depth. Other well documented examples of post-seismic transients, not related to shallow afterslip, are from subduction-zone earthquakes in Japan (Thatcher, 1986, Kasahara, 1981).

Using simple models of post-seismic relaxation, Thatcher (1974, 1983) concluded that the deformation can be explained by either the viscous relaxation of a ductile (asthenospheric) layer underlying an elastic (lithospheric) plate, or by the downward propagation of aseismic slip along a lower crustal extension of the fault zone. Many mechanical models of deep seated deformation transients following large dip-slip and strike-slip earthquakes have been proposed (Bott and Dean, 1973, Nur and Mavko, 1974, Anderson, 1975, Savage and Prescott, 1978, Budianski and Amazigo, 1976, Rundle and Jackson, 1977, Cohen, 1979, Lehner et al., 1981, Li and Rice, 1987), however, there is a lack of adequate data to test and differentiate between them.

Fault creep at shallow depths (0 to 3 km) has been observed after several strike-slip earthquakes along the San Andreas fault system and typically decays exponentially within a few years of the earthquake (Smith and Wyss, 1968, Bilham, 1989). Post-seismic creep at intermediate depth, on aseismic patches adjacent to seismic ruptures on the Calaveras fault, has been inferred from trilateration measurements (Oppenheimer et al., 1990).

Observations of historic seismicity patterns indicate that earthquakes tend to propagate along fault zones rupturing fault segments immediately

adjacent to, and within several years of a previously active break. Examples involving strike-slip faults have been reported along the North Anatolian fault system (Toksöz et al., 1979), in NE China preceding the 1975 Haicheng earthquake (Scholz, 1977), the Calaveras fault zone (Oppenheimer et al., 1990), and the San Andreas fault zone (Savage, 1971, Wood and Allen, 1973). In the 19th century, earthquakes along the San Andreas fault and the Hayward fault in the San Francisco Bay area occurred in clusters spread over several years (Ellsworth, 1990). This suggests the existence of transient processes that occur over characteristic time scales of several years. Lacking more geodetic data on the time dependent deformation around previously ruptured fault segments, we can only speculate on the mechanics of post-seismic deformation and the relation between strain transients and the clustering of earthquakes.

The M 7.1 Loma Prieta earthquake of October 17, 1989, occurred on a previously unrecognized fault plane along a restraining bend of the San Andreas fault zone. The earthquake ruptured a buried 35 km long fault dipping 70° to the SW from about 8km to 18km depth, with comparable strike-slip and reverse dip-slip components of about 1.5 m, based on the distribution of aftershocks (Dietz and Ellsworth, 1990) and geodetic data (Lisowski et al., 1990a, Marshall et al., 1991, Snay et al., 1991, Williams and Segall, 1992). However, the slip distribution is more complex in detail, with slip of up to 5 m occurring on two patches to the NW and the SE of the hypocenter (Beroza, 1991, Hartzell et al., 1991, Steidl, 1991, Wald et al., 1991).

Despite occurring away from the more densely populated regions of the San Francisco Bay area, damage from the Loma Prieta earthquake was considerable at distances of up to 100 km from the epicenter. Understandably, the earthquake has focused much attention on the possibility of earthquakes on faults even closer to major population centers. The Hayward fault last ruptured in 1836 and 1868 on its northern and southern segments respectively, whereas the northern San Francisco Peninsula segment of the San Andreas fault slipped about 2-4 m during

the 1906 earthquake and ruptured previously in 1838 (Ellsworth, 1990). In 1865, an earthquake in the southern San Francisco Bay area may have ruptured the San Andreas fault through the Santa Cruz Mountains, the Loma Prieta fault that ruptured in 1989, or possibly one of the faults of the Foothills thrust system NE of the San Andreas fault (Tuttle and Sykes, 1992). Several thrust faults along the San Andreas fault (Aydin and Page, 1984) may also represent significant seismic risks (Kovach and Beroza, 1993, Tuttle and Sykes, 1992). Evidence that earthquakes on various fault strands in the San Francisco Bay area occurred previously in clusters or sequences, warrant intensive studies of the strain transients following the 1989 earthquake rupture.

Measurements of surficial post-seismic slip subsequent to the Loma Prieta earthquake find shallow displacements to be generally less than ~ 1 cm in the first year after the earthquake (Behr et al., 1990, Langbein, 1990, Rymer, 1990). Aftershocks occurred on the Loma Prieta rupture, as well as on adjacent faults, for months subsequent to the earthquake. However, the cumulative slip of aftershocks (~ 5 mm; (King et al., 1990) is too small to be detected geodetically. Behr et al. (1993) find that slip rates on the creeping section of the San Andreas fault near San Juan Bautista accelerated from a pre-earthquake rate of 7-8 mm/yr to a rate of ~13 mm/yr since the earthquake. About 2-3 cm of excess slip occurred over the northernmost 15 km of the creeping section in the 3 years following the earthquake, probably down to a depth of 1-3 km (Gwyther et al., 1992, Behr et al., 1993). Surficial creep rates on the southern Hayward fault have decreased from 3-9 mm/yr to about half the pre-earthquake rates. Near the fault's SE end, where the right-lateral creep rate was highest, it has been slipping left-laterally since the earthquake (Lienkaemper et al., 1992) with a possible reversal in early 1993 [Lienkaemper, 1993, pers. commun.]. The magnitude of the observed shallow creep transients (retardation as well as accelerations) is not expected to significantly affect the far-field displacement field of the southern San Francisco Bay area.

In this study we analyze Global Positioning System (GPS) data from (1) the Black Mountain profile across the San Andreas fault 30 km NW of the Loma Prieta rupture (Bürgmann and Segall, 1991), (2) the Loma Prieta profile through the epicentral region (Lisowski et al., 1991a), and (3) a 5-station monitor network (Fig. 5.1). The San Francisco Bay area monitor network had also been continuously measured for several years prior to the earthquake (Lisowski et al., 1990b). We also compute the displacements of Bay area VLBI stations relative to a North American reference frame from data courtesy of Doug Caprette, NASA Goddard Space Flight Center. The GPS network geometry was chosen to measure post-seismic transients away from and along the San Andreas fault trace. Our objectives were to determine the amount and nature of deformation following the Loma Prieta earthquake and to examine the consequences for the potential of future earthquakes on the peninsular San Andreas fault and other faults in the San Francisco Bay region.

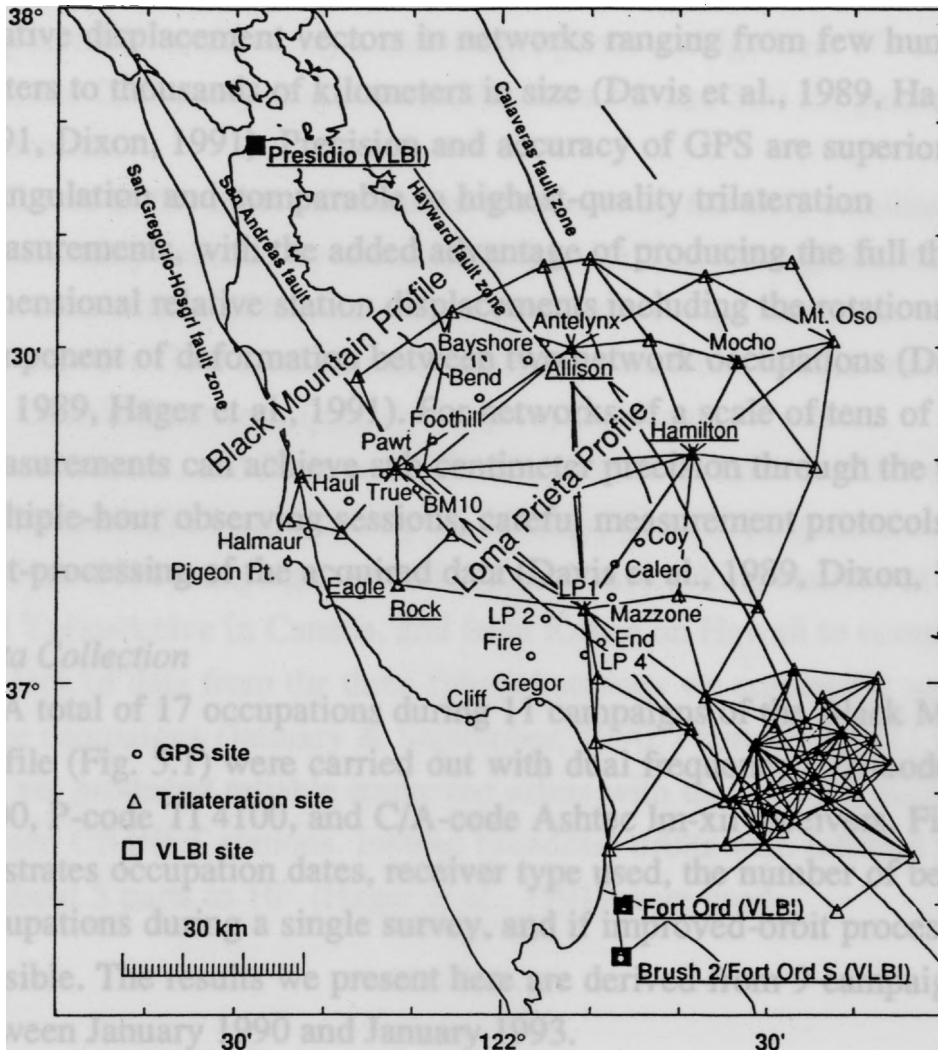


Fig. 5.1 Trilateration network, GPS and VLBI station locations in the south San Francisco Bay-Monterey Bay area. Pre-earthquake measurements are from trilateration and from VLBI and GPS measurements at the underlined stations. Names are shown for the GPS and VLBI stations occupied following the Loma Prieta earthquake.

METHODS: GPS DATA COLLECTION, PROCESSING, AND ERROR ANALYSIS

Within the last 10 years the Global Positioning System (GPS) has proven to be a powerful and cost-effective tool for the measurement of relative displacement vectors in networks ranging from few hundred meters to thousands of kilometers in size (Davis et al., 1989, Hager et al., 1991, Dixon, 1991). Precision and accuracy of GPS are superior to triangulation and comparable to highest-quality trilateration measurements, with the added advantage of producing the full three-dimensional relative station displacements including the rotational component of deformation between two network occupations (Davis et al., 1989, Hager et al., 1991). For networks of a scale of tens of km, GPS measurements can achieve sub-centimeter precision through the use of multiple-hour observing sessions, careful measurement protocols, and post-processing of the acquired data (Davis et al., 1989, Dixon, 1991).

Data Collection

A total of 17 occupations during 11 campaigns of the Black Mountain profile (Fig. 5.1) were carried out with dual frequency C/A-code Trimble 4000, P-code TI 4100, and C/A-code Ashtec Im-xii receivers. Figure 5.2 illustrates occupation dates, receiver type used, the number of benchmark occupations during a single survey, and if improved-orbit processing was possible. The results we present here are derived from 9 campaigns between January 1990 and January 1993.

TI 4100 and Ashtec carrier phase and pseudorange data were collected at 30-s intervals during 6-hour long occupations, whereas the Trimble receivers recorded data in 15-s intervals for 6 to 12 hours (occupation times exceeding 8 hours in the May 1992 campaign appear to have contributed significantly to the precision of this survey). Occupation times were chosen to achieve GPS-satellite configurations that maximize the number of satellites visible during an experiment.

Data Analysis

Our GPS data analysis follows the methods described by Davis and others (Davis et al., 1989). Doubly-differenced, ionosphere-free carrier phase observations are processed to estimate station coordinates, tropospheric zenith delays, and integer phase ambiguities. We use the Bernese GPS analysis software (Versions 3.2 and 3.3) for parameter estimation.

Errors in the orbit information broadcast by the GPS satellites can be significantly reduced by monitoring the satellites from global tracking networks with well known station coordinates (e.g., Larson et al., 1991). We improve GPS satellite orbits utilizing data from fiducial stations of the CIGNET network (usually Mojave, California, Westford, Massachusetts, and Richmond, Florida) with well known relative coordinates (SV6 provided by M. Murray, pers. communication). During the June 1991 campaign we added data from tracking stations at Penticton and Yellowknife in Canada, and from Kokee on Hawaii to compensate for the lack of data from the three fiducial stations we commonly use. In three campaigns (January & September, 1990, February, 1991) we have not yet produced reliable improved orbits with the tracking data from the chosen CIGNET stations. Instead broadcast orbits with inferred precision of about 5 parts in 10^7 (Hager et al., 1991) were used.

Summary of Data (Black Mountain Profile)

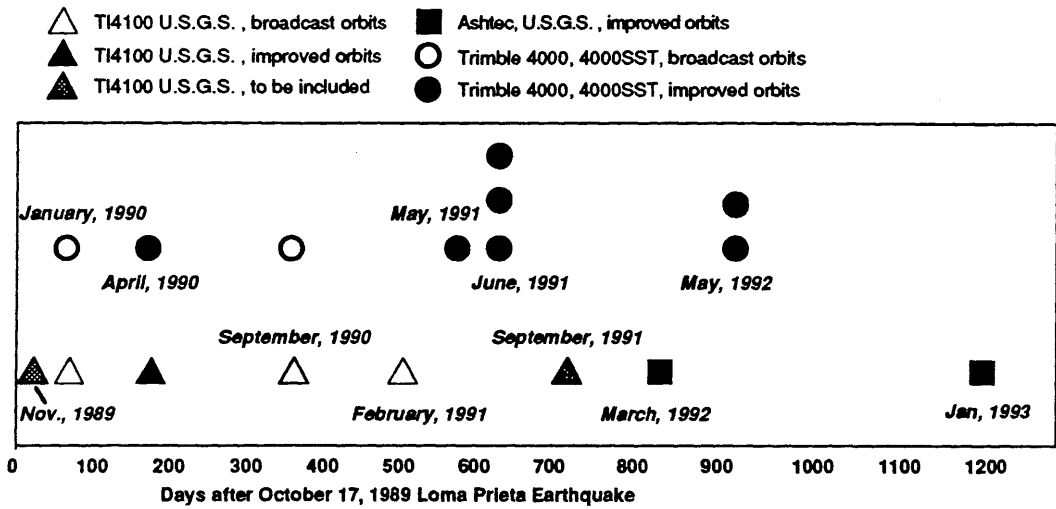


Fig. 5.2 Occupation schedule of the Black Mountain profile following the Loma Prieta earthquake. Two campaigns, November 1989 and September 1991 have not yet been included in the analysis.

For the Trimble and Ashtec data, we determine receiver clock corrections at each measurement point using C/A-code pseudorange data; whereas we estimate corrections with a polynomial in time using p-code pseudorange data for the TI 4100 data (Davis et al., 1989). Differencing the carrier phase from a given satellite received at two stations (single difference) and differencing the phase measurements of two satellites received at one station eliminates most receiver and satellite oscillator errors (Hager et al., 1991). All double-difference carrier-phase residuals were visually inspected after processing the data with an automatic cycle-slip fixing program to remove remaining cycle slips and outliers. Carrier phase cycle-slips are caused by the loss of signal for one or more epochs and lead to an offset in the residual by an integer number of wavelengths.

All data were processed with a satellite elevation cut-off angle of 15° , because higher cut-off angles appear to reduce the short-term repeatability of the station coordinates. Carrier phase data from GPS satellites are known only up to an integer number of wavelengths. These so-called integer ambiguities can be resolved utilizing phase and pseudorange measurements (Blewitt, 1989). Ambiguity resolution leads to significant improvements in baseline precision, however, bias fixing becomes more difficult with C/A receivers, for baselines exceeding 10's of km, under adverse ionospheric conditions, and for insufficiently long occupation times (Davis et al., 1989, Blewitt, 1989). We initially resolve 'wide-lane' ambiguities (a linear combination of the two carrier frequencies L1 and L2 with a wavelength of 86 cm). Using the resolved wide-lane ambiguities we can fix the remaining linearly independent integer-cycle ambiguity using the ionosphere-free linear combination. This combination of the two L-band frequencies (L3) eliminates most first-order effects of dispersive ionosphere delays that affect longer baselines. Practically all integer-cycle ambiguities in the doubly differenced phase measurements were reduced to integer values in the local data. Final coordinate estimates of the local stations were determined by processing the combined local and fiducial data using the ionosphere-

free linear combination of the L1 and L2 phases and the resolved integer biases of the local data. In the same process, we estimate atmospheric propagation delay parameters (solving for a constant zenith delay parameter for each station for ~8-hour periods), satellite orbit parameters, and synchronization errors (Davis et al., 1989).

Data Precision And Accuracy

The short-term precision of GPS measurements depends on error sources related to satellite and receiver clocks, propagation delays, satellite orbit and constellation characteristics, length and time of observation, the geographic location of a network, receiver types and post-processing software, and set-up procedures (Larson and Agnew, 1991). Through the use of optical plummets and a careful antenna set up and centering routine with several redundant height measurements, our absolute set-up errors are estimated to be less than 1-2mm in all coordinate components. Four receiver station days were left out in the final computations as operators noted significant shifts in antenna positions during the surveys caused by bovine impact or tripod instability (occupations of Halmaur in May 1992 and January 1993, Antelynx in May 1992, and Bayshore in January 1993). Benchmark occupations usually lasted about 6 hours, but in the May 1992 survey, occupation times of up to 14 hours were used.

Station Bayshore was disturbed by vehicle impact in the fall of 1990. Following this, a tie between the old and a new reference mark was measured in December 1990. In May and June 1991 the old benchmark was surveyed, and the position of the reference mark at the time of these campaigns was calculated from the established tie. The reference mark was disturbed as well in late 1992. Figure 5.3 shows the relative displacement before and after the first benchmark disturbance determined by subtracting the tie from the later measurements. Because the tie was measured after the disturbance we can not know the true offset. Therefore displacement rates in the following analysis are based on data

collected after the incident, from February 1991 to May 1992. This results in larger error associated with the velocity vector of Bayshore.

During the June 1991 and the May 1992 campaigns most baselines were measured 2-to-4 times to estimate the precision of the survey results. Furthermore the profile was measured within the same week with TI4100 and Trimble receivers in the January, April, and September campaigns of 1990. The average, unweighted repeatabilities of the measured baselines in the June 1991 survey are 5.3 mm in the N , 5.8 mm in the E, and 20.1 mm in the vertical component. The central station foothill that was used as a fiducial site in five surveys through June 1991 has caused concern due to its position near a fence and high vegetation. In fact, the repeatability of baselines formed to foothill in the June 1991 campaign is about twice that of the other baselines. The average precision of repeated station estimates in the May 1992 campaign is 2.7 mm in the N , 1.6 mm in the E, and 26.4 mm in the vertical component. Occupations of up to 14 hours clearly improved the horizontal precision of these measurements, however, other factors, such as satellite coverage and operator errors may have affected the reported precision.

The day-to-day precision of repeated measurements is practically independent of the length of the orbital arcs we estimate (1 to 4 days) and is about equal for broadcast and improved orbits. However, the apparent network dilation and rotation caused by the choice of orbits can be significant and clearly affect the accuracy of our measurements. Broadcast-orbit solutions can introduce spurious rotations of up to 5-10 mm across the Black Mountain profile, indicating the importance of orbit improvement.

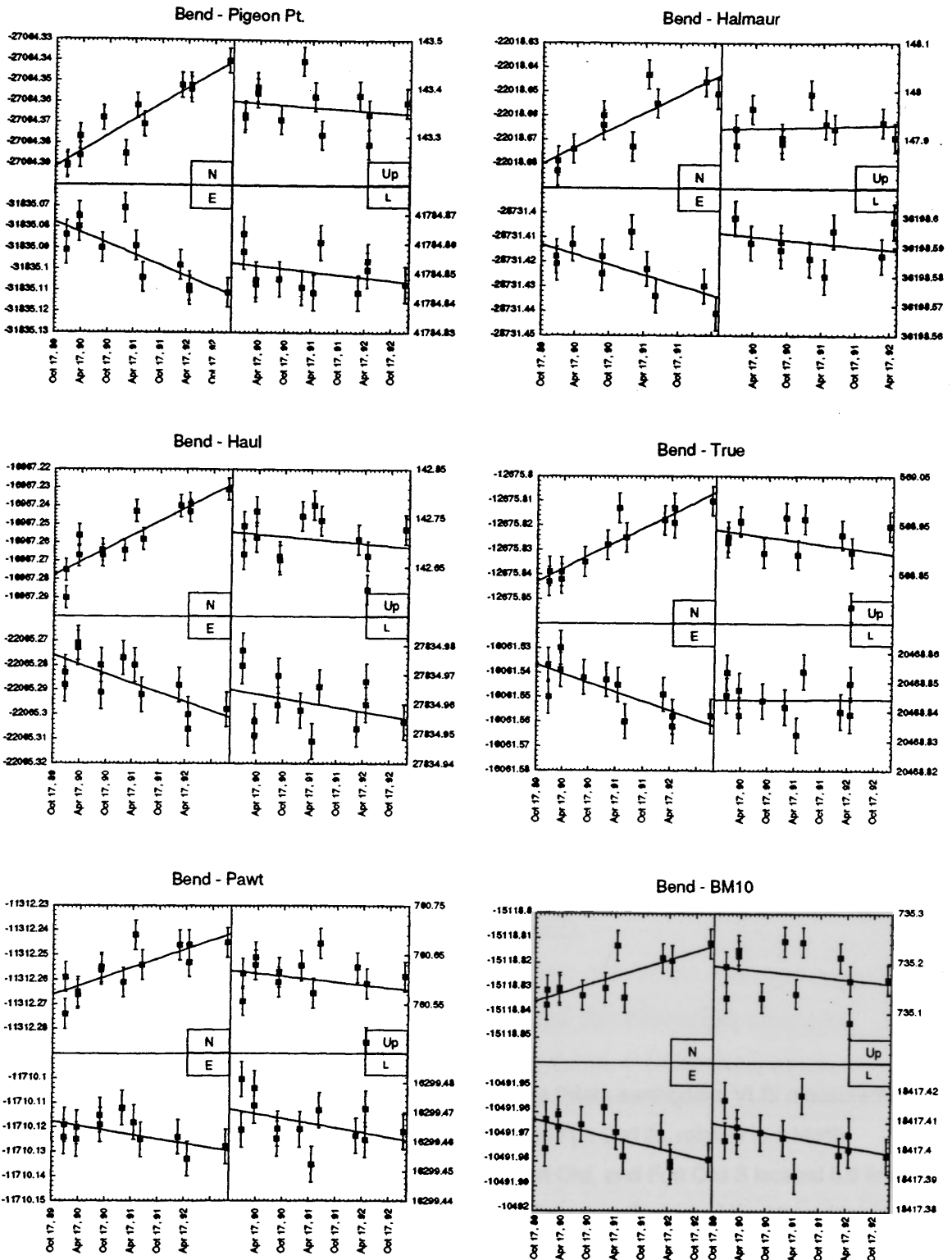
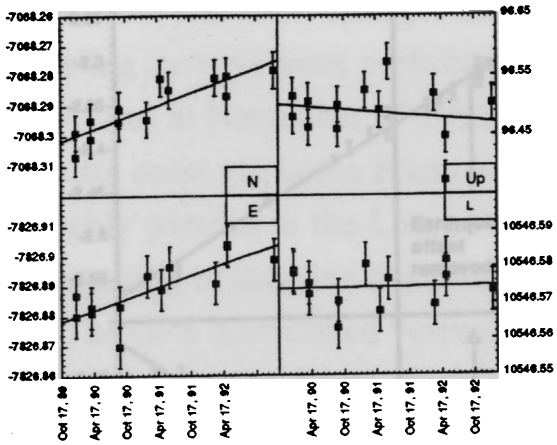
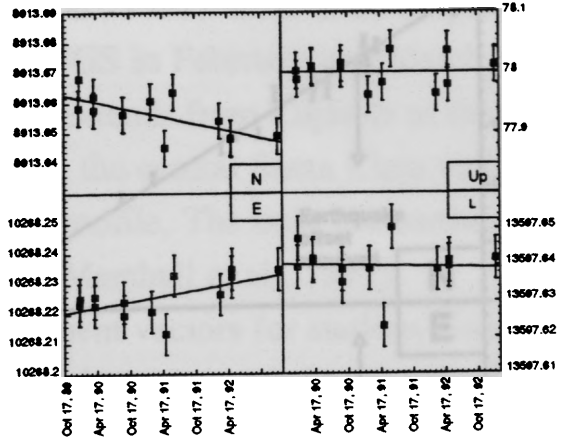


Fig. 5.3 Relative changes in the N, E, and vertical baseline components and line length changes along the Black Mountain profile with respect to site Bend as a function of time. The slope of the line fitted to the data is the relative station velocity.

Bend - Foothill



Bend - Antelnyx



Bend - Bayshore/Bayshore m 1

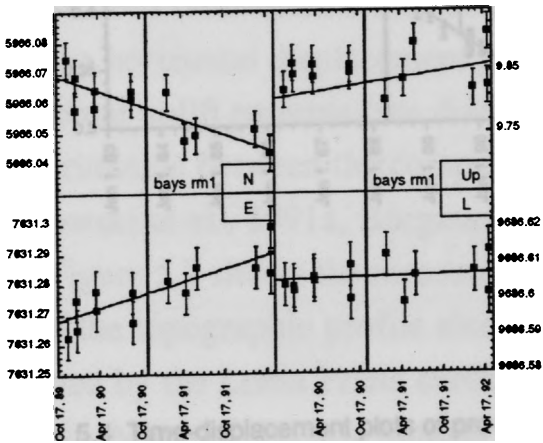


Fig. 5.3 cont.

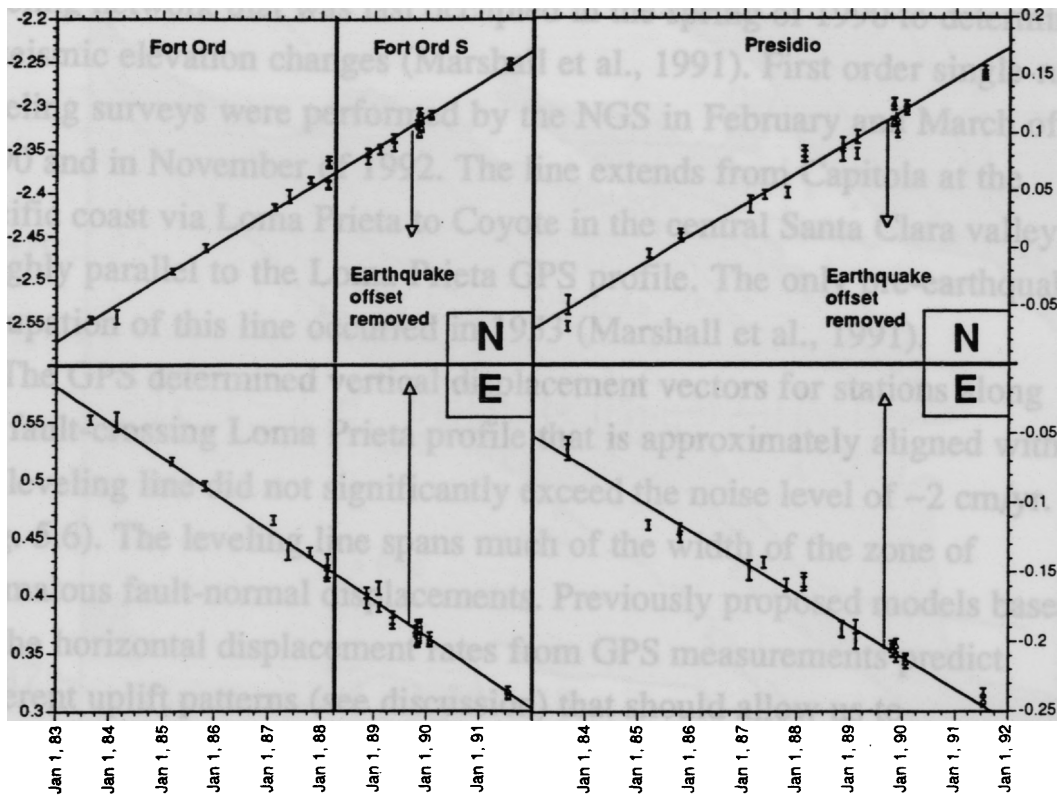


Fig. 5.4 Time-displacement plots of pre- and post-Loma Prieta earthquake VLBI measurements in the San Francisco Bay area (Presidio, Fort Ord, and Fort Ord S), relative to a North American reference frame. The displacements of Fort Ord, and Fort Ord S located 8.9 km to the S are shown on the same plot. Loma Prieta earthquake offsets and the offset introduced in the 1988 change of stations (Fort Ord to Fort Ord S) have been removed from the data (Clark et al., 1990). The line fits are based on the pre-earthquake data at Presidio, and on the Fort Ord data between 1983 and early 1988. The pre- and post-seismic displacement rates at Presidio and at Fort Ord/Fort Ord S are not significantly different.

METHODS: LEVELING DATA AND ANALYSIS

A leveling line across the epicentral area of the M 7.1, 1989 Loma Prieta earthquake (Line 4 of Marshall et al., 1991, Fig. 5.5) has been resurveyed to measure elevation changes associated with the apparently accelerated post-seismic velocity field. This line is part of a larger leveling network that was last occupied in the spring of 1990 to determine coseismic elevation changes (Marshall et al., 1991). First order single-run leveling surveys were performed by the NGS in February and March of 1990 and in November of 1992. The line extends from Capitola at the Pacific coast via Loma Prieta to Coyote in the central Santa Clara valley, roughly parallel to the Loma Prieta GPS profile. The only pre-earthquake occupation of this line occurred in 1953 (Marshall et al., 1991).

The GPS determined vertical displacement vectors for stations along the fault-crossing Loma Prieta profile that is approximately aligned with the leveling line did not significantly exceed the noise level of ~ 2 cm/yr. (Fig. 5.6). The leveling line spans much of the width of the zone of anomalous fault-normal displacements. Previously proposed models based on the horizontal displacement rates from GPS measurements predict different uplift patterns (see discussion) that should allow us to discriminate between the competing models (Linker and Rice, 1991, Lisowski et al., 1991a, Bürgmann et al., 1992).

Figure 5.7 shows the measured post-seismic elevation changes together with the topographic profile along the line and the elevation changes caused by the Loma Prieta earthquake along Line 4 (Marshall et al., 1991). Many of the benchmarks were set during the first post-seismic survey, only four benchmarks constrained the peak uplift during the Loma Prieta earthquake. The data are listed in Table 1 together with the station names and the benchmark locations.

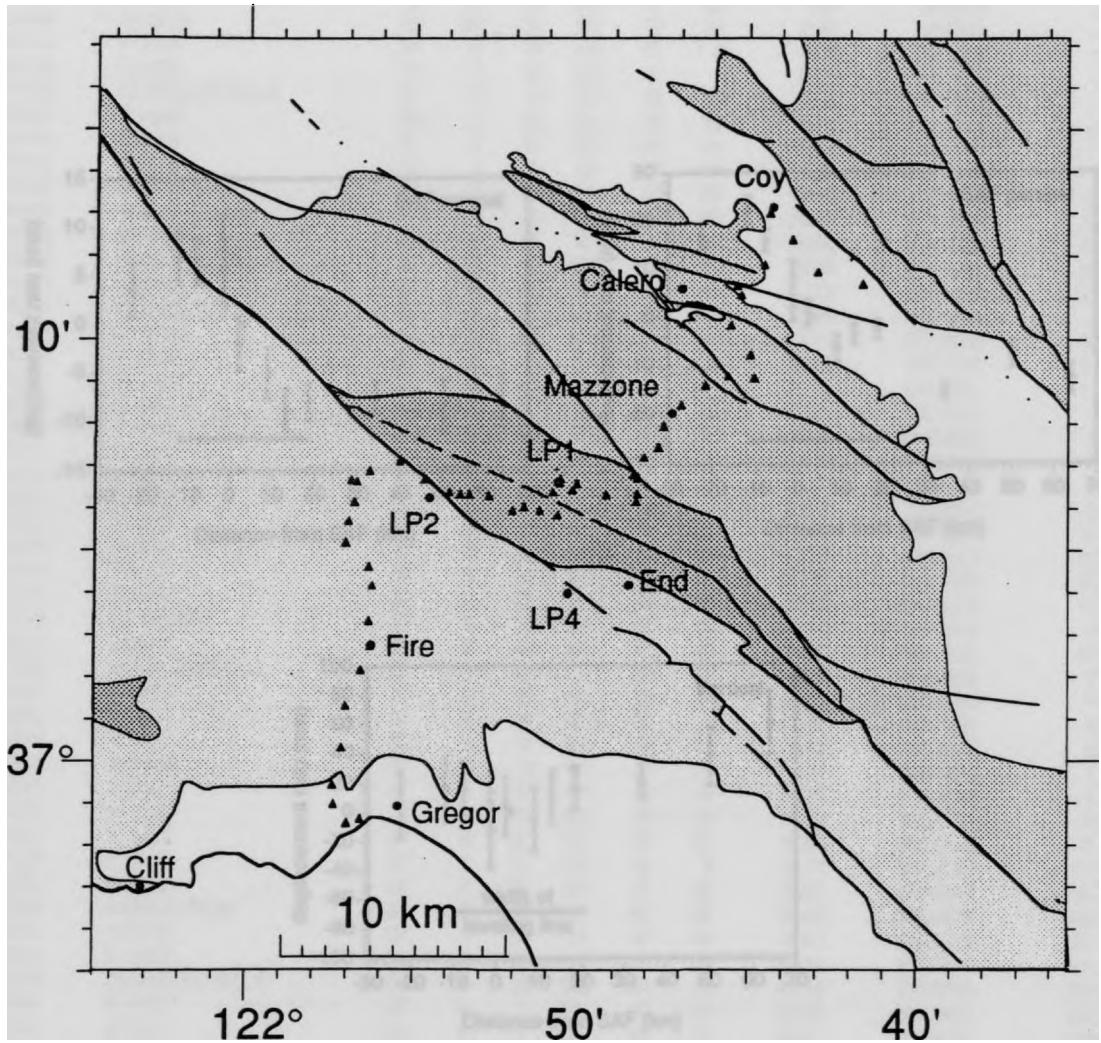


Fig. 5.5 Schematic geologic map of southern San Francisco Bay area showing the location of benchmarks (triangles) of the leveling line. Sites on bedrock (shaded patterns) are not significantly effected by ground-water level changes. Also shown are the location of the nearby stations of the GPS Loma Prieta profile.

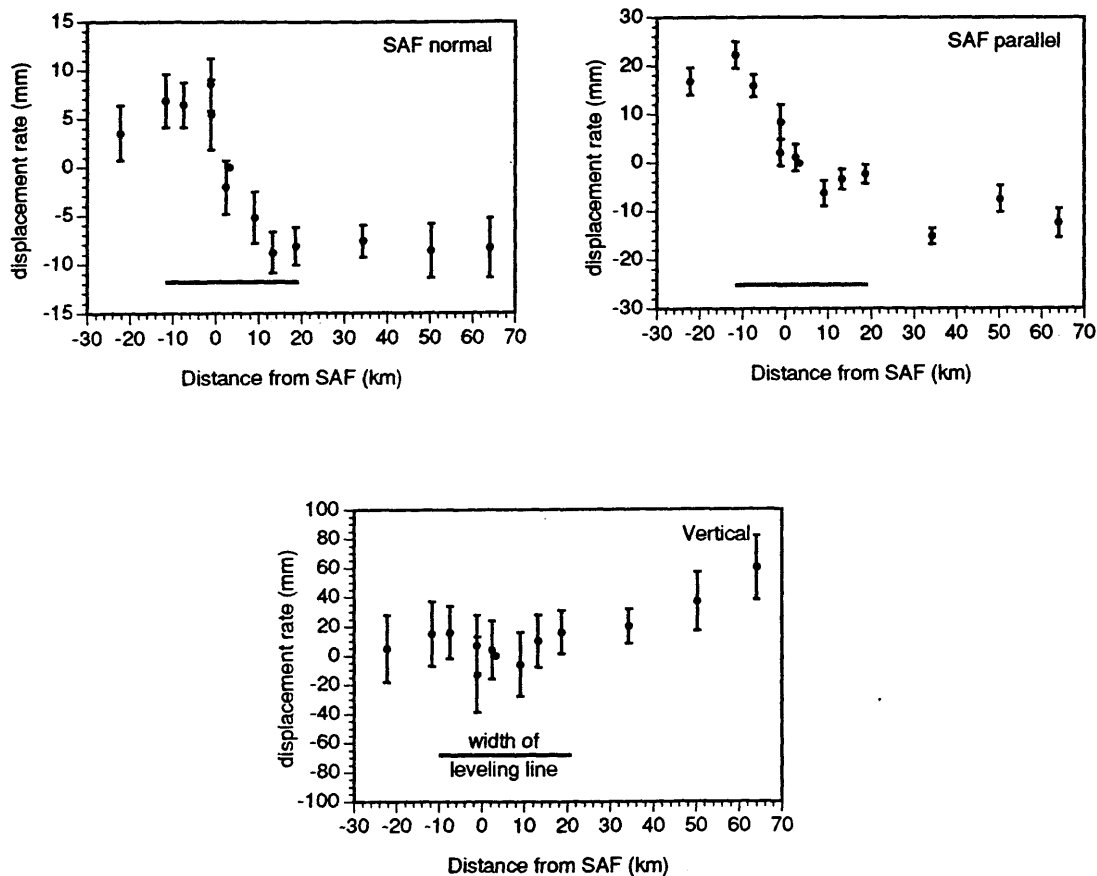


Fig. 5.6 Fault parallel and perpendicular site velocities and uplift rates along the Loma Prieta profile determined from repeated GPS measurements between January 1990 and December 1992; the time spanned by the two leveling surveys. Uplift does not exceed the noise level (1 Sigma = ~2 cm/yr) of the GPS-derived vertical displacements. The leveling survey spans much of the width of anomalous fault perpendicular velocities (thick line).

ACRN	Normal Designation	Latitude			Longitude			Distance (km)	Height (1992) (m)	1992-1990 (mm)
		°	'	"	°	'	"			
GU2285	M 1237	36	58	53	121	56	11	0.85	22.7060	-2.02
GU2286	N 1237	36	58	37	121	56	35	0.00	24.6180	0.00
GU2287	Z 212	36	58	31	121	56	58	0.54	19.4696	0.86
GU2290	P 1237	36	58	23	121	57	10	1.01	16.5193	2.60
GU4168	N 1456	36	58	59	121	57	22	1.63	10.9074	3.72
GU4169	32 WLS	36	59	26	121	57	24	2.47	12.5871	3.23
HS5194	P 1456	37	0	19	121	57	8	4.08	32.4363	3.48
HS5195	Q 1456	37	1	18	121	57	1	6.09	63.0128	3.22
HS5196	CHISELED SQ. A	37	2	9	121	56	35	7.89	69.6912	3.32
HS5197	R 1456	37	2	44	121	56	18	9.12	70.7524	-0.12
HS5198	S 1456	37	3	19	121	56	21	10.31	80.9344	4.43
HS5199	T 1456	37	4	9	121	56	15	12.02	141.7645	6.43
HS5200	U 1456	37	4	36	121	56	21	12.86	176.5290	10.26
HS5201	1940	37	5	1	121	56	57	14.16	253.9460	13.55
HS5202	28 WLS	37	5	41	121	56	57	15.53	339.1622	13.21
HS5203	CHISELED SQ. B	37	6	8	121	56	47	16.45	394.0883	23.41
HS5210	Z 1456	37	6	39	121	56	52	17.76	437.1345	21.01
HS5204	BURDETT	37	6	37	121	56	43	18.06	458.0249	4.42
HS5205	27 WLS	37	6	52	121	56	20	18.76	471.7535	16.74
HS5206	V 1456	37	7	6	121	55	26	20.21	477.2755	11.84
HS5207	W 1456	37	6	40	121	54	40	21.61	548.6984	11.84
HS5208	X 1456	37	6	22	121	53	56	22.91	572.6101	6.25
HS5209	Y 1456	37	6	19	121	53	36	23.59	609.2242	6.21
HS5211	A 1457	37	6	19	121	53	20	24.46	687.6756	4.31
HS5212	B 1457	37	6	17	121	52	45	25.39	762.6576	7.22
HS5213	C 1457	37	5	56	121	52	2	26.77	768.5816	-5.93
HS5214	D 1457	37	6	1	121	51	42	27.45	844.0607	12.75
HS5215	E 1457	37	5	56	121	51	13	28.06	906.5542	12.67
HS5216	F 1457	37	5	49	121	50	41	29.12	939.1038	12.04
HS5217	G 1457	37	6	22	121	50	49	30.50	1024.9336	11.68
HS5218	LP RESET	37	6	39	121	50	38	31.95	1154.1363	8.68
HS5219	LOMA	37	6	41	121	50	35	31.97	1154.7195	10.40
HS5220	LOMA PRIETA 1	37	6	35	121	50	37	32.13	1152.2434	7.90
HS5221	H 1457	37	6	25	121	50	14	31.51	906.7855	7.49
HS5222	J 1457	37	6	35	121	50	6	31.97	870.7284	8.80
HS5223	K 1457	37	6	18	121	49	14	33.50	788.3253	5.26
HS5224	HJH 55	37	6	9	121	48	20	34.91	728.1352	1.93
HS5225	L 1457	37	6	19	121	48	18	35.70	600.7683	-1.48
HS5226	M 1457	37	6	41	121	48	19	36.52	480.6714	-7.92
HS5227	N 1457	37	6	47	121	48	25	37.59	364.0149	-7.39
HS5228	P 1457	37	7	11	121	48	6	38.71	300.7025	-17.70
HS5230	Q 1457	37	7	25	121	47	40	39.81	279.0617	-18.29
HS5229	ANGLE IRON	37	7	25	121	47	39	39.82	276.6817	-18.66
HS5231	HJH 53	37	7	56	121	47	30	40.91	246.2474	-20.28
HS5232	R 1457	37	8	26	121	46	58	42.34	227.6313	-21.64
HS5233	CHISELED SQ. C	37	8	54	121	46	15	43.83	207.0110	-20.22
HS5234	S 1457	37	9	7	121	45	35	44.98	203.2404	-21.88
HS5235	SPIKE	37	9	7	121	45	35	45.01	201.8287	-32.57
HS5236	T 1457	37	9	5	121	44	49	46.25	191.4214	-23.77
HS5237	U 1457	37	9	37	121	44	56	47.28	230.5187	-25.24
HS5239	HJH 51	37	10	20	121	45	30	48.98	156.2777	-26.88
HS5240	V 1457	37	11	3	121	45	12	50.86	145.6818	-28.85
HS5241	W 1457	37	11	16	121	45	19	51.57	94.4624	-31.73
HS5242	X 1457	37	11	47	121	44	31	53.08	76.8338	-32.99
HS2775	L 174	37	12	22	121	43	41	54.74	79.7462	-37.71
HS2776	P 19	37	13	0	121	44	21	56.29	77.5943	-36.48
HS2773	Y 176	37	11	39	121	42	56	56.48	88.5071	-39.85
HS5407	HPGN CA 04 03	37	11	20	121	41	38	58.86	102.2432	-

Table 5.1 Post-seismic elevation changes along leveling Line 4

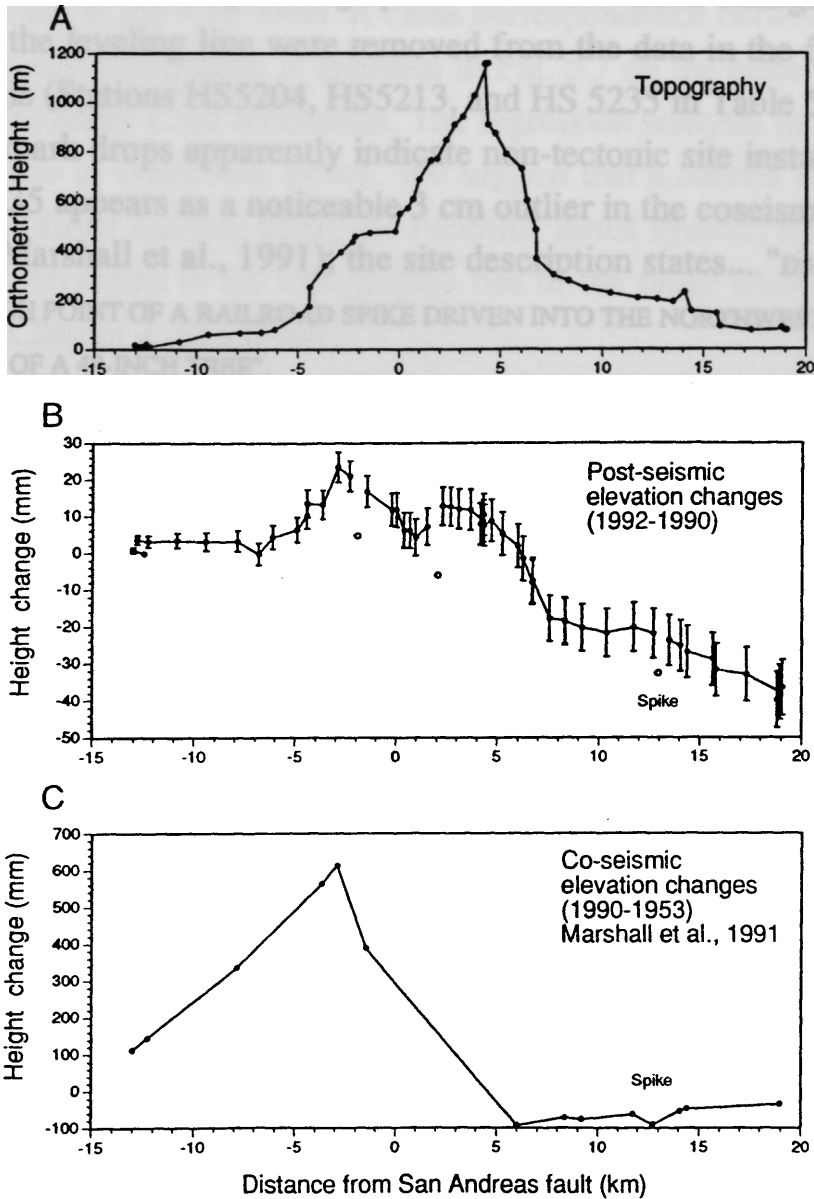


Fig. 5.7 Elevation changes following the Loma Prieta earthquake determined by leveling. (a) Topographic profile along Line 4 across Loma Prieta. (b) Difference in relative heights measured in January and February 1990 and November 1992. Random errors accumulate with the square root of line length along the line. Three drop outs due to site instability are apparent. (c) Elevation changes along Line 4 during the 1989 Loma Prieta earthquake. Uplift is centered SW of the San Andreas fault, Loma Prieta peak subsided.

Corrections and error analysis

Three downward pointing spikes of the elevation changes recorded along the leveling line were removed from the data in the following analysis (Stations HS5204, HS5213, and HS 5235 in Table 5.1). These benchmark drops apparently indicate non-tectonic site instability. Station HS 5235 appears as a noticeable 3 cm outlier in the coseismic results as well (Marshall et al., 1991); the site description states... "DATUM POINT IS THE HIGH POINT OF A RAILROAD SPIKE DRIVEN INTO THE NORTHWEST FACE OF THE TRUNK OF A 48-INCH TREE".

The data are corrected for systematic errors due to level collimation, rod calibration, thermal expansion of the rod tapes, earth tides and associated gravitational effects, and atmospheric refraction by the NGS. Elevations are given as normal orthometric heights (Table 5.1). We examine the corrections applied by NGS by plotting the correction of each section difference and the cumulative magnitude of corrections along the leveling line (Fig. 5.8a). The corrections cause up to 4 mm height differences. Between 20 and 40 km along the line (the zone of highest post-seismic uplift) the correction suggests that the raw data underestimates the elevation by up to 4 mm.

Random error is expected to accumulate with the square root of distance and was estimated as $0.8 \text{ mm}/\sqrt{\text{km}}$ for the first post-earthquake survey based on double-run sections (Marshall et al., 1991). The corresponding error of the second post-seismic survey is $0.65 \text{ mm}/\sqrt{\text{km}}$ based on 10 double-run sections. Random error estimates based on the observed misclosure of circuits that included Line 4 in 1990 are $2.5 \text{ mm}/\sqrt{\text{km}}$ (Marshall et al., 1991), however, it is not possible to know how much Line 4 itself contributes to the misclosure.

Slope-dependent systematic errors may have been caused by errors in the rod correction applied to the leveling data (e.g., Stein, 1981). We test for the accumulation of elevation-dependent errors by performing an unweighted least squares fit of geodetic tilt onto topographic slope along individual sections (Stein, 1981). We removed outliers that are apparent

spikes in the data (Fig. 5.7). The correlation shown in Fig. 5.8b is not significant at the 95% level. A close correspondence between elevation change and topography is apparent in Fig. 5.7 on the eastern flank of the southern Santa Cruz Mountains. The regression analysis indicates that this is not due to systematic errors. We suggest that a current deformation source (thrust faulting along the Foothills thrust system) may in the past have contributed to the topographic rise of the range (Arrowsmith et al., 1992, Chapter 4, this thesis).

The five northeastern most stations along Line 4 are located in unconsolidated Santa Clara Valley sediments. They may be affected by well-water withdrawal and seasonal changes in water level. The following analysis shows that water induced subsidence is not a significant problem. Subsidence corrections can be estimated if a pre-earthquake elevation change had been determined and can be corroborated by well-water level changes. No subsidence corrections were applied by Marshall et al. (1991) to the coseismic elevation changes of Line 4 because no pre-earthquake elevation-change record exists and because most of the benchmarks are on bed rock. Figure 5.9 shows a close-up view of the distribution of leveling benchmarks and nearby water wells in Santa Clara Valley. Also shown are the depth-to-water-table curves for three of the wells. On average, the ground water table of eight wells dropped 18 ± 7 m between the two post-seismic surveys. Taking the northeastern most bedrock station (HS5240) as a reference site, the sites located in the Santa Clara Valley sediments subsided by up to 10 mm in the same time period.

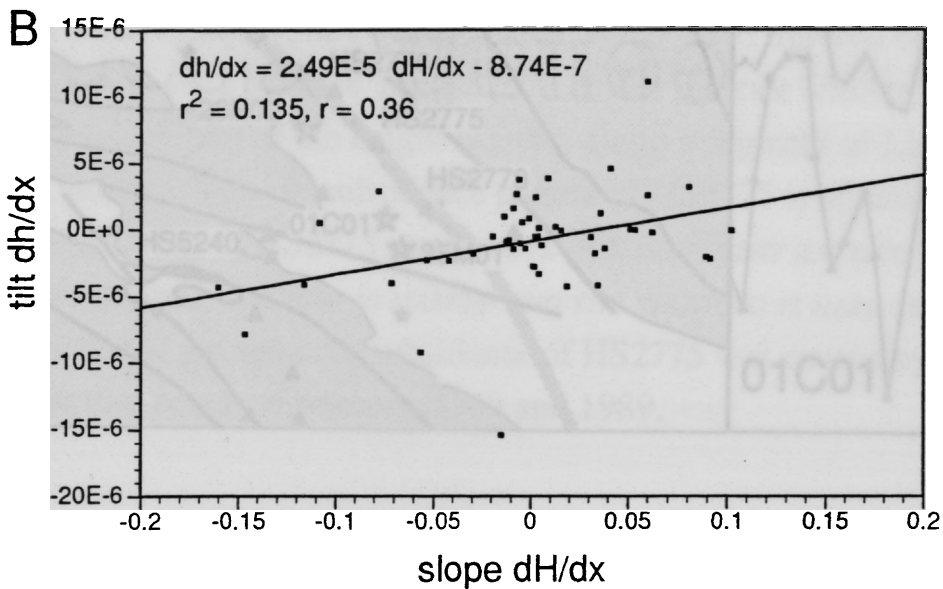
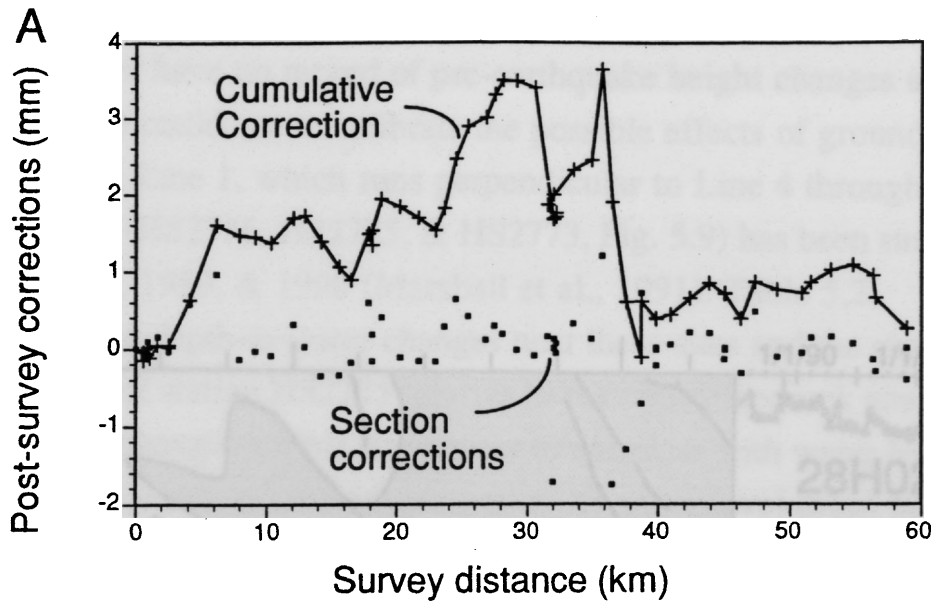


Fig. 5.8 Corrections and error analysis. (a) Comparison of uncorrected relative height measurements and the relative heights after corrections for systematic errors due to level collimation, rod calibration, thermal expansion of the rod tapes, earth tides and associated gravitational effects, magnetic effects, and atmospheric refraction by the NGS. The differences for each leveled section (squares) and the cumulative magnitude of corrections along the leveling line (crosses) indicate that the raw data underestimated the magnitude of uplift by up to 4 mm. (b) Test for slope-dependent errors caused by rod calibration errors. Tilt is plotted against topographic slope revealing no significant correlation that would indicate systematic rod-related errors after the NGS corrections.

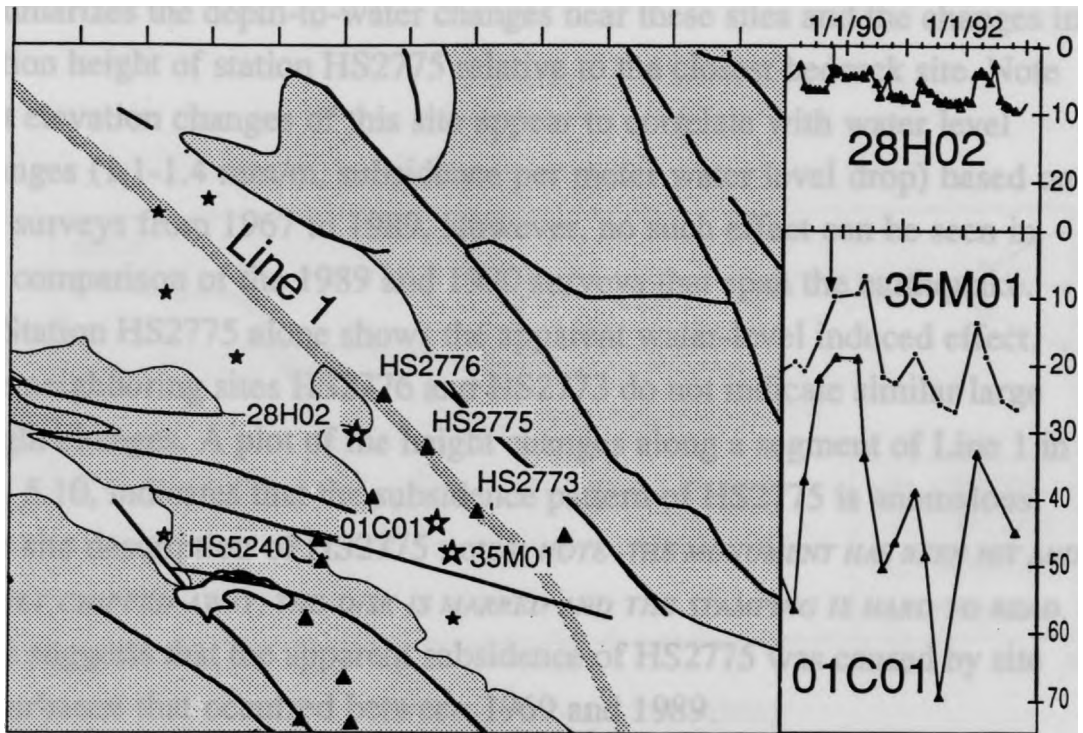


Fig. 5.9 Close-up of NE section of leveling line showing the location of leveling benchmarks (triangles) and water wells (stars) used to test for correlation between ground water-table changes and height changes along Line 1 in the last 20 years (Thick shaded line) . The insets show that well water levels subsided during the post-seismic period because of seasonal variations. On average, the water level subsided 18 ± 7 m in eight wells.

Whereas we have no record of pre-earthquake height changes along Line 4 that we could use to calibrate the possible effects of ground water-level changes, Line 1, which runs perpendicular to Line 4 through three common sites (HS2776, HS2775, & HS2773, Fig. 5.9) has been surveyed in 1967, 1969, 1989, & 1990 (Marshall et al., 1991). Table 5.2 summarizes the depth-to-water changes near these sites and the changes in station height of station HS2775 relative to the closest bedrock site. Note that elevation changes of this site appear to correlate with water level changes (1.1-1.4 mm/m, subsidence per meter water level drop) based on the surveys from 1967 to 1989. However, no such effect can be seen in the comparison of the 1989 and 1990 surveys that span the earthquake.

Station HS2775 alone shows the apparent water-level induced effect. The neighboring sites HS2776 and HS2773 do not indicate similar large height changes. A plot of the height changes along a segment of Line 1 in Fig. 5.10, indicates that the subsidence pattern of HS2775 is anomalous. The site description of HS2775 notes: *NOTE--THE MONUMENT HAS BEEN HIT AND PARTLY CHIPPED AWAY, THE DISK IS MARRED AND THE STAMPING IS HARD TO READ.* This suggests that the apparent subsidence of HS2775 was caused by site disturbance that occurred between 1969 and 1989.

Table 5.2 Well water changes between surveys of Line 1
Height change relative to bedrock site

Mean Well Level Change (n=8)	1992-1990(HS5240-HS2775)		mm/m
-18.30 ±7.4	-8.9 mm	->	0.5
Mean Well Level Change (n=2)	1989-1967(HS4141-HS2775)		
-23.90	-34 mm	->	1.4
Mean Well Level Change (n=2)	1989-1969(HS4141-HS2775)		
-32.25	-37 mm	->	1.1
Mean Well Level Change (n=2)	1990-1989(HS4141-HS2775)		
23.80	2.5 mm	->	0.1

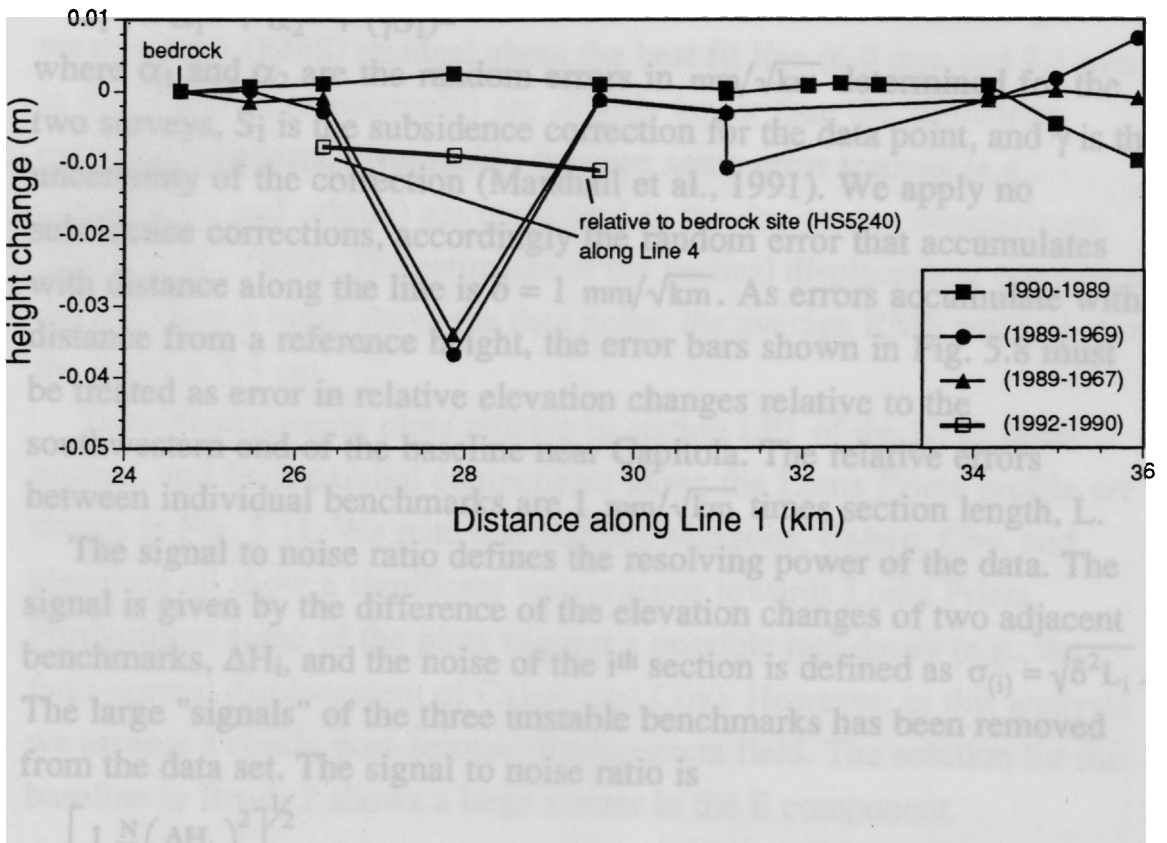


Fig. 5.10 Height changes relative to a bedrock site 24 km along leveling Line 1 of Marshall et al. (1991). The line runs approximately perpendicular to Line 4 and includes three stations surveyed with Line 4 (Fig. 5.9). Site HS2775 near 28 km apparently dropped between 1969 and 1989, probably because the site was damaged during this time. The three sites surveyed in 1992 are shown relative to the nearest bedrock site (HS5240) along Line 4.

The height correction suggested by the correlation between site elevations of HS2776 and water-level changes is 0.04 - 0.08 mm/m. A water-table drop of 18 m between 1990 and 1992 would suggest that a correction of $\sim +1$ mm be applied for the stations located in the Santa Clara sediments. As this appears to be well within the noise level of the leveling data, we conclude that no height corrections caused by well water level changes are necessary.

Assuming that the errors of the two campaigns are not correlated, the relative uncertainty of the determined elevation change of a point is

$$\delta_i^2 = \alpha_1^2 + \alpha_2^2 + (\gamma S_i)^2$$

where α_1 and α_2 are the random errors in $\text{mm}/\sqrt{\text{km}}$ determined for the two surveys, S_i is the subsidence correction for the data point, and γ is the uncertainty of the correction (Marshall et al., 1991). We apply no subsidence corrections, accordingly the random error that accumulates with distance along the line is $\delta = 1 \text{ mm}/\sqrt{\text{km}}$. As errors accumulate with distance from a reference height, the error bars shown in Fig. 5.8 must be treated as error in relative elevation changes relative to the southwestern end of the baseline near Capitola. The relative errors between individual benchmarks are $1 \text{ mm}/\sqrt{\text{km}}$ times section length, L .

The signal to noise ratio defines the resolving power of the data. The signal is given by the difference of the elevation changes of two adjacent benchmarks, ΔH_i , and the noise of the i^{th} section is defined as $\sigma_{(i)} = \sqrt{\delta^2 L_i}$. The large "signals" of the three unstable benchmarks has been removed from the data set. The signal to noise ratio is

$$\left[\frac{1}{N} \sum_i^N \left(\frac{\Delta H_i}{\sigma_i} \right)^2 \right]^{1/2} = 3.9.$$

Where $N=53$ is the total number of sections used in the calculation (Marshall et al., 1991). This value compares with the signal to noise ratio of 9.3 of the coseismic uplift along Line 4 that had very large elevation changes (Fig. 5.7), but also much larger associated errors (Marshall et al., 1991).

POST-LOMA PRIETA EARTHQUAKE DISPLACEMENT FIELD

Horizontal displacement field from GPS

Figure 5.3 shows the changes with time of the relative station coordinates along the Black Mountain profile in the N, E, and vertical components, and line-length changes, relative to station Bend (Fig. 5.1). The least-squares estimates of the relative station velocities are shown. Within the measurement errors we see no evidence for changes in velocity during the ~3 years following the earthquake. The average root-mean-square (RMS) residual about the best fit line (6.0 mm and 7.1 mm in the N and E, respectively) are slightly larger than the short-term precision estimates, presumably because some error sources (e.g., atmospheric and orbital) are correlated in the day-to-day comparisons (Davis et al., 1989). The estimates of the vertical displacement component did not show a trend above the data noise; the average RMS residual about the mean is 3.3 cm.

Time-displacement plots relative to station LP1 of the N, E, fault-normal, and fault-parallel components along the Loma Prieta profile are shown in Fig. 5.11. We note that stations Mazzone, Calero, Coy, and Hamilton all show a significant convergence towards Loma Prieta. Furthermore some of the plots suggest a possible rate decay (e.g., the fault-normal displacement of Calero and Coy). However, in this analysis we assume a steady post-seismic displacement field. The solution for the baseline to Brush 2 shows a large scatter in the E component.

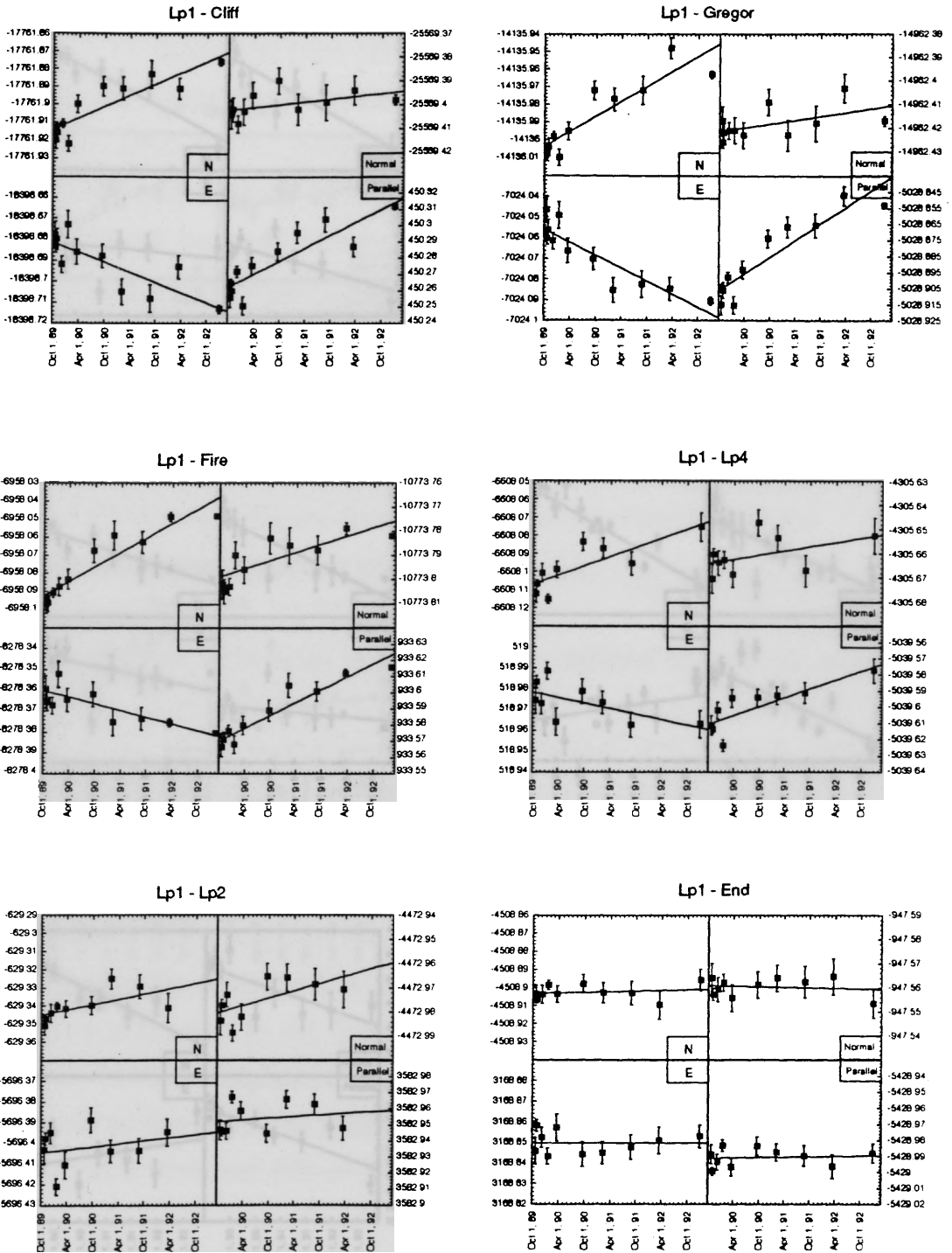


Fig. 5.11 Changes in the N, E, and fault-normal and parallel station positions along the Loma Prieta profile as a function of time.

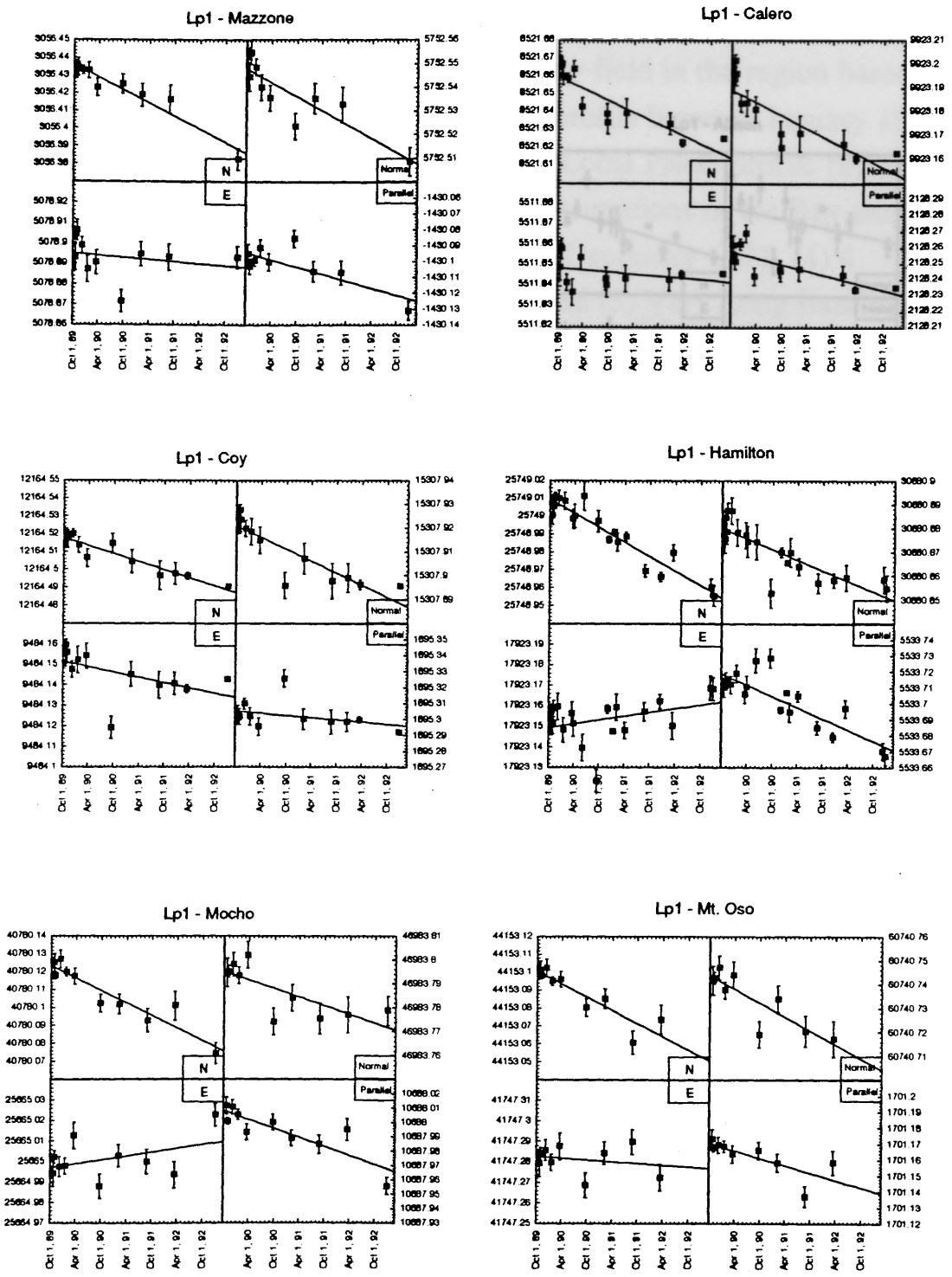


Fig. 5.11 cont. Fault normal convergence NE of the San Andreas fault (Mazzone through Hamilton) appear to have leveled off in late 1991.

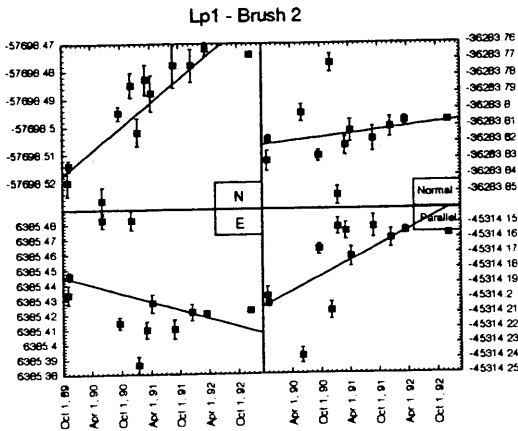
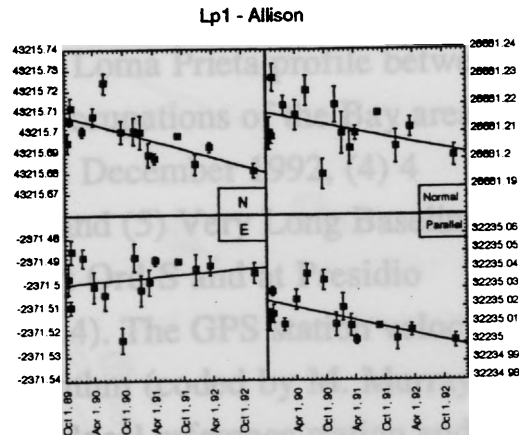
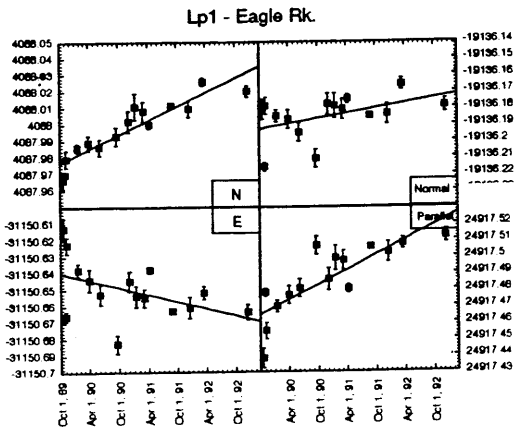


Fig. 5.11 cont.

Figure 5.12 shows the post-seismic velocity field in the region based on (1) 9 occupations of the Black Mountain profile between January 1990 and January 1993, (2) 12 occupations of the Loma Prieta profile between October 1989 and January 1993, (3) 12-14 occupations of the Bay area monitor-network between October 1989 and December 1992, (4) 4 occupations of ties between LP1 and Bend, and (5) Very Long Baseline Interferometry (VLBI) data collected at Fort Ord S and at Presidio between October 1989 and July 1991 (Fig. 5.4). The GPS station velocities were determined using a least squares algorithm (coded by M. Murray) that computes station velocities relative to a local reference station and the associated 95% error ellipses from the station coordinates and the associated covariance matrices of each campaign.

The velocities of the VLBI stations Fort Ord S and Presidio are shown relative to a North American reference frame defined by a fixed origin at the Westford, Massachusetts VLBI station and a fixed azimuth from Westford to the VLBI station at Richmond, Florida (Clark et al., 1990). The GPS network is tied to the VLBI reference frame through the common site at Fort Ord S/Brush 2.

Also shown in Fig. 5.12 are the pre-earthquake velocities (see below) for comparison assuming that Mt. Oso (the easternmost station) did not change its velocity. Stations SW of the San Andreas fault move approximately parallel to the San Andreas fault. Station Foothill is anomalous, having a higher NW-directed velocity than stations immediately to the SW. The most noteworthy result is the apparent zone of convergence centered NE of Loma Prieta mountain (more apparent in Fig. 5.12).

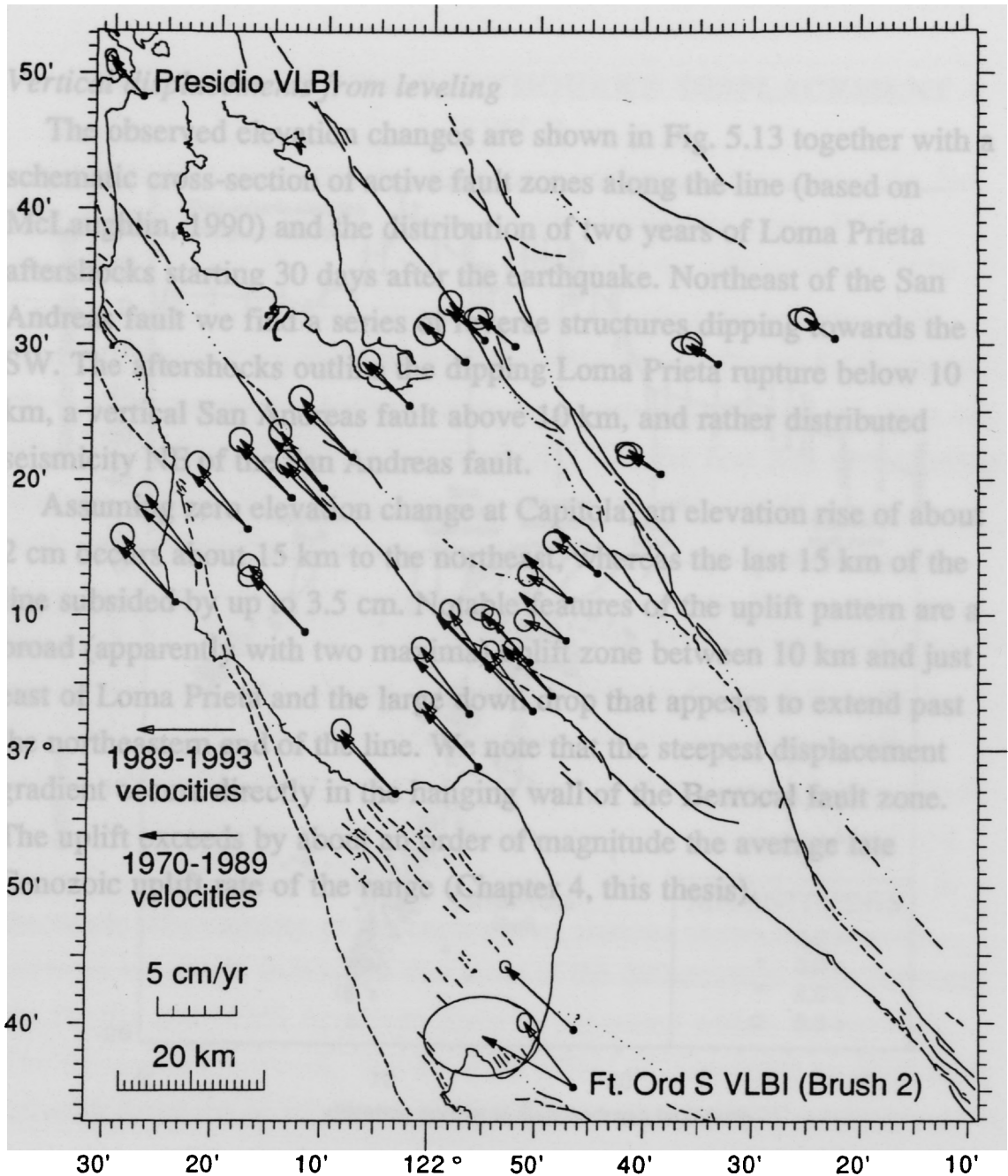


Fig. 5.12 Post-seismic velocity field from GPS and VLBI measurements. The velocities and associated errors were computed relative to stable North America. The GPS network is tied to the VLBI reference frame through the common site at Fort Ord S-Brush 2. A shift of the whole network relative to the pre-earthquake velocities shown in Fig. 5.14a indicates that the tie to the VLBI network is in error in one of the surveys. Therefore we show the pre-earthquake velocities under the assumption that Mt. Oso was not affected by the post-seismic transients.

Vertical displacements from leveling

The observed elevation changes are shown in Fig. 5.13 together with a schematic cross-section of active fault zones along the line (based on McLaughlin, 1990) and the distribution of two years of Loma Prieta aftershocks starting 30 days after the earthquake. Northeast of the San Andreas fault we find a series of reverse structures dipping towards the SW. The aftershocks outline the dipping Loma Prieta rupture below 10 km, a vertical San Andreas fault above 10 km, and rather distributed seismicity NE of the San Andreas fault.

Assuming zero elevation change at Capitola, an elevation rise of about 2 cm occurs about 15 km to the northeast, whereas the last 15 km of the line subsided by up to 3.5 cm. Notable features of the uplift pattern are a broad (apparently with two maxima) uplift zone between 10 km and just east of Loma Prieta and the large down drop that appears to extend past the northeastern end of the line. We note that the steepest displacement gradient occurs directly in the hanging wall of the Berrocal fault zone. The uplift exceeds by about an order of magnitude the average late Cenozoic uplift rate of the range (Chapter 4, this thesis).

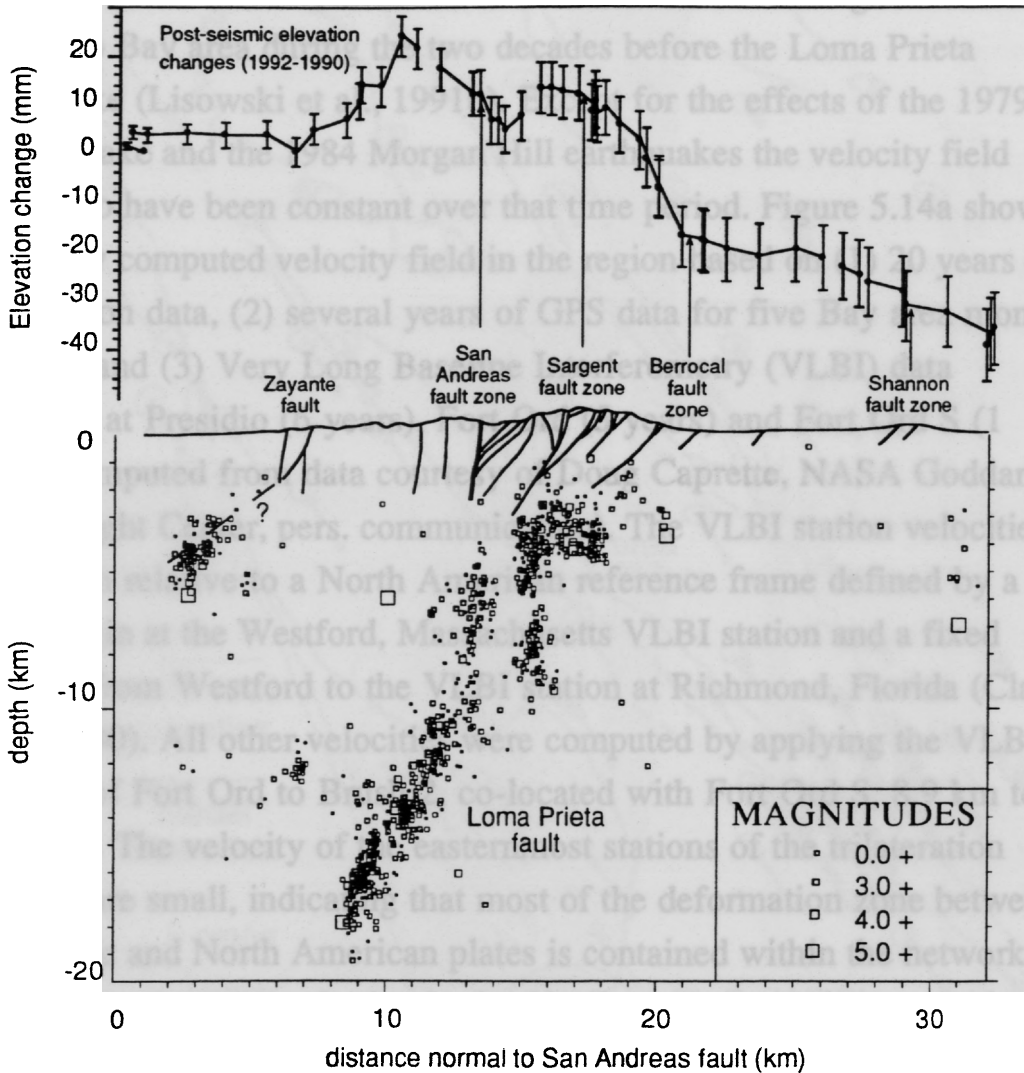


Fig. 5.13 SW-to-NE cross-section (Gregor to Coy in Fig. 5.1) of the geology (modified from McLaughlin, 1990) and Loma Prieta aftershocks across the San Andreas fault system. Also shown are the post-seismic elevation changes from leveling. Note that the steepest gradient in the elevation changes is located in the hanging wall of the Berrocal fault, which also appears to be associated with high aftershock activity. The plotted earthquakes are from a 15 km wide zone centered on the line of section (box in Fig. 5.17) and include all well-located events from one month after the Loma Prieta earthquake until December, 1992.

PRE-LOMA PRIETA EARTHQUAKE DISPLACEMENT FIELD

Trilateration measurements have been carried out throughout the San Francisco Bay area during the two decades before the Loma Prieta earthquake (Lisowski et al., 1991b). Except for the effects of the 1979 Coyote Lake and the 1984 Morgan Hill earthquakes the velocity field appears to have been constant over that time period. Figure 5.14a shows the newly computed velocity field in the region based on (1) 20 years of trilateration data, (2) several years of GPS data for five Bay area monitor stations, and (3) Very Long Baseline Interferometry (VLBI) data collected at Presidio (6 years), Fort Ord (5 years) and Fort Ord S (1 year) (computed from data courtesy of Doug Caprette, NASA Goddard Space Flight Center, pers. communication). The VLBI station velocities are shown relative to a North American reference frame defined by a fixed origin at the Westford, Massachusetts VLBI station and a fixed azimuth from Westford to the VLBI station at Richmond, Florida (Clark et al., 1990). All other velocities were computed by applying the VLBI velocity of Fort Ord to Brush 2, co-located with Fort Ord S, 8.9 km to the south. The velocity of the easternmost stations of the trilateration network are small, indicating that most of the deformation zone between the Pacific and North American plates is contained within the network. The trilateration network, that by itself offers no constraint on rigid-body network rotations or translations, is also linked to the GPS network through common benchmarks (or ties between co-located trilateration and GPS benchmarks) at Loma Prieta, Eagle Rock, Allison, Hamilton, and Brush 2 (Fig. 5.1).

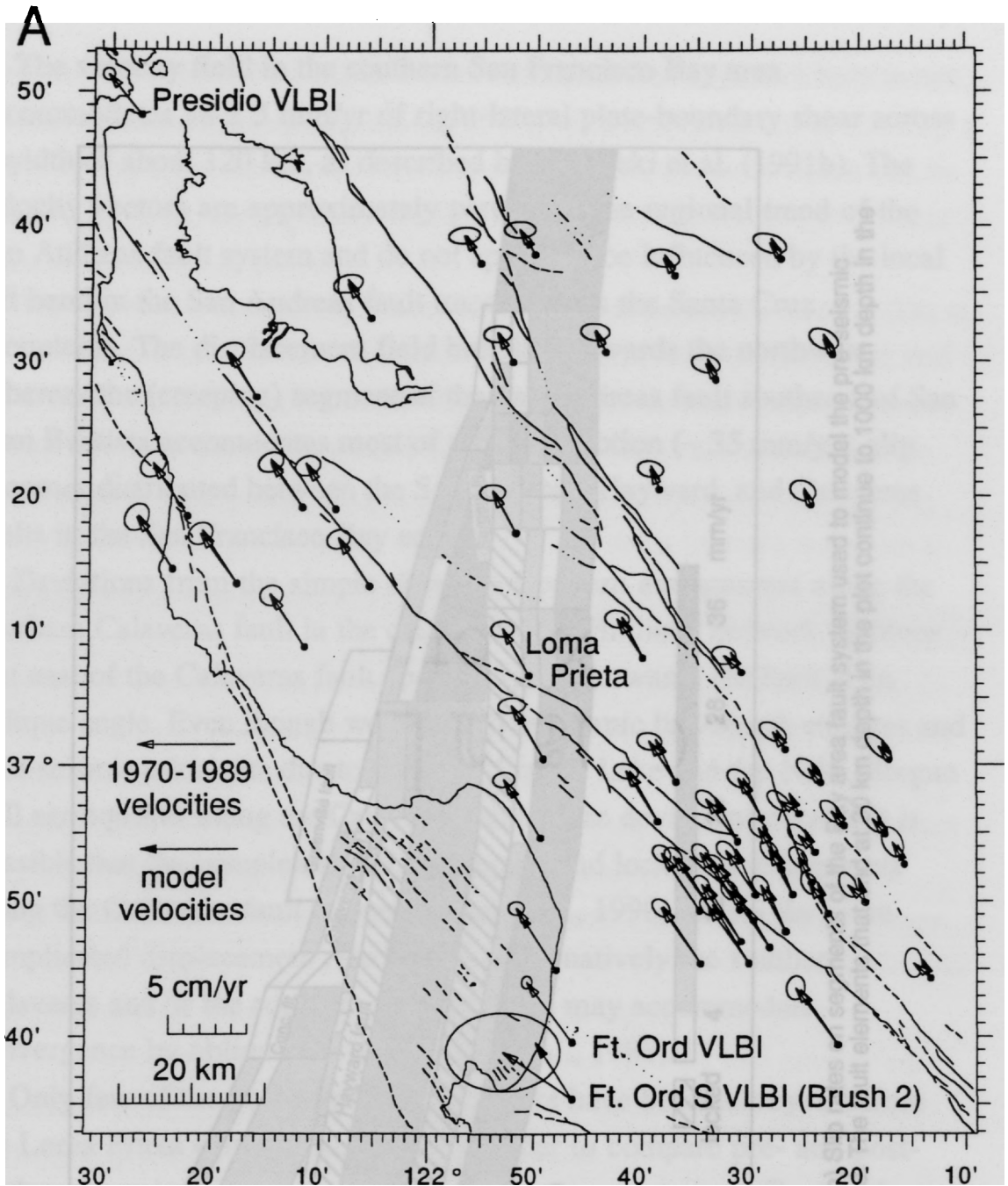


Fig. 5.14 (a) Comparison of pre-Loma Prieta earthquake site velocities (with 95% error ellipses) in the southern San Francisco Bay region determined from VLBI, trilateration, and GPS measurements with displacements computed from an elastic model (filled arrow heads, no ellipses) derived by linear inversion of the pre-seismic data. All displacements are shown relative to a North American VLBI reference frame.

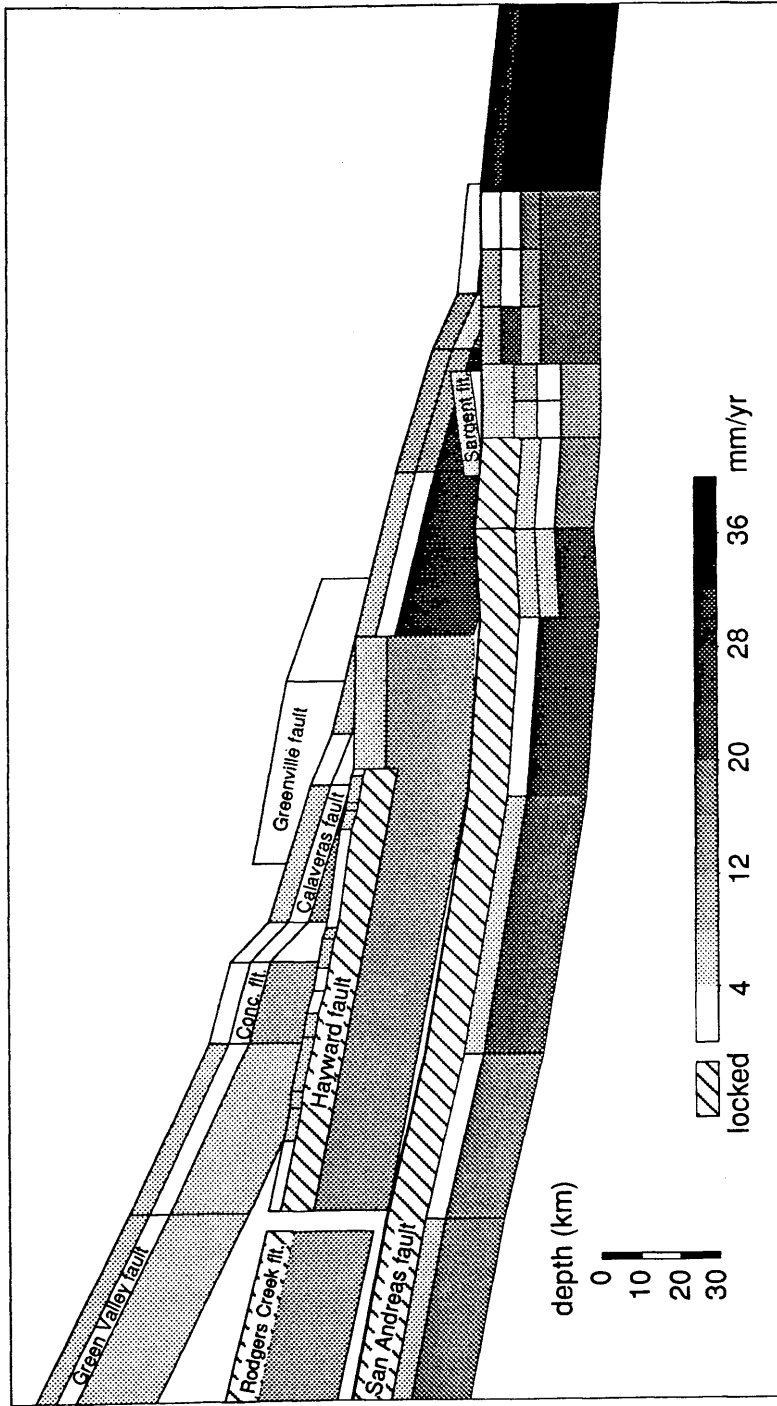


Fig. 5.14 cont. (b) Slip rates on segments of the Bay area fault system used to model the pre-seismic displacement field. The fault elements that end at 30 km depth in the plot continue to 1000 km depth in the model.

The velocity field in the southern San Francisco Bay area accommodates 38 ± 5 mm/yr of right-lateral plate-boundary shear across a width of about 120 km, as described by Lisowski et al. (1991b). The velocity vectors are approximately parallel to the regional trend of the San Andreas fault system and do not appear to be influenced by the local left bend in the San Andreas fault trace through the Santa Cruz Mountains. The displacement field broadens towards the northwest. Whereas the (creeping) segment of the San Andreas fault southeast of San Juan Bautista accommodates most of the plate motion (~ 35 mm/yr), slip becomes distributed between the San Andreas, Hayward, and Calaveras faults in the San Francisco Bay area.

Deviations from the simple shear flow pattern are apparent along the southern Calaveras fault in the closely spaced Hollister network. Stations just east of the Calaveras fault appear to move towards the fault at an oblique angle. Even though we removed coseismic line length changes and post-seismic transients due to the 1979 Coyote Lake and the 1984 Morgan Hill earthquakes along the Calaveras fault, these deviations persist. It is possible that the complex series of creeping and locked fault segments along the Calaveras fault (Oppenheimer et al., 1990) causes the more complicated displacement rate vectors. Alternatively the southern Calaveras and or the southern Sargent faults may accommodate convergence by oblique slip (Matsu'ura et al., 1986).

Only few of the post-seismic benchmarks have been surveyed before the Loma Prieta earthquake, so that in order to compare pre- and post-earthquake velocities we must interpolate between stations. To do this, we developed a mechanical model of the pre-seismic displacement field. Uniform-slip boundary elements in an elastic, homogenous, and isotropic half space represent the Bay area faults. Inter-seismic shear about a locked upper crustal strike-slip fault can be approximated by slip on a buried fault plane below the seismic zone at a rate comparable to the average geologic slip rate of the fault (e.g., Lisowski et al., 1991b). Surface creep on the Hayward, Calaveras, and the central San Andreas

fault can be modeled by shallow fault elements. Our objective here is not to find the correct kinematic model of Bay area tectonics, but to develop a close fitting approximation of the pre-seismic velocity field which can be used to compute the expected velocities of stations for which pre-seismic velocities are not available.

We develop a best fitting model using a linear inversion method (Du et al., 1992) that inverts the horizontal displacement field (trilateration and GPS data) for right-lateral strike slip magnitudes on individual segments of the Bay area faults shown in Fig. 5.14b. All faults are assumed to be vertical with no dip-slip component. A priori constraints of the starting model come from geologically determined slip rates (closely based on a compilation of Lienkaemper et al., 1992). The fault model predicts the following features (Fig. 5.14b): (1) Deep (> 15 km) slip on the peninsular segment of the San Andreas fault at about 20-25 mm/yr; (2) deep slip (> 11 km) on the Hayward fault at about 14 mm/yr; (3) deep slip (> 10 km) on the northern Calaveras fault at about 10-12 mm/yr and at up to 28 mm/yr on the southern Calaveras fault; and (4) shallow creep on the East Bay and southern San Andreas at rates comparable to the measured a priori values. The deep slip rate on the southern Calaveras fault appears too high and may be related to the effects of the Coyote Lake and Morgan Hill earthquakes that occurred on the fault during the measurement period. More complex models with denser grid spacing and smoothing constraints may allow us to determine a more detailed view of the inter-seismic slip distribution on the Bay area faults.

Figure 5.14a shows a comparison of the measured station velocities and the model displacements with the station at Loma Prieta serving as reference site (i.e., the model velocities are adjusted so that Loma Prieta moves at the measured velocity). We note that most velocities are fit well within their 95% uncertainties except for several of the sites near the southern Calaveras fault. The model slightly underpredicts the velocities southwest of the San Andreas fault south of Loma Prieta. The model faults shown in Fig. 5.14b can now be used to compute the predicted pre-

seismic displacements of the post-seismic network. Figure 5.12 shows the measured post-seismic velocities in comparison with pre-earthquake velocities, either measured at these sites or derived from the mechanical model. For this comparison we adjusted the pre-earthquake velocities by a rigid body translation so that Mt. Oso moves at the post-earthquake velocity.

DATA INTERPRETATION AND MODEL

Post-seismic strain anomaly

Over the 60 km long Black Mountain profile, from the Pacific coast (Pigeon Pt.) to just east of the Hayward fault (Antelinx), 22 ± 5 mm/yr of right-lateral shear has occurred along the profile since the earthquake. The post-seismic displacement rates do not differ significantly from the pre-earthquake rate of 20 ± 4 mm over approximately the same width.

Whereas only minor changes have been observed along the Black Mountain profile 44 km NW of the 1989 epicenter, measurements of the Loma Prieta profile show significant changes in displacement rates from pre-earthquake values (Lisowski et al., 1991). GPS stations within 20 km from the San Andreas fault, show significant deviations in both magnitude and orientation from pre-seismic values. The difference between the post- and pre-earthquake velocities plotted in Fig. 5.15a represents the component of the measured signal that exceeds the secular deformation field. At sites where velocities have been measured before and after the earthquake the difference between the two vectors and its uncertainty is shown. Elsewhere, the predicted post-seismic displacements from the boundary element model are subtracted from the post-seismic measurements, and the error ellipses are determined under the assumption that the errors in the pre-earthquake velocities are equal to those in the post-earthquake data. The plotted velocity vectors are shown assuming that the motion of Mt. Oso is not affected by the Loma Prieta earthquake.

Significant velocity increases and reorientations occurred in the near field of the earthquake rupture. Fault-parallel velocities increased to the SW of the San Andreas. There has also been a large fault-normal contraction, centered to the NE of the San Andreas fault. We find that the post-seismic displacement rates at distances $>\sim 20$ km from the epicenter are indistinguishable, within errors, from secular displacement rates. A noticeable exception is the displacement vector of Brush 2, 50 km to the S. As the VLBI results indicate that the co-located Fort Ord S shows no significant changes in displacement rate or orientation (Fig. 5.4), it appears that the GPS-determined velocity of Brush 2 is in error. A large scatter in the east component of Brush 2 in the time-displacement plot in Fig. 5.11 may be caused by unresolved or incorrectly resolved ambiguities in several of the solutions used to compute this vector (M. Lisowski, pers. comm.). The uplift pattern determined from leveling (Fig. 5.13) is considered to be caused by transient deformation only. Geologic uplift rates (Chapter 4 this thesis) and uplift rates from our model of the pre-seismic deformation field are ≤ 1 mm/yr, one order of magnitude less than the measured uplift.

Alternative Models

The post-seismic displacement pattern following the Loma Prieta earthquake has also been interpreted by Linker and Rice (1991, 1993) and by Lisowski and others (1991a). Linker and Rice (1991, 1993) model the displacement field resulting from the interaction of the earthquake rupture with a linear viscoelastic relaxation zone below, that represents the deep aseismic portion of the fault. They also developed a non-linear model that assumes rate- and state-dependent friction on the deep aseismic region of the fault zone. Their models, involving a relatively deep deformation source below the coseismic rupture, predict the fault-parallel velocities of the Loma Prieta profile well, but do not predict the observed fault-normal velocity component and appear to overpredict the rates in the Black Mountain profile.

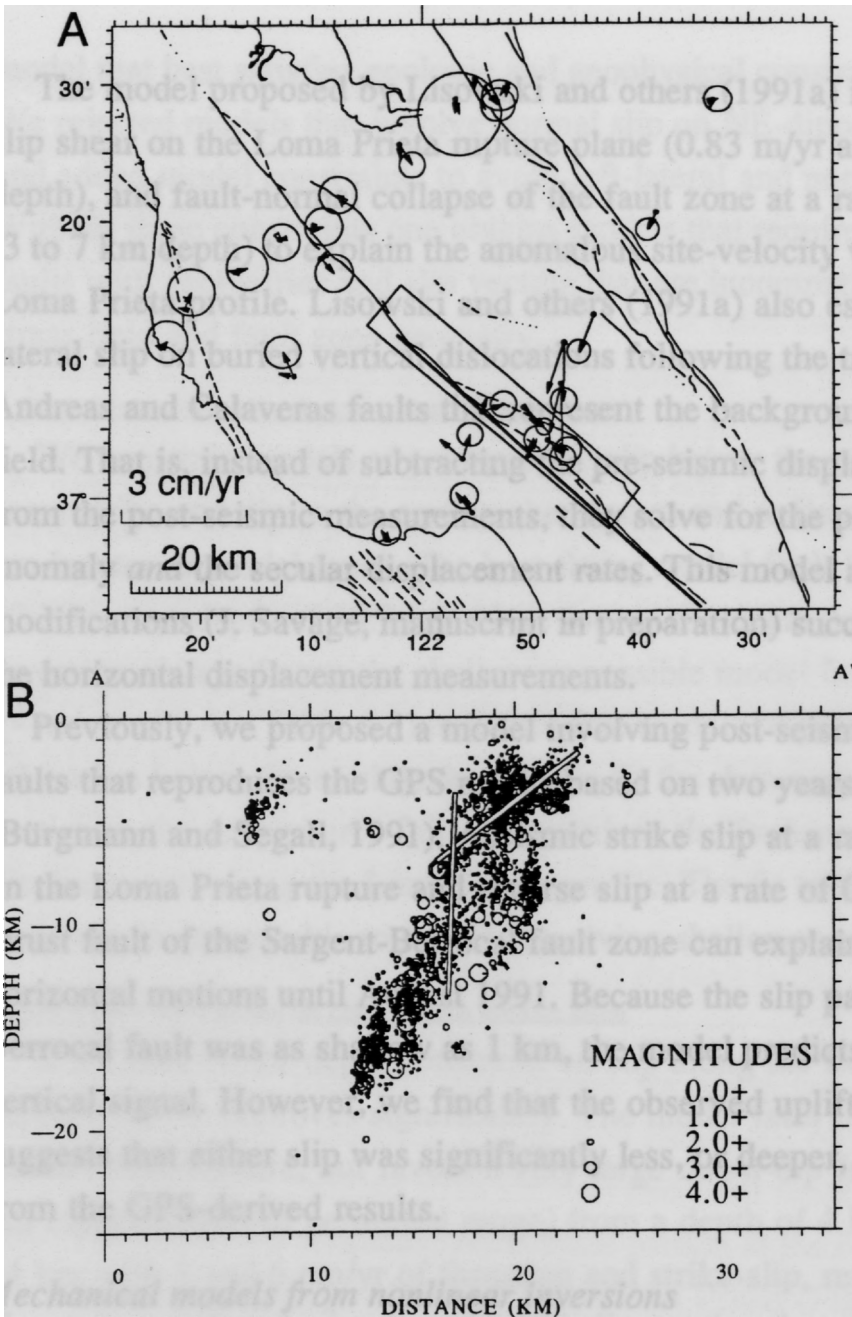


Fig. 5.15 (a) Post-seismic station velocities with pre-seismic displacement rates subtracted from measured rates. Also shown are the displacements computed from a boundary element model involving slip on two faults. The two rectangles show the projections of the faults used to compute the modeled station displacements. (b) Cross-section showing the two model faults and aftershocks. The first fault lies approximately in the vertical band of San Andreas fault seismicity above the Loma Prieta rupture, the second fault lies in a cluster of seismicity NE of the San Andreas fault.

The model proposed by Lisowski and others (1991a) involves strike-slip shear on the Loma Prieta rupture plane (0.83 m/yr at 4 to 11 km depth), and fault-normal collapse of the fault zone at a rate of 0.11 m/yr (3 to 7 km depth) to explain the anomalous site-velocity vectors along the Loma Prieta profile. Lisowski and others (1991a) also estimate right-lateral slip on buried vertical dislocations following the traces of the San Andreas and Calaveras faults that represent the background displacement field. That is, instead of subtracting the pre-seismic displacement field from the post-seismic measurements, they solve for the post-seismic anomaly *and* the secular displacement rates. This model and later modifications (J. Savage, manuscript in preparation) successfully predict the horizontal displacement measurements.

Previously, we proposed a model involving post-seismic creep on two faults that reproduces the GPS results based on two years of data (Bürgmann and Segall, 1991). Aseismic strike slip at a rate of 0.17 m/yr on the Loma Prieta rupture and reverse slip at a rate of 0.10 m/yr on a thrust fault of the Sargent-Berrocal fault zone can explain the observed horizontal motions until August 1991. Because the slip patch on the Berrocal fault was as shallow as 1 km, the model predicts a very large vertical signal. However, we find that the observed uplift (Fig. 5.14) suggests that either slip was significantly less, or deeper, than inferred from the GPS-derived results.

Mechanical models from nonlinear inversions

We model the displacements with rectangular dislocations in an elastic half-space (e.g., Okada, 1985). A nonlinear optimization algorithm is used to determine the fault parameters (length, depth, width, dip, strike, location, and the amounts of strike slip, dip slip, and opening) of one or two faults that best reproduce the GPS and leveling data by minimizing the weighted residual sum of squares (Williams et al., 1993, Arnadottir, Ph.D. thesis, 1993). We develop a series of models to evaluate the previously proposed models of post-seismic relaxation and to develop a

model that best satisfies geologic and geophysical constraints (Table 5.3). We rejected models that involve normal slip on NE-dipping fault planes and added model constraints to avoid left-lateral and normal fault slip. Without these constraints one obtains models that require slip on unknown faults with geometries and slip vectors that are incompatible with the local stress field and fault zone geometry.

1. Post-seismic relaxation below Loma Prieta rupture

We constrain models of post-seismic slip below the rupture to be of the same strike and dip as the earthquake rupture and to lie at a depth of 18 km (center of model fault). The best-fitting model fault lies at a depth of 17.3 km to a depth of 18.7 km. If we loosen the depth constraint, the inversion always favors the shallowest possible model fault. A reduced χ^2 -value of 8.46 (Table 5.3) indicates that models of post-seismic relaxation below the earthquake rupture fit the data very poorly. In particular the deep source fails to reproduce the fault-normal displacements along the Loma Prieta profile. The fit to the leveling data, however, is comparable to models involving shallower sources.

2. Slip and/or contraction on Loma Prieta rupture zone

If we remove the depth constraint on slip along the Loma Prieta rupture, the fit improves significantly. The model fault lies close to the Loma Prieta rupture, but favors a very large down-dip fault width of 20 km (upper bound of permitted range) from a depth of 4 km to a depth of 24 km with 3 and 6 cm/yr of thrusting and strike-slip, respectively. However, a reduced χ^2 -value of 7.46 indicates that the model is not able to adequately fit the data.

Lisowski and others (1991a) suggested that fault-zone compaction following the Loma Prieta rupture may explain the fault-normal motion. We find that the addition of opening motion to the list of fault parameters improves the model fit significantly (reduced χ^2 -value of 4.62). The inversion favors a fault of maximum permitted down-dip width from 4 to

24 km depth with 4 cm/yr of thrusting, 5 cm/yr of strike-slip, and 3 cm/yr of fault-zone compaction.

3. Slip and/or collapse on Loma Prieta rupture zone and creep below

We examine the displacements from slip and compaction along the Loma Prieta rupture together with accelerated fault creep below. This represents a combination of the previous models. We find that adding a second fault below the Loma Prieta rupture does not improve the model fit. The GPS and leveling data do not reveal any deep accelerated deformation below the Loma Prieta rupture.

4. Models including reverse fault slip northeast of San Andreas fault

We find that a model that includes slip on two faults, reverse and strike-slip on a vertical fault in the San Andreas fault zone and thrusting on a fault NE of the San Andreas, provides the best fit to the data (Fig. 5.15 and 5.16). The lengths of the model faults are not well constrained by the existing network and extend further than the coseismic Loma Prieta rupture.

The fit to the GPS results (Brush 2 not shown) is shown in Fig. 5.15a. We note that the model predicts the displacements well except for four stations (Fire, LP2, Mazzone and Calero), for which the model shows more northwesterly velocities. Figure 5.16 shows the observed and predicted elevation changes from the best two fault model. The model does not predict the continued subsidence pattern at the NE end of Line 4 and overpredicts uplift of the area near Loma Prieta (Fig. 5.14).

A reduced χ^2 -value of 3.4 indicates that the model does not fully explain the data within the reported errors. This may be caused by an underestimate of the errors in the determination of the post-seismic anomaly. Alternatively the misfit may indicate that our model insufficiently represents the physical processes responsible for the deformation. Material heterogeneities, multiple fault surfaces, complex slip distributions, and distributed inelastic deformation may contribute to the misfit.

Data	Model	Length along strike (km)	Depth to center (km)	Width along dip (km)	Dip (° SW)	Azimuth (°)	Location East (km)	Location North (km)	Dip-slip (m/yr)	Strike-slip (m/yr)	Opening (m/yr)	Chisq (GPS)	Chisq reduced
GPS & leveling	Down-dip of LP fault fault slip only	32.48	18	1.43	70	132	-3.44	-0.96	-0.29	1.90	<i>none</i>	688.5	794.9
GPS & leveling	"Loma Prieta fault" fault slip only	33.54	13.88	20*	70	132	-3.03	3.74	-0.03	0.06	<i>none</i>	540.3	663.7
GPS & leveling	"Loma Prieta fault" with fault zone collapse	37.42	14.16	20*	70	132	-1.49	2.25	-0.04	0.05	-0.03	313.1	411.0
GPS & leveling	LP fault slip & collapse and creep below	37.62	9.1	7.64	70	132	-0.86	4.82	-0.06	0.05	-0.04	298.1	392.9
GPS & leveling	2-fault model fault slip only	20.78	18	5	70	132	-2*	-2*	-0.09	0.33	<i>none</i>	182.9	264.8
GPS & leveling	2-fault model fault slip only	59.87	7.93	7.76	-89.96	138.91	7.71	-1.42	-0.06	0.05	<i>none</i>	182.9	264.8
		45*	4.52	8.26	-34.7	138.8	1*	6.85	-0.06	0*	<i>none</i>		

* Hit upper or lower boundary of parameter range

Table 5.3 Fault parameters for geodetically determined models from non-linear inversion of GPS and leveling data.

Locations of the center of the faults are given relative to the Loma Prieta mainshock hypocenter. A reduced chisq-value of one would indicate that the mechanical model fully represents the physical situation and that the error estimates are correct. Two-fault models and models with fault-zone collapse result in a better fit than models assuming one slipping fault.

Discussion of model results

We find that the observed post-seismic deformation does not suggest significant accelerated fault creep below the Loma Prieta rupture. Compaction and slip of the earthquake rupture at a few cm/yr may help explain some of the fault normal displacements, but does not provide a very good fit to the data. Our preferred model involves contemporaneous oblique-slip and thrust faulting at high rates on two faults with similar strikes. The inferred slip on the San Andreas fault from about 4 to 12 km depth may represent creep above and surrounding the two high-slip asperities that released most of the earthquake moment (Beroza, 1991, Hartzell et al., 1991, Steidl, 1991, Wald et al., 1991). The reverse component on the vertical San Andreas fault and thrusting NE of the San Andreas fault may be caused by the stress perturbation from the obliquely slipping Loma Prieta rupture (see below).

Fully unconstrained models favor normal slip on faults off any of the recognized faults in the area, but provide better fits. That is we had to add positivity constraints to restrict models to right-lateral strike slip and reverse slip. Reoccupation of a denser GPS network between and along the existing GPS profiles will provide the necessary control and resolution power to improve the models presented here.

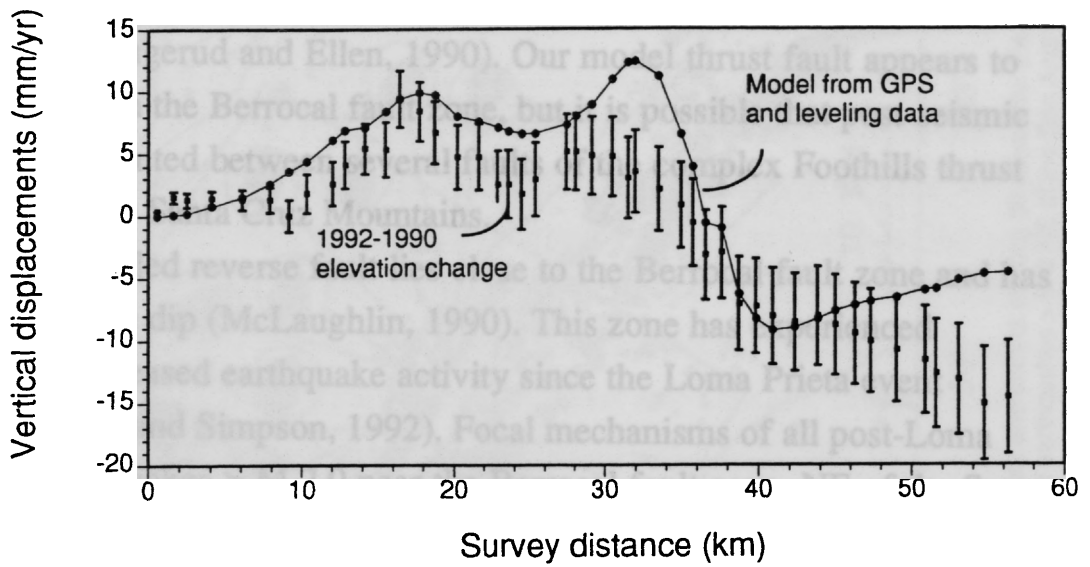


Fig. 5.16 Measured elevation changes (squares) and vertical displacements predicted from the two-fault model (circles) shown in Fig. 5.15. The model predicts the overall pattern of uplift, but overestimates uplift near 35 km and does not predict the continued drop off at the NE end of Line 4.

DISCUSSION

Thrusting Northeast of the San Andreas Fault

Northeast of the San Andreas fault are several sub-parallel SW-dipping faults, including the Monte Vista, Berrocal, and Shannon faults (Fig. 5.13, Aydin and Page, 1984), with a dominant component of thrust motion (McLaughlin, 1990). Some of these faults appear to have been active in the Quaternary as evidenced by offset young alluvial deposits and soil horizons (McLaughlin, 1990, Haugerud and Ellen, 1990). Broad zones of compressional surface deformation during the Loma Prieta earthquake follow the trend of these fault zones intermittently over a total distance of ~20 km (Haugerud and Ellen, 1990). Our model thrust fault appears to coincide with the Berrocal fault zone, but it is possible that post-seismic slip is distributed between several faults of the complex Foothills thrust system of the Santa Cruz Mountains.

The modeled reverse fault lies close to the Berrocal fault zone and has a comparable dip (McLaughlin, 1990). This zone has experienced strongly increased earthquake activity since the Loma Prieta event (Reasenber and Simpson, 1992). Focal mechanisms of all post-Loma Prieta earthquakes $> M 2.0$ near the Berrocal fault zone, NE of the San Andreas, indicate that these events occurred predominantly on reverse faults (Fig. 5.17). The seismicity near the Loma Prieta rupture on the other hand is very complex with all types of fault plane solutions (Oppenheimer, 1990). Note that the fault slip we model exceeds by several orders of magnitude the slip accumulated in aftershocks and must be aseismic.

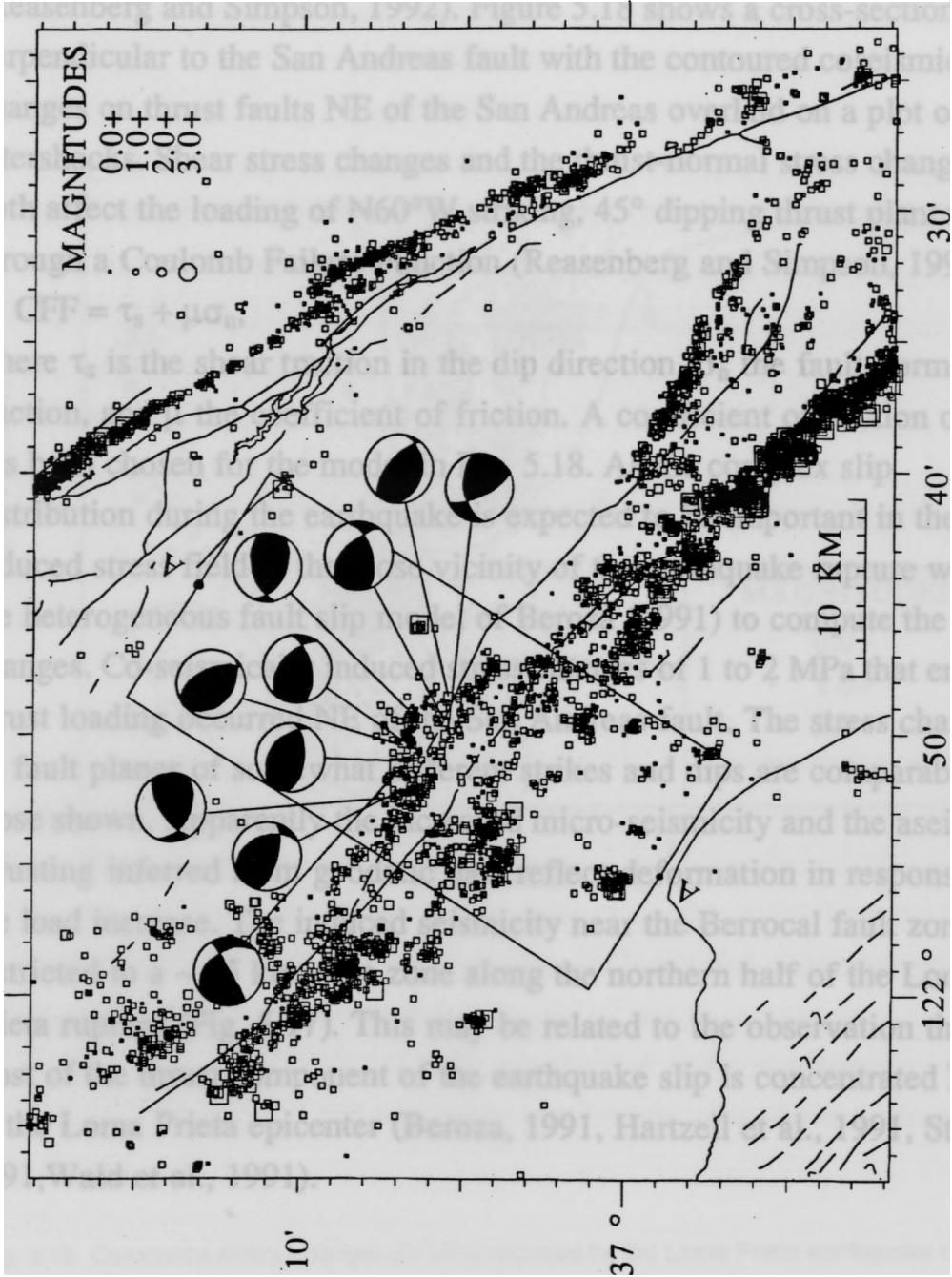


Fig. 5.17 Map view of Loma Prieta aftershocks starting 30 days after the Loma Prieta earthquake until October 1992 and focal plane solutions of earthquakes > M 2 NE of the San Andreas near the Berrocal fault zone.

Stress redistribution accompanying the Loma Prieta mainshock would increase the loading on thrust faults NE and updip of the rupture (Reasenber and Simpson, 1992). Figure 5.18 shows a cross-section perpendicular to the San Andreas fault with the contoured coseismic stress changes on thrust faults NE of the San Andreas overlaid on a plot of the aftershocks. Shear stress changes and the thrust-normal stress changes both affect the loading of N60°W striking, 45° dipping thrust planes through a Coulomb Failure Function (Reasenber and Simpson, 1992)

$$\text{CFF} = \tau_s + \mu\sigma_n,$$

where τ_s is the shear traction in the dip direction, σ_n the fault-normal traction, and μ the coefficient of friction. A coefficient of friction of 0.6 has been chosen for the model in Fig. 5.18. As the complex slip distribution during the earthquake is expected to be important in the induced stress field in the close vicinity of the earthquake rupture we used the heterogeneous fault slip model of Beroza (1991) to compute the stress changes. Co-seismically induced stress changes of 1 to 2 MPa that enhance thrust loading occurred NE of the San Andreas fault. The stress changes on fault planes of somewhat different strikes and dips are comparable to those shown. Apparently the increased micro-seismicity and the aseismic thrusting inferred from geodetic data reflect deformation in response to the load increase. The induced seismicity near the Berrocal fault zone is restricted to a ~ 15 km wide zone along the northern half of the Loma Prieta rupture (Fig. 5.17). This may be related to the observation that most of the thrust component of the earthquake slip is concentrated NW of the Loma Prieta epicenter (Beroza, 1991, Hartzell et al., 1991, Steidl, 1991, Wald et al., 1991).

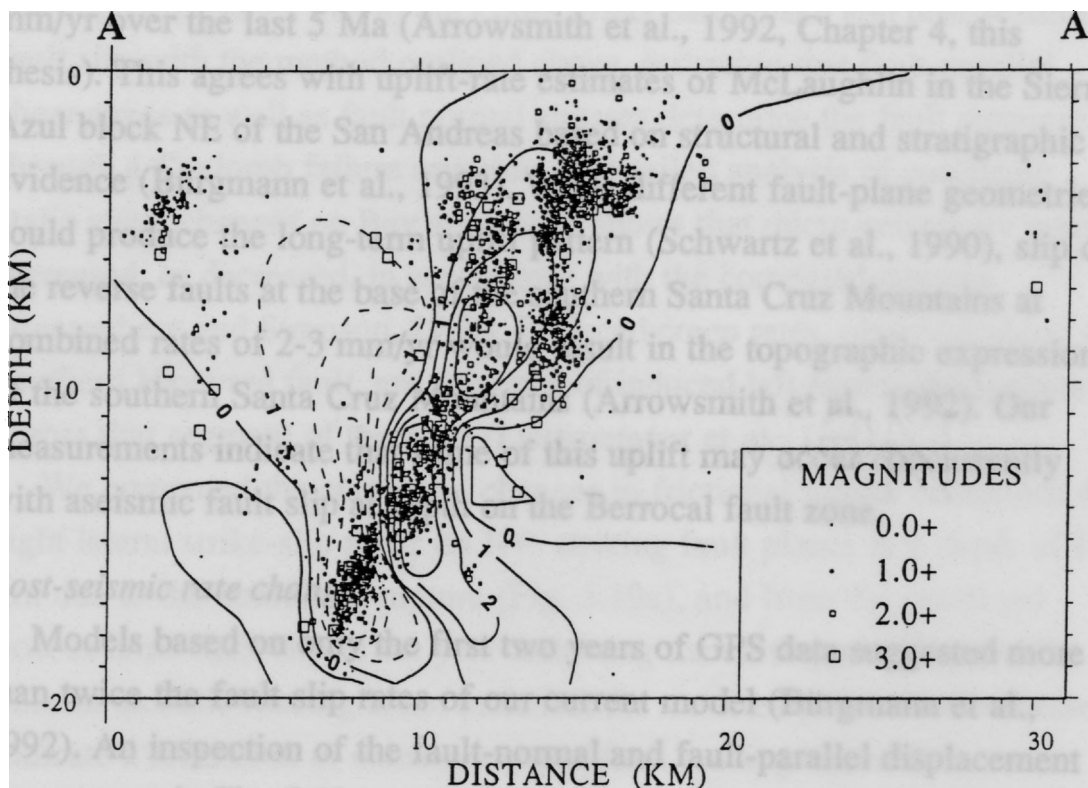


Fig. 5.18 Contoured stress changes (in MPa) induced by the Loma Prieta earthquake on 45° SW dipping fault planes. The coseismic displacement distribution determined by Beroza (1991) is discretized into 272 uniform slip fault elements in an elastic, isotropic, and homogeneous halfspace. Both fault-normal stresses and dip-parallel shear stresses influence the faults through a Coulomb failure criterion with a coefficient of friction $\mu = 0.6$.

An enigma associated with the Loma Prieta earthquake was the observation that the highest topography of the Santa Cruz Mountains around Loma Prieta subsided by ~10 cm during the earthquake (Lisowski et al., 1990a). Long term uplift rates in the Loma Prieta area deduced from apatite fission track dating and geomorphic analyses average about 1 mm/yr over the last 5 Ma (Arrowsmith et al., 1992, Chapter 4, this thesis). This agrees with uplift-rate estimates of McLaughlin in the Sierra Azul block NE of the San Andreas based on structural and stratigraphic evidence (Bürgmann et al., 1993). While different fault-plane geometries could produce the long-term uplift pattern (Schwartz et al., 1990), slip on the reverse faults at the base of the southern Santa Cruz Mountains at combined rates of 2-3 mm/yr would result in the topographic expression of the southern Santa Cruz Mountains (Arrowsmith et al., 1992). Our measurements indicate that some of this uplift may occur concurrently with aseismic fault slip at depth on the Berrocal fault zone.

Post-seismic rate changes

Models based on only the first two years of GPS data suggested more than twice the fault slip rates of our current model (Bürgmann et al., 1992). An inspection of the fault-normal and fault-parallel displacement components in Fig. 5.12 suggests that there may be a consistent decrease of the post-seismic rates, in particular the fault-normal displacements. Future work is planned to develop a model of the post-seismic deformation that includes a possible rate change in the analysis. Additional GPS surveys are needed to confirm the possible rate decay after about 2 years.

IMPLICATIONS FOR SEISMIC HAZARD IN THE SAN FRANCISCO BAY REGION

Continued slip at decimeter rates on faults in the San Francisco Bay region will change the loading of nearby segments of the San Andreas fault and the Hayward fault. We modeled the change in loading on NW striking fault planes due to the Loma Prieta earthquake and post-seismic fault slip with the method outlined above, assuming that fault-parallel shear stress as well as fault normal stresses determine the fault response through a Coulomb failure criterion. A detailed analysis of coseismic static stress changes on Bay area faults shows that micro-seismicity rates increased, or decreased, in accordance with the computed stresses (Reasenberg and Simpson, 1992). Reduced creep rates, observed along the southern Hayward fault, are evidence of induced left-lateral shear stress across that segment of the fault (Lienkaemper et al., 1992).

We computed the contoured changes in frictional failure conditions for right lateral strike-slip shear on NW striking fault planes at a depth of 10 km due to the coseismic rupture (Fig. 5.19a), and from the predicted post-seismic fault slip in the year following the earthquake (Fig. 5.19b). Secular tectonic loading is not included, the modeled post-seismic stresses indicate a relaxation or enhancement of fault loading above the background. The results are only directly applicable to N45°W striking fault planes, however, deviations of fault strike by up to 10° do not change the pattern significantly. We find that the post-seismic fault slip further increases the load on the San Andreas fault immediately to the NW of the Loma Prieta rupture, while the combined coseismic and post-seismic effects have a retarding effect on the Hayward fault zone and most of the Calaveras and San Gregorio-Hosgri fault zones. The yearly post-seismic stress changes are about an order of magnitude less than those induced coseismically. If the Loma Prieta earthquake stress changes advanced the occurrence of the next earthquake N of the rupture by 2-25 years (Reasenberg and Simpson, 1992), then the post-seismic changes enhance this effect by almost 10% per year.

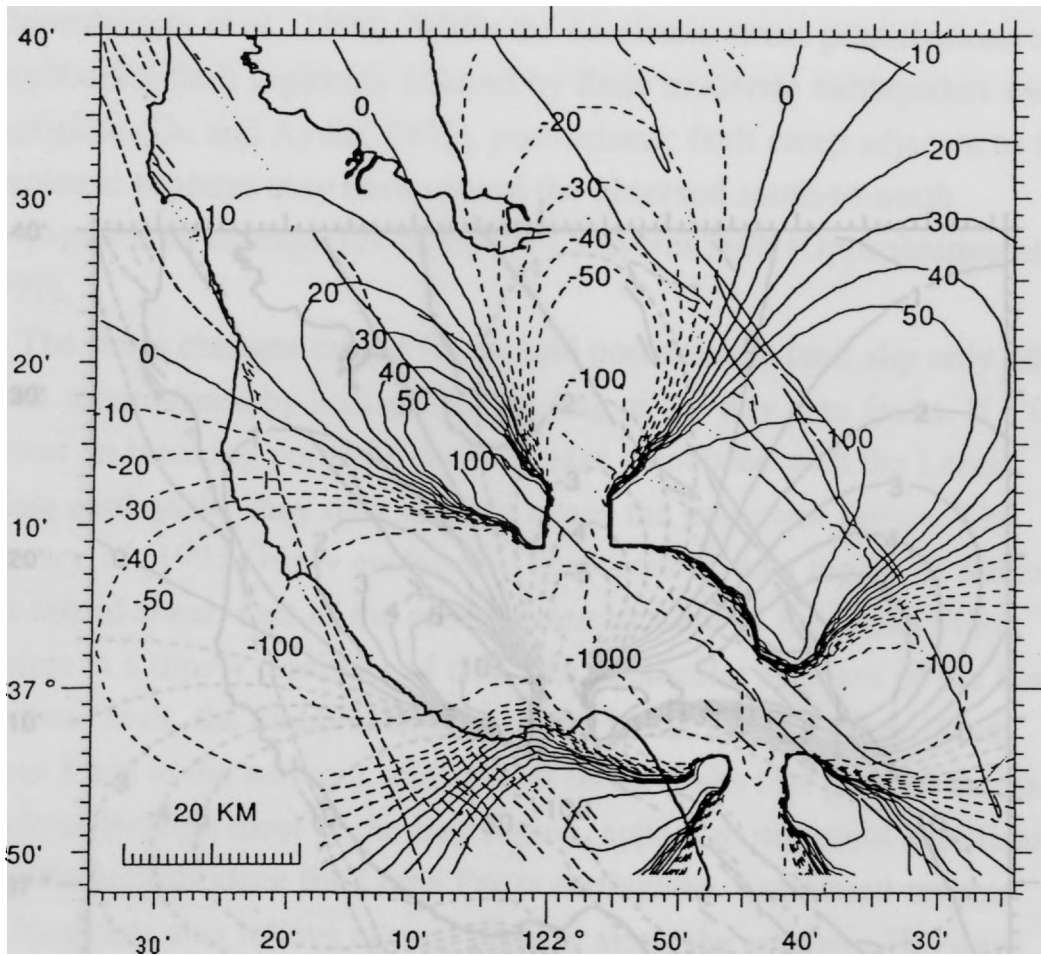


Fig. 5.19 (a) Horizontal stress changes (in kPa) at 10 km depth on N45°W striking strike-slip faults caused by the Loma Prieta earthquake. Both fault-normal stresses and dip-parallel shear stresses effect the loading of the fault through a Coulomb failure criterion assuming a coefficient of friction $\mu = 0.6$. The peninsular segment of the San Andreas fault, the northernmost segment of the creeping section of the San Andreas, and the central Calaveras fault experienced increased right-lateral stress (positive), whereas the San Gregorio-Hosgri and the southern Hayward fault show a stress decrease.

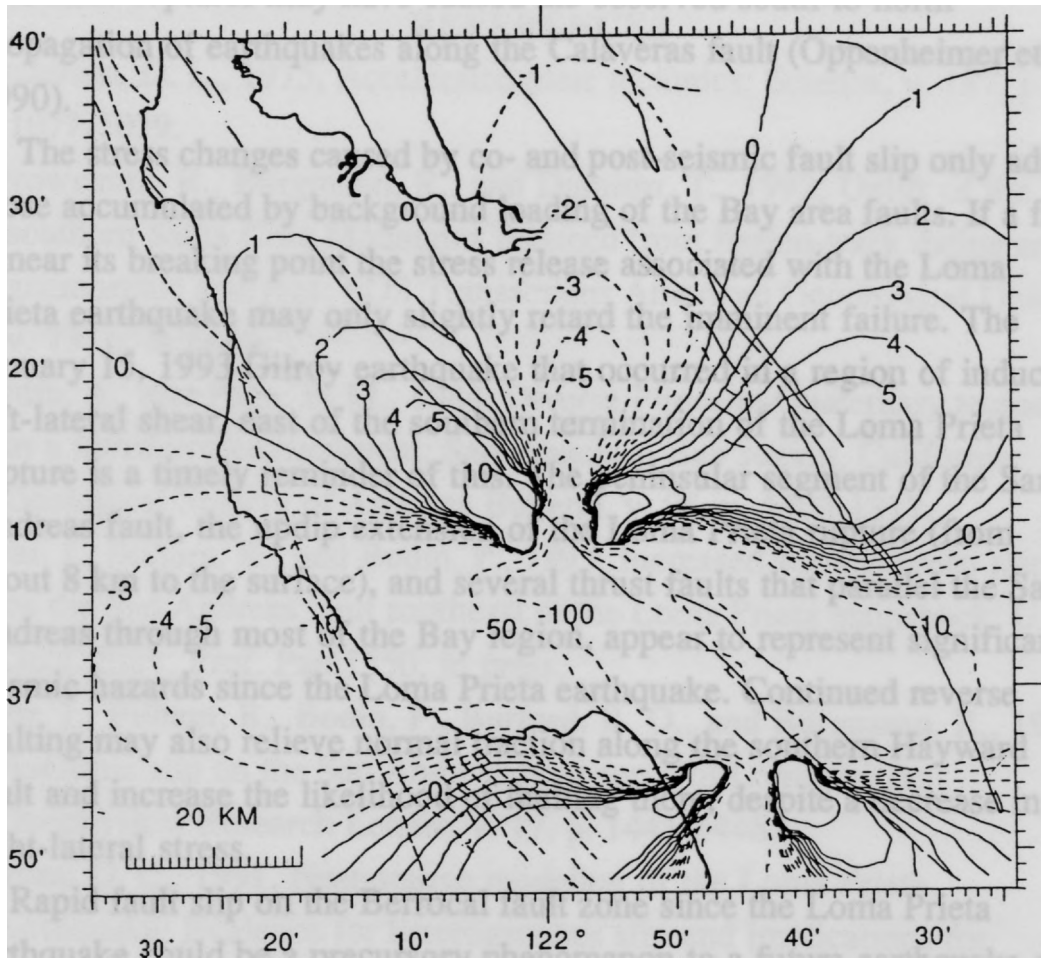


Fig. 5.19 cont. (b) Stress changes (in kPa) induced by post-seismic slip inferred from geodetic data. The pattern of post-seismic stress changes is similar, but of lower magnitude, to the coseismically induced static stress changes.

Similar post-seismic adjustments occurred following the 1979 Coyote Lake and the 1984 Morgan Hill earthquakes along the Calaveras fault (Oppenheimer et al., 1990). While the coseismic stress perturbations on neighboring fault segments induced by these moderate earthquakes were negligible (Du and Aydin, 1993), post-seismic fault creep adjacent to the coseismic ruptures may have caused the observed south-to-north propagation of earthquakes along the Calaveras fault (Oppenheimer et al., 1990).

The stress changes caused by co- and post-seismic fault slip only add to those accumulated by background loading of the Bay area faults. If a fault is near its breaking point the stress release associated with the Loma Prieta earthquake may only slightly retard the imminent failure. The January 15, 1993 Gilroy earthquake that occurred in a region of induced left-lateral shear, east of the southern termination of the Loma Prieta rupture is a timely reminder of this. The peninsular segment of the San Andreas fault, the updip extension of the Loma Prieta rupture (from about 8 km to the surface), and several thrust faults that parallel the San Andreas through most of the Bay region, appear to represent significant seismic hazards since the Loma Prieta earthquake. Continued reverse faulting may also relieve normal traction along the southern Hayward fault and increase the likelihood of faulting there, despite a decrease in right-lateral stress.

Rapid fault slip on the Berrocal fault zone since the Loma Prieta earthquake could be a precursory phenomenon to a future earthquake on this fault. While records of historic seismicity in the area reach only as far back as the early 19th century, they show that the last 80 years have been marked by unusual seismic quiescence. In 1865, a $\sim M 6.5$ earthquake may have ruptured a thrust fault NE of the San Andreas with two $> M 5$ foreshocks in the preceding year (Tuttle and Sykes, 1992). This earthquake was preceded by a $M \sim 7$ break in 1838 that involved the peninsular San Andreas fault segment and maybe the Loma Prieta fault segment, and followed in 1868 by a large earthquake on the southern

Hayward fault (e.g., Tuttle and Sykes, 1992). An earthquake comparable to the 1865 event constitutes a significant hazard to the south San Francisco Bay region. Our results suggest one possible mechanism by which earthquakes may influence the seismicity in the region in the years following the original rupture.

REFERENCES

- Anderson, D. L., 1975, Accelerated plate tectonics: *Science*, v. 187, p. 1077-1079.
- Arrowsmith, R., Bürgmann, R., and Dumitru, T., 1992, Uplift of the southern Santa Cruz Mountains deduced from fission-track dating and geomorphic analyses: *EOS Transactions American Geophysical Union*, v. 73, p. in press.
- Aydin, A., and Page, B. M., 1984, Diverse Pliocene-Quaternary tectonics in a transform environment, San Francisco Bay region, California: *Geological Society of America Bulletin*, v. 95, p. 1303-1317.
- Behr, J., Bilham, R., and Bodin, P., 1993, Increased surface creep rates on the San Andreas fault southeast of the Loma Prieta mainshock: *U.S. Geol. Surv. Prof. Pap.* 1550, in press.
- Behr, J., Bilham, R., Bodin, P., Burford, R. O., and Bürgmann, R., 1990, Aseismic slip on the San Andreas fault south of Loma Prieta: *Geophysical Research Letters*, v. 17, p. 1445-1448.
- Beroza, G. C., 1991, Near-source modeling of the Loma Prieta earthquake: Evidence for heterogeneous slip and implications for earthquake hazard: *Bulletin of the Seismological Society of America*, v. 81, p. 1603-1621.
- Bilham, R., 1989, Surface slip subsequent to the 24 November 1987 Superstition Hills, California, earthquake monitored by digital creepmeters: *Bulletin of the Seismological Society of America*, v. 79, p. 424-450.

- Blewitt, G., 1989, Carrier phase ambiguity resolution for the Global Positioning System applied to geodetic baselines up to 2000 km: *Journal of Geophysical Research*, v. 94, p. 10187-10203.
- Bott, N. H. P., and Dean, D. S., 1973, Stress diffusion from plate boundaries: *Nature*, v. 243, p. 339-341.
- Budianski, B., and Amazigo, C., 1976, Interaction of fault slip and lithosphere creep: *Journal of Geophysical Research*, v. 81, p. 4897-4900.
- Bürgmann, R., Arrowsmith, R., Dumitru, T., and McLaughlin, R., 1993, Rise and fall of the southern Santa Cruz Mountains, California, deduced from fission track dating, geomorphic analysis, and geodetic data: *Journal of Geophysical Research*, in review.
- Bürgmann, R., and Segall, P., 1991, Postseismic GPS monitoring NW of the 1989 Loma Prieta rupture zone: *EOS Transactions American Geophysical Union*, v. 72, p. 119.
- Bürgmann, R., Segall, P., Lisowski, M., and Svarc, J. P., 1992, Rapid aseismic slip on the Berrocal fault zone following the Loma Prieta earthquake: *EOS Transactions American Geophysical Union*, v. 73, p. 119.
- Clark, T. A., Ma, C., Sauber, J. M., Ryan, J. W., Gordon, D., Shaffer, D. B., Caprette, D. S., and Vandenberg, N. R., 1990, Geodetic measurements of deformation in the Loma Prieta, California earthquake with Very Long Baseline Interferometry.: *Geophysical Research Letters*, v. 17, p. 1215-1218.
- Cohen, S. C., 1979, Postseismic surface deformations due to lithospheric and asthenospheric viscoelasticity: *Geophysical Research Letters*, v. 6, p. 129-131.
- Davis, J. L., Prescott, W. H., Svarc, J. L., and Wendt, K. J., 1989, Assesment of Global Positioning System measurements for studies of crustal deformation: *Journal of Geophysical Research*, v. 94, p. 13635-13650.

- Dietz, L. D., and Ellsworth, W. L., 1990, The October 17, 1989, Loma Prieta, California, earthquake and its aftershocks: Geometry of the sequence from high-resolution locations: *Geophysical Research Letters*, v. 17, p. 1417-1420.
- Dixon, T. H., 1991, An introduction to the global positioning system and some geological applications: *Reviews of Geophysics*, v. 29, p. 249-276.
- Du, Y., and Aydin, A., 1993, Stress transfer during three sequential moderate earthquakes along the central Calaveras fault, California: *Journal of Geophysical Research*, v. 98, p. 9947-9962.
- Du, Y., Aydin, A., and Segall, P., 1992, Comparison of various inversion techniques as applied to the determination of a geophysical deformation model for the 1983 Borah Peak earthquake: *Bulletin of the Seismological Society of America*, v. 82, p. 1840-1866.
- Ellsworth, W. L., 1990, Earthquake history, 1769-1989 *in* Wallace, R. E., ed., *The San Andreas fault system, California, U.S. Geological Survey Professional Paper 1515*, p. 153-181.
- Gwyther, R. L., Gladwin, M. T., and Hart, R. H. G., 1992, A shear strain anomaly following the Loma Prieta earthquake: *Nature*, v. 356, p. 142-144.
- Hager, B. H., King, R. W., and Murray, M. H., 1991, Measurements of crustal deformation using the Global Positioning System: *Annual Review of Earth and Planetary Sciences*, v. 19, p. 351-382.
- Hartzell, S. H., Stewart, G. S., and Mendoza, C., 1991, Comparison of L_1 and L_2 norms in a teleseismic waveform inversion for the slip history of the Loma Prieta, California, earthquake: *Bulletin of the Seismological Society of America*, v. 81, p. 1518-1539.
- Haugerud, R. A., and Ellen, S. D., 1990, Coseismic ground deformation along the northeast margin of the Santa Cruz Mountains *in* Schwartz, D. P., and Ponti, D. J., ed., *Field guide to neotectonics of the San Andreas fault system, Santa Cruz Mountains, in light of the Loma*

- Prieta earthquake: U.S. Geological Survey, Open File Report, 90-274, p. 32-37.
- Kasahara, K., 1981, Earthquake mechanics: Cambridge Earth Science Series, Cambridge, Cambridge University Press, 248 p.
- King, G. C. P., Lindh, A. G., and Oppenheimer, D. H., 1990, Seismic slip, segmentation, and the Loma Prieta earthquake: Geophysical Research Letters, v. 17, p. 1449-1452.
- Kovach, R. L., and Beroza, G. C., 1993, Seismic potential from reverse faulting on the San Francisco Peninsula: Bulletin of the Seismological Society of America, in press.
- Langbein, J. O., 1990, Post-seismic slip on the San Andreas fault at the northwestern end of the 1989 Loma Prieta earthquake rupture zone: Geophysical Research Letters, v. 17, p. 1223-1226.
- Larson, K. M., and Agnew, D. C., 1991, Application of the Global Positioning System to crustal deformation measurements 1. Precision and accuracy: Journal of Geophysical Research, v. 96, p. 16547-16565.
- Larson, K. M., Webb, F. H., and Agnew, D. C., 1991, Application of the Global Positioning System to crustal deformation measurements 2. The influence of errors in orbit determination networks: Journal of Geophysical Research, v. 96, p. 16567-16584.
- Lawson, J. J., 1908, The California earthquake of April 18, 1906: Report of the State Earthquake Investigation Commission: Carnegie Institution of Washington Publication, v. 87,
- Lehner, F. K., Li, V. C., and Rice, J. R., 1981, Stress diffusion along rupturing plate boundaries: Journal of Geophysical Research, v. 86, p. 6155-6169.
- Li, V. C., and Rice, J. R., 1987, Crustal deformation in great California earthquake cycles: J.Geophys.Res., v. 92, p. 11533-11551.
- Lienkaemper, J. J., Galehouse, J. S., and Simpson, R. W., 1992, Hayward fault, California: Longterm creep rates versus slower creep since 1989 Loma Prieta earthquake: EOS Transactions American Geophysical Union, v. 73, p. 119.

- Linker, M. F., and Rice, J. R., 1991, The effective viscosity of the San Andreas fault beneath the seismogenic zone: Constraints from the response to the 1989 Loma Prieta earthquake: EOS Transactions American Geophysical Union, v. 72, p. 310-311.
- Linker, M. F., and Rice, J. R., 1993, Models of postseismic deformation and stress transfer associated with the 1989 Loma Prieta earthquake: U.S. Geol. Surv. Prof. Pap. 1550, in press.
- Lisowski, M., Prescott, W. H., Savage, J. C., and Johnston, M. J., 1990a, Geodetic estimate of coseismic slip during the 1989 Loma Prieta, California earthquake: Geophysical Research Letters, v. 17, p. 1437-1440.
- Lisowski, M., Prescott, W. H., Savage, J. C., and Svarc, J. L., 1990b, A possible geodetic anomaly observed prior to the Loma Prieta, California, earthquake: Geophysical Research Letters, v. 17, p. 1211-1214.
- Lisowski, M., Savage, J. C., and Prescott, W. H., 1991a, Surface deformation after the Loma Prieta, California, earthquake: EOS Transactions American Geophysical Union, v. 72, p. 119.
- Lisowski, M., Savage, J. C., and Prescott, W. H., 1991b, The velocity field along the San Andreas fault in central and southern California: Journal of Geophysical Research, v. 96, p. 8369-8389.
- Marshall, G. A., Stein, R. S., and Thatcher, W., 1991, Faulting geometry and slip from co-seismic elevation changes: The October 17, 1989 Loma Prieta, California, earthquake: Bulletin of the Seismological Society of America, v. 81, p. 1660-1693.
- Matsu'ura, M., Jackson, D. D., and Cheng, A., 1986, Dislocation model for aseismic crustal deformation at Hollister, California: Journal of Geophysical Research, v. 91, p. 12661-12674.
- McLaughlin, R., 1990, Stop 4. Sargent fault zone at Loma Prieta *in* Schwartz, D. D., and Ponti, D. J., ed., Field guide to neotectonics of the San Andreas fault system, Santa Cruz Mountains, in light of the 1989

- Loma Prieta earthquake: Menlo Park, U.S. Geological Survey Open File Report, 90-274, p. 19-22.
- Nur, A., and Mavko, G., 1974, Postseismic viscoelastic rebound: *Science*, v. 183, p. 204-206.
- Okada, Y., 1985, Surface deformation due to shear and tensile faults in a half-space: *Bulletin of the Seismological Society of America*, v. 75, p. 1135-1154.
- Oppenheimer, D. H., 1990, Aftershock slip behavior of the 1989 Loma Prieta, California earthquake: *Geophysical Research Letters*, v. 17, p. 1199-1202.
- Oppenheimer, D. H., Bakun, W. H., and Lindh, A. G., 1990, Slip partitioning of the Calaveras fault, California, and prospects for future earthquakes: *Journal of Geophysical Research*, v. 95, p. 8483-8498.
- Reasenber, P. A., and Simpson, R. W., 1992, Response of regional seismicity to the static stress change produced by the Loma Prieta earthquake: *Science*, v. 255, p. 1687-1690.
- Rundle, J. B., and Jackson, D. D., 1977, A three-dimensional viscoelastic model of a strike-slip fault: *Geophys. J. R. Astron. Soc.*, v. 49, p. 575-591.
- Rymer, M. J., 1990, Near-fault measurement of postseismic slip associated with the 1989 Loma Prieta, California, earthquake: *Geophysical Research Letters*, v. 17, p. 1789-1792.
- Savage, J. C., 1971, A theory of creep waves propagating along a transform fault: *Journal of Geophysical Research*, v. 76, p. 1954-1966.
- Savage, J. C., and Prescott, W. H., 1978, Asthenosphere readjustment and the earthquake cycle: *Journal of Geophysical Research*, v. 83, p. 3369-3376.
- Scholz, C. H., 1977, A physical interpretation of the Haicheng earthquake prediction: *Nature*, v. 267, p. 121-124.
- Schwartz, S. Y., Orange, D. L., and Anderson, R. S., 1990, Complex fault interactions in a restraining bend on the San Andreas fault,

- southern Santa Cruz Mountains, California: *Geophysical Research Letters*, v. 17, p. 1207-1210.
- Smith, S. W., and Wyss, M., 1968, Displacement on the San Andreas fault subsequent to the 1966 Parkfield earthquake: *Bulletin of the Seismological Society of America*, v. 58, p. 1955-1973.
- Snay, R. A., Neugebauer, H. C., and Prescott, W. H., 1991, Horizontal deformation associated with the Loma Prieta earthquake: *Bulletin of the Seismological Society of America*, v. 81, p. 1647-1659.
- Steidl, J. H., Archuleta, R. J., and Hartzell, S. H., 1991, Rupture history of the 1989 Loma Prieta, California, earthquake: *Bulletin of the Seismological Society of America*, v. 81, p. 1573-1602.
- Stein, R. S., 1981, Discrimination of tectonic displacement from slope-dependent errors in geodetic leveling from southern California, 1953-1979 *in Earthquake Prediction - An International Review*, Maurice Ewing Series: American Geophysical Union, 4, p. 441-456.
- Thatcher, W., 1974, Strain release mechanism of the 1906 San Francisco earthquake: *Science*, v. 184, p. 1283-1285.
- Thatcher, W., 1983, Nonlinear strain buildup and the earthquake cycle on the San Andreas fault: *Journal of Geophysical Research*, v. 88, p. 5893-5902.
- Thatcher, W., 1986, Cyclic deformation related to great earthquakes at plate boundaries *in Recent Crustal Movements of the Pacific Region*: Wellington, New Zealand, Royal Society of New Zealand Bulletin, 24, p. 245-272.
- Toksöz, M. N., Shakal, A. F., and Michael, A. J., 1979, Space-time migration of earthquakes along the North Anatolian fault zone and seismic gaps: *Pure and Applied Geophysics*, v. 117, p. 1258-1270.
- Tuttle, M. P., and Sykes, L. R., 1992, Re-evaluation of several large historic earthquakes in the vicinity of the Loma Prieta and Peninsular segments of the San Andreas fault, California: *Bulletin of the Seismological Society of America*, v. 82, p. 1802-1820.

- Wald, D. J., Helmberger, D. V., and Heaton, T. H., 1991, Rupture model of the 1989 Loma Prieta earthquake from the inversion of strong-motion and broadband teleseismic data: *Bulletin of the Seismological Society of America*, v. 81, p. 1540-1572.
- Williams, C. R., Arnadottir, T., and Segall, P., 1993, Coseismic deformation and dislocation models of the 1989 Loma Prieta earthquake derived from Global Positioning System measurements: *Journal of Geophysical Research*, v. 98, p. 4567-4578.
- Williams, C. R., and Segall, P., 1992, 1989 Loma Prieta earthquake displacements measured with the Global Positioning System: *U.S. Geol. Surv. Prof. Pap. 1550*, in press.
- Wood, M. D., and Allen, S. S., 1973, Recurrence of seismic migrations along the central California segment of the San Andreas fault system: *Nature*, v. 244, p. 213-215.